UNIVERSITY COLLEGE LONDON

Faculty of Mathematics and Physical Sciences

Department of Physics & Astronomy

A MID-INFRARED STUDY OF DUST EMISSION FROM CORE-COLLAPSE SUPERNOVAE

Thesis submitted for the Degree of Doctor of Philosophy
of the University of London

by

Joanna Natalina Fabbri

Supervisors:

Prof. Michael J. Barlow

Prof. Jonathan M. C. Rawlings

Examiners:

Prof. Stephen Eales

Dr. Serena Viti

May 13, 2011

To my family and friends, without whom this journey would not have been possible.

Declaration

I, Joanna Natalina Fabbri, confirm that the work presented in this thesis is my own. Where information has been derived from other sources, I confirm that this has been indicated in the thesis.

"Share your knowledge. It is a way to achieve immortality."

– The Dalai Lama

"I don't want to achieve immortality through my work...
...I want to achieve it through not dying."

– Woody Allen

Abstract

The aim of this thesis has been to help elucidate the potential contribution of core-collapse supernovae (SNe) to the dust-enrichment of galaxies. It has long been hypothesised that SNe are a major source of dust in the Universe, an assumption that has gained support with the discovery that many of the earliest-formed galaxies are extremely dusty and infrared-luminous, as evidenced by the efficient detection of their redshifted infrared emission at submillimeter wavelengths. Massive-star, core-collapse SNe, of Types II, Ib and Ic, arising from the starbursts that power these galaxies, are plausible sources of this dust. However, very little is currently known about how much dust forms in SN outflows. To this end, sensitive mid-infrared surveys for thermal dust emission from recent core-collapse SNe have been conducted with the *Spitzer Space Telescope* and mid-infrared detectors on the Gemini telescopes, in order to seek evidence for dust formation and evolution in SN ejecta. Of the 30 SNe observed, only *five* were robustly detected. These were comprised of four Type II-P SNe: SN 2002hh, SN 2003gd, SN 2004dj and SN 2004et; and the Type IIn SN 1999bw. The mid-infrared data of SN 2004et were incorporated with optical and near-infrared data to provide a comprehensive study of this SN from days 64 to 2151 post explosion. Radiative transfer models predict up to $1.5{\times}10^{-3}$ $M_{\odot}$ of dust had condensed in the ejecta of SN 2004et by day 690. Upper limits to mid-infrared fluxes are presented for 25 supernova and used to obtain upper limits to their dust masses in the mid-infrared. The results from this research add to the weight of observational evidence which suggests the ejecta of core-collapse SNe do not produce sufficient dust, at least during the first 3 or 4 years after outburst, to explain the masses of dust derived for some galaxies in the early Universe.

Acknowledgements

The first thank you goes to my PhD supervisor Mike Barlow whose unwavering help and support have been above and beyond the call of duty. Your infallible wisdom and famous red pen have helped me to achieve this PhD, and I am immensely grateful for the opportunities you have provided me with, and for your encouragement and reassurance right to the end.

To my parents and to my sister, thank you for your unconditional love, patience and support. You have no idea. I literally couldn't have done it without you. Mum, your home-cooked meals made the numerous occasions of three meals a day at my desk bearable and delicious, as did your pizzas, Dad! Thank you for providing the roof over my head which allowed me the luxury of completing this PhD, and for not asking too many questions (even when it was driving you crazy not to). Vicky, thank you for your generosity, for understanding me, for running with me and for keeping me sane.

To my boyfriend, Fab. My best friend. Whilst each has played their own important part in helping me to achieve this PhD, I seriously doubt I could have seen it through to the end without you. You have been my constant and my rock, through both the darkest and the happiest moments. To have shared this experience with you was alone worth doing the PhD for. Thank you is not enough... but one day we will both go to Hawaii!

My time at UCL has been *long* and I have many colleagues/friends/office mates, past and present, to thank for helping make the tough times easier and the whole experience much more pleasurable. Not all are mentioned here, but you know who you are. In no particular order, special thanks to Barbara Ercolano, Sam Searle, Simon Hodges, Will Nicholson, Iris Yiu, Dugan Witherick, Fiona Groenhout (honorary astronomer), John Deacon, Adam Burnley, Matt North, Nutan Rajguru, Bethan James and Jamie Noss.

All those thesis-encouraging and (equally important) thesis-distracting chats, the late-night Housman Room sessions, the good food shared, and the runs around Regent's Park - we have had truly great times and I have so many happy memories. Roger Wesson gets a special thank you for his time answering all those Questions I Couldn't Ask Mike, and for the split eye when playing squash! It's been a pleasure.

I would also like to thank all the SEEDS members, particularly Ben Sugerman for mentoring me in the practicalities of research and for the occasional 'tough love' email. Thank you for your extensive time and friendship.

To all my friends and family whom I love dearly, and with whom spending time with has often been sacrificed in the pursuit of this PhD, thank you for your patience, love and support. To name a few names: Gemma, Tara, Sarah, Sara, Jessica, Eve, Emma, Catherine, Amira, the Sidoli's, Gerard, and my Nan. But there are more of you and you are all just as important.

A final thank you to George, Arnaud and Isaac for their happiness, friendship and JD and cokes, during those numerous visits to the Housman Room. I must also mention the many staff of ULU Gordons cafe for their supply of caffeine and pain au chocolate - a small slice of romance to start (many of) my thesis-writing days!

Thank you. Grazie. Arigato gozaimashita. Gamsa hamnida. Mahalo.

Contents

List of Figures

List of Tables

Chapter 1

Introduction

1.1 The role of interstellar dust in astrophysics

Interstellar dust is pervasive, existing in a wide variety of astrophysical environments. These submicron-sized grains, predominantly of carbonaceous and siliceous composition, are found in the interplanetary medium of our solar system; the circumstellar media of evolved stars; the interstellar medium (ISM) of normal galaxies like the Milky Way; in star formation regions of nearby and distant (extremely luminous) galaxies; as well as in circumnuclear tori around active galactic nuclei; and in proto-planetary disks around massive young stellar objects (Li 2009).

By scattering, absorbing and re-emitting light to longer wavelengths, these grains affect our view of the Universe. It was via the obscuration of starlight that the existence of interstellar dust was first inferred (Trumpler 1930) and, for the same reason, was historically considered as somewhat of an astrophysical nuisance that needed to be corrected to interpret the observations. However, this view changed radically in the following decades, particularly with the advent of infrared and submillimetre telescopes, and the study of dust is now arguably among the most important fields of modern astronomy.

Although dust constitutes only about 1 % of the interstellar mass (e.g., Whittet 2003), it is the dominant opacity source and thus plays a key role in regulating the energy balance of the ISM. It makes a significant contribution both as a heating agent for the interstellar gas via the emission of photoelectrons where ultra-violet (UV) fields are present, and as

a coolant in dense regions via infrared emission (Draine 2003). Interstellar dust also has a crucial impact on the chemistry of the ISM, acting as a sink of heavy elements, and as an effective catalyst for the formation of molecular hydrogen and other molecules, as well as acting as a shield from photodissociating UV photons in dense clouds (Li 2009). The same dust provides the basic building blocks for the formation of planetesimals in protoplanetary disks around main-sequence stars, and is potentially important in the synthesis of organic molecules which lead to life (Boulanger et al. 2000).

Interstellar dust can clearly have a far-reaching impact upon many aspects of astrophysics. Yet the origin of these grains and how efficiently they are produced and destroyed is still uncertain.

1.2 The life cycle of interstellar dust

Since dust is formed from heavy elements in the gas phase, it follows that the life cycle of dust is intimately associated with the evolution of the stars in whose interiors chemical elements are synthesised via nuclear burning processes, and then ejected during the last stages of their lives. The dust cycle begins with the nucleation and growth of condensates in the envelopes of these evolved stars, which are rapidly mixed with other gas and dust in the ISM (Whittet 2003; Tielens et al. 2005). In the ISM, dust is subjected to cycles of destruction and reformation. Dust is swept up and processed by the strong expanding shocks of supernova explosions, subjecting them to various destructive processes, including thermal sputtering, vaporisation, and shattering of large grains into smaller fragments via collisions (Barlow 1978; Dwek 1998). In the denser regions of molecular clouds ($n_H \geq 10^3\,\mathrm{cm}^{-3}$) grain growth can occur through ice mantle formation and coagulation. Cloud collapse and star formation incorporates some of this dust into young stars, and a further fraction will be included in the surrounding planet-forming disk. The complete cycle, from injection by a star until formation of a new star or associated planets, is estimated to typically take $\sim 2 \times 10^9$ years, by Tielens et al. (2005), who have summarised current estimates for the gas and dust inputs to the ISM of our galaxy from various classes of evolved stars. Their review highlights the large uncertainties in dust mass injection rates for some of these stellar types.

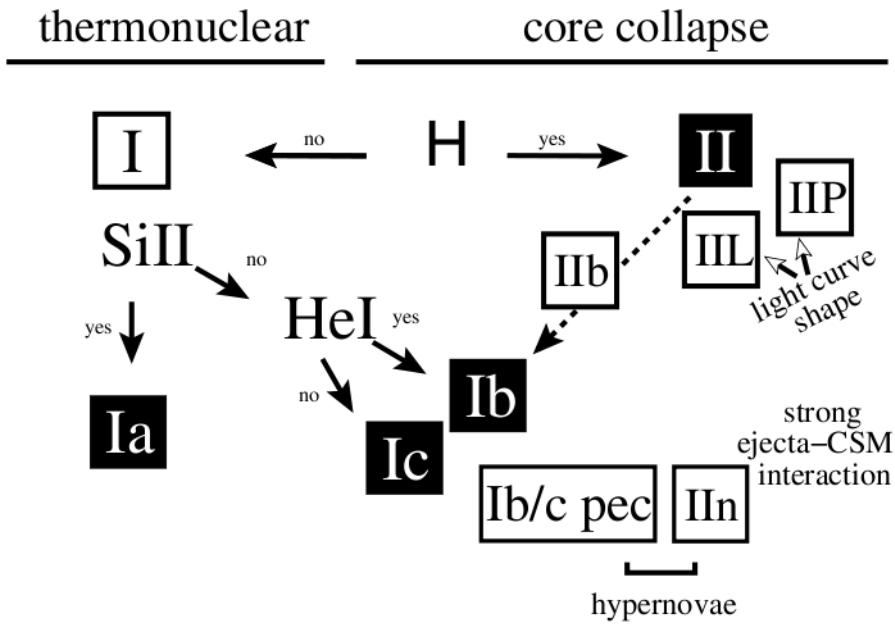

Figure 1.1: The classification scheme of supernovae (SNe) (from Turatto 2003). Type I and II SNe are defined by the absence or presence of hydrogen lines in their spectra, respectively. Sub-classifications are based on further spectral features and light curve information as described in Section 1.3.1.

1.3 Dust production by supernovae

Supernovae (SNe) occupy a pivotal position in modern astrophysics, not only because of their importance as cosmic distance indicators but due to the prime role that they play in determining the overall energetics, mass recycling rate and heavy-element enrichment of galaxies.

1.3.1 Supernova types

Supernovae are primarily classified by the appearance of their optical spectra, usually near the time of maximum light. Filippenko (1997) provides a thorough review of the SN types and the criteria used to classify them, and further reviews and updates on the subject were given by Turatto (2003) and Smartt (2009). The two main classes of SNe are Types I and II which are respectively defined by the absence or presence of hydrogen lines in their spectra. Sub-classifications are based on further spectral features and light curve information. Figure 1.1 illustrates the current classification scheme (taken from Turatto 2003).

The location of SNe within their host galaxies indicates distinct explosion mechanisms. Type Ia SNe are found to occur in all galaxies types, including ellipticals, with no particular concentration in the star formation regions of spiral arms, implying that they do not have massive star progenitors (Branch et al. 1995). Instead it is assumed that they result from the thermonuclear explosion of low mass carbon-oxygen white dwarf stars when they reach a critical mass (the Chandrasekhar limit) after accreting matter from a binary companion (e.g., Woosley & Weaver 1986). This is in contrast with the other Type I SNe (Ib/c) and the Type II SNe which are not seen in early type galaxies but are strongly associated with the star formation regions of spiral and irregular galaxies, implying that these SNe result from the core collapse of massive ($M \gtrsim 8\,M_{\odot}$) stars (Filippenko 1997; Turatto 2003, and references therein). The observed kinetic energies of these core-collapse supernovae (hereafter, CCSNe) are $\sim 10^{51}$ erg, with integrated luminosities usually between 1–10 % of this value (Smartt 2009).

CCSNe, the subject of this thesis, are typically categorised into five major types based on their spectral features and light curve information (Leonard 2010):

1. **II-P** (plateau) are defined by the presence of strong hydrogen lines in their spectra. Their luminosity stops declining shortly after peak brightness forming a plateau phase for 2–3 months as the recombination wave recedes through the massive ($\sim 10\,M_{\odot}$) hydrogen envelope releasing the energy deposited by the shock;

2. **II-L** (linear) show hydrogen in their spectra and a smooth, linear decline in luminosity after maximum, most likely due to a lower mass envelope;

3. **IIn** (narrow) have spectra dominated by strong emission lines, particularly hydrogen, often with complex multi-component profiles but always including a strong narrow component and lacking the broad absorption components typical in other Type II SNe. The spectral and photometric evidence suggests interaction between the SN ejecta and a dense circumstellar medium (CSM);

4. **IIb** have early time spectra showing hydrogen similar to Type II SNe but, at later times, evolve hydrogen-deficient spectra similar to Type Ib/c SNe;

5. **Ib/c** show no evidence for hydrogen in their spectra at any time. Whilst Type Ib SNe are generally defined by unambiguous helium features in their spectra and Type Ic SNe are helium poor, it can often be difficult to distinguish between them

and they are sometimes grouped to refer to Ibc or Ib/c. A few percent of all Type Ic SNe are associated with long gamma-ray bursts (Hartmann 2010). They show much broader spectral lines than typical Type Ic SNe, due to high-velocity ($v/c \sim 0.1$) outflows interpreted as resulting from extremely energetic explosions ($> 10^{52}$ erg), hence they are sometimes referred to as "hypernova".

The ordering of the above SN types is thought to reflect an increasing degree of mass-loss, or envelope stripping, of the progenitor star prior to explosion, from the least affected massive hydrogen envelopes of Type II-P to the most stripped, hydrogen-deficient Type Ib/c.

Current estimates of the proportion of each sub-type in a volume-limited sample (Smartt 2009) show that Type II-P are the most common of the CCSNe ($\sim 60\,\%$), followed by Type Ib/c ($\sim 30\,\%$), and the remaining rarer Type II-L, IIn and IIb SNe ($\sim 10\,\%$). Of course, there are often variations on these major sub-categories, for example SN 1987A (discussed in Section 1.3.4) is usually referred to as a Type II-P but was clearly peculiar.

1.3.2 Evidence for dust formation in SNe

Theoretical studies

It has long been hypothesised that supernovae (SNe) are a major source of dust in the Universe. Cernuschi et al. (1967) first proposed that the expansion phase after the SN explosion could provide the right conditions for dust condensation of carbon grains in the cooling ejecta. Subsequent early theoretical studies suggesting SNe as significant producers of interstellar dust included Hoyle & Wickramasinghe (1970), Clayton (1979), and Dwek & Scalo (1980).

More recent SN dust formation models based on classical nucleation theory, such as those of Kozasa et al. (1991); Clayton et al. (2001); Todini & Ferrara (2001) and Nozawa et al. (2003), predicted that ~ 0.1–$1\,\mathrm{M}_\odot$ of dust should condense in the ejecta a few years after explosion, for stellar progenitor masses in the range of CCSNe (12–$40\,\mathrm{M}_\odot$). These dust mass predictions correspond to condensation efficiencies for the available refractory elements of 0.1–0.3.

Dust in high-redshift galaxies

The assumption that CCSNe should constitute a significant source of dust in the universe, gained support with the discovery that many of the earliest-formed galaxies known are extremely dusty and IR-luminous, as evidenced by the efficient detection of their red-shifted thermal dust emission at submillimetre wavelengths (e.g., Ivison et al. 2000; Bertoldi et al. 2003). The inferred far-IR luminosities ($\gtrsim 10^{13}\,L_{\odot}$) of samples of $z \gtrsim 6$ quasars are consistent with emission from warm dust ($T < 100\,K$), with dust masses in excess of $10^{8}\,M_{\odot}$(Bertoldi et al. 2003; Robson et al. 2004; Beelen et al. 2006; Dwek et al. 2007). Some of these high-z galaxies formed less than ~ 1 Gyr after the Big Bang, strongly suggesting that the dust must have condensed around relatively high-mass stars, e.g., core-collapse SNe which inject their nucleosynthetic products and newly condensed dust into the ISM relatively promptly after their formation. Massive-star SNe, of Type II, Ib/c, arising from the starbursts that power these galaxies, are plausible sources of this dust. Starburst durations are estimated at about 10^{8} years, so low-mass star Type Ia SNe are unlikely to be responsible for the dust seen.

Although it is generally accepted that a significant Galactic contribution comes from dust condensation in the stellar winds of AGB stars, SNe must be considered as a potential major source of dust injection into the ISM.

Meteorite inclusions

Supporting evidence for dust formation by at least some supernovae comes from precise isotopic abundance ratio studies of grain inclusions found in meteorites. Many of these inclusions exhibit isotopic distributions that differ significantly from those found in the Sun and Earth, and have consequently been labelled as "presolar" grains, or "stardust" (e.g., Nittler et al. 1996; Clayton et al. 1997; Travaglio et al. 1999). Whilst many of these grains have isotopic distributions consistent with the slow-neutron capture processes (the *s*-process) inside AGB stars, some have distributions characteristic of the rapid-neutron captures (*r*-process) inside SNe, responsible for the synthesis of heavier elements during such an event. A further example, is the presence of ^{44}Ti, which is only produced in SNe, in some presolar grains at the time of their formation, inferred from the large excesses of its daughter isotope ^{44}Ca.

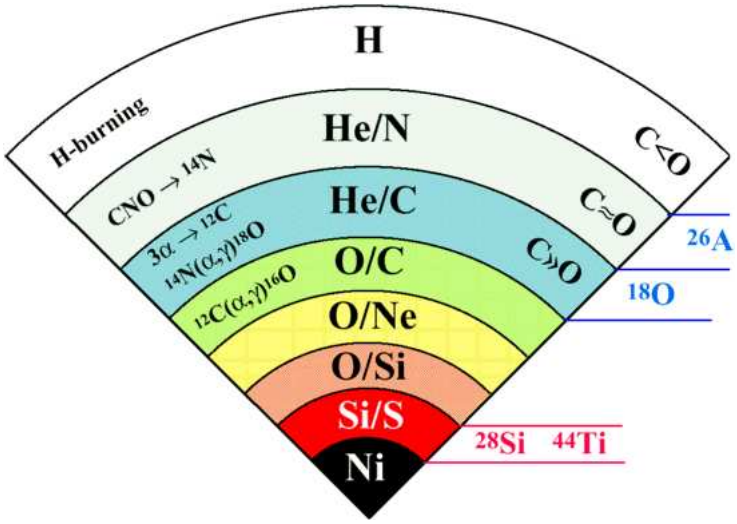

Figure 1.2: Onion-shell structure of a pre-supernova massive star[1].

Presolar dust grains identified as supernovae condensates have been mainly carbonaceous. Silicon carbide (SiC) grains of type X (X stands for "eXotic") have isotopic compositions distinct from the bulk of SiC grains; ~1 % of all presolar SiC grains found in primitive meteorites are of type X, and they are thought to come from Type II SNe (Amari et al. 1992; Lodders & Amari 2005; Hoppe et al. 2010). Silicon nitride (Si_3N_4) and low-density graphite have similar isotopic compositions to the SiC-type X grains and have also been related to SNe. SNe are also likely to have contributed to meteoritic nanodiamonds (Lodders & Amari 2005). Surprisingly few oxide presolar grains of SN origin have been identified, despite the fact that ^{16}O is the third most abundant isotope ejected from SNe and that, overall, SN ejecta have C/O<1 which implies there should be many more SN oxide than carbonaceous grains (Amari & Lodders 2007, and references therein). Lodders & Amari (2005) suggest that this could be because SN oxide grains are too small ($<< 0.1$ μm) to be recovered from meteorites by current presolar grain separation procedures.

Just prior to its explosion as a supernova, a massive star has an onion-shell structure, consisting of different layers that contain the products of nuclear burning at increasing temperatures from the surface to the core. Figure 1.2 schematically illustrates the pre-supernova structure of a massive star, with each layer indicated by the most abundant elements[1]. However, presolar grains provide evidence for turbulent mixing in the ejecta

[1]Figure obtained from the Washington University in St. Louis 'Presolar Grain Research' pages at http://presolar.wustl.edu/work/grains.html

during the explosion: ^{44}Ti and ^{28}Si, which are both synthesised deep in the interior of Type II SNe, are present in graphite grains that must have formed in a carbon-rich environment, such as the outer helium-rich layers of a massive progenitor star, where C>O is a necessary condition for such grains to form (e.g., Travaglio et al. 1999).

1.3.3 Early infrared observations

Early near-infrared (NIR) observations of some SNe were obtained. The Type II-L SN 1979C (Merrill 1980), the Type II-L SN 1980K (Telesco et al. 1981), the untyped SN 1982E (Graham et al. 1983; Graham & Meikle 1986), the Type II SN 1982L, the Type Ib SN 1982R (Graham & Meikle 1986), and the Type II-L SN 1985L (Elias et al. 1986) all revealed excess IR emission that was attributed as thermal emission due to dust, the origin of which was less certain. Whilst emission from dust freshly synthesised in the SN ejecta was proposed for SN 1980K (Dwek et al. 1983) and SN 1985L (Elias et al. 1986), the most common explanation was that the IR emission originated from pre-existing circumstellar dust heated by the initial SN flash (an IR "echo", Bode & Evans 1980; Dwek 1983; Graham & Meikle 1986). These first IR observations of SNe were fragmentary, and showed that early and consistent monitoring of SNe during the expected epochs of dust formation and beyond was critical for understanding the nature and origin of the emission.

1.3.4 SN 1987A

Such an opportunity fortuitously presented itself with the explosion of SN 1987A in the Large Magellanic Cloud (LMC), which at a distance of ~ 50 kpc was the closest supernova in almost 400 years. Its discovery on 24 February 1987, by Ian Shelton and Oscar Duhalde at Las Campanas, Chile (Kunkel et al. 1987), initiated the immediate response of frequent and intense multi-wavelength observations over the coming years, providing a wealth of observational data and discoveries. Observational 'firsts' included the detection of neutrinos, confirming predictions of the hydrodynamic core-collapse explosion mechanism; the observation of the progenitor star from archival images; signatures of a non-spherical explosion and mixing in the ejecta; the direct observation of explosive nucleosynthesis, including the accurate mass determination of ^{56}Ni and other radioactive isotopes; as well as the birth of the supernova remnant in real time, following the subsequent interaction of the supernova shock with the circumstellar material (Fransson et al. 2007). Figure 1.3

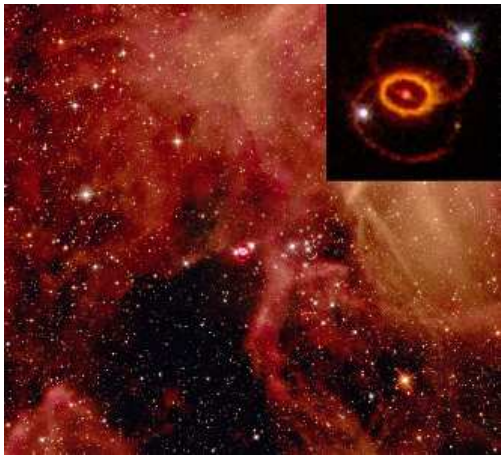

Figure 1.3: SN 1987A in the LMC at a distance of ∼ 50 kpc. The close-up view clearly shows the circumstellar rings around SN 1987A, with the ejecta from the supernova explosion at the centre of the inner (equatorial) ring (image obtained from the SN 1987A Wikipedia pages[2] showing a composite of two public domain NASA images taken with the *Hubble Space Telescope*).

shows a composite *HST* image[2] of SN 1987A in the LMC, clearly showing the inner equatorial and outer circumstellar rings. The presence of hydrogen lines in the spectra of SN 1987A and the detection of neutrinos confirmed it was a Type II event, but it was unusual compared to other Type II SNe in that it was several magnitudes dimmer at visual maximum, and it exhibited a very rapid spectral evolution, seemingly consistent with the much higher than expected expansion velocities from studies of the hydrogen absorption profiles in the early spectra. These unexpected characteristics indicated that its atmosphere was more compact than the red supergiants that give rise to normal Type II SNe, and tied in with the compact nature of the progenitor star which was identified as a blue supergiant, Sk –69°202 (Hillebrandt et al. 1987). Extensive reviews of SN 1987A are given by Arnett et al. (1989) and McCray (1993).

With its remarkable proximity, SN 1987A provided a unique in situ test bed for the early SN dust models. Even before such observations had revealed evidence of any dust production, Gehrz & Ney (1987) predicted that dust would begin to form in the ejecta of SN 1987A ∼ 250–330 days after explosion, based on comparisons with dust formation in classical novae. Dwek (1988) developed this idea further by discussing conditions for dust formation in the ejecta in two zones: the outer hydrogen envelope and the inner metal-rich layers (mantle). He found that the onset of dust formation could occur as early

[2]Figure obtained from http://en.wikipedia.org/wiki/SN_1987A

as 140–340 days after explosion in the hydrogen envelope, and ≥ 400 days in the higher density region of the inner mantle.

Lending initial support to the predictions, molecules, which are believed to be an inevitable precursor to dust, were detected in the spectra of SN 1987A. IR molecular bands of CO (the fundamental emission band at 4.6 μm and first overtone at 2.3μm) and SiO (the fundamental band at 7.9 μm) were present from as early as 112 days after explosion, before any direct detection of dust, and stayed until > day 615 (CO) and < day 578 (SiO) (e.g., Spyromilio et al. 1988; Roche et al. 1991; Wooden et al. 1993).

IR spectroscopic studies of SN 1987A also demonstrated the presence of an IR excess. From ∼ 350 days Meikle et al. (1993) found an increase in the 4 μm continuum, which became prominent by ∼ 550 days (Roche et al. 1993). From their three-component fits to the 2–100 μm continuum emission of SN 1987A, Wooden et al. (1993) found an IR excess (compared to a hot blackbody component and contributions from free-bound and free-free radiation), approximated by a graybody, from as early as day 60 (T_d ∼ 1600 K) that began to dominate the shape of the observed continuum by day 615 (T_d ∼ 400 K). They determined that the contribution of this thermal IR component to the total bolometric luminosity increased from 2–3 % at days 60, 260 and 415 to 45 % by day 615. Figure 1.4 shows the spectral energy distributions of SN 1987A from Wooden et al. (1993) at days 260 and 615, with the IR excess, peaking at ∼ 8 μm, clearly visible by day 615.

Whilst there was initial speculation as to the possible origins of the IR excess (Roche et al. 1989 suggested that the source was an IR echo due to circumstellar matter illuminated by the optical-UV flash of the supernova), evidence soon followed that proved the majority of the IR continuum emission came from the SN ejecta.

At ∼ 530 days, asymmetries were seen in the profiles of several optical emission lines of SN 1987A, with the peak velocities blue-shifting by ∼ 500–700 km s^{-1} (Danziger et al. 1989; Lucy et al. 1989, 1991). It was recognised that similar profiles would be expected if dust condensed within the ejecta so that emission from the far (receding) side of the expanding material suffered more internal extinction (absorption/scattering) than that from the near side. Lucy et al. (1989) modelled these observations and found that reasonable fits to the profiles were obtained with dust uniformly distributed within the ejecta out to a velocity of ∼ 2000 km s^{-1}, i.e., within the inner metal-rich zone.

These results were supported by studies of the temporal evolution of the bolometric light curve embracing the assumed epoch of dust formation. The decline of the late-

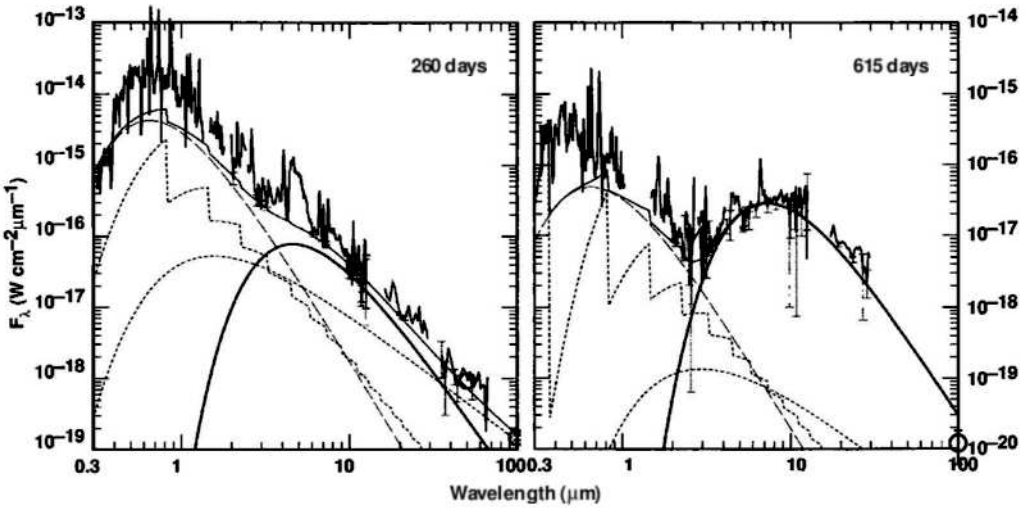

Figure 1.4: Optical and KAO IR spectrophotometry of SN 1987A by Wooden et al. (1993). A three-component continuum model is shown for hot gas (long-dashed lines), free-free and bound-free emission (dotted lines), and warm dust (solid lines). Dust emission first appears at day 260, was unambiguous by day 615 and began fading rapidly about 400 days later.

time bolometric light curve of a SN (the 'radioactive tail') is expected to be powered by γ-ray deposition due to the radioactive decay of ^{56}Co (with half-life, $\tau_{1/2}$ = 77.3 days; a product of the explosively synthesised ^{56}Ni, $\tau_{1/2}$ = 5.9 days) $\rightarrow$ ^{56}Fe (Colgate & McKee 1969; Woosley et al. 1989). After $\sim$ 520 days, the optical light curves of SN 1987A began to decline more steeply than before, but the addition of the increased IR emission at this time accurately accounted for the optical deficit such that the bolometric light curve continued to follow the decay of ^{56}Co (Whitelock et al. 1989; Suntzeff & Bouchet 1990).

The contemporaneous phenomena of (i) a dominant mid-IR continuum excess with (ii) an observed drop in the optical light curve indicating increased internal extinction, but an overall bolometric luminosity that satisfied the energy budget of the SN emission as due to the radioactive decay of ^{56}Co, and (iii) the asymmetric blue-shifted line profiles, unequivocally demonstrated the formation of dust in the ejecta SN 1987A between 500 and 600 days after explosion, and possibly from as early as 350 days (Wooden 1997).

The presence of clumped dust was inferred from the wavelength-independent circumstellar extinction observed in SN 1987A (Lucy et al. 1991) and by the theoretical expectation that Rayleigh-Taylor instabilities should form in the post-shock ejecta (Chevalier & Klein 1978; Herant & Woosley 1994). Wooden et al. (1993) used a simple analytic clumped dust model with graphite grains to estimate an ejecta dust mass of a (3–5) $\times 10^{-4}$ M$_\odot$ for

SN 1987A at days 615 and 775. Ercolano et al. (2007) revisited the dust modelling of SN 1987A at these epochs with a Monte Carlo three-dimensional radiative transfer code (MOCASSIN; Ercolano et al. 2003, 2005). Results for their best-fit clumpy graphite models yielded dust masses between (6.5–7.5) $\times 10^{-4}\,M_{\odot}$, and up to $\sim 1 \times 10^{-3}\,M_{\odot}$ for a variety of mixed (by mass) astronomical silicate and graphite grain compositions, although they concluded that mainly carbon-based grains provided the best fits to the observed spectral energy distributions.

1.3.5 Dust in other massive-star supernovae

SN 1990I

SN 1990I was discovered on 27 April 1990 in NGC 4650A ($D \sim 46.4$ Mpc [3]) by Pizarro et al. (1990). It was originally classified as a Type Ia SN but subsequent early spectra led to its re-classification as a core-collapse event of Type Ib. Optical photometry and spectroscopy from around maximum light to ~ 400 days post-explosion were analysed by Elmhamdi et al. (2004). They noted that after day 240 the optical light curve began to decline more steeply than would be expected from the radioactive decay of ^{56}Co combined with the decreasing deposition of γ-rays (expected as the ejecta expand), and more steeply than that of the Type IIb SN 1993J. They also reported a significant blue shifting ($\sim 600\,\mathrm{km\,s^{-1}}$) of the [O I] 6300 Å emission line between days 237 and 258. The contemporaneous nature of the apparent increase in optical extinction observed from the light curves, with the blue-shifted emission line profiles led the authors to conclude that dust had formed within the ejecta of SN 1990I ~ 250 days after explosion. This was considerably earlier than observed for SN 1987A and Elmhamdi et al. (2004) suggested that this might be a phenomenon of Type Ib SNe due to rapid cooling in the relatively low-mass ejecta of these SNe. Unfortunately, no IR data exist for this SN.

SN 1998S

SN 1998S was discovered on 2 March 1998 in NGC 3877 ($D \sim 15.5$ Mpc [3]) by the Beijing Astronomical Observatory (BAO) Supernova Survey (Li et al. 1998). Its classification as a Type IIn SN by Filippenko & Moran (1998) implied that the ejecta was interacting with the CSM at early times. Optical and NIR photometric and spectroscopic studies were

[3]Source: NASA/IPAC Extragalactic Database at http://nedwww.ipac.caltech.edu/

carried out by Fassia et al. (2000), Gerardy et al. (2000) and Pozzo et al. (2004), from soon after explosion for over 3 years.

Gerardy et al. (2000) reported the detection of the first overtone of CO emission near 2.3 μm at days 95 and 225, which appeared to have faded away by day 355. It was the third detection of its kind in Type II SNe, suggesting that the CO molecule was fairly common in these SNe. The fading of the red wing of the complex (multi-component) Hα and He I profiles between days 260 and 355 (Gerardy et al. 2000) and from post-day 300 to almost 2 years (Pozzo et al. 2004) was interpreted as likely being due to dust formation in the ejecta. Figure 1.5 shows the Hα profile evolution between days 81 and 463, with the red wing clearly diminished at late times. A late rise was observed in the NIR continuum emission towards longer wavelengths after day 225, and the SED at this epoch was well-matched by a $\sim$1200 K blackbody (Gerardy et al. 2000). The SED at $\sim$1 year was similarly defined by Pozzo et al. (2004), the temperature of which declined over later epochs. Gerardy et al. (2000) concluded that whilst there was strong evidence for dust formation in the ejecta, it was not clear whether the observed NIR emission was from the ejecta or from pre-existing CSM dust. Pozzo et al. (2004) on the other hand ruled out an origin from freshly condensed ejecta dust as the observed IR emission exceeded the radioactive luminosity by a substantial factor. They argued that the emission was likely to be from newly-formed dust in a cool dense shell (CDS) produced by the ejecta shock/CSM interaction, with an estimated dust mass of $\geq 10^{-3}$ M$_\odot$ forming about a year after explosion, although they could not rule out an IR echo. An earlier NIR excess at day 130 was attributed to an IR echo driven by the UV-optical flash heating pre-existing CS grains (Fassia et al. 2000; Pozzo et al. 2004).

SN 1999em

The Type II-P SN 1999em was discovered on 29 October 1999 in NGC 1637 ($D \sim 11$ Mpc [3]) at an unfiltered magnitude of 13.5 by the Lick Observatory Supernova Search (LOSS) (Li 1999*b*). No infrared data was available for this SN but optical photometry and spectroscopy, taken from several days after explosion to day 642, were analysed by Elmhamdi et al. (2003*b*). The evolution of the late-time spectra demonstrated a blueshifting of the [O I] 6300 Å and Hα line profiles between days 465 and 510 which, together with an increase in the expected decline of the optical light curves at day 510 compared to the linear decay trend of previous epochs, led the authors to interpret these as signatures of

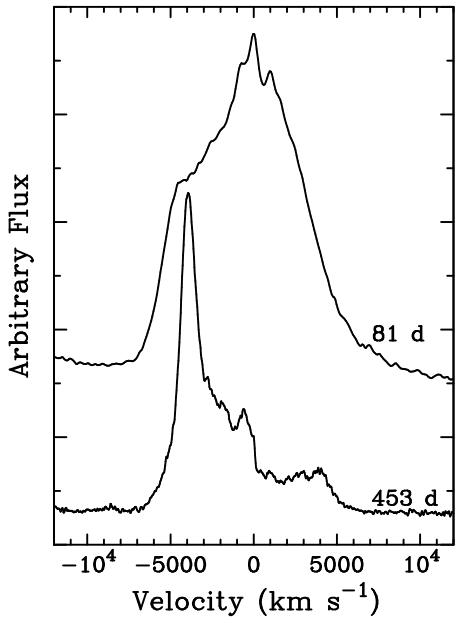

Figure 1.5: Evolution of Hα line profiles in SN 1998S, showing the preferential extinction of redshifted emission at late times, presumably caused by dust condensing in the ejecta.

dust condensation during this period. Subsequent photometry by Leonard et al. (2003) demonstrated that the fall-off in the V-band light curve was similar to that of SN 1987A. However, Elmhamdi et al. (2003*b*) noted that the epoch of dust formation and the distribution of the dust, indicated by fits to the blue-shifted line profiles, differed from those of the peculiar Type II SN 1987A. For SN 1999em, the blue-shifted line profiles had been observed by day 510, whereas this phenomenon emerged only after day 526 for SN 1987A (Lucy et al. 1989). The models required to fit the flat-topped [O I] 6300 Å doublet profiles of SN 1999em required dust optical depths $\gg 10$ and constrained the dusty zone to the inner-most metal-rich regions of the ejecta bounded by expansion velocities of $\sim 800\,\mathrm{km\,s^{-1}}$. The day 600 line profile fits for SN 1987A by Lucy et al. (1989) implied a dust optical depth ≈ 1, and a dusty zone with a boundary velocity ~ 2 times larger than that modelled for SN 1999em. Based on those models, Elmhamdi et al. (2003*b*) estimated that a moderate dust mass of $10^{-4}\,\mathrm{M_\odot}$ had formed in the ejecta of SN 1999em.

1.3.6 Supernova remnants

Young, ejecta-dominated supernova remnants (SNRs) offer an alternative in which to observe dust that has formed in the SN ejecta, before it is dispersed and mixed into the

general ISM. Thermal IR emission is expected from dust that is collisionally-heated in the post-shocked gas. Evidence for emission from dust has been found in a few young SNRs.

Cassiopeia A (Cas A) has been identified as the product of a hydrogen-deficient Type IIb CCSNe (Krause et al. 2008*a*) and is the youngest known core-collapse SNR in the Milky Way at ∼ 335 years old. It has been extensively studied in the IR and exhibits clear evidence for dust formation in its ejecta (Lagage et al. 1996), although the amount of dust has been controversial. Estimates of the dust mass have ranged from $\sim 10^{-3}\,M_{\odot}$ for dust temperatures of 90–350 K (Arendt et al. 1999; Douvion et al. 2001*b*), to ~ 0.02–$0.05\,M_{\odot}$ for 65–265 K dust emitting from 5 to 70 μm, particularly in a bright ring coincident with the reverse shock (Rho et al. 2008). Arendt et al. (1999) estimated a significant cold dust (52 K) component of $\sim 0.4\,M_{\odot}$ in the remnant from fits to *IRAS* 60- and 100-μm fluxes. Much greater masses (2–4 $M_{\odot}$) of cold (15–20 K) dust were inferred from 450- and 850-μm SCUBA observations by Dunne et al. (2003), however Krause et al. (2004) argued that most of the excess sub-mm emission was due to dust in foreground molecular clouds and derived an upper limit of $0.2\,M_{\odot}$ of cold dust within the remnant. Dunne et al. (2009) reported that the 850-μm emission from Cas A was polarised at a significantly higher level than its radio synchrotron emission and attributed this to $\sim 1\,M_{\odot}$ of cold dust or a significantly smaller quantity of iron needles (Dwek 2004). Recent imaging with *Herschel* PACS and SPIRE instruments (70–500 μm), confirmed and resolved for the first time a cool (∼ 35 K) dust component emitting at 70–160 μm, interior to the reverse shock, with an estimated mass of $0.075\,M_{\odot}$ (Barlow et al. 2010), consistent with the BLAST results of Sibthorpe et al. (2010). These results were also consistent with the models of Nozawa et al. (2010) who found that the observed IR SED of Cas A was reproduced by $0.008\,M_{\odot}$ of shock-heated warm dust and $0.072\,M_{\odot}$ of unshocked cool dust (∼ 40 K) in the remnant's interior. Barlow et al. found no direct evidence for significant quantities of cold (< 25 K) dust, although the cause of the 850-μm excess emission is still unresolved.

Kepler is a young Galactic SNR (∼ 400 years) which possibly originated from a Type Ia SN with a significant surrounding CSM/ISM (Blair et al. 2007, and references therein), although there are arguments for a Type Ib CCSNe origin (Morgan et al. 2003). Douvion et al. (2001*a*) estimated a dust mass of $\sim 10^{-4}\,M_{\odot}$ with an astronomical silicates grain model of temperature 107 K from fits to ISOCAM spectra (6.5–16 μm) and previously published *IRAS* photometry (12–100 μm). Blair et al. (2007) modelled dust emission from *Spitzer* IRAC and MIPS observations (3.6–160 μm) with a power-law grain size distribution,

including grain heating and sputtering by X-ray-emitting gas. They estimated a total dust mass of $5.4 \times 10^{-4}\,M_{\odot}$ ($2.4 \times 10^{-3}\,M_{\odot}$ before sputtering), and concluded this was mainly swept up CSM/ISM grains heated in the primary blast wave with no evidence for ejecta-condensed dust. From the lack of emission at 160 μm, Blair et al. ruled out the presence of large quantities of cold dust. This latter conclusion was in contrast with the results of Morgan et al. (2003), who found evidence for a large cold dust (17 K) component from 450- and 850-μm SCUBA observations of the remnant. They estimated a total dust mass for Kepler in the range of 0.3–3 $M_{\odot}$ (the range being dependent on the adopted value of the dust mass absorption coefficient, κ), although after a more accurate subtraction of the synchrotron component (and investigation of a negligible contribution from foreground molecular clouds), this was revised down slightly by Gomez et al. (2009) to 0.1–1.2 $M_{\odot}$. Whether the dust originated from CS material or the SN ejecta was uncertain.

The Tycho SNR is thought to be the ∼440 year old remnant of a Type Ia SN (Krause et al. 2008*b*). Douvion et al. (2001*a*) used a two-component temperature model, with astronomical silicate grains, to fit the *ISO* and *IRAS* data of Tycho, estimating $\sim 10^{-4}\,M_{\odot}$ of warm (∼107 K) dust and $3 \times 10^{-3}\,M_{\odot}$ of cool (∼55 K) dust. Whilst they determined that the warm IR emission originated from collisional heating of dust around the shock front, they suggested that the cool dust was probably not directly associated with the remnant. From 9–160 μm imaging with AKARI, compared with X-ray and CO images, Ishihara et al. (2010) found results for warm dust consistent with those of Douvion et al. (2001*a*) in each of two bright spots located in the north east (NE) and north west (NW) of the remnant, with the origin of the dust from the NE boundary likely due to ambient clouds interacting with the shock front. The source of the NW warm dust was unclear due to the absence of prominent interstellar clouds and they could not rule out that this region contained dust mostly of SN ejecta origin. They found that the 140- and 160-μm bands were dominated by cold dust emission (22 K) from the surrounding ISM near the NE boundary, with an estimated dust mass of 0.3 $M_{\odot}$.

1.3.7 The three signatures of ejecta-condensed dust

The production of dust in supernovae results in three distinct observable signatures that can be used to estimate the total amount of dust that condensed in their ejecta:

1. the appearance of excess thermal IR emission. However, this signature alone can be

compromised by pre-existing nearby dust (e.g., circumstellar dust), which can be heated by the SN UV-optical light flash.

2. a contemporaneous decrease in the UV-optical light curve of the SN due to an increase in the extinction by the newly formed dust. Pre-existing dust cannot produce an observable dip in the SN light curve.

3. the appearance of asymmetric blue-shifted emission lines, caused by the ejecta dust preferentially obscuring the emission from the receding (red-shifted) part of the ejecta.

Method (1) is normally required if dust masses are to be derived, but it must be supported by one or both of (2) and (3) for conclusive evidence of an origin of dust formed in the SN ejecta.

1.4 Thesis outline and the SEEDS collaboration

The aim of this thesis is to help elucidate the potential contribution of core-collapse supernovae to the dust-enrichment of galaxies. To this end, sensitive mid-infrared surveys for thermal dust emission from recent supernovae have been conducted with the *Spitzer Space Telescope* and with the Gemini telescopes, in order to seek evidence for dust formation and evolution in supernova ejecta.

The research presented in this thesis represents my contribution within a larger international collaboration, known as SEEDS – the Survey for the Evolution of Emission from Dust in Supernovae. The SEEDS team is comprised of 11 core members. Other than myself, they are: Prof. Michael J Barlow (University College London – UCL), Dr. Roger Wesson (UCL), Dr. Barbara Ercolano (University Observatory Munich), Dr. Ben K Sugerman (Goucher College), Dr. Geoffrey C. Clayton (Louisiana State University – LSU), Dr. Jennifer Andrews (LSU), Dr. Joseph Gallagher (Raymond Walters College), Dr. Margaret Meixner (Space Telescope Science Institute – STScI), Dr. Masaaki Otsuka (STScI), and Dr. Doug Welch (McMaster University). The group has been addressing the role CCSNe and their progenitors play in the dust budget of galaxies using *Spitzer*, *HST* and Gemini since 2004.

My role, from inception of the collaboration, has centred on the processing and analysis of the mid-IR data of the initial sample of 30 SNe presented herein, including: deriving

upper limits to the flux densities for non-detected SNe; leading the multi-epoch, multi-wavelength study of SN 2004et (the role of other SEEDS members in this work has been clearly identified in the relevant chapter); measurement and preliminary analysis of the Type II SN 1999bw; and involvement in the measurement and analysis of SN 2002hh and SN 2003gd, where the research was led by other SEEDS members. The following paragraph outlines the structure of the thesis.

Chapter 2 begins by introducing the SEEDS sample of SNe observed. I then present the observations of 21 CCSNe obtained with the Gemini telescopes, the focus of the chapter, which includes an overview of the telescopes and instruments used, details of the observations, and a description of the data processing and photometric analysis techniques applied to these data. Mid-IR flux densities, and robust upper limits to the flux densities for non-detections, from the Gemini data are presented and discussed. Chapter 3 presents the mid-IR observations of 18 CCSNe obtained with the *Spitzer Space Telescope*, and similarly includes an overview of the telescope and instruments used, details of the observations, a brief description of the *Spitzer* pipelines and additional steps for processing the data, as well as parameters for the photometric analysis techniques presented in Chapter 2 specific to the *Spitzer* data. Flux densities, and robust upper limits to the flux densities for non-detections, from the *Spitzer* data are presented and discussed. Chapter 4 discusses in greater detail the mid-IR evolution of three SNe detected and monitored during the survey, those of the Type II SNe: SN 1999bw, SN 2002hh and SN 2003gd, including a summary of the published SEEDS results for SN 2002hh and SN 2003gd. Chapter 5 presents an analysis of the multi-epoch observations of the Type II-P SN 2004et, including interpretation of new optical and NIR SEEDS data. Multi-wavelength light curves are used to construct optical–IR spectral energy distributions (SEDs) for multiple epochs. The SEDs are fitted with multiple blackbody components in order to investigate the luminosity evolution of the SN, providing constraints on the time-dependent evolution of the dust properties. Preliminary results from Monte Carlo radiative transfer modelling to estimate the dust mass best representing the observed SEDs are discussed and compared with results from other studies of this object. Finally, Chapter 6 summarises the results of the work presented in this thesis and draws some preliminary conclusions as to the likely contribution of Type II core-collapse supernovae to the dust enrichment of galaxies. It also provides a discussion of potential future work.

Chapter 2

Gemini Observations of Supernovae

2.1 Introduction

Mid-infrared (mid-IR) observations of supernovae (SNe) have been obtained with instruments on the Gemini telescopes and the *Spitzer Space Telescope* over the years 2001 – 2008. This chapter starts by describing the complete sample of observations with both telescopes, and then focuses solely on the Gemini data. The *Spitzer* data are discussed separately in Chapter 3. The current chapter includes a discussion of ground-based mid-IR astronomy and a brief description of the Gemini Observatory and the instruments used. It describes the Gemini observations, the data reduction and flux calibration processes, and the flux measurement techniques. Mid-IR flux densities, and upper limits for non-detections, of the Gemini SNe sample are also presented and discussed.

2.2 The sample definition and selection

The sample presented in this thesis consists of 30 core-collapse SNe from massive stars, 21 of which were observed between 2001 and 2008 with the ground-based Gemini North and South telescopes (hereafter, Gemini-N and -S), and 18 of which were observed between 2004 and 2008 with the *Spitzer Space Telescope* (hereafter, *Spitzer*).

For the initial observing programmes, the Padova-Asiago online Supernova Catalogue was used to select accessible and nearby massive star SNe of Types II, Ib and Ic, aged

between 1 and 5 years, since these encompass the optimum ages for detection in the mid-IR as predicted by both nucleation theory (e.g., Todini & Ferrara 2001 as discussed in Section 1.3) and the observed behaviour of SN 1987A (Danziger et al. 1989; Lucy et al. 1989; Suntzeff & Bouchet 1990; Lucy et al. 1991; Wooden et al. 1993). Variations in the targets between the different programmes were made due to visibility constraints, sensitivities of the telescopes/instruments used, and to maximise the sample size.

For the early Gemini observations, SNe were chosen to have $V_{max} < 17$ mag and radial velocities $\lesssim 3000$ km s^{-1}. Prior to these observations only SN 1987A had been detected at mid-IR wavelengths and since SN 1987A had often been considered to be a peculiar Type II supernova there were no prior guidelines as to how bright a 'normal' dust forming supernova might be in the mid-IR. For the later programmes, including the *Spitzer* observations, stricter distance constraints of the targets were applied based on the sensitivity limits of the telescopes/instruments for each observing programme, the brightness of the only well-studied supernova in the mid-IR, SN 1987A, and the upper limits observed for earlier targets in our programme. Those for the first *Spitzer* observations were limited to radial velocities not greater than 1720 km s^{-1} (or ~24 Mpc, for $H_0 = 73$ km s^{-1} Mpc^{-1}).

The complete sample of SNe that forms part of the current SEEDS program is presented in Table 2.1, in order of ascending R.A. Its columns contain the following data:

1. Supernova name.

2. and 3. Equatorial coordinates (J2000.0) from optical photometry as reported in the literature, generally from the IAU Circulars.

4. SN type.—taken from the Padova-Asiago online Supernovae Catalogue[1], and cross-referenced with David Bishop's online supernovae pages[2] which primarily sources information from the IAU and CBET circulars.

5. Date of discovery of the SN.—from the Padova-Asiago Supernovae Catalogue and David Bishop's supernova web pages (as referenced above).

6. SN host galaxy name.

[1]The Padova-Asiago supernova catalogue is at http://web.pd.astro.it/supern/snean.txt
[2]David Bishop's supernovae website can be found at http://www.supernovae.net/snimages/, currently hosted by the International Supernova Network, and the Astronomy Section of the Rochester Academy of Sciences, and supported by Tenagra Observatory.

Table 2.1: The Sample – Supernova and host galaxy properties (see notes to the table in the text).

SN..	R.A. (J2000.0)	Decl. (J2000.0)	SN Type	Discovery Date	Galaxy	Gal. Type	V_h [km s^{-1}]	SN offset from centre [″]	D [Mpc]	Observations
(1)	(2)	(3)	(4)	(5)	(6)	(7)	(8)	(9)	(10)	(11)
..2002ap	01 36 23.85	+15 45 13.2	Ib/c pec	2002-01-29.4	NGC 628 (M74)	SAc	657	258W 108S	9.3[a]	SST:SINGS;Gem:04a,05a,05b
..2003gd	01 36 42.65	+15 44 19.9	II-P	2003-06-11.12	NGC 628	SAc	657	13E 160S	9.3[a]	SST:SINGS,P30494,P40010;Gem:05a,05b
..2003B	02 46 13.78	-30 13 45.1	II	2003-12-28.09	NGC 1097	SBb	1274	68W 163N	17.4	SST:SINGS;Gem:04a
..1999eu	02 46 20.79	-30 19 06.1	II pec	1999-11-05	NGC 1097	SBb	1274	23E 157S	17.4	SST:SINGS
..2003bg	04 10 59.42	-31 24 50.3	IIb	2003-02-25.7	M-05-10-15	SBc	1320	16W 25S	18.1	SST:P03333
..2002kg	07 37 01.83	+65 34 29.3	IIn	2002-10-26	NGC 2403	SBc	130	72E 96S	3.3[b]	SST:SINGS
..2004dj	07 37 17.02	+65 35 57.8	II-P	2004-07-31.76	NGC 2403	SBc	130	160E 10N	3.3[b]	SST:SINGS,P30494,P40010; Gem:06a,06b,07a
..2003Z	09 07 32.46	+60 29 17.5	II	2003-01-29.7	NGC 2742	Sc	1273	8W 31N	17.4	SST:P03333
..2003jg	09 45 38.40	-31 11 19.9	Ib/c	2003-10-24.8	NGC 2997	SAc	1087	11W 6N	10.3[c]	SST:P03333;Gem:04a
..1999gi	10 18 16.66	+41 26 28.2	II-P	1999-12-9.82	NGC 3184	SB	588	4W 61N	8.1	SST:SINGS
..1999bw	10 19 46.81	+45 31 35.0	IIn	1999-04-15.2	NGC 3198	SBc	663	86W 84S	13.7[d]	SST:SINGS,SST:P20320,P40010
..2001fv	11 04 01.66	+28 01 55.7	II	2001-11-03.175	NGC 3512	Sc	1469	21W 11S	20.1	SST:P03333
..2002ji	11 22 53.15	+16 35 10.0	Ib/c	2002-11-30.84	NGC 3655	Sc	1457	22W 14S	20.0	SST:P03333
..2004C	11 27 29.72	+56 52 48.2	Ic	2004-01-12.5	NGC 3683	SBc	1716	17W 10N	23.5	SST:P03333
..1999D	11 28 28.42	+58 33 38.7	II	1999-01-16	NGC 3690	IBm pec	3033	19W 5S	41.5	Gem:01a
..1999an	12 01 10.57	+14 06 12.3	II	1999-03-07	IC 755	SBb	1501	2E 3S	20.6	Gem:01a
..1999gq	12 33 48.32	+15 10 48.2	II	1999-12-23	NGC 4523	Sm	260	5E 46N	13.0[e]	Gem:01a
..2001gd	13 13 23.89	+36 38 17.7	IIb	2001-11-24.32	NGC 5033	Sc	877	46W 198N	12.0	SST:SINGS;Gem:05a
..2005cs	13 29 53.37	+47 10 28.2	II	2005-06-27.933	NGC 5194 (M51)	Sc	600	15W 78S	8.4[f]	Gem:06a,07a
..2002ed	14 06 38.22	-05 27 28.0	II-P	2002-07-24	NGC 5468	Scd	2842	55E 15S	38.9	Gem:04a
..2001bq	14 17 42.14	-07 25 00.7	II	2001-05-10.3	NGC 5534	Sab pec	2633	28E 2N	36.1	Gem:04a
..2002ao	14 29 35.74	-00 00 55.8	IIb/Ic	2002-01-25.5	UGC 9299	Sd pec	1539	16E 10N	21.1	SST:P03333;Gem:04a
..2002ds	15 13 35.73	-20 40 38.5	II	2002-06-25.3	E581-G25	SBd pec	2268	68E 7S	31.1	Gem:04a
..2001X	15 21 55.45	+05 03 42.1	II-P	2001-02-27.8	NGC 5921	SBbc	1480	16W 32S	20.3	Gem:04a
..2000cb	16 01 32.15	+01 42 23.0	II	2000-04-27	IC 1158	Sc	1927	30W 4S	26.4	Gem:04a
..1999ac	16 07 15.01	+07 58 20.4	Ia pec	1999-02-26	NGC 6063	Scd:	2848	24E 30S	39.0	Gem:01a
..2002hh	20 34 44.29	+60 07 19.0	II-P	2002-10-31.1	NGC 6946	SB(c)	48	61W 114S	5.9[g]	SST:SINGS,P20320,P30494; Gem:04b,05a,05b,06a,06b,07a
..2004et	20 35 25.33	+60 07 17.7	II-P	2004-09-22.983	NGC 6946	SB(c)	48	247E 115S	5.9[g]	SST:SINGS,P20320,P30494,P40010,P60071; Gem:05a,06a,07a,07b
..1999el	20 37 17.83	+66 06 11.5	IIn	1999-10-20	NGC 6951	Sbc	1331	22E 8S	18.2	Gem:01a
..2001ig	22 57 30.69	-41 02 25.9	IIb/Ib/c	2001-12-10.43	NGC 7424	Scd	939	139E 109N	11.5[h]	Gem:04a

7. Classification of galaxy type.—as listed in the NASA/IPAC Extragalactic Database (NED).[3]

8. V_h.—Heliocentric radial velocity in kilometres per second, from the NED.

9. Coordinate offset, to the nearest arcsecond, of the SN from the centre of its host galaxy.

10. D.—Distance to the host galaxy in Mpc. Unless otherwise indicated, these are derived using Hubble's Law, $V = H_0 D$, where V (equivalent to V_h in the table) is the observed heliocentric recessional velocity of the galaxy in $\mathrm{km\,s^{-1}}$ as taken from the NED and H_0 is the Hubble constant, $H_0 = 73\ \mathrm{km\,s^{-1}\ Mpc^{-1}}$ (Spergel et al. 2006). References for redshift-independent distances are: [a] Hendry et al. (2005),[b] Karachentsev et al. (2004),[c] average distance from NED from 3 references using the Tully-Fisher relationship,[d] Freedman et al. (2001),[e] Shanks et al. (1992),[f] Feldmeier et al. (1997),[g] Karachentsev et al. (2000),[h] from NED using the Tully-Fisher relationship.

11. List of observations for each SN for which the data are presented in this thesis. The Gemini observing year is split into semesters 'A' and 'B' which refer to the periods February 1 – July 31 and August 1 – January 31. *Spitzer* Cycles 1, 2, 3 and 4 refer to the periods July 1 2004 – May 31 2005, June 1 2005 – May 31 2006, June 1 2006 – June 30 2007, and July 1 2007 – June 30 2008 respectively. Unless otherwise indicated, all observing programs have Principal Investigator (PI) Barlow.

    —Gem:01a – An early pilot program, GN-2001A-C-10, with OSCIR on Gemini-N in semester 2001A;

    —Gem:04a – Program GS-2004A-Q-1 with T-ReCS on Gemini-S in semester 2004A with roll-over into semester 2004B;

    —Gem:04b – Director's Discretionary Time (DDT) program, GN-2004B-DD-4, with Michelle on Gemini-N for follow-up observations of SN 2002hh in semester 2004B;

    —Gem:05a/05b/06a – Long-term status project GN-2005A-Q-20 with Michelle on Gemini-N, with observations spanning semesters 2005A, 2005B and 2006A;

    —Gem:06b – Program GN-2006B-Q-1 with Michelle on Gemini-N in semester 2006B;

    —Gem:07a – Program GN-2007A-Q-5 with Michelle on Gemini-N in semester

[3] http://nedwww.ipac.caltech.edu

2007A;

—Gem:07b – Program GN-2007B-Q-4 with Michelle on Gemini-N in semester 2007B;

—SST:SINGS – Cycle 1 of the *Spitzer Space Telescope* SINGS Legacy project, program 00159 (PI: Kennicutt);

—SST:P03333 – *Spitzer* General Observer (GO) program 03333 in Cycle 1;

—SST:P00230 – *Spitzer* DDT program 00230 for follow-up observations of SN 2002hh in Cycle 1;

—SST:P20320 – *Spitzer* Cycle 2 GO program 20320 (PI: Sugerman);

—SST:P30494 – *Spitzer* Cycle 3 GO program 30494 (PI: Sugerman);

—SST:P40010 – *Spitzer* Cycle 4 GO program 40010 (PI: Meixner);

—SST:P60071 – *Spitzer* Cycle 6 GO program 60071 (PI: Andrews).

In the overall sample of 30 supernovae, there are 23 SNe of Type II and their subsets (see Section 1.3.1 for a review of these), four Type Ib/c SNe, two ambiguous classifications straddling Types IIb and Ib/c, and one peculiar Type Ia.

2.3 Ground-based mid-IR astronomy and the Gemini Observatory

The Gemini Observatory is a multi-national partnership consisting of twin 8.1-m optical/infrared telescopes: Gemini North, located on the summit of Mauna Kea in Hawaii at an altitude of 4213 m (~13,800 ft); and Gemini South, located on Cerro Pachón in Chile, at an elevation of 2722 m (~9000 ft). Positioned on dry and stable sites, the telescopes are able to take advantage of some of the best atmospheric conditions and provide complete coverage of the Northern and Southern skies.

The observational capabilities of 8-m class telescopes, such as those of the Gemini Observatory, in the mid-IR are much greater than those of previous ground-based telescopes. Mid-IR photometric systems on 4-m class telescopes lacked the necessary sensitivity and angular resolution to detect, for example, dust emission from other extragalactic SNe at the same intrinsic levels as the much closer SN 1987A. The comparatively large enhancement in the point-source flux sensitivity of mid-IR instruments on Gemini over the previous class of telescopes/instruments is due to the combination of: increased instrument sensitivity, the four times larger telescope collecting area and much lower emissivity

of the telescopes compared to 4-m telescopes, and a fully sampled 8-m telescope diffraction limit at 10 μm (FWHM 0.″3) which is matched, for the first time, to the seeing at that wavelength. This makes Gemini mid-IR imaging much better suited to the detection of extragalactic SNe.

All ground-based infrared astronomy is limited to a greater or lesser extent by the Earth's atmosphere. Infrared astronomy in general also depends greatly on the contamination from sources other than those one wishes to study. The atmospheric transmission at mid-IR wavelengths is discussed in Section 2.3.1. The current techniques employed to minimise confusion from background thermal radiation are discussed in Section 2.3.2, together with the associated overheads incurred as a result of these techniques, which were considerable with the Gemini telescopes at the time of the observations presented herein.

Section 2.3.3 describes each of the Gemini instruments used for the SNe observations. A considerable amount of time was spent setting up the Gemini queue mode observations, and a summary of the steps used to define the observations with the Gemini Observing Tool (OT) is provided in Appendix A.

2.3.1 Atmospheric transmission

The terrestrial atmosphere is largely opaque at most infrared wavelengths longer than 1 μm due to absorption by various atmospheric gases, in particular, water vapour, carbon dioxide, ozone and methane. Fortunately, there are a series of wavelength ranges, or transmission "windows", over which the atmosphere is mostly transparent, thus enabling ground-based infrared astronomy.

Gemini's mid-IR instruments, Michelle and T-ReCS, make use of the atmospheric transmission windows at approximately 7.5 – 14 and 17 – 25 μm for imaging, spectroscopy and (for Michelle only) imaging polarimetry. Figure 2.1 shows theoretical spectra of the atmospheric transmission over Mauna Kea, Hawaii for this mid-IR wavelength region[4] and the transmission curves of the filters used for the mid-IR observations presented in this thesis[5]. As is evident from panel (a) of Figure 2.1, the atmospheric transmission profile in the 7.5 – 14 μm window is characterised by absorption mainly due to carbon dioxide and ozone, whereas the increased atmospheric absorption in the 17 – 25 μm

[4]Raw data files to produce this plot were obtained via:
http://www.gemini.edu/sciops/telescopes-and-sites/observing-condition-constraints/transmission-spectra
[5]http://www.gemini.edu/sciops/instruments/michelle/imaging/filters

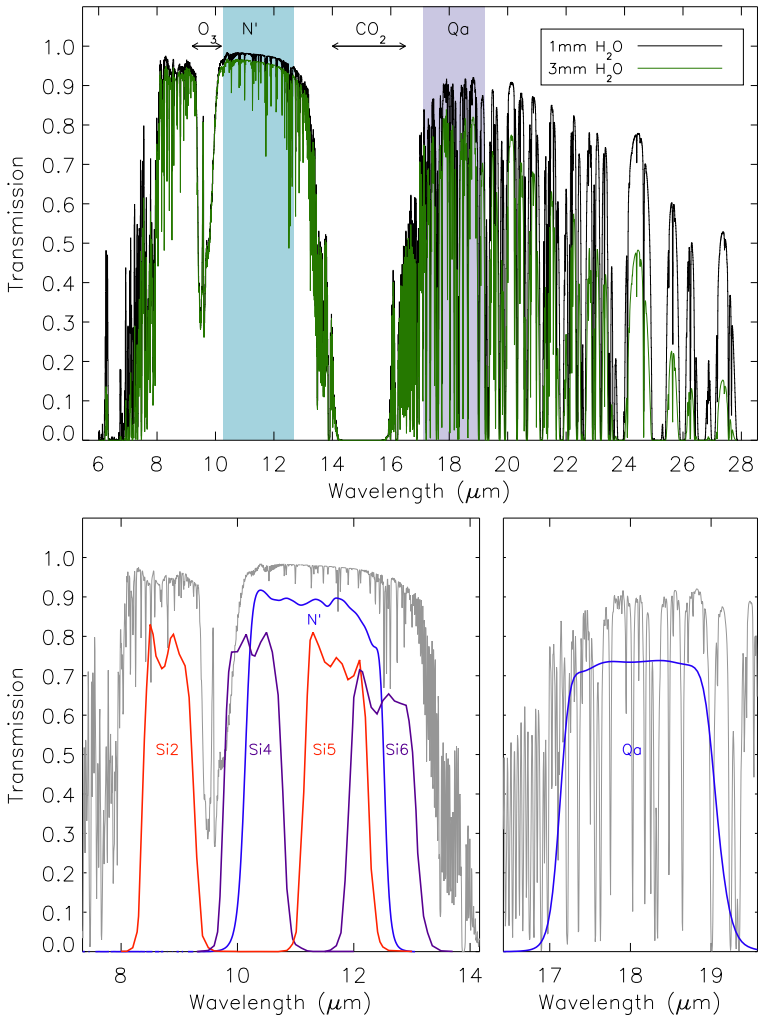

Figure 2.1: (a) Theoretical spectra of the atmospheric transmission above Mauna Kea (6–28 μm) as shown by the curves for 1.0 (grey) and 3.0 mm (black) of H_2O at airmass = 1.5. Data to produce this plot were obtained from the Gemini Observatory and were generated using the ATRAN modelling software (Lord 1992); (b) Transmission curves of the N′ (11.2 μm), Si-2 (8.8 μm), Si-4 (10.3 μm), Si-5 (11.6 μm), Si-6 (12.5 μm), and (c) Qa (18.1 μm) filters, plotted with the atmospheric transmission for 1.0 mm of H_2O at an airmass of 1.5 (grey curves) over the relevant wavelength regions.

window is dominated by water vapour. As can be seen from the 1.0 and 3.0 mm H_2O curves, an increase in water vapour column above the site reduces the transmission, and results in an increase in the sky background.

The transmissions of the various Michelle and T-ReCS filters are affected differently by the various atmospheric components. The "cleanest" filters in the window centred at 10 μm are the medium-band N' filter and the narrow silicate-band filters Si-2 and Si-5. Since the Si-4 filter is affected strongly by ozone (but only slightly by water vapour) observations should be made as close to the meridian as possible. Figure 2.1 (b) shows the transmission curves of the N'(11.2 μm), Si-2 (8.8 μm), Si-4 (10.3 μm), Si-5 (11.6 μm) and Si-6 (12.5 μm) filters, plotted with the atmospheric transmission for 1.0 mm of H_2O at an airmass of 1.5 over the 7.5 – 14 μm wavelength region. The medium-band Qa filter is the cleanest in the 20 μm window, although it is not comparable to any of the better 10 μm filters. Observations with all of the Q filters are highly dependent on water vapour, and their transmittances are not very high even at the zenith and when the water column is low. Figure 2.1 (c) shows the transmission curve of the Qa (18.1 μm) filter, plotted with the atmospheric transmission for 1.0 mm of H_2O at an airmass of 1.5 over the 16.5 – 19.5 μm wavelength region.

2.3.2 Chopping and nodding and observing overheads

Ground-based observing in the mid-IR (~ 3 – 25 μm) is different to observing in the optical or near-IR due to the very high thermal background flux. Contributing to this is the thermal radiation from the sky, which in the best parts of the N band window (near 11.5 μm) is about 240 Jy per square arcsecond and even brighter still in the Q band (17 – 25 μm).

The thermal background is also contributed to by the telescope itself. The Gemini mirrors have a silver coating to reduce their total thermal emission, and hence that of the telescope. Yet even with such infrared-optimisation, the background is large compared to the flux of most astronomical sources. Therefore, when observing with mid-IR instruments such as T-ReCS and Michelle, "chopping" and "nodding" techniques are needed to provide accurate removal of the high sky and telescope background.

Sky noise is suppressed by chopping – a technique where the secondary mirror is oscillated in a square wave pattern at a frequency of typically 3 Hz, observing two fields, or "beams". At the start of an integration sequence, Beam A is used to refer to the

"on source" position containing the science target, and Beam B refers to the nearby "off source" position on the sky. The pair of images from Beams A and B are then subtracted. However, background removal is not exact since the optical path differs for the two chop positions, so the background level is also slightly different. To remove (most of) this offset the entire telescope is moved or nodded at a typical rate of about twice per minute, so that the target and reference positions are switched, i.e., the on-source position is now in Beam B. T-ReCS has an ABAB nodding pattern, whereas Michelle uses an ABBA sequence which is more time efficient and cancels the linear component of any temporal background variations. In the usual method of beam-switching, the nod is set to be parallel to and the same amplitude as the chop. Subtracting a pair of beam-switched chop-nod observations results in a final frame containing three separate images of the target: a guided positive central image, corresponding to half of the integration time, and two displaced, unguided negative images of the target, each corresponding to a quarter of the integration time. If the chop and nod are set large enough the negative images fall off the array and are not seen. The maximum chop throw at Gemini is 15 arcseconds. The default chop-nod method of beam-switching was adopted for the mid-IR observations discussed in Section 2.4.

Mid-IR observing overheads can be significant, so it is important to take these into account when applying for time on any of Gemini's mid-IR instruments.

Each new imaging target incurred a configuration overhead of 15 minutes with T-ReCS or 10 minutes with Michelle. This included slewing, centring and setting the PWFS for tip-tilt AO correction on a guide star.

The time spent actually integrating on the source for a typical chop-nod observation is about 30% (T-ReCS) or 25% (Michelle) of the elapsed time. Thus, an on-source integration of 30 minutes takes about 1.9 hours (including set-up) with T-ReCS and about 2.2 hours with Michelle. The observing efficiency of Michelle in the Qa band (18.2 μm) is even lower, at about 21%. However, in semester 2007A a new observing mode (longer frame time and fewer read-resets) was implemented for the Qa filter which increased the observing efficiency in this filter by about 40%. The large overheads are due to the motion and settling of the chopping secondary mirror, re-acquiring guiding after each chop cycle, and reading out the array.

A larger chop throw than the maximum of 15 arcseconds (i.e., to take the chop off the detector) was planned by Gemini but has not been implemented, and Gemini does

not currently guide on the "off" nod position. Since this "off" position often falls on the detector, the implementation of guiding on it would have increased the mid-IR observing efficiency by a factor of two in imaging.

2.3.3 The Gemini instruments

The Gemini instruments OSCIR, T-ReCS and Michelle were used to carry out mid-IR imaging of 21 core-collapse SNe during the years 2001-2007. Table 2.2 provides details of the instruments and filters used for all observations.

OSCIR - Instrument description

OSCIR – the Observatory Spectrometer and Camera for the InfraRed – consisted of a mid-IR imager optimised for the wavelength range 8 – 25 μm and a low/medium-resolution (R = 100 – 1000) spectrograph, and was built by the University of Florida and NASA Marshall Space Flight Center[6]. It was on loan to Gemini-N and -S during 2000 and 2001, but was superseded by the facility mid-IR instruments, T-ReCS and Michelle. There was, however, a gap of nearly 3 years when no mid-IR instrument was available on either telescope. Details of OSCIR's detector size, plate scale and field of view in its imaging mode are provided in Table 2.2. Only the broad N-band filter was used for program GN-2001A-C-10.

T-ReCS - Instrument description

T-ReCS – the Thermal-Region Camera Spectrograph – is a mid-IR imager and long-slit spectrograph optimised for the 8 – 26 μm wavelength region (for low-resolution – $R \sim 100$ near 10 μm and $R \sim 80$ near 20 μm for long-slit spectroscopy), built by the University of Florida for Gemini South (Telesco et al. 1998). Medium-resolution ($R \sim 1000$ near 10 μm) spectroscopy is also available with a wavelength coverage of 8 – 13 μm. Figure 2.2[7] shows the T-ReCS optical path from the entrance window to the focal-plane array. Combined with Gemini's fast tip-tilt compensating secondary mirror, T-ReCS yields nearly diffraction-limited 10 μm images (FWHM $\lesssim 0\farcs4$) under most seeing conditions.

[6] http://www.gemini.edu/sciops/instruments/oscir/oscirIndex.html
[7] Obtained from the Gemini T-ReCS web pages at:
http://www.gemini.edu/sciops/instruments/t-recs/references/optomechanical-layout

Table 2.2: Details of Gemini Observatory instruments and filters in their imaging configuration for the SNe programmes. "GN" and "GS" refer to the instruments' host telescope, either Gemini-N or Gemini-S. All detectors are Raytheon arsenic-doped silicon impurity band conductor (Si:As IBC) arrays. Information was obtained from the Gemini website[1].

Instrument	Detector size [pix^2]	Plate scale [arcsec/pix]	Field of view [arsecond^2]	Filter	λ_{eff} [μm]	$\Delta\lambda$ [μm]	Sensitivity[2] [mJy]
OSCIR, GN	128×128	0.084	11×11	N (broad)	10.75	8.1 – 13.4	0.6[3]
T-ReCS, GS	320×240	0.09	28.8×21.6	N (broad)	10.36	7.7 – 13.0	1.4
Michelle, GN	320×240	0.1005	32×24	N′	11.2	10.1 – 12.5	1.1
				Qa	18.1	17.1 – 19.1	12
				Si-2	8.8	8.4 – 9.3	2.9
				Si-4	10.3	9.8 – 10.8	2.5
				Si-5	11.6	11.2 – 12.3	2.1
				Si-6	12.5	11.9 – 13.1	2.9

[1] Source of information in this table: http://www.gemini.edu.
[2] Filter sensitivities are for a point source, assuming a S/N of 5 with 30 mins on-source integration time.
[3] OSCIR broad N-band filter sensitivity is a preliminary value from the first OSCIR engineering run, and makes some unverified assumptions about the telescope performance (Source: http://www.gemini.edu/sciops/instruments/oscir/oscirSensitivity.html).

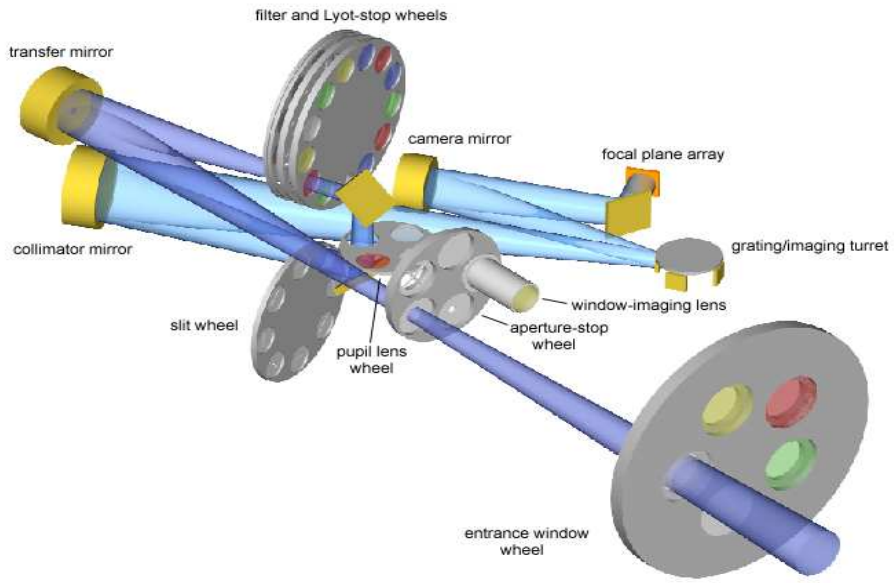

Figure 2.2: The optical path of the Thermal-Region Camera Spectrograph (T-ReCS) on Gemini-S, from the entrance window to the focal-plane array.

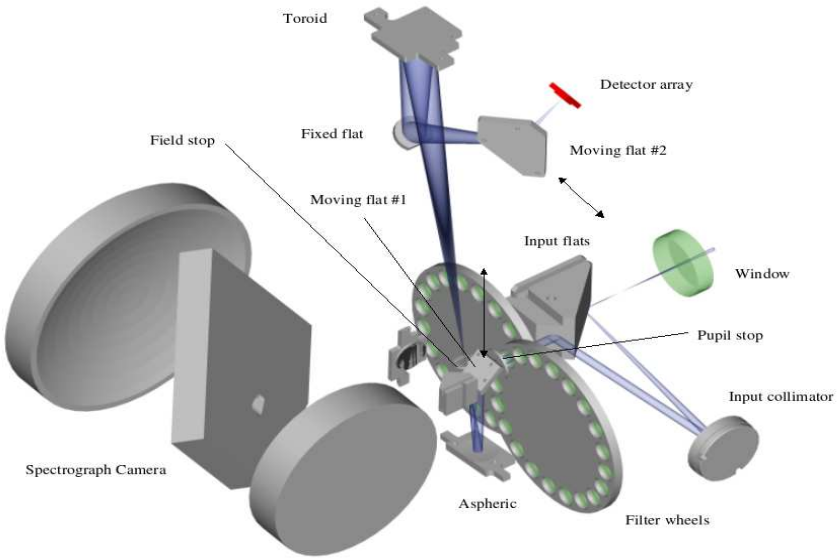

Figure 2.3: The optical path of Michelle on Gemini-N, from the entrance window to the detector array.

Details of T-ReCS's detector size, plate scale and field of view in its imaging mode are provided in Table 2.2. The Si:As IBC Raytheon detector has a switchable-capacitance i.e., there is a deep-well mode for high background imaging and a medium-well mode for general imaging and spectroscopy.

The instrument's imaging capabilities include broad-band filters (N, Q) and 15 narrow-band filters in the optimised wavelength range. A further 3 filters are available in the range $\sim 1 - 5$ μm, although these are limited by low detector quantum efficiency at short wavelengths and are mainly useful for target acquisition of bright sources.

As discussed in Section 2.3.2, the most accurate removal of the mid-IR sky and telescope background is achieved by the technique of chopping and nodding. At the time of the observations the maximum chop throw allowed on Gemini was 15 arcseconds, smaller than the T-ReCS field of view of 28.8×21.6 square arcseconds.

Michelle - Instrument description

The Michelle (Mid-IR eChelle) spectrograph and imager was built by the Astronomy Technology Centre (ATC) at the Royal Observatory of Edinburgh for shared use by both Gemini-N and the United Kingdom Infrared Telescope (UKIRT) (Glasse et al. 1997). Its first light was on UKIRT in August 2001, and its first usage on Gemini-N was in the first

half of 2002, becoming a permanent instrument on Gemini-N in 2004. Figure 2.3[8] shows Michelle's optical path layout from the entrance window to the detector array.

In its imaging mode, Michelle is optimised for the 7 – 26 μm wavelength region. Further details such as detector size, plate scale and field of view for Michelle in its imaging configuration can be found in Table 2.2. The instrument's imaging capabilities include semi-broad filters (N', Qa) and 6 narrow-band silicate filters in the optimised wavelength range. Whilst broad-band filters (N, Q and Q') exist for Michelle, imaging is not usually available with these due to array saturation problems. Michelle uses the same type of detector as T-ReCS: a Si:As IBC Raytheon detector with a switchable-capacitance. The $0\farcs10 \times 0\farcs10$ detector pixels critically sample the diffraction limited mid-IR Gemini PSF (FWHM $\sim 1.22\,\lambda/D \sim 0\farcs31$ at 10 μm, $\sim 0\farcs63$ at 20 μm). The default technique of beam-switch chopping and nodding was employed for the observations, using the maximum chop throw of 15″, smaller than the Michelle field of view of 32″×24″.

2.4 The Gemini observations

The following section describes each of the Gemini SNe programs carried out during the years 2001 to 2008, with the mid-IR instruments OSCIR, T-ReCS and Michelle. The tables for each program provide details of the targets and observations, including measured flux densities, and upper limits for non-detections. Listed are: SN type; age in days since explosion/discovery at the date of observation; host galaxy and radial velocity, V_h, in km s^{-1}; adopted distance, D, in Mpc (references for the distances are provided in the notes to Table 2.1); UT date and start time of observation; on-source integration time; mean airmass (interpolated linearly to midway through the observations); measured flux density, F_ν, in mJy, and upper limits for non-detections in the same units. The final column of each table gives the flux density/upper limit scaled to the distance of SN 1987A at 50 kpc (see discussion in Section 2.7). A description of the data reduction and flux measurement techniques follows in Sections 2.5 and 2.6. The results are discussed in Section 2.7.

2.4.1 Gemini-North/OSCIR program GN-2001A-C-10, May 2001

Two classical nights of OSCIR time on Gemini-N were allocated to this programme on 4 and 5 May 2001 (Project ID [PID]: GN-2001A-C-10, PI: Barlow). Unfortunately, two-

[8]Private communication from Dr Alistair Glasse, October 17 2006.

Table 2.3: Observation details and flux densities/3-σ upper limits for Gemini-N/OSCIR programme GN-2001A-C-10. N-band (10.75 μm) observations taken on May 6, 2001 UT.

Target	SN type	Age [days]	Host galaxy	V_h [km s^{-1}]	D [Mpc]	UT start	On-source time [s]	Mean airmass	F_ν / 3-σ upper limit [mJy]	50 kpc flux/ 3-σ upper limit [Jy]
SN 1999D	II	841	NGC 3690	3033	41.5	08:36:43.7	903.1	1.43	1.3 ± 0.4	896 ± 276
SN 1999an	II	791	IC 755	1501	20.6	09:50:00.7	903.1	1.36	≤ 1.1	≤ 187
SN 1999gq	II	500	NGC 4523	260	13.0	11:50:53.7	903.1	2.23	≤ 1.7	≤ 115
SN 1999ac	Ia $_{pec}$	800	NGC 6063	2848	39.0	13:12:42.7	903.1	1.21	≤ 1.2	≤ 730
SN 1999el	IIn	564	NGC 6951	1331	18.2	14:22:03.7	903.1	1.49	≤ 1.7	≤ 225

thirds of the time was lost due to telescope acquisition and guiding problems. Observing commenced a third of the way into the second night (6 May 2001 UT), allowing N-band imaging observations to be made of five recent SNe. Conditions were clear and dry, with humidity less than 20 percent. Table 2.3 lists details of the targets and observations, including measured flux densities and upper limits for non-detections. *These measurements of the OSCIR data were made by Scott Fisher at Gemini, an early collaborator on the SNe project, before my own work commenced on the project from 2004. The early 2001 sample has not been presented elsewhere, and has been included in this work for completeness.*

μ UMa and α CrB were used as flux standard stars (Cohen et al. 1999), with each observed for an on-source time of 43 seconds. 3-σ upper limits to the flux densities were determined from background statistics and scaled to a diffraction-limited size aperture with a radius of $\sim$4 OSCIR pixels (equivalent to an area of $\sim$50 pixels^2) at 10.75 μm, as described in Section 2.6.3. For airmasses $\leq$ 1.4, the N-band 3-σ sensitivity limits for 903 s on-source integration time were between 1.1 and 1.2 mJy.

2.4.2 Gemini-South/T-ReCS program GS-2004A-Q-1, March – December 2004

After the OSCIR observations in May 2001, no mid-IR instruments were available on either of the Gemini telescopes until 2004. 15 hours of Michelle queue time observations were awarded for June/July 2003 (PID: GN-2003A-Q-60, PI: Barlow) but all Michelle 03A programmes were subsequently cancelled by Gemini due to the instrument's unavailability.

Semester 2004A therefore represented the first opportunity to resume the programme since 2001A. Michelle was unavailable during 2004A on Gemini-N, but 30 hours of T-ReCS queue time on Gemini-S were awarded, with roll-over into semester 2004B (PID: GS-2004A-Q-1, PI: Barlow). A list of accessible nearby SNe with $V_{max} < 17$ mag and host galaxy radial velocities < 3000 km s^{-1}, discovered between February 2000 and August 2002 (since these were expected to have the optimum ages for 10-μm detection in mid-2004), was compiled using the Padova-Asiago online Supernovae Catalogue.

T-ReCS was used in queue mode to image 10 SNe with its broad N-band filter (10.36 μm) over semesters 2004A and 2004B. Table 2.4 provides observation details and flux density limits for the SN observations executed between March 4 and December 4 2004. The number of consecutive observations of a SN (on the same night) are indicated by the multiplier in the ninth column of Table 2.4. Where there were such multiple obser-

vations, the UT start time is that for the first of the sequence and the upper flux limit is that for the final averaged-combined image. The *total time on-source* is the total time in seconds spent integrating on the target field for each observation. Each observation had an effective on-source frame time of 3.6 seconds, equivalent to the on-source time per saveset (pair of coadded frames from each chop position). This is a consequence of the raw data structure and of the averaging of these raw frames during the data reduction process (discussed in more detail in Appendix B, Section B.2). Mean (i.e., mid-observation) airmasses were in the range 1.02 – 1.50, with an average mid-observation airmass for the sample of 1.20. Where there are consecutive observations of the same SN, mean airmasses for the individual observations are listed. The maximum chop throw of 15 arcseconds was used for each observation and, where appropriate, the orientation of the detector was varied to avoid potential contamination from bright neighbours. Since the SNe were too faint to see on the detector array, reasonable pointing accuracy (within 0.″5 radius of the nominal position) was ensured using the User1 astrometry method described in Appendix A.

With the ratio of *time awarded* to *SNe observed* being greater for the T-ReCS programme than for the previous OSCIR program, it was possible to allow longer exposure times per target. For on-source integration times greater than 900 s, it was recommended that repeat, or multiple step, observations were used to achieve the desired total time. This added negligible time to overheads but limited any data lost in the case of a problem during observations and allowed pausing of the sequence if weather conditions deteriorated. Each target had a minimum of three exposures with individual on-source integration times ranging from 608 – 652 s (see Table 2.4 for a breakdown of these). The majority of SNe were observed in the N-band for a total time of 1824 s on-source, yielding 3-σ detection limits ranging between 0.49 mJy and 1.01 mJy (a mean of 0.74 mJy). Standard 'baseline calibration' observations obtained by Gemini staff were used to calibrate all data for this programme, using the flux standard stars α CMa, α Hya, α TrA, HD 32887, 35536, 123139, 133774 and 196171 from Cohen et al. (1999). Total on-source exposure times for the standard stars ranged from 36 – 65 seconds, each having the same on-source frame time as the SN observations of 3.6 seconds. Upper limits to the flux densities are 3-σ upper limits in a diffraction-limited aperture with a radius of ~3.6 T-ReCS pixels (equivalent to an area of ~40 pixels^2) at 10.36 μm.

Table 2.4: Observation details and 3-σ upper limits to the flux densities for Gemini-S/T-ReCS program GS-2004A-Q-1. Broad N-band (10.36 μm) observations of 10 SNe were taken between March and December 2004.

Target	SN type	Age [days]	Host galaxy	V_h [km s^{-1}]	D [Mpc]	UT date	UT start	Total time on-source [s]	Mean airmass	3-σ upper flux limit [mJy]	50 kpc 3-σ upper limit [Jy]
SN 2001bq	II	1029	NGC 5534	2633	36.1	2004-03-04	06:00:36.0	3 × 608.1	1.22, 1.14, 1.10	≤ 1.01	≤ 527
SN 2003jg	Ib/c	139	NGC 2997	1087	10.3	2004-03-11	01:46:11.5	3 × 608.1	1.03, 1.01, 1.01	≤ 0.85	≤ 36.1
SN 2002ao	IIb/Ic	776	UGC 9299	1539	21.1	2004-03-11	06:48:22.0	3 × 608.1	1.18, 1.16, 1.16	≤ 0.82	≤ 146
SN 2002ds	II	626	E581-G25	2268	31.1	2004-03-12	07:02:20.0	3 × 608.1	1.06, 1.02, 1.02	≤ 0.77	≤ 298
SN 2000cb	II	1417	IC 1158	1927	26.4	2004-03-14	07:23:21.1	3 × 651.6	1.28, 1.21, 1.18	≤ 0.67	≤ 187
SN 2001X	II-P	1112	NGC 5921	1480	20.3	2004-03-15	08:14:47.6	2 × 608.1	1.23, 1.24	≤ 0.89	≤ 147
SN 2002ed	II-P	647	NGC 5468	2842	38.9	2004-05-01	04:51:50.1	3 × 608.1	1.14, 1.20, 1.30	≤ 0.75	≤ 454
SN 2001X	II-P	1160	NGC 5921	1480	20.3	2004-05-02	05:52:02.1	1 × 608.1	1.25	≤ 1.14	≤ 188
SN 2002ap	Ib/c $_{pec}$	980	NGC 628	657	9.3	2004-10-05	03:38:55.1	3 × 608.1	1.57, 1.48, 1.44	≤ 0.59	≤ 20.4
SN 2003B	II	301	NGC 1097	1274	17.4	2004-10-24	05:55:11.0	3 × 608.1	1.02, 1.07, 1.13	≤ 0.49	≤ 59.3
SN 2003B	II	304	NGC 1097	1274	17.4	2004-10-27	04:00:46.3	1 × 608.1	1.02	≤ 1.12	≤ 136
SN 2001ig	IIb/Ib/c	1053	NGC 7424	939	11.5	2004-10-28	00:36:51.8	4 × 608.1	1.02, 1.02, 1.04, 1.17	≤ 0.59	≤ 31.2
SN 2001ig	IIb/Ib/c	1090	NGC 7424	939	11.5	2004-12-04	00:50:07.4	3 × 608.1	1.16, 1.26, 1.39	≤ 0.69	≤ 36.5

2.4.3 Gemini-North/Michelle Director's Discretionary program GN-2004B-DD-4, September – October 2004

Our first use of Michelle on Gemini-N was for Director's Discretionary Time (DDT) observations of SN 2002hh awarded in semester 2004B (published by Barlow et al. 2005). A small percentage of the total observing time on Gemini-N/S is available for such DDT proposals.

SN 2002hh was our first positive detection of a SN in the mid-IR using publicly available *Spitzer* SINGS Legacy data taken in 2004 (see Chapter 3). Second-epoch observations were therefore important to constrain the evolution of the dust temperature and the emitting radius and mass of dust. The field immediately around the SN was extremely crowded, so Gemini observations – having ten times higher angular resolution than *Spitzer* – allowed much more precise separation of the emitting sources in the complex region around the SN.

To gauge necessary integration times, a blackbody was fit to the first epoch of *Spitzer* data to enable predictions of fluxes at 10 and 20 μm. The Michelle Integration Time Calculator (ITC) was then used to estimate the on-source time required to yield a reasonable signal-to-noise ratio. 900 s on-source was requested in both the N′ (11.2 μm) and Qa (18.1 μm) filters. Details of the DDT observations and flux densities of SN 2002hh are presented in Table 2.5. Central wavelengths and bandwidths of each filter used have already been defined in Table 2.2. For Michelle, the effective on-source *frame* time (given in the eleventh column of Table 2.5) is equivalent to the on-source time per nod position. This is a consequence of the structure of the raw data and the method of averaging the raw data frames during the reduction process (discussed in more detail in Appendix B, Section B.2). The stars HD 10380 and 192781 (Cohen et al. 1999) were used as flux standards, with each observed for a total on-source time of 47 seconds in the N'and Qa filters. Respective on-source frame times of 11.76 seconds and 6.8 seconds in N'and Qa are the same as those for the SN observations.

2.4.4 Gemini-North/Michelle program, February 2005 – July 2008

In 2005, a total of 41 hours of queue time observations were awarded for a long-term status project with Michelle on Gemini-N, spanning semesters 2005A (allocation: 25 hours), 2005B (8 hours) and 2006A (8 hours). Long-term project status was requested

Table 2.5: Observation details and flux densities of SN 2002hh with Gemini-N/Michelle Director's Discretionary program GN-2004B-DD-4, September – October 2004.

Target	SN type	Age [days]	Host galaxy	V_h [km s^{-1}]	D [Mpc]	UT date	Filter	UT start	Time on-source Total [s]	Time on-source Frame [s]	Mean airmass	F_ν [mJy]	50 kpc flux [Jy]
SN 2002hh	II-P	696	NGC 6946	48	5.9	2004-09-26	N′	07:06:03.4	1×1081.9	11.76	1.35	11.0 ± 0.4	153 ± 5.6
" "	"	704	" "	"	"	2004-10-04	Qa	06:54:59.3	1× 816.0	6.80	1.39	27.1 ± 5.2	377 ± 72

in order to obtain high-angular mid-IR imaging of a new sample of SN, synchronised with complementary *Spitzer* observations, and to monitor the time evolution of the dust emission of any *Spitzer*/Gemini detections by way of follow-up observations. The overall programme ID was GN-2005A-Q-20, although semesters 2005B and 2006A were assigned separate queue program references of GN-2005B-Q-2 and GN-2006A-Q-1 respectively. A further four semesters of Michelle queue time were awarded from 2006 to 2008: programs GN-2006B-Q-1, GN-2007A-Q-5, GN-2007B-Q-4 and GN-2008B-Q-44.

Details of the SN observations and measured flux densities/upper limits for each program are provided in Table 2.6. The number of sequential observations of a SN in one night is indicated by the multiplier in the tenth column of Table 2.6. Where there were multiple observations, flux densities and upper limits are for the final averaged-combined images. Mean (i.e., mid-observation) airmasses were in the range 1.02 – 1.74, with an average mid-observation airmass for the sample of 1.36. The telescope and instrument were set-up similarly as for the previous T-ReCS observations, with a maximum chop throw of 15 arcseconds, and the orientation of the detector set so as to avoid contamination from bright neighbours. The User1 astrometry method (described in Appendix A) was used to centre the SNe on the array. Total on-source exposure times for the flux standard stars were of order 47 – 94 s in N′ 54 – 82 s in Qa and 50 s for the four narrow band silicate filters. On-source frame times in the relevant filters are the same as those for the SN observations, as detailed in Table 2.6. Upper limits to the flux densities are 3-σ upper limits in a diffraction-limited aperture with a radius of ∼3.5 Michelle pixels (equivalent to an area of ∼38 pixels^2) at 11.2 μm, and a radius of ∼5.6 Michelle pixels (equivalent to an area of ∼98 pixels^2) at 18.1 μm. Further information regarding each program is discussed below.

GN-2005A-Q-20 observations, February – July 2005

The initial sample observed during the first semester of 2005 were five massive star SNe accessible from Gemini-N, with ages ranging from a few hundred to 1278 days, in galaxies with radial velocities from 48 km s^{-1} to 657 km s^{-1} and distances ranging from 6 to 12 Mpc.

All five targets were observed in the medium N′-band filter (11.2 μm), with three out of five SN observed twice, and individual on-source exposure times of order 1000 s. Following its detection with the *Spitzer Space Telescope* and consequent Gemini Director's Discretionary Time with Michelle in semester 2004B, SN 2002hh was also observed in

the medium Qa-band filter (18.1 μm). To get a better constraint on the spectral energy distribution (SED) of this SN, additional narrow-band observations were taken with silicate filters Si-2 (8.8 μm), Si-4 (10.3 μm), Si-5 (11.6 μm) and Si-6 (12.5 μm). Table 2.6 provides details of the SN observations for this program, carried out between February 28 and July 31 2005, and the flux densities measured. The stars HD 8388, 73108 and 198149 (Cohen et al. 1999) were used as flux standards.

GN-2005B-Q-2 observations, August 2005

Three SNe imaged previously with Michelle were observed during the 8 hours allocated for semester 2005B: SN 2003gd and SN 2002ap were observed in Michelle's N′ filter, and there was continued monitoring of SN 2002hh in bands N′ and Qa. Total on-source integration times were 1082 and 1250 s for the N′ and Qa filters respectively. Table 2.6 provides details of the SN observations carried out in August 2005 and the flux densities measured. The stars HD 8388 and 198149 (Cohen et al. 1999) were used as flux standards.

GN-2006A-Q-1 observations, April – June 2006

In the final semester (2006A) of this long-term project, four SNe were observed in Michelle's N′ filter. This included further follow-up observations of SN 2002hh and SN 2004et in NGC 6946, and new observations of two recent SNe, 2004dj and 2005cs, with typical total on-source times of *c*.1300 s. Table 2.6 provides details of the SN observations carried out between April 6 and June 20 2006, and the flux densities measured. The stars HD 73108, 128902 and 192781 (Cohen et al. 1999) were used as flux standards.

GN-2006B-Q-1 observations, September/October 2006 and March 2007

A further 8 hours were allocated in semester 2006B for more Michelle SN observations. Continued N′ and Qa band monitoring of SN 2002hh was carried out in September and October 2006. The total on-source integration time in the N′ filter was *c*.1400 s. For the Qa observations, 4×400 s on-source exposures were planned. The first of these was attempted on September 21 2006 but was aborted by the observer as the precipitable water vapour content had increased to greater than 2.0 mm. The second 400 s Qa exposure was taken the following night. Ideally all observations in one filter should be taken in one night, but deteriorating conditions often prevent this. The final two Qa observations were

executed on October 14 2006. Planned observations of two other SNe, 2004dj and 2004et, were not possible that semester due to time lost through a combination of unfortunate factors: failure of the OT's automatic time accounting and loss of the use of Michelle for a month due to an earthquake early in the semester. However, the N' and Qa band observations of SN 2004dj were carried out in March 2007, with total on-source integration times of *c*.2260 s and 1300 s in N' and Qa respectively. Details of the science observations and flux densities for this program are provided in Table 2.6. The stars HD 73108 and 192781 (Cohen et al. 1999) were used as flux standards.

GN-2007A-Q-5 observations, March – April 2007

In semester 2007A, 16 hours were awarded for Michelle follow-up imaging of four supernovae: SN 2002hh, SN 2004dj, SN 2004et and SN 2005cs. N'-band observations of all four SNe are presented here. Total on-source integration times range from *c*.1700 s to 2260 s. SN 2002hh and SN 2004dj were also been observed in the Qa filter, with total on-source integration times of *c*.970 s and *c*.1300 s respectively. Details of the science observations and flux densities are provided in Table 2.6. The stars HD 73108, 128902, 192781 and 198149 (Cohen et al. 1999) were used as flux standards.

GN-2007B-Q-4 and GN-2008B-Q-44 observations, June - July 2008

In semester 2007B, 13.4 hours were awarded to continue monitoring late-time Michelle mid-IR photometry of the four supernovae observed in the previous semester: SN 2002hh, SN 2004dj, SN 2004et and SN 2005cs. The N'-band observations of SN 2004et are presented in this thesis. Scheduling issues meant that the target was actually observed in semester 2008A. Faults with the telescope interrupted the observations of SN 2004et resulting in 7/8 of the requested data being obtained, amounting to a total on-source integration time of *c*.1950 s. A further 11.9 hours were awarded in semester 2008B for continued monitoring of SN 2004et with Michelle, and for late-time optical imaging with GMOS-N. Similar observations were also allocated for the Type IIn supernova, SN 2008S, which had recently been discovered (February 2008) in the same galaxy. The Michelle N'-band and GMOS-N observations of SN 2004et are presented in this thesis – see this chapter for Michelle results, but also refer to Chapter 5 for a thorough analysis of all mid-IR data (Gemini and *Spitzer*) for SN 2004et, including a discussion of the optical

photometry.

Details of the mid-IR science observations and the flux measurements for SN 2004et from these programs are provided in Table 2.6. The stars HD 192781 and 198149 (Cohen et al. 1999) were used as flux standards.

Table 2.6: Observation details and flux densities/3-σ upper limits for Gemini-N/Michelle programs GN-2005A-Q-20, GN-2005B-Q-2, GN-2006A-Q-1, GN-2006B-Q-1, GN-2007A-Q-5, GN-2007B-Q-4 and GN-2008B-Q-44 between February 2005 and July 2008. Bandwidths and effective wavelengths of the filters are provided in Table 2.2.

Target	SN type	Age [days]	Host galaxy	V_h [km s^{-1}]	D [Mpc]	UT date	Filter	UT start	On-source time Total [s]	On-source time Frame [s]	Mean airmass	F_ν / 3-σ upper limit [mJy]	50 kpc flux/ 3-σ upper limit [Jy]
GN-2005A-Q-20													
SN 2001gd	IIb	1192	NGC 5033	877	12.0	2005-02-28	N′	10:23:37.7	2 ×1081.9	11.76	1.18, 1.07	≤ 0.26	≤ 15.0
SN 2002hh	II-P	930	NGC 6946	48	5.9	2005-05-18	N′	13:07:43.5	1 × 564.5	23.52	1.40	8.6 ± 0.4	120 ± 5.6
" "	"	945	" "	"	"	2005-06-02	Si-2	11:55:45.3	2 × 466.6	12.96	1.43, 1.38	11.5 ± 1.8	160 ± 25
" "	"	946	" "	"	"	2005-06-03	Si-4	12:02:46.3	1 × 529.9	11.04	1.40	7.6 ± 1.2	106 ± 17
" "	"	"	" "	"	"	2005-06-03	Si-5	12:40:19.8	1 × 622.1	12.96	1.35	6.0 ± 0.6	84 ± 8.4
" "	"	"	" "	"	"	2005-06-03	Si-6	13:17:48.8	1 × 564.5	11.76	1.32	5.7 ± 0.9	79 ± 13
SN 2004et	II-P	311	" "	"	"	2005-07-30	N′	08:59:39.1	1 ×1081.9	11.76	1.33	1.7 ± 0.2	24 ± 2.8
SN 2002ap	Ib/c $_{pec}$	1278	NGC 628	657	9.3	2005-07-30	N′	13:52:42.7	1 ×1081.9	11.76	1.04	≤ 0.38	≤ 13.1
SN 2003gd	II-P	781	" "	"	"	2005-07-31	N′	12:07:41.3	2 ×1081.9	11.76	1.28, 1.08	≤ 0.30	≤ 10.4
GN-2005B-Q-2													
SN 2002hh	II-P	1007	NGC 6946	48	5.9	2005-08-03	N′	08:05:26.5	1 ×1081.9	11.76	1.37	8.3 ± 0.3	116 ± 4.2
" "	"	"	" "	"	"	2005-08-03	Qa	09:17:04.0	2 × 625.6	6.80	1.32, 1.34	24.0 ± 6.4	334 ± 89
SN 2003gd	II-P	784	NGC 628	657	9.3	2005-08-03	N′	14:02:04.5	1 ×1081.9	11.76	1.02	≤ 0.53	≤ 18.3
SN 2002ap	Ib/c $_{pec}$	1301	" "	"	"	2005-08-22	N′	13:51:11.2	1 ×1081.9	11.76	1.02	≤ 0.50	≤ 17.3
GN-2006A-Q-1													
SN 2004dj	II-P	614	NGC 2403	130	3.3	2006-04-06	N′	06:32:36.8	1 ×1317.1	11.76	1.58	1.9 ± 0.3	8.3 ± 1.3
SN 2005cs	II-P	284	M51	600	8.4	2006-04-07	N′	11:19:06.2	1 ×1317.1	11.76	1.17	≤ 0.36	≤ 10.2

cont. on next page

Table 2.6 cont.

Target	SN type	Age [days]	Host galaxy	V_h [km s^{-1}]	D [Mpc]	UT date	Filter	UT start	On-source time Total [s]	On-source time Effective [s]	Mean airmass	F_ν / 3-σ upper limit [mJy]	50 kpc flux/ 3-σ upper limit [Jy]
SN 2004et	II-P	597	NGC 6946	48	5.9	2006-05-12	N′	14:32:07.9	1 × 811.4	11.76	1.32	≤ 0.51	≤ 7.1
" "	"	599	" "	"	"	2006-05-14	N′	13:55:22.4	1 × 376.3	11.76	1.36	≤ 0.79	≤ 11.0
SN 2002hh	II-P	1297	" "	"	"	2006-05-20	N′	13:01:34.4	1 ×1317.1	11.76	1.37	6.7 ± 0.4	93 ± 5.6
" "	"	1328	" "	"	"	2006-06-20	N′	13:40:42.2	1 × 705.6	11.76	1.34	7.6 ± 0.5	106 ± 7.0
GN-2006B-Q-1													
SN 2002hh	II-P	1421	NGC 6946	48	5.9	2006-09-21	N′	06:18:35.2	2 × 705.6	11.76	1.31, 1.32	5.8 ± 0.2	81 ± 2.8
" "	"	1422	" "	"	"	2006-09-22	Qa	07:00:04.7	1 × 408.0	6.80	1.32	≤ 14.3	≤ 199
" "	"	1444	" "	"	"	2006-10-14	Qa	06:40:45.1	2 × 408.0	6.80	1.39, 1.49	≤ 12.1	≤ 169
SN 2004dj	II-P	965	NGC 2403	130	3.3	2007-03-23	Qa	05:19:36.0	4 × 324.5	10.14	1.43–1.46	≤ 4.40	≤ 19.2
" "		967	" "	"	"	2007-03-25	N′	05:18:28.0	4 × 564.5	11.76	1.43–1.56	1.6 ± 0.3	7.0 ± 1.3
GN-2007A-Q-5													
SN 2005cs	II-P	628	M51	600	8.4	2007-03-17	N′	12:48:55.3	4 × 564.5	11.76	1.15–1.37	≤ 0.38	≤ 10.7
SN 2004dj	II-P	984	NGC 2403	130	3.3	2007-04-11	N′	05:42:23.8	3 × 564.5	11.76	1.48–1.74	≤ 0.45	≤ 2.0
" "	"	987	" "	"	"	2007-04-14	Qa	05:30:07.9	4 × 324.5	10.14	1.47–1.60	≤ 8.42	≤ 37
SN 2004et	II-P	1020	NGC 6946	48	5.9	2007-07-09	N′	11:41:49.6	3 × 564.5	11.76	1.31–1.38	≤ 0.40	≤ 5.6
SN 2002hh	II-P	1722	" "	"	"	2007-07-19	N′	09:21:55.0	3 × 564.5	11.76	1.31–1.37	7.2 ± 0.2	100 ± 2.8
" "	"	"	" "	"	"	"	Qa	11:55:59.0	3 × 324.5	10.14	1.34–1.37	≤ 8.60	≤ 120
GN-2007B-Q-4 and GN-2008B-Q-44													
SN 2004et	II-P	1368	NGC 6946	48	5.9	2008-06-21	N′	13:03:26.1	3.4× 564.5	11.76	1.32–1.45	1.04 ± 0.21	14.4 ± 3.0
" "	"	1386	" "	"	"	2008-07-09	N′	12:20:30.7	4 × 564.5	11.76	1.33–1.55	1.02 ± 0.22	14.1 ± 3.1

2.5 Gemini mid-IR data reduction

This section provides a brief outline of the software and steps used to reduce the mid-IR Gemini data presented in this chapter. A more detailed description of the software used and techniques employed can be found in Appendix B.

The data reduction software used for Gemini mid-IR observations is an external package layered upon IRAF[9], known as the Gemini IRAF package. The package contains suites of tasks for processing data from the various Gemini instruments.

2.5.1 OSCIR data reduction

The following tasks in the `oscir` suite of the Gemini IRAF package were used to process the Gemini-N/OSCIR SN data presented in Section 2.4.1: `ohead`, `oview`, `obackground` and `oreduce`. A typical data reduction sequence with a brief description of each task is listed below:

1. `ohead` and `oview` were used to respectively check the FITS file header information and inspect raw data frames.

2. `obackground` was used to analyse the background levels in the reference frames and identify any bad nodsets or savesets to be omitted in the final data coaddition.

3. `oreduce` was used to derive the chop and nod differences and average these to get a 2-dimensional image. Bad nodsets or savesets, identified with the `obackground` task, are input here for exclusion from the final averaged-combined frame.

A more detailed description of the OSCIR data format and each of the Gemini IRAF tasks is provided in Appendix B, Section B.1.

2.5.2 T-ReCS and Michelle data reduction

Raw science and calibration data files from the early queue-mode SN observations were distributed to PIs by Gemini on a compact disc, but by mid-2005 became available (together with ancillary files such as observation logs and weather images) much more efficiently and quickly via the Gemini Science Archive (GSA), hosted by the Canadian

[9]IRAF is distributed by the National Optical Astronomy Observatory, which is operated by the Association of Universities for Research in Astronomy (AURA) under cooperative agreement with the National Science Foundation.

Table 2.7: Gemini IRAF MIDIR tasks for T-ReCS/Michelle data reduction

Task name	*Instrument*/Description	Used
	T-ReCS, Gemini-S	
TVIEW	(Interactively) inspects each frame in a raw T-ReCS file	yes
TBACKGROUND	Performs statistics on frames in a raw T-ReCS file	yes
TCHECKSTRUCTURE	Checks the structure of a raw T-ReCS file	no
TPREPARE	Prepares T-ReCS data for reduction with the MIDIR tasks	yes
	Michelle, Gemini-N	
MVIEW	(Interactively) inspects each frame in a Michelle raw file	yes
MCHECKHEADER	Makes Michelle headers GSA-compatible	yes
MPREPARE	Prepares Michelle data for reduction with the MIDIR tasks	yes
	Both	
MIVIEW	Views data frames that have been M/TPREPARE'd	yes
MIFLAT	Derives flat fields for images	no
MISTACK	Coadds ("averages" or "sums") nod images within a given data file	yes
MIREGISTER	Registers and coadds nod images within a given data file	no
MIREDUCE	Reduces T-ReCS/Michelle images by calling the other tasks	yes

Astronomy Data Centre (CADC)[10]. Proprietary data is accessed with a registered CADC username and password and directly downloaded from the online database.

The Gemini IRAF `midir` suite contains tasks for processing the mid-IR imaging data from the Michelle and T-ReCS instruments. There are tasks specific to each instrument, and tasks which are common to both. Table 2.7 provides a brief description of the tasks available in the `midir` package and indicates which of the these were used for reducing the Gemini data discussed in this chapter. The reduction process was automated for batch processing of the T-ReCS or Michelle raw input files using one call to the `mireduce` task. This task in turn calls the relevant tasks described in Table 2.7 to produce the final averaged-combined images.

A more detailed description of the T-ReCS and Michelle data formats and of each of the `midir` tasks can be found in Appendix B, Section B.2.

[10]http://www2.cadc-ccda.hia-iha.nrc-cnrc.gc.ca/gsa/

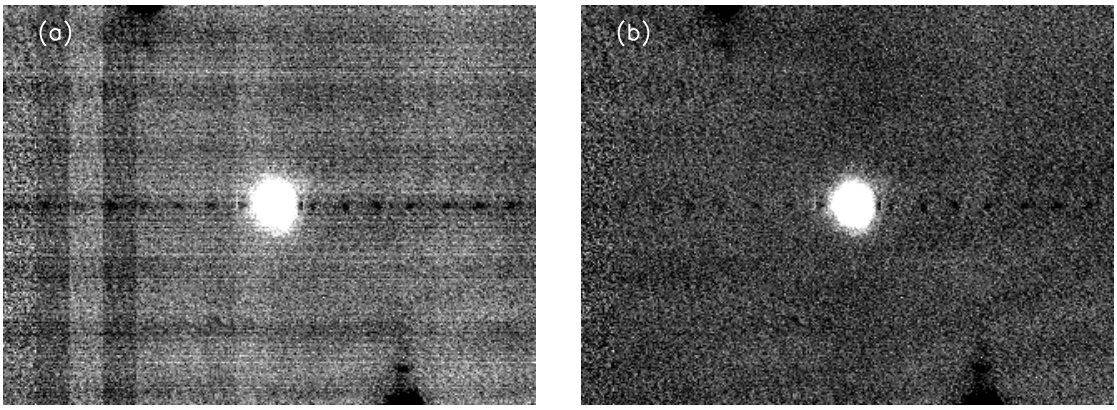

Figure 2.4: Example of an N′-band Michelle image of a standard star (a) before and (b) after cleaning. Panel (a) shows the vertical and horizontal striping often seen in reduced Gemini mid-IR images. The "hammer effect" seen here as the depressed response in every channel of the array at the same row as the bright source, is not so easily removed.

2.5.3 Final image manipulation: cleaning and combining

In many cases, the reduced mid-IR images showed similar broad horizontal and/or vertical striping, an example of which is shown in Figure 2.4 (a). Two custom IDL routines (not part of any Gemini supported software package) used to clean the data were obtained from our Gemini Contact Scientist[11]: '`noise_maskh.pro`' which removes the horizontal banding, and '`noise_maskv.pro`' which removes the vertical striping, including any channel to channel noise. A more detailed description of the IDL routines is given in Appendix B, Section B.3. Figure 2.4 (b) shows an example of a cleaned image.

The cleaning had little effect on the fluxes measured for the standards and the fainter SNe detections, however, the photometric uncertainties introduced as a result of the image cleaning techniques are included within the general uncertainties discussed in Section 2.6.4.

Multiple same-filter images of a science target taken during one night were coadded with the IRAF task `imcombine` using the default option of averaging the frames. For images with SN detections, a Gaussian filter was first applied to smooth the images to be coadded, which were then blinked in the image display application to check for relative positional offsets of the source on the array. The Gaussian-smoothed data could be used to help determine accurate offsets in image coordinates X and Y, which were then applied

[11] IDL routines (written by James M. De Buizer, Gemini Observatory, Southern Operations Center, October 2003 and modified by Marshall Perrin, UC Berkeley, June 2005) obtained via private communication with Scott Fisher at Gemini, February 6 2006.

with the IRAF task `imshift` to align the un-smoothed images before final coaddition.

2.5.4 Flux calibration

As discussed in Section 2.4, flux standard stars for each of the Gemini programs were observed on the same night as the science targets, in the appropriate filters and at closely-matched airmasses to the science observations, as part of the Gemini baseline calibration set.

To flux calibrate the T-ReCS and Michelle Gemini science data, it was necessary to determine the fluxes of the relevant observed standard stars at the effective wavelengths of the filters used. This was done by convolving the adopted SED of the standard (in $F(\lambda)$ units) with the appropriate T-ReCS/Michelle filter and atmospheric profiles, using the Starlink package DIPSO as described in the bullet points below. Template model spectra of the standard stars (Cohen et al. 1999) were obtained from the Gemini website[12]. The filter and atmospheric transmission data were also obtained from the Gemini web pages[13].

- ASCII format data of the template model spectra of the standard stars and the relevant filter and atmospheric transmission profiles were read into DIPSO, using the `alasrd` command.
- The filter and transmission profiles were convolved using the `amult` command, which multiplies the Y values in a specified stack entry by the values in the current arrays. The data in the current arrays are mapped onto the X grid of the specified stack data, so the stack entry with coarsest X grid of data, was mapped onto the finer X grid of data "popped" into the current array.
- The convolved filter and transmission data were integrated with the DIPSO command `integrate` which estimates the area under the current arrays using simple trapezoidal integration.
- The template model spectrum of the standard star was then convolved with the filter and transmission profiles, using the `amult` command as previously described. The

[12]Now obtainable from this link:
http://www.iop.org/EJ/article/1538-3881/117/4/1864/template21.tar.gz.
[13]T-ReCS and Michelle filter transmission data were obtained from:
http://www.gemini.edu/sciops/instruments/t-recs/imaging/filters (T-ReCS) and
http://www.gemini.edu/sciops/instruments/michelle/imaging/filters (Michelle).
Atmospheric transmission data was obtained from:
http://www.gemini.edu/sciops/ObsProcess/obsConstraints/atm-models/mktrans_nq_10_15.dat.

result was integrated with the `integrate` command, to give the total in-band flux through the atmosphere and filter.

- The 'mean' flux of the standard star over the filter and atmospheric transmission profiles was calculated by dividing the total in-band flux of the stellar spectrum by the integrated atmosphere and filter transmissions.
- The wavelength at which the monochromatic flux of the template stellar spectrum was equal to the 'mean' flux derived above was adopted as the effective wavelength.

A list of the standard stars used to flux calibrate the Gemini data obtained between 2004 and 2008, together with their measured in-band flux and the mean flux (in F_λ and F_ν units) at the measured effective wavelength (λ_{eff}) of the filters used are presented in Table 2.8. The seventh column lists the Gemini programs in which those standards stars were observed. The Gemini webpages now have a tool available to calculate in-band brightness values for mid-IR standard stars[14]. This was used to double-check the values measured from the template spectra in the method described above, and the measured brightnesses are within 5% of those determined from the online tool. The N-band fluxes of the standard stars for the OSCIR program in 2001 were approximated by the 10.1 μm magnitudes from Tokunaga (1984), giving 90.92 Jy for μ UMa and 4.69 Jy for α CrB.

Finally, to complete the science image calibration, aperture photometry was performed on the standard stars to calculate the flux conversion factor in mJy/count. Multi-aperture photometry was carried out using IRAF's `phot` task to determine which aperture size contained most of the flux of the standard star by inspecting plots of counts versus aperture radius and noting the radius at which the counts levelled off. Overplotting apertures on the image of the standard star with the IRAF `tvmark` task, and adjusting the contrast, helped to visually confirm the optimal aperture size for encompassing the complete flux of the star, and the corresponding counts were noted. Airmass corrections were applied to the counts of the standard star, normalising to an airmass of 1.00, using the median extinctions through the relevant broad and narrow band filters for Mauna Kea as given in Table 2.9[15]. The airmass-corrected flux conversion factor was then simply calculated by converting the units of the mean flux of the star at the effective wavelength (F_ν at λ_{eff}

[14]The Gemini mid-IR standard star in-band flux calculator can be found on the Michelle Mid-IR Resources page at: http://www.gemini.edu/sciops/instruments/michelle/mid-ir-resources.

[15]Adapted from Table 1 of Krisciunas et al. (1987) and reproduced on the Gemini website at: http://www.gemini.edu/sciops/telescopes-and-sites/observing-condition-constraints/extinction#MK%20thermal-infrared%20extinction.

Table 2.8: Standard stars for all Gemini programs, 2004 – 2008.

Target	Filter	In-band flux [W cm^{-2}]	F_λ at λ_{eff} [W cm^{-2} μm^{-1}]	λ_{eff} [μm]	F_ν at λ_{eff} [Jy]	Programs observed in*
α CMa	N	1.59E-15	4.14E-16	9.92	135.7	04A
α Hya	N	1.47E-15	3.84E-16	10.11	131.0	04A
α TrA	N	1.51E-15	3.93E-16	10.05	132.2	04A
HD 8388	N′	3.74E-17	1.83E-17	11.23	7.7	05A,05B
HD 10380	N′	5.30E-17	2.59E-17	11.18	10.8	04B
HD 12929	Qa	2.35E-17	2.38E-17	17.85	25.3	04B
HD 32887	N	6.09E-16	1.59E-16	9.98	52.8	04A
HD 35536	N	8.19E-17	2.13E-17	9.98	7.1	04A
HD 73108	N′	3.07E-17	1.50E-17	11.23	6.3	05A,06A,06B,07A
" "	Qa	2.26E-18	2.29E-18	18.05	2.5	06B,07A
HD 123139	N	6.46E-16	1.69E-16	9.97	55.9	04A
HD 128902	N′	2.44E-17	1.19E-17	11.22	5.0	06A,07A
HD 133774	N	1.33E-16	3.47E-17	9.98	11.5	04A
HD 192781	N′	2.06E-17	1.00E-17	11.22	4.2	06A,06B,07A,07B,08B
" "	Qa	1.62E-18	1.64E-18	17.62	1.7	04B,06B,07A
HD 196171	N	2.33E-16	6.08E-17	9.98	20.2	04A
HD 198149	N′	5.19E-17	2.53E-17	11.22	10.6	05A,05B
" "	Qa	3.65E-18	3.70E-18	18.23	4.1	05A,05B
" "	Si-2	4.14E-17	6.54E-17	8.75	16.7	05A
" "	Si-4	2.48E-17	3.52E-17	10.30	12.5	05A
" "	Si-5	1.80E-17	2.17E-17	11.64	9.8	05A
" "	Si-6	1.21E-17	1.67E-17	12.43	8.6	05A

* Gemini program abbreviations key:
04A: GS-2004A-Q-1, 04B: GN-2004B-DD-4, 05A: GN-2005A-Q-20, 05B: GN-2005B-Q-2, 06A: GN-2006A-Q-1, 06B: GN-2006B-Q-1, 07A: GN-2007A-Q-5, 07B: GN-2007B-Q-4, 08B: GN-2008B-Q-44.

in Table 2.8) from Jy to mJy and then dividing this by the number of airmass-corrected counts measured from the aperture photometry.

2.6 Flux density measurements: detections and upper limits

Both aperture photometry and PSF-fitting techniques were used throughout this thesis to measure the flux densities of the mid-IR SN detections. For the Gemini data, the few SN detected were isolated sources on a relatively uniform background for which aperture photometry was appropriate. However, for the *Spitzer* data, the relatively low spatial resolution of the space telescope often resulted in crowded fields with varying backgrounds, making aperture photometry difficult and imprecise. For these data, PSF-fitting was empirically found to be a more robust flux measurement technique.

For consistency of approach, PSF-fitted photometry was adopted as the main method for measuring the SN brightness for *all* data and the results presented in this and subsequent chapters were obtained using PSF-fitting techniques.

Table 2.9: Median extinctions through broad-band filters for Mauna Kea (Kriscinunas et al. 1987), adopted for airmass corrections of Gemini data.

Wavelength [μm]	Filter bandwidth	Extinction [mag/airmass]
8.7	narrow	0.12
10.0 (N)	broad	0.15
10.3	narrow	0.07
11.6	narrow	0.08
12.5	narrow	0.13
20.0 (Q)	broad	0.42

However, aperture photometry was also performed in a number of cases to compare with the fluxes measured from PSF-fitting, providing a sanity check on the results. Consequently, the techniques and software used for both methods are described in the following sections.

2.6.1 Aperture photometry with IRAF `phot`

Aperture photometry of the SN detections was carried out with the IRAF `phot` task.

`phot` computes and outputs accurate centres (image x and y coordinates), sky values, magnitudes and equivalent counts for one or more objects in the specified image, whose input coordinates are read from a text file, or from the image display cursor in interactive mode. Various parameters can be set to control the photometry. For the `phot` task, the image data characteristics are specified in `datapars`; the centring and sky-fitting algorithms are defined by setting the parameters in `centerpars` and `fitskypars`; and the photometry parameters are defined in `photpars`.

The input image coordinates of the objects for the `phot` task were measured interactively from the image display in the graphics window with the IRAF `imexamine` command. Roughly centring the cursor on the object and hitting the 'x' key returned the cursor (x,y) position to the IRAF terminal, which was then copied into a text file for reading into the `phot` task.

The aperture radius size (parameter: **aperture**), in pixels, was chosen to be approximately equal to, or just greater than, the object's FWHM, which was investigated using the radial profile function (keystroke 'r') of the `imexamine` task. For example, this was

found to be between 3 and 5 pixels for the Michelle N′ filter at 11.2 μm, corresponding to an angular sizes of 0.″3–0.″5 for the image pixel size of 0.″1×0.″1. A mode sky-fitting algorithm (**salgorithm**) was used and the sky annuli parameters, of starting radius (**annulus**) and width (**dannulus**) in pixels, were set such that the sky annulus was positioned a few pixels in radius beyond the object aperture and at least 10 pixels in width. A centroid algorithm (**calgorithm**) within a box-size (**cbox**) of dimension 5 × 5 pixels was used for computing the object centres. The effective gain (**epadu**) and array readout noise (**readnoise**) were also set as part of the `datapars` parameters to achieve accurate background statistics for the noise model. For a stacked image that is an average of N frames, these parameters are defined as follows:

$$\textit{effective gain} = N \times \textit{gain}$$
$$\textit{effective readnoise} = \sqrt{N} \times \textit{readnoise}.$$

The Gemini detectors have a readnoise of about 3500 electrons, and the gain (in general, about 500 electrons/ADU) was obtained from the FITS image header information.

A typical call to the `phot` task for carrying out photometry of a SN detection is as follows:

```
 ecl> phot image=gemini_sn_image.fits coords=gemini_sn_image.coo \\
»> output=default readnoise=24250 epadu=24000 itime=11.76 \\
»> calgorithm=centroid cbox=5 salgorithm=mode annulus=10 dannulus=10 \\
»> aperture=4 interactive- verify-
```

The counts output from the `phot` task were airmass-corrected in the same way as for the standard stars, by normalising to an airmass of 1.00 using the median extinctions through the relevant broad and narrow band filters for Mauna Kea as given in Table 2.9. The airmass-corrected counts were then converted to F_ν units by multiplying with the flux conversion factor, as derived from the standard stars described previously in Section 2.5.4.

As is generally the case for aperture photometry of point sources, aperture sizes used to measure the SN detections were smaller than those used to measure the brighter standards. A larger aperture obviously contains more stellar flux, but this can be inappropriate for fainter sources since noise can tend to dominate and result in imprecise fluxes. For such fainter sources, the maximum signal-to-noise is usually found at some intermediate

aperture radius which does not necessarily contain all of the stellar flux. As previously described, this optimal aperture size for the detections was estimated as being close to the FWHM of the stellar profile (usually up to one or two pixels larger).

Approximate aperture corrections (Stetson 1990) were used to rectify the problem of the 'missing flux' which results from using a smaller aperture. These were estimated from aperture photometry of the standard stars by taking the ratio of the number of counts in the large aperture (used to determine the flux conversion factor) to the number of counts in the smaller aperture (used to do photometry on the SN). The airmass-corrected flux densities of the SN detections were then scaled by this aperture-correction factor to provide the final flux densities.

2.6.2 PSF-fitted photometry with IRAF `daophot`

Fluxes of the SN detections were measured using PSF-fitted photometry as implemented in IRAF `daophot`, which uses the task structure and algorithms of the DAOPHOT II software package (Stetson 1992, 1987) within the IRAF data reduction and analysis environment. The process uses a non-linear least squares algorithm to simultaneously fit the sky and flux of a point source using either a user-supplied PSF or one created from isolated, bright sources in the science data to be measured. A detailed discussion of how to use the IRAF `daophot` package for carrying out photometry in crowded fields can be found in Davis (1994), but an overview of the general PSF-fitting method, with details of the sub-tasks and parameters used for the data in this thesis, is given in Appendix C.

In the case of the Gemini data, the only star available to create the PSF model was the standard star used for flux calibration of the SN data, since there were no other appropriate sources in the field of view of the science observations.

The standard star calibration observations were taken immediately before or after the science observations of the SN, and variations in the airmass for each observation were accounted for by applying airmass corrections to the science (SN) and calibration (standard star) data before construction of the PSF model and the PSF-fitting. The airmass corrections were calculated in the same way as for the aperture photometry by normalising to an airmass of 1.00 using the median extinctions through the relevant broad and narrow band filters for Mauna Kea (given in Table 2.9). For the Michelle N' detections, airmass corrections ranged from 4–9 %. For the single broad Qa band detection of SN 2002hh on 3 August 2005, an airmass correction of ~ 14 % was applied, whereas corrections for the

narrow silicate filter observations of SN 2002hh in June 2005 were around 4 %.

After applying the airmass corrections to the data, the PSF model was constructed from the standard star using the IRAF `daopsf` task written by SEEDS collaborator Dr B. E. K. Sugerman, as described in Appendix C. The aperture radius for the photometry used to set the magnitude of the PSF model within the `daopsf` task was chosen to be the same size as the PSF radius, i.e., the PSF should measure 100 % of the flux.

For PSF-fitting of the SN detections, the size of the fitting radius was chosen to be approximately equivalent to the FWHM of the stellar profile, but was occasionally varied by 1 or 2 pixels to optimise the fits. The sky background was modelled during the PSF-fitting process, using sky annuli at appropriate distances around the SN, avoiding any contaminating sources. In most cases, the `allstar` task used to do the actual PSF-fitting was successful in centring on the SN profile via its centroiding algorithm. However, if the SN was quite faint, this algorithm was turned off such that the PSF-fitting was centred directly on the input coordinates corresponding to the SN position. The final PSF-fitted and subtracted images were inspected alongside the un-subtracted images to check the goodness of the fits. The airmass-corrected counts were converted to F_ν units by multiplying with the flux conversion factor derived previously (Section 2.5.4) to provide the final flux densities.

Flux densities estimated from aperture photometry were within 20 % of those determined from PSF-fitting, and on average were consistent to within 10 %. The final flux densities presented in Tables 2.3–2.6 are those measured from PSF-fitting.

2.6.3 Non-detections – upper limits to flux densities

The flux density upper limits presented in this chapter were determined from noise statistics of the final reduced, combined and flux calibrated images using the following method:

- For each of the Gemini images with non-detections, noise statistics were investigated with the IRAF `imstat` task which, amongst other values, returns the standard deviation of the pixel distribution. This gave an estimate of the average noise per pixel (σ_{pix}, in units of mJy/pixel). A comparison of the standard deviation for the entire image frame was compared with the average of the standard deviations of four smaller, separate regions within the image to check the consistency of the noise

around the frame.

- From σ_{pix}, a 1-sigma limit was calculated by measuring how many pixels would be in a diffraction-limited aperture of radius = $1.22(\lambda/D)$ at the effective wavelength of the filter used (λ) for the diameter of the Gemini telescopes (D = 8.1 m), and then multiplying the value of noise per pixel (σ_{pix}) by the square root of the number of pixels (N_{pix}).
- The result was then multiplied by 3 to obtain a 3-sigma upper limit ($3\sigma_{lim}$) to the flux. Hence:

$$3\sigma_{lim} = 3 \times (\sigma_{pix}) \times \sqrt{N_{pix}}$$

2.6.4 Error analysis

The flux density errors provided in Tables 2.3–2.6 are statistical errors (σ_{stat}) output from the IRAF PSF-fitting task `daophot`. However, they do not take into account systematic photometric uncertainties introduced by the calibration and flux measurement techniques.

Calibration errors (σ_{cal}) arise from a number of sources, including: the accuracy of the fluxes derived from the standard star template spectra provided by Cohen et al. (1999); the image "cleaning" with the IDL routine (see Section 2.5.3); the choice of aperture size used to measure the counts corresponding to the total flux of the standard star; the size and position of the sky annuli for background subtraction during the aperture photometry; and any differences in flux conversion factors derived on nights where more than one standard was available. Uncertainties are also likely to be introduced from airmass and aperture corrections to the counts of the standard stars. For those parameters it was possible to vary, the change in flux of the SN detection was investigated in a few cases and the standard deviation from the average flux was found to be within 15%.

Photometric uncertainties introduced during the flux measurement process (σ_{flux}) arise from the image cleaning; the choice of aperture size and sky annuli for the aperture photometry; the accuracy of the PSF model and the fits in the case of PSF-fitting; and the choice of appropriate airmass and aperture corrections. By investigating the impact of changing these parameters in a few cases, σ_{flux} was estimated to be within 20%.

The final overall uncertainty in the flux density measurement can be estimated by summing the statistical and systematic errors in quadrature as follows (the individual errors are assumed to be equally weighted):

$$\sigma_{tot} = \sqrt{\sigma_{stat}^2 + \sigma_{cal}^2 + \sigma_{flux}^2}$$

With regard to the upper limits measured, calibration errors are a source of uncertainty and a σ_{cal} of 15% also applies. An alternative method of estimating the upper limits was tried in a number of cases, whereby PSFs of unit flux were created with the `daopsf` task in IRAF, scaled to a sensible faint flux starting from 1 or 2 sigma above the background, and added in random locations to a Gemini image frame of a non-detection (which basically just includes background noise). The confidence level at which the various fake stars could be detected by eye and recovered with PSF-fitting techniques was recorded for the various fluxes tried, and at the 95% confidence level this was interpreted as a 5-sigma flux from which a 3-sigma upper limit could be estimated. This was quite a laborious method, which was impractical to perform for every image, but perhaps provides a more realistic handle on the upper limits. Differences between the upper limits derived from the techniques described here and in Section 2.6.3 are of the order of 20%.

2.7 Discussion of results

Mid-IR photometry of 21 SNe was obtained with three different instruments on the Gemini telescopes from 2001 to 2008. Of the whole sample, only *three* SNe (SN 2002hh, SN 2004dj and SN 2004et) were robustly detected, and consequently monitored, with Michelle on Gemini-N. There was also one apparent marginal (~ 3-σ) detection of SN 1999D in NGC 3690, with OSCIR on Gemini-N. At an estimated Hubble distance of 42 Mpc (V_h = 3033 km s^{-1}, NED), and as the most distant SN in the whole mid-IR sample, this is a very surprising result and its plausibility is discussed briefly below. The remaining four SNe observed with OSCIR (between 1.4 to 2.2 years after explosion, and at distances between 13 and 40 Mpc) were non-detections. Of the 10 SNe observed with the T-ReCS broad N-band filter on Gemini-S in 2004, none were detected. Their epochs varied between 5 months and almost 5 years post explosion and their distances ranged from $\sim$ 10–40 Mpc. Based on the lack of success in the earlier programs, a closer sample of SNe (3–12 Mpc) were chosen for the Gemini-N Michelle observations during 2005–2008. As already noted, this yielded 3 detections, all of which were the most common CCSNe of Type II-P, and represented the closest of the sample: SN 2002hh and SN 2004et both occurred in the face-on spiral galaxy NGC 6946 at a distance of 5.9 Mpc (Karachentsev et al. 2000), and SN 2004dj

occurred in the spiral galaxy NGC 2403 at a distance of ∼3.3 Mpc (Karachentsev et al. 2004). Monitoring of these SNe with Michelle continued throughout the programme, spanning epochs from 300 to 1700 days post explosion. The four remaining SNe observed with Michelle (the Type IIb SN 2001gd, the peculiar Type Ib/c 2002ap, and the Type II-P SNe 2003gd and 2005cs) were not detected, although the mid-IR detection of SN 2003gd in NGC 628 (D = 9.3 Mpc; Hendry et al. 2005) with *Spitzer* has been the subject of analysis by the SEEDS team, and is discussed in Chapters 3 and 4 (Section 4.4).

Figure 2.5 shows the 10-μm flux densities and upper limits of the Gemini SEEDS SNe sample, scaled to a distance of 50 kpc (measured as part of this work and presented in Tables 2.3–2.6), and plotted as a function of time (days) since explosion. The distance-scaling allows for a comparison with the 10-μm flux densities of SN 1987A at similar epochs, which are also shown in the figure. The data for SN 1987A were taken from Bouchet et al. (1989), Bouchet & Danziger (1993) and Wooden et al. (1993). The figure caption provides a further explanation of the symbols and labelling. (A similar figure is provided for the 8-μm SNe data obtained with the *Spitzer Space Telescope* in the discussion section of Chapter 3 – Figure 3.7).

It should be noted that whilst reference is made to "10-μm" fluxes for the values plotted in Figure 2.5, the different Gemini instrument filters had slightly different effective wavelengths (λ_{eff}) and bandwidths ($\Delta\lambda$). These were given in Table 2.2 for each instrument/filter used for the Gemini observations, but are summarised for Figure 2.5 as follows: the broad N-band filters used with OSCIR and T-ReCS had λ_{eff} = 10.75 μm ($\Delta\lambda$: 8.13–13.36 μm) and λ_{eff} = 10.36 μm ($\Delta\lambda$: 7.70–12.97 μm), respectively, whilst the slightly narrower Michelle N' filter has λ_{eff} = 11.2 μm ($\Delta\lambda$ 10.1–12.5 μm). The Bouchet et al. (1989) and Bouchet & Danziger (1993) data for SN 1987A from days 14–1030 were taken with the narrow-band N2 filter, λ_{eff} = 9.69 μm ($\Delta\lambda$: 1.65 μm FWHM), and for days 1031–1493 (when the SN was very faint) with the broad N-band filter, λ_{eff} = 10.36 μm ($\Delta\lambda$: 5.2 μm FWHM), on the IR photometer attached to the 1-, 2.2- and 3.6-m telescopes at the European Southern Observatory (ESO) in La Silla, Chile. The 10 μm data of SN 1987A from Wooden et al. (1993) were measured directly from the IR continuum distributions plotted in fig. 2 of their paper.

The brightest detection was that of the Type II SN 1999D in NGC 3690. A single observation of this supernova was taken with Gemini-OSCIR in May 2001, when the SN was ∼850 days past maximum. Although it was measured as a 3.4-σ detection, with a 50-

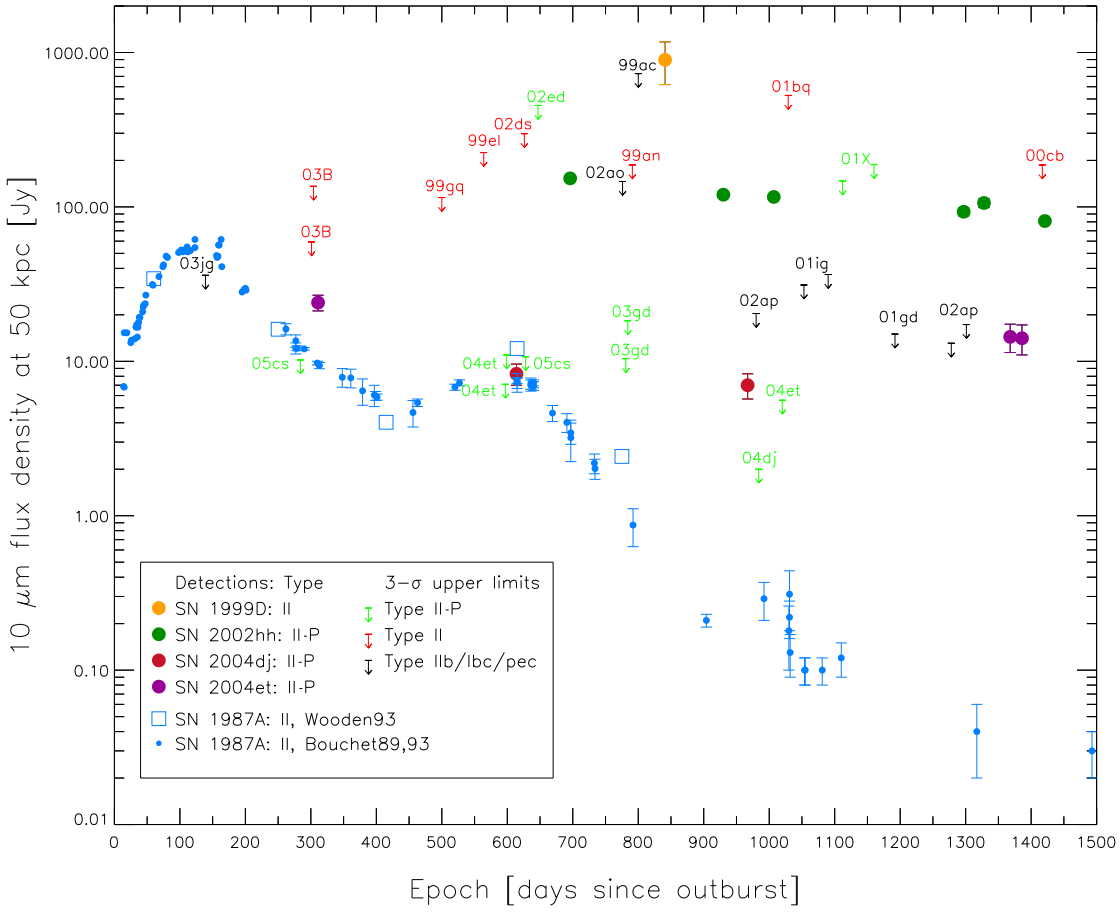

Figure 2.5: 10-μm flux densities and upper limits of the Gemini SEEDS SNe, scaled to a distance of 50 kpc, as a function of time (days) since explosion. The distance-scaling allows for a comparison with the 10-μm flux densities of SN 1987A at similar epochs. The data for SN 1987A are indicated by the small blue, filled circles (Bouchet et al. 1989; Bouchet & Danziger 1993) and the unfilled squares (Wooden et al. 1993). Detections for the SEEDS sample are shown as filled coloured circles identified in the key above. For non-detections, the upper limits to the flux densities are shown as downward-pointing arrows and are labelled with the SN name, abbreviated to the last two digits of the year and the letter suffix, e.g., SN 2003gd is labelled "03gd". The upper limits are also colour-coded by SN type (see key for a broad split into 3 categories, and Table 2.1 for a list of the individual SN types).

kpc flux density of almost 900 Jy it is approximately 1000 times brighter than SN 1987A at similar epochs and about 16 times brighter than SN 1987A's peak 10 μm emission (at ∼ 150 days). It is also a factor of 6 brighter than the second brightest detection in the Gemini sample (SN 2002hh). The source was clearly very faint and about 1.″2 from the centre of the array, although this was likely to be within the pointing errors of Gemini-North at the time. From a pre-explosion *HST*-WFPC2 image on 17 September 1994, Van Dyk et al. (1999) reported that there were two unresolved star clusters (*F*606*W* ∼ 20.2 and 19.8 mag) within a 2″ error circle around the SN's position. The edge of a large extended source is also seen towards the north-east side of the Gemini-OSCIR image. From a comparison with the archival *HST*-WFPC2 *F*606*W* image taken in September 1994, it seems likely that the extended source seen at the edge of the OSCIR image is a bright emission region, possibly an HII or starburst region, at the outer east edge of NGC 3690. The galaxy is part of a interacting system (also known as Arp 299), that has produced a number of starburst regions and 6 detected SNe, including SN 1999D. However, there were no other sources visible in the OSCIR mid-IR image so it is difficult to compare with the better resolved *HST* optical image of the region. Archival *Spitzer* IRAC images from December 2003 (PI: Fazio, program ID: 32), ∼ 1800 days after explosion, show there is no source coincident with the SN position in any waveband from 3.6–8.0 μm. Given the difficulty in confirming the SN position from the Gemini-OSCIR image, and the brightness implied by the large distance to the SN compared to SN 1987A and the rest of the Gemini detections (discussed below), it would be very surprising that the SN had been detected.

SN 2002hh is the second brightest detection at 10 μm and is unusual in that it stayed at a similar flux level for ∼ 1000 days, with only a slight decline (by a factor of ∼ 1.5) in the broad N′ light curve from days 696 to 1722. At the first of these epochs, day 696, the SN was a factor of ∼ 40 brighter than SN 1987A at the same epoch, and by day 1000 was ∼ 380 × as bright. SN 2002hh was also monitored with *Spitzer* as part of the SEEDS programme, confirming a similarly bright and slow mid-IR evolution (Chapter 3). That a light echo from nearby (circumstellar or interstellar) material is the most likely explanation for the optical and infrared observations of SN 2002hh was concluded from SEEDS analyses of the mid-IR (Barlow et al. 2005) and optical data (Welch et al. 2007) (see also Pozzo et al. 2006; Meikle et al. 2006). A summary of the SEEDS analyses can be found in Chapter 4, Section 4.3.

SN 2004dj is the only SN of the sample detected at approximately the same 10 μm

brightness level as SN 1987A at an equivalent epoch during their evolution. Interestingly, this occurred at about day 615, the epoch by which SN 1987A had a clear mid-IR excess that was attributed to dust formation in the SN ejecta (e.g., Wooden et al. 1993, and Section 1.3.4). However, by the second epoch of Gemini-Michelle observations almost a year later (day 967), the 10-μm flux of SN 2004dj had only faded by a factor of 1.2, compared to the much steeper fading of SN 1987A, by a factor ∼35 from days 600–900. The roughly linear 10-μm decline of SN 1987A between days 600 and 900 was shown by Suntzeff et al. (1991) to approximately follow the radioactive decay of ^{56}Co, providing strong support for evidence that the thermal emission of SN 1987A was associated with ejecta dust heated by the energy source of the nebular. Although the 10-μm light curve of SN 2004dj is not well-sampled, a more plausible source for the comparatively strong late-time mid-IR emission (see also Chapter 3) could be an IR echo from the initial SN UV-optical flash, re-radiated by pre-existing circumstellar dust.

It should be noted that SN 2004dj appeared to have faded beyond detection by the third epoch of Michelle N′ observations at day 984, only 17 days after the previous N′ detection. However, the (distance-scaled) day 984 3-σ flux upper limit of 2 Jy at 10 μm is inconsistent with the distance-scaled 8-μm flux detection of SN 2004dj with *Spitzer* of 6 Jy at day 996, and the SN continued to be detected at 8 μm until day 1372 (with a distance-scaled flux of ∼4 Jy; Chapter 3, Figure 3.7). The target coordinates for the Michelle observations on day 984 were correct, and assuming correct pointing information in the headers, the position of the SN was expected to appear slightly off-centre on the array, but no source is evident anywhere on the image. I also created a fake star at the derived 10-μm flux upper limit of 0.45 mJy (≈ to the distance-scaled upper limit of 2 Jy) and added this in a random position to the image. The fake source was clearly detected. The reason for the non-detection with Michelle at day 984 remains unclear.

SN 2004et was similar in brightness to SN 1987A at early times (at day 311, SN 2004et was about 2.5 × brighter) but at days 1368 and 1386 was still very bright (only a factor of ∼1.7 fainter than at day 300) and about 350 times brighter than SN 1987A at the same epoch. However, the SN was not detected by two Michelle observations close to day 600 and by a later observation at day 1020, indicating that the SN may have faded after day 300 and risen again by day 1395. More frequent observations with *Spitzer* confirmed this result (Chapter 3), with the increased sensitivity of *Spitzer* and difference imaging techniques allowing the detection of the SN to fainter levels: the 50-kpc 10-μm upper

limits of 7 and 11 Jy at days 597 and 599 respectively, are consistent with the measured *Spitzer* IRAC 8-μm brightness of ∼5 Jy at day 690. At day 1014, the SN was marginally detected at 8 μm with a 50-kpc flux of 1.6 ± 1.1 Jy, compared to the 10-μm upper flux limit of 5.6 Jy at day 1020 (fluxes and upper limits quoted are those distance-scaled to 50 kpc). A thorough discussion of the mid-IR evolution of SN 2004et is presented in Chapter 5, together with an analysis of complimentary SEEDS optical and NIR data.

Also of note from Figure 2.5 are the flux upper limits which are close to the measured 10-μm flux densities of SN 1987A at similar epochs, such as those of the Type Ibc SN 2003jg at day 139, and the Type II-P SN 2005cs at days 284 and 628. The latter epoch for SN 2005cs is especially interesting as this was around the epoch of dust formation for SN 1987A, and suggests that this SN did not produce as much (if any) dust as SN 1987A at similar epochs.

2.8 Summary

In this chapter the complete sample of supernovae forming part of this thesis was introduced, providing an overview of the mid-IR observations carried out with the Gemini telescopes – whose data were the focus of the remainder of the chapter – and those with the *Spitzer Space Telescope* – discussed in detail in Chapter 3.

The description of the Gemini data which followed included a discussion of the Gemini telescopes and the instruments used, allowing for a comparison of these ground-based mid-IR observations with the space-based mid-IR observations of the *Spitzer Space Telescope*, discussed in the following chapter.

A breakdown of the observations over numerous semesters from the years 2001 to 2008 showed a progression and refinement of the Gemini SN sample, lowering the distance limits and monitoring the flux evolution of those detected, as well as occasionally including suitable new SNe in the sample as and when they were discovered optically. The data reduction and analysis techniques used to achieve the tabulated Gemini flux densities or upper limits were described, along with the flux measurement methods used e.g., aperture photometry or PSF-fitting, which are also applicable to the *Spitzer* data in Chapter 3.

Of the 21 SNe observed with the Gemini telescopes only *three* SNe were robustly detected, and consequently monitored: the Type II-P supernovae SN 2002hh, SN 2004dj

and SN 2004et, all of which were the closest SNe in the sample, at distances between 3.3 and 5.9 Mpc. The mid-IR evolution of these objects are further summarised in the general discussion of the *Spitzer* observations in Chapter 3 (Section 3.6), with a thorough analysis of the optical and infrared evolution of SN 2004et provided in Chapter 5, and an overview of the results for SN 2002hh presented in Chapter 4. It has not been possible to confirm the 10-μm detection of SN 1999D in NGC 3690, but at a distance of ∼ 42 Mpc, it would be unusually bright at any epoch.

The remaining 17 SNe not detected with Gemini ranged from distances of 8.4 Mpc (SN 2005cs) to ∼ 40 Mpc, with an average distance of about 20 Mpc, for a range of epochs spanning ∼ 140–1400 days post explosion.

Chapter 3

Spitzer Observations of Supernovae

3.1 Introduction

Mid-IR observations of 18 core-collapse SNe have been obtained with instruments on the *Spitzer Space Telescope* over the years 2004 – 2008. This chapter describes the observations, including a description of the telescope and instruments used, and a summary of the data processing and analysis. Mid-IR flux densities, and upper limits for non-detections, of the *Spitzer* sample are also presented and discussed.

3.2 Space-based mid-IR astronomy & the *Spitzer Space Telescope*

The *Spitzer Space Telescope* ("*Spitzer*") – the fourth and final of NASA's Great Observatories – was launched into an Earth-trailing heliocentric orbit on 25 August 2003 (Werner et al. 2004). With an 85-centimetre diameter primary mirror, it was capable of imaging and spectroscopy in the 3.6 to 160 μm wavelength range, until the exhaustion of liquid helium on 15 May 2009, after which it commenced its 'warm mission' using the IRAC 3.6 and 4.5 μm channels only.

Unlike ground-based observations, space-based mid-IR astronomy has the advantage of being above the turbulence, absorption, and high thermal background radiation caused by the Earth's atmosphere. Thermal radiation from the telescope structure itself is still a problem for mid-IR observations from space. However, *Spitzer*'s cryogenic telescope assembly (CTA) was capable of minimising this effect to obtain higher sensitivities than those achievable from the ground (by two or more orders of magnitude). The CTA

consists of the telescope assembly, the cryogenic portions of the three science instruments, a superfluid helium Dewar, and various thermal shields. A telescope temperature as low as ~6 K is required to reduce the telescope thermal background enough for observing at the longest wavelengths. *Spitzer*'s Earth-trailing solar orbit also contributes to the efficiency of the cryothermal design, with the main advantage being that it is away from the heat of the Earth which, in turn, enabled the novel "warm-launch" architecture and extensive use of radiative cooling. The "warm launch" design allowed for a smaller total observatory mass than the more conventional "cold launch" design employed in previous infrared space missions such as the *Infrared Astronomical Satellite* (*IRAS*) and *Infrared Space Observatory* (*ISO*). This is because most of the mass of the CTA is external to the cryostat vacuum shell, allowing for a much smaller vacuum pressure vessel. The majority of the CTA is launched at ambient temperature and only begins to cool when in-orbit (hence the term "warm launch").

A disadvantage for space-based observatories is that the launch rocket pay-loads restrict the aperture size, limiting the spatial resolution compared to larger ground-based observatories. In a real sense, space and ground-based facilities are therefore complementary with the former, such as *Spitzer*, delivering huge advantages in sensitivity and the latter, such as the Gemini Observatory, offering higher spatial resolution.

The *Spitzer* cryogenic lifetime requirement of 2.5 years of normal operations passed on 26 April 2006. The mission had a cryogenic lifetime of over 5.5 years. The extended mission, operating the telescope for imaging at the shortest wavelengths of 3.6 and 4.5 μm only, started on 15 May 2009 and is expected to last up to an additional 5 years.

3.2.1 The *Spitzer* instruments

The three science instruments for imaging and spectroscopy are the Infrared Array Camera (IRAC), the Multiband Imaging Photometer for Spitzer (MIPS) and the InfraRed Spectrograph (IRS). A schematic view of the *Spitzer* focal plane in Figure 3.1 (taken from Chapter 2 of the Spitzer Observer's Manual - Version 7.1 issued by the Spitzer Science Center December 8 2006; hereafter referred to as the "SOM") shows how the science instrument apertures are projected onto the sky. A summary of the instrument characteristics is given in Table 3.1.

The instruments, all three of which were used for the data presented in this thesis, are described in the following sections.

Table 3.1: Summary of *Spitzer* instrumentation, adapted from Table 2.2 of the SOM.

Wavelength [μm]	Mode (IRAC, MIPS)/ Module (IRS)	Array Type	Resolving Power	Field of View	Pixel Size [″]	Sensitivity[a] [μJy] (5 σ in 500 s incl. confusion)
		IRAC: InfraRed Array Camera				
3.6	Ch1 - Imaging	InSb	4.7	5.′21×5.′21	1.221	1.6 (3.4)[b]
4.5	Ch2 - Imaging	InSb	4.4	5.′18×5.′18	1.213	3.1 (4.3)
5.8	Ch3 - Imaging	Si:As (IBC)	4.0	5.′21×5.′21	1.222	20.8 (21)
8.0	Ch4 - Imaging	Si:As (IBC)	2.8	5.′21×5.′21	1.220	26.9 (27)
		MIPS: Multiband Imaging Photometer for Spitzer				
24	Ch1 - Imaging	Si:As (IBC)	5	5.′4×5.′4	2.55	110[c]
70	Ch2 - Wide FOV	Ge:Ga	4	5.′2×2.′6	9.98	7.2 mJy[d]
	Ch2 - Narrow FOV/ Super Res	Ge:Ga	4	2.′7×1.′4	5.20	14.4 mJy
55 – 95[e]	Ch2 - SED	Ge:Ga	15-25	0.′32×3.′8	10.1	82/201/447 mJy (at 60/75/90 μm)
160	Ch3 - Imaging	Ge:Ga (stressed)	5	0.′53×5.′3	16×18	29 (40) mJy[f]
		IRS: Infrared Spectrograph				
5.2 – 14.5	Short-Low	Si:As (IBC)	60 – 127	3.″7×57.″0	1.8	250[g]
13.5 – 18.7	Peak-up Blue	Si:As (IBC)[h]	∼3	1.′0×1.′2	1.8	116
18.5 – 26.0	Peak-up Red					80
9.9 – 19.6	Short-High	Si:As (IBC)	∼600	4.″7×11.″3	2.3	1.2×10^{-18} W m^{-2}
14.0 – 38.0	Long-Low	Si:Sb (IBC)	57 – 126	10.″6×168.″0	5.1	1500
18.7 – 37.2	Long-High	Si:Sb (IBC)	∼600	11.″1×22.″3	4.5	2×10^{-18} W m^{-2}

[a] Sensitivities are for point sources, and are only representative. See Chapters 6–8 of the SOM for more detail.
[b] IRAC sensitivity is given for intermediate background. The first number in each case is without confusion, and the second number (in parentheses) includes confusion. See also IRAC Chapter 6 of the SOM.
[c] MIPS sensitivity is given for low background.
[d] 70 μm can be confusion limited; see the MIPS Chapter 8 of the SOM for more details.
[e] Because of a bad readout at one end of the slit, the spectral coverage for 4 columns of the array is reduced to about 65–90 μm.
[f] 160 μm is often confusion limited; the first number is without confusion, and the second number (in parentheses) includes confusion.
[g] IRS sensitivity is given for low background at high ecliptic latitude. Note that for IRS, sensitivity is a strong function of wavelength.
[h] For recommended flux density range for peak-up target, see IRS Chapter 7 of the SOM.

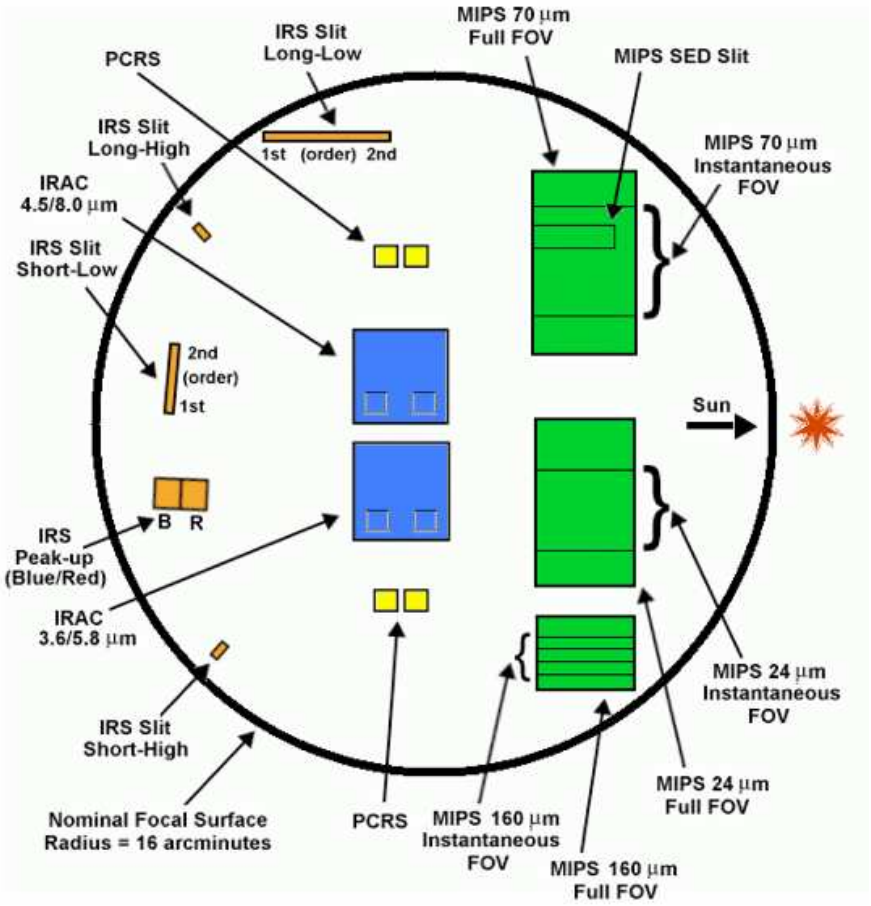

Figure 3.1: Schematic diagram of the *Spitzer* focal plane showing the nominal field-of-view locations of the science instruments projected onto the sky. Taken from Chapter 2 of the SOM).

The Infrared Array Camera - IRAC

The Infrared Array Camera (IRAC) is a four-channel camera that provides simultaneous $5\farcm2 \times 5\farcm2$ broadband images at 3.6, 4.5, 5.8, and 8 μm (Fazio et al. 2004). Two adjacent fields of view are imaged in pairs (3.6 and 5.8 μm; 4.5 and 8.0 μm) using dichroic beamsplitters. The diffraction limited angular resolution of *Spitzer* in the four IRAC channels is $1\farcs07$ at 3.6 μm, $1\farcs33$ at 4.5 μm, $1\farcs72$ at 5.8 μm and $2\farcs37$ at 8.0 μm. All four detector arrays in the camera have dimensions of 256 pixels × 256 pixels, with a pixel size of $\sim 1\farcs2 \times 1\farcs2$. The two short wavelength channels use indium antimonide (InSb) detector arrays and the two longer wavelength channels use arsenic-doped silicon (Si:As) impurity band conduction (IBC) detectors.

Figure 3.2 shows the IRAC cryogenic assembly. The Focal Plane Assemblies include the detector arrays and associated components. The IRAC optical layout is shown in

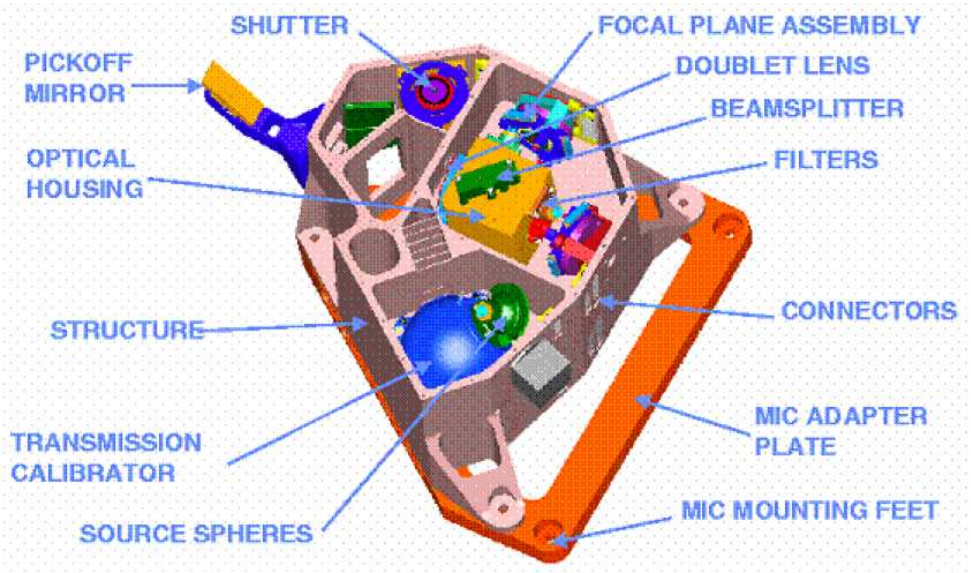

Figure 3.2: The IRAC cryogenic assembly model, with the top cover removed to show the inner components. Taken from IRAC Chapter 6 of the SOM.

Figures 3.3 and 3.4. Channels 1 and 3 view the same telescope field (within a few pixels), and Channels 2 and 4 view a different field simultaneously (see Figure 3.1 of the *Spitzer* field of view).

The Multiband Imaging Photometer for Spitzer - MIPS

The Multiband Imaging Photometer for Spitzer (MIPS) provides simultaneous broadband imaging at wavelengths of 24, 70, and 160 μm, and low-resolution spectroscopy in the 55 and 95 μm wavelength region (Rieke et al. 2004).

The instrument contains 3 separate detector arrays each of which resolves the telescope Airy disk with pixel sizes $\leq \lambda/2D$. All three arrays view the sky simultaneously, with multiband imaging at a given point provided via telescope motions. The 24 μm camera provides a 5.′4 × 5.′4 field of view. The 70 μm camera was designed to have a ∼5.′0 × 5.′0 field of view, but a cabling problem compromising the outputs of half the array results in a field of view of 5.′2 × 2.′6. The 70 μm array also has a narrow field of view/higher magnification mode, and addionally can be used in a spectroscopic mode. The 160 μm array projects to the equivalent of a 0.′5 × 5.′3 field of view. The diffraction limited angular resolution of *Spitzer* in the three MIPS channels is 7.″11 at 24 μm, 20.″72 at 70 μm and 47.″37 at 160 μm. Corresponding pixel sizes on the detectors are 2.″55 at 24 μm, 9.″98 at 70 μm for the 5.′2 × 2.′6 field of view, and 16″ × 18″ at 160 μm.

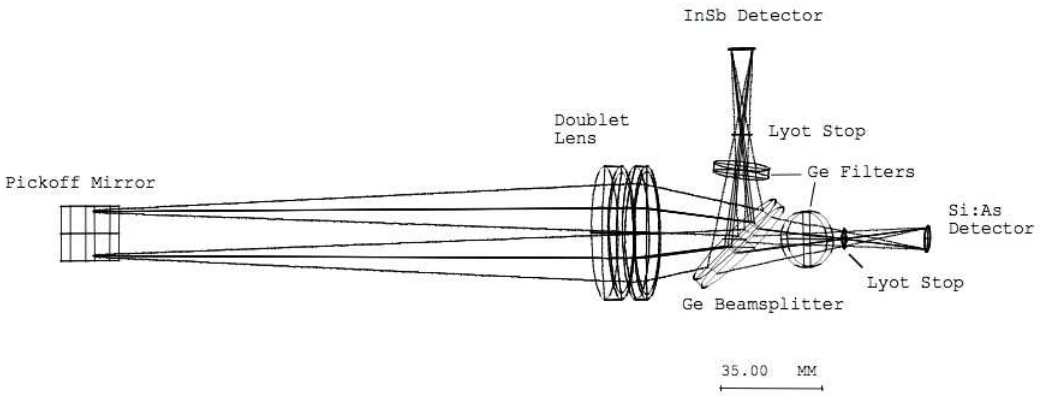

Figure 3.3: The IRAC optical layout, top view. The layout is similar for both pairs of channels; the light enters the doublet and the long wavelength passes through the beamsplitter to the Si:As detector (Channels 3 and 4), with the short wavelength light reflected to the InSb detector (Channels 1 and 2). Taken from IRAC Chapter 6 of the SOM.

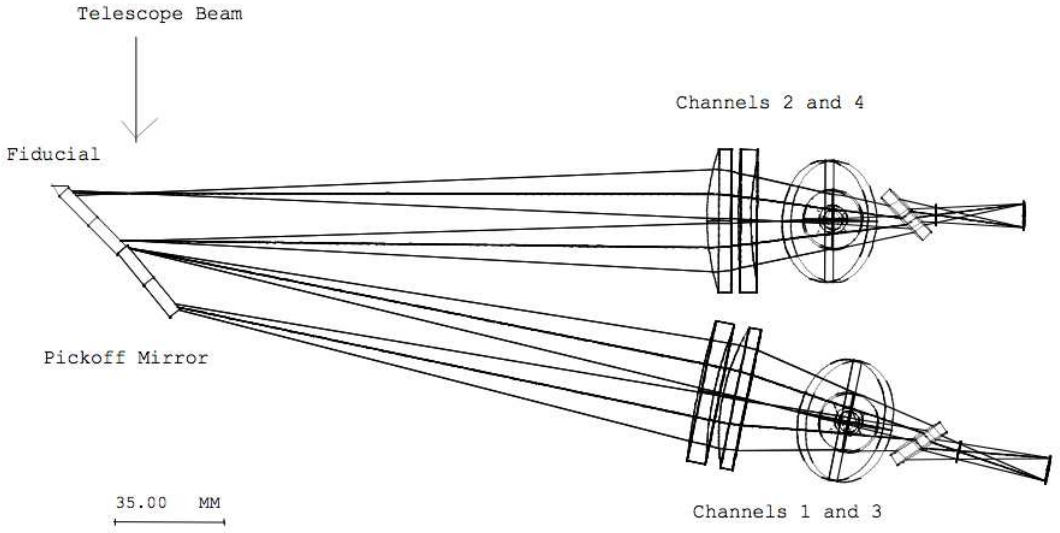

Figure 3.4: The IRAC optical layout, side view. The Si:As detectors are shown at the far right of the figure, the InSb arrays are behind the beamsplitters. Taken from IRAC Chapter 6 of the SOM.

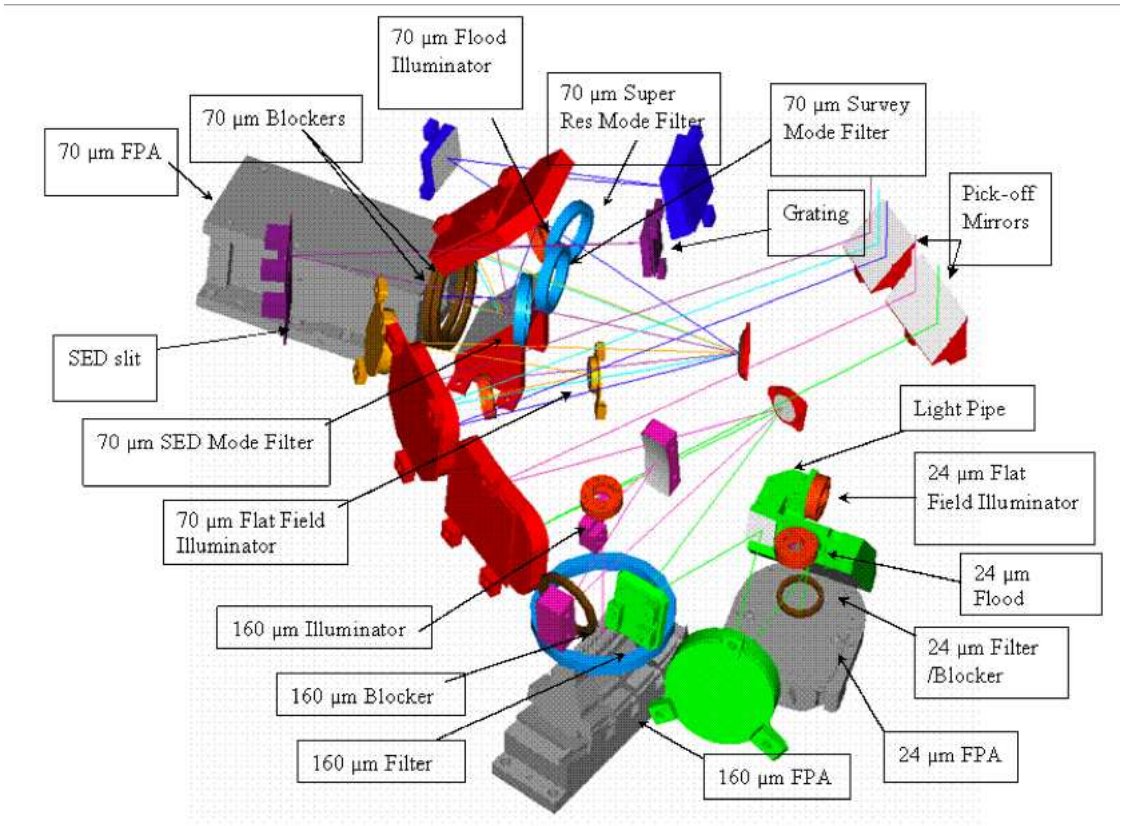

Figure 3.5: Schematic diagram of the optical layout within the MIPS cold assembly: detectors (Focal Plane Arrays), and optical elements and paths. Two mirror facets are attached to the Cryogenic Scan Mirror Mechanism (CSMM): one mirror feeds the 70 µm optical train (normal field-of-view, narrow field-of-view and spectrometer/SED), while the second mirror feeds both the 24 µm and 160 µm optical trains. *Spitzer*'s central axis and the telescope focal plane are to the right in this view. Taken from MIPS Chapter 8 of the SOM.

At 24 µm, Si:As IBC detectors are used, whereas for the two longer-wavelength channels, gallium-doped germanium (Ge:Ga) photoconductors are the only detectors that can operate at the temperature available in the *Spitzer* cryostat.

The MIPS cryogenic scan mirror mechanism (CSMM) is intrinsic to all observational operations, enabling image motion compensation during scanned imaging and one dimensional dithering for all 3 arrays, as well as selection of band and observing mode.

Figure 3.5 provides a schematic illustration of the physical layout of the major optical elements within the MIPS cold assembly: The 24 µm Si:As, 70 µm Ge:Ga, and 160 µm stressed Ge:Ga Focal Plane Arrays (FPAs), movable scan mirror, and fixed mirrors and grating. Two mirrors in the telescope focal plane deflect light into the instrument where it is reflected back by two mirrors to form pupils at the two facets of the CSMM. The CSMM deflects the light into the desired optical train: light is simultaneously sent into

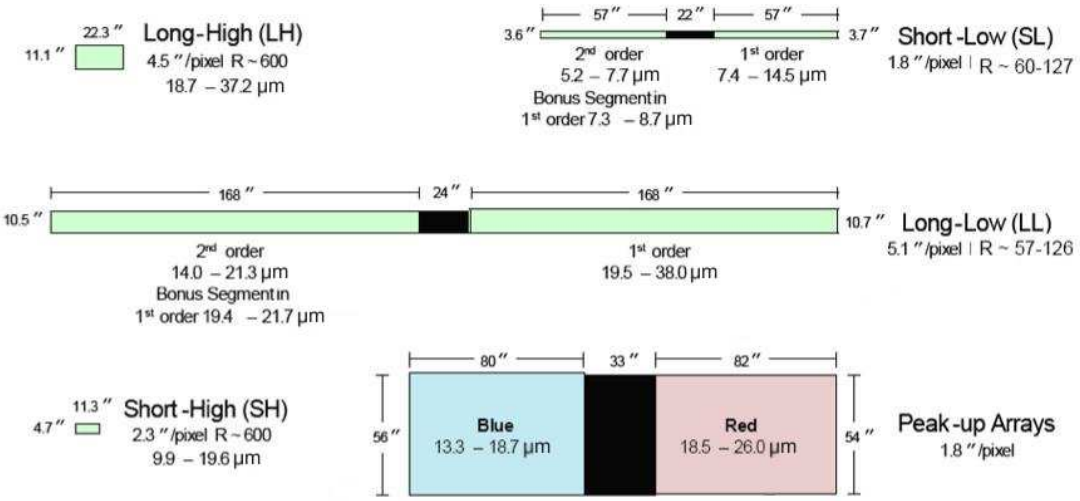

Figure 3.6: Schematic representation of the IRS slits and peak-up apertures. Note that the IRS slits are not parallel in the *Spitzer* focal plane - Figure 3.1 shows the relative positions and angles of the slits/apertures. Taken from IRS Chapter 7 of the SOM.

the 3 widefield optical trains, or into the 70 μm narrow field-of-view train, or into the 55 μm SED optical train.

MIPS had four operating modes: Photometry, Scan Mapping, Spectral Energy Distribution (SED), and Total Power Measurement. See Section 3.2.2 for a summary of the *Spitzer* observing modes. The majority of the MIPS 24 μm observations presented in this thesis were obtained in photometry mode, although the SINGS Legacy observations (described in Section 3.3.1) with MIPS were obtained in Scan Mapping mode.

The Infrared Spectrograph - IRS

The Infrared Spectrograph (IRS) contains the primary spectroscopic functions for *Spitzer*, with four modules capable of low and moderate resolution spectroscopy in the 5.2 to 38.0 μm wavelength range (Houck et al. 2004). There are also two small imaging subarrays ("peak-up arrays") which allow for accurate positioning of sources in any of the IRS slits, and can provide science-quality images for photometric or structural information – known as IRS Peak-Up Imaging (PUI). Both a red (18.5–26.0 μm; $\lambda_{eff} = 22.3$ μm) and a blue (13.3–18.7 μm; $\lambda_{eff} = 15.8$ μm) filter are available, the latter of which was designed to fill the wavelength gap between IRAC and MIPS (for ease of reference, the blue PUI filter is referred to as the 16 μm filter throughout this thesis). Parallel red and blue peak-up images are obtained simultaneously, with a field-of-view seen by each filter of ~55″ × 81″,

separated by a 33″-wide vignetted zone (see Figure 3.6). The images are 30×45 pixels in size and have a native plate scale of ∼1.″8 per pixel.

For the data presented here, the IRS has been mainly used for its imaging capabilities, i.e., PUI mode, with the blue peak-up array at 16 μm during *Spitzer* Cycles 3 and 4. The diffraction limited angular resolution of *Spitzer* is 4.″74 at 16 μm.

Table 3.1 provides details of the instrument characteristics for the spectroscopic and imaging modes of the IRS. Figure 3.6 provides a schematic representation of the various IRS modules.

3.2.2 Observing with the *Spitzer Space Telescope*

Observing time with *Spitzer* was split into four main categories, outlined below. The observations reported here were obtained in categories 1–2 only:

1. General Observations (GOs) – Open to all investigators worldwide on a competitive basis, the GO Program comprises the majority of community observing time on *Spitzer*, allowing scientists to conduct independent research programs with new observations. Most of the observing time available during *Spitzer*'s science mission, typically more than 5000 hours annually, is devoted to peer-reviewed GO investigations. The SEEDS consortium was allocated 9.4 hours in Cycle 1, 6.4 hours in Cycle 2, 11.7 hours in Cycle 3 and 16.1 hours in Cycle 4.

   Targets of opportunity (ToOs) are special cases of GO programs, designed for observations of transient or other time-limited phenomena. They account for a small percentage of the available observing time. For example, time was set aside for up to 10 ToOs in *Spitzer* Cycle 3.

2. Legacy Science Programs – The Legacy Programs are major observing projects that are required to deliver large and coherent data sets (often including ancillary data from other telescopes), without proprietary periods, to the community. The motivation for such programs was the desire to create an early substantial and enduring database of archived observations to be utilised by subsequent *Spitzer* researchers. The six original Legacy programs were selected for *Spitzer* Cycle 1 in November 2000 and comprised 3160 hours of observing time. Five additional Legacy projects were selected for Cycle 2 and a further eight for Cycle 3. We

made extensive use of serendipitous observations of recent SNe acquired during the SINGS Legacy Survey of nearby galaxies.

3. Director's Discretionary Time (DDT) – Five percent of the total *Spitzer* observing time is allocated by the SSC Director for DDT programs. Such time is intended to facilitate proposals that address emerging scientific topics or areas missed in the proposal review process (*not used for data presented in this thesis*).

4. Guaranteed Time Observations (GTOs) – These refer to the proportion of observing time (15–20%) reserved for the Principal Investigators (PIs) of the three science instrument teams and members of the *Spitzer* science team (*not used for data presented in this thesis*).

Spitzer observing schedules are developed and defined during the proposal phase, such that full details of targets, instrument set-up and exposure times are ready for submission to the SSC as part of the application for telescope time. The majority of information required for planning observations with the *Spitzer Space Telescope* is provided by the *Spitzer* Science Center (SSC), which is accessed online at http://ssc.spitzer.caltech.edu. For successful proposals, the schedules are uploaded to the SSC servers for transmission to the spacecraft. The Spitzer Planning Observations Tool (SPOT) is the software used for defining and submitting observations at the proposal stage. An overview of the functions of SPOT and, more specifically, the parameters used to set up the *Spitzer* observations described in this thesis are described in Appendix D.

The IRAC, IRS Peak-Up Imaging (PUI) and MIPS observing modes, or Astronomical Observation Templates (AOTs), used for the *Spitzer* observations presented in this thesis are outlined in Table 3.2. For each AOT, an Astronomical Observation Request (AOR) is defined within SPOT to provide the complete target, telescope and instrument parameters required to carry out the desired observations. A more thorough description of each observing mode is provided in Appendix D.

Table 3.2: The four *Spitzer* observing modes used for GO and SINGS Legacy data presented in this thesis.

Spitzer observing mode	Description
IRAC Mapping/Photometry	Simultaneous imaging at wavelengths of 3.6, 4.5, 5.8 and 8.0 μm, over the two 5.′2 × 5.′2 fields of view.
MIPS Photometry and Super-Resolution Imaging	Imaging photometry and high-resolution imaging at 24, 70 and 160 μm.
MIPS Scan Mapping	For large field maps at 24, 70 and 160 μm. Maps are constructed from 5′-wide (2.5′-wide for full coverage at 70 μm) strips between 0.5° and 6° in length. The slow telescope scanning is combined with motion compensation using a cryogenic scan mirror.
IRS Peak-Up Imaging	Peak-up array imaging only, in two filters over wavelengths 13.5 – 18.5 μm and 18.5 – 26 μm and a field of view of ∼ 1 arcmin^2.

3.3 The *Spitzer* observations

3.3.1 The SINGS Legacy program: 00159

The *Spitzer* Infrared Nearby Galaxies Survey (SINGS; previously the SIRTF Nearby Galaxies Survey; PI: Kennicutt) was one of the six original Cycle 1 *Spitzer* Legacy Science Programs. Specifically, SINGS was a comprehensive infrared imaging and spectroscopic survey of 75 nearby galaxies ($D < 30$ Mpc), the primary aim of which was to characterise the large-scale infrared emission of nearby galaxies across a broad range of galaxy properties and star formation environments (see Kennicutt et al. 2003 for a more detailed description).

The first stage of the SINGS program carried out in Cycle 1 was to fully image each of the 75 galaxies with IRAC and MIPS and to provide partial, low-resolution spectral mapping with IRS and MIPS, in order to characterise global-infrared and star-forming properties. Archival SINGS IRAC and MIPS 24 μm photometric data of 7 galaxies containing 11 supernovae from the Cycle 1 stage are presented in this thesis.

The SINGS observations

Observations of the 11 supernovae were taken between 1 May 2004 and 12 May 2005. Table 3.3 provides details of the observations together with the flux densities, or flux-

density upper limits, measured. IRAC observations were carried out in accordance with the SINGS IRAC observing strategy (Kennicutt et al. 2003). For galaxies larger than the 5′.2 size of the IRAC detectors, observations were taken in a mosaic pattern, offsetting the field of view by ∼50% each time. This process was repeated twice, with observations separated by at least 24 hours to best correct for asteroids and detector artifacts. Points in the central mosaic regions were imaged eight times and the outermost regions four times. Observations were taken with IRAC in its High Dynamic Range mode, with a 30 s frame time and an additional one second exposure taken at each pointing to provide data in cases where the main observation was saturated.

The SINGS MIPS observations were obtained using the Scan Mapping mode in two separate visits to the galaxy. Separate visits allowed asteroids to be recognized and provided observations at orientations up to a few degrees apart to ease removal of detector artifacts. As a result of redundancy inherent in the scan mapping mode, each pixel in the core map area was effectively observed 40, 20, and 4 times at 24, 70, and 160 μm, respectively, resulting in integration times per pixel of ∼ 160 s, 80 s, and 16 s, respectively. See Appendix D for further details of the observation set-up.

The IRAC and MIPS 24 μm flux densities and upper limits listed in Table 3.3 are those measured from the SINGS final image mosaics of the galaxies, which result from the combined images taken over two separate nights from each detector – see Section 3.4.3 for discussion of the SINGS enhanced pipeline used to produce these mosaics. The IRAC images of NGC 6946 are an exception, since a fault with the telescope meant that the two IRAC observations were separated by more than 6 months. In this case, the standard SSC pipeline mosaic images – of SN 2002hh and SN 2004et in NGC 6946 – from the individual nights were analysed.

3.3.2 Cycle 1 General Observations (GO) program: 03333

Targets suitable for our first *Spitzer* GO program were selected based on the fluxes of SN 1987A – usually termed an atypical Type II supernova – since little was known about the mid-infrared emission of Type II SNe and SN 1987A was the best-studied example at that time. Late-time mid-IR fluxes of the SN (7.5 Jy at 8.0 μm and 10.6 Jy at 24 μm on day 615 after explosion; Wooden et al. 1993) and *Spitzer* sensitivity estimates using the "EX-PET" Extragalactic Performance Estimation Tool[1] indicated that SN 1987A could have been

[1]Found online at http://ssc.spitzer.caltech.edu/tools/expet/index.html

Table 3.3: Observation details and flux densities/upper limits for SNe from the Cycle 1 *Spitzer* SINGS Legacy programme, P00159: IRAC and MIPS observations, May 2004 – May 2005. Exposure times in the fifth column take the form $a \times b = c$, where a is equivalent to the effective on-source frame time for a single exposure, b is the number of on-source dithered exposures for each IRAC map or the number of on-source exposures as a result of the redundancy in the MIPS 24 μm scan-mapping, and c is the total on-source exposure time.

Target	SN type	UT date	Age [days]	Exp. time [s]	Flux density/upper limit [μJy]					8.0 μm flux density/ upper limit scaled to 50 kpc [Jy]
					IRAC				MIPS	
					3.6 μm	4.5 μm	5.8 μm	8.0 μm	24.0 μm	
***Host galaxy: NGC 628, $V_h = 657$ km s^{-1}, $D = 9.3$* Mpc**										
SN 2002ap	Ib/c pec	2004-07-28	908	26.8 × 8 = 214.4	≤ 10	≤ 10	≤ 50	≤ 75	···	≤ 2.6
		2005-01-23	1090	3.67 × 44 = 161.5	···	···	···	···	≤ 500	···
SN 2003gd	II-P	2004-07-28	499	26.8 × 8 = 214.4	21.0 ± 3.3	74.9 ± 3.7	76.1 ± 27.9	170 ± 18	···	5.9 ± 0.6
		2005-01-23	678	3.67 × 47 = 172.5	···	···	···	···	543 ± 88	···
***Host galaxy: NGC 1097, $V_h = 1274$ km s^{-1}, $D = 17.4$* Mpc**										
SN 1999eu	II pec	2004-07-23	1719	26.8 × 8 = 214.4	≤ 20	≤ 20	≤ 50	≤ 75	···	≤ 9.1
		2005-01-30	1913	3.67 × 46 = 168.8	···	···	···	···	≤ 250	···
SN 2003B	II	2004-07-23	205	26.8 × 8 = 214.4	≤ 20	≤ 10	≤ 50	≤ 150	···	≤ 18.2
		2005-01-30	399	3.67 × 44 = 161.5	···	···	···	···	≤ 350	···
***Host galaxy: NGC 2403, $V_h = 130$ km s^{-1}, $D = 3.3$* Mpc**										
SN 2002kg	IIn	2004-10-12	713	26.8 × 8 = 214.4	≤ 30	≤ 30	≤ 75	≤ 75	···	≤ 0.33
		2004-10-12	717	3.67 × 45 = 165.2	···	···	···	···	≤ 350	···
SN 2004dj	II-P	2004-10-12	94	26.8 × 8 = 214.4	8100 ± 515	8500 ± 313	5920 ± 174	3690 ± 133	···	16.1 ± 0.6
		2004-10-12	73	3.67 × 43 = 157.8	···	···	···	···	722 ± 18	···
***Host galaxy: NGC 3184, $V_h = 588$ km s^{-1}, $D = 8.1$* Mpc**										
SN 1999gi	II-P	2004-11-27	1814	26.8 × 8 = 214.4	≤ 50	≤ 50	≤ 150	≤ 400	···	≤ 10.5
		2005-05-12	1981	3.67 × 47 = 172.5	···	···	···	···	≤ 5480	···

cont. on next page

Table 3.3 cont.

Target	SN type	UT date	Age [days]	Exp. time [s]	Flux density/upper limit [μJy]					8.0 μm flux density/ upper limit scaled to 50 kpc [Jy]
					IRAC				MIPS	
					3.6 μm	4.5 μm	5.8 μm	8.0 μm	24.0 μm	
***Host galaxy: NGC 3198, $V_h = 663$ km s^{-1}, $D = 13.7$* Mpc**										
SN 1999bw	IIn	2004-05-01	1842	26.8 × 8 = 214.4	10.9 ± 1.0	38.6 ± 1.9	121 ± 6	213 ± 12	···	16.0 ± 0.9
		2004-12-03	2059	3.67 × 46 = 168.8	···	···	···	···	≤ 650	···
***Host galaxy: NGC 5033, $V_h = 877$ km s^{-1}, $D = 12.0$* Mpc**										
SN 2001gd	IIb	2004-06-22	941	26.8 × 8 = 214.4	≤ 29	≤ 26	≤ 43	≤ 157	···	≤ 9.0
		2004-07-03	950	3.67 × 46 = 168.8	···	···	···	···	≤ 186	···
***Host galaxy: NGC 6946, $V_h = 48$ km s^{-1}, $D = 5.9$* Mpc**										
SN 2002hh	II-P	2004-06-10	590	26.8 × 4 = 107.2	940 ± 260	1170 ± 290	3840 ± 760	13400 ± 1930	···	187 ± 27
		2004-07-09	619	3.67 × 46 = 168.8	···	···	···	···	27390 ± 2220	···
		2004-11-25	758	26.8 × 4 = 107.2	1060 ± 300	1130 ± 270	3750 ± 700	12110 ± 1710	···	169 ± 24
SN 2004et	II	2004-06-10	-104	26.8 × 4 = 107.2	83.8 ± 10.2	45.4 ± 8.3	178 ± 25	412 ± 51	···	5.7 ± 0.7
		2004-07-09	-75	3.67 × 44 = 161.5	···	···	···	···	376 ± 25	···
		2004-11-25	64	26.8 × 4 = 107.2	17490 ± 532	13040 ± 745	10050 ± 179	6020 ± 91	···	83.8 ± 1.3

detected fairly straightforwardly out to distances of ∼ 24 Mpc by IRAC and ∼ 15 Mpc by MIPS at 24 μm. A number of the originally proposed target list at closer distances were consequently discovered to be included in the SINGS observations of nearby galaxies and were dropped from the program, since cross-program duplicate observations of targets were not permitted by the *Spitzer* science team at that time (despite the temporal-variation expected in mid-IR observations of core-collapse SNe). In any event, the Legacy data would be publicly available from the archive for analysis.

Seven core-collapse SNe were observed with IRAC and MIPS as part of our first *Spitzer* GO program in Cycle 1. All, except one, of the IRAC and MIPS observations were taken between 29 October 2004 and 20 July 2005 (a delayed MIPS observation of SN 2002ao was obtained later than half-way through Cycle 2, on 18 February 2006). Table 3.4 provides details of the complete set of observations and fluxes measured.

For the IRAC Photometry/Mapping AORs (described in Section 3.2.2), the Full Array readout mode was used with frame times of 100 s for each observation, equivalent to an effective exposure time per frame of 96.8 s. Both mapping and dithering techniques were used. A 2-row-by-1-column map grid in array coordinates was defined, with offsets of ∼ 400″ (equivalent to the *array size + the gap size between the two IRAC fields of view*), which results in equal coverage of the array size of ∼ 5′ in both the 4.5/8.0 μm and 3.6/5.8 μm IRAC fields of view. A small cycling dither pattern with 6 offset positions was executed in each field of view, yielding total effective exposure times of 580.8 s per target per filter. Total AOR durations (i.e., the total time required to execute the observation, including time on source and the various overheads) were on the order of 1530 s per target.

MIPS imaging was carried out in the 24 μm band only, and raster mapping was not necessary. For the MIPS Photometry/Super-resolution AORs (described in Section 3.2.2), the large field size was used with 10 cycles of 14×10 second exposures per target, and a sky offset of 10.0 arcseconds. Total on-source exposure times were approximately 1400 s per target and AOR durations were on the order of 2620 s per target.

3.3.3 Cycle 2 GO program: 20320

The observing strategy for Cycle 2 was revised in light of the mid-IR non-detections of all SNe at distances greater than about 14 Mpc for the Gemini observations in 2001 and 2004, and those from *Spitzer* Cycle 1 GO program 03333. The relative success of the SINGS observations, with detections of 5 (at distances ∼ 3.3–13.7 Mpc) out of 11 SNe (the

Table 3.4: Observation details and flux densities/upper limits for the *Spitzer* Cycle 1 GO programme, P03333: IRAC and MIPS observations, October 2004 – July 2005. Exposure times in the fifth column take the form $a \times b = c$, where a is equivalent to the effective on-source frame time, b is the number of frame repeats (usually as a result of dithering techniques), and c is the total on-source exposure time.

Target	SN type	UT date	Age [days]	Exp. time [s]	Flux density/upper limit [μJy]					8.0 μm flux density/ upper limit scaled to 50 kpc [Jy]
					IRAC				MIPS	
					3.6 μm	4.5 μm	5.8 μm	8.0 μm	24.0 μm	
***Host galaxy: M-05-10-15, V_h = 1320 km s^{-1}, D = 18.1* Mpc**										
SN 2003bg	IIb	2005-01-17	692	96.8 × 6 = 580.8	≤ 5	≤ 6	≤ 50	≤ 70	···	≤ 9.2
		2005-02-28	734	10.0 × 140 = 1400.0	···	···	···	···	≤ 260	···
***Host galaxy: NGC 2742, V_h = 1273 km s^{-1}, D = 17.4* Mpc**										
SN 2003Z	II	2004-10-29	639	96.8 × 6 = 580.8	≤ 12	≤ 11	≤ 50	≤ 180	···	≤ 21.8
		2005-04-03	795	10.0 × 140 = 1400.0	···	···	···	···	≤ 500	···
***Host galaxy: NGC 2997, V_h = 1087 km s^{-1}, D = 10.3* Mpc**										
SN 2003jg	Ib/c	2004-12-16	419	96.8 × 6 = 580.8	≤ 490	≤ 415	≤ 1760	≤ 6780	···	≤ 288
		2005-05-13	567	10.0 × 140 = 1400.0	···	···	···	···	≤ 53300	···
***Host galaxy: NGC 3512, V_h = 1469 km s^{-1}, D = 20.1* Mpc**										
SN 2001fv	II	2004-12-21	1144	96.8 × 6 = 580.8	≤ 8	≤ 7	≤ 20	≤ 77	···	≤ 12.4
		2005-05-12	1286	10.0 × 140 = 1400.0	···	···	···	···	≤ 700	···
***Host galaxy: NGC 3655, V_h = 1457 km s^{-1}, D = 20.0* Mpc**										
SN 2002ji	Ib/c	2004-12-17	748	96.8 × 6 = 580.8	≤ 47	≤ 42	≤ 245	≤ 910	···	≤ 146
		2005-05-18	900	10.0 × 140 = 1400.0	···	···	···	···	≤ 7400	···
***Host galaxy: NGC 3683, V_h = 1715 km s^{-1}, D = 23.5* Mpc**										
SN 2004C	Ic	2005-04-05	449	10.0 × 140 = 1400.0	···	···	···	···	≤ 169250	···
		2005-05-06	480	96.8 × 6 = 580.8	≤ 4600	≤ 3100	≤ 18800	≤ 57700	···	≤ 12750
***Host galaxy: UGC 9299, V_h = 1539 km s^{-1}, D = 21.1* Mpc**										
SN 2002ao	IIb/Ic	2005-07-20	1272	96.8 × 6 = 580.8	≤ 14	≤ 15	≤ 25	≤ 50	···	≤ 8.9
		2006-02-18	1485	10.0 × 140 = 1400.0	···	···	···	···	≤ 875	···

remainder at ∼ 9–17.4 Mpc), indicated observations should be limited to SNe at distances of less than about 15 Mpc and preferably within 10 Mpc. With a lack of suitable new targets falling within this criteria, the Cycle 2 program was used solely for follow-up observations of three SNe detected in the previous SINGS observations.

6.4 hours were awarded in Cycle 2 for multiple epoch imaging of SN 1999bw, SN 2002hh and SN 2004et with IRAC and MIPS. The observations were carried out between 19 July 2005 and 4 May 2006. Table 3.5 provides details of the observations and fluxes measured. Only the IRAC data for SN 2002hh is presented here.

Full Array readout mode was used for the IRAC photometry. An image to encompass both SN 2002hh and SN 2004et in the same galaxy, NGC 6946, was constructed with the celestial mapping mode. A 2-row-by-1-column map grid was defined, with a step size of 311″ and a position angle of 88 degrees. Sensitivities based on the 2004 flux levels for both objects were calculated with EX-PET using medium backgrounds. Frame times of 2 s (equivalent to an effective exposure time of 1.2 s per frame) with a 12-point Reuleaux dither pattern were sufficient to achieve signal-to-noise (S/N) ratios greater than 5 in each IRAC channel. Total effective exposure times were 14.4 s per target per filter. SN 2002hh and SN 2004et were observed three times during Cycle 2, with a separation between epochs of 2–3 months. AOR durations for each visit were on the order of 800 s. For SN 1999bw, S/N ratios in excess of 20 were predicted by the EX-PET for frame times of 30 s with a 12-point dither sequence, allowing considerable margin for the SN to fade and still be detected. Mapping was not necessary in this case. An effective exposure time per frame of 26.8 s yielded a total effective exposure time of 321.6 s. There were two such IRAC visits to SN 1999bw in Cycle 2, each separated by about 5 months and with AOR durations of approximately 1180 s.

MIPS 24 μm photometry was obtained in Cycle 2, with three epochs of observations for SN 2004et, and two for SN 1999bw. The complimentary MIPS and IRAC observations were never separated by more than two weeks, and were generally taken within a few days of each other. Each SN was imaged separately and raster mapping was not necessary. The small field size was used for all observations, with a sky offset of 300.0 arcseconds. Exposure times were 10 s for SN 2004et, with just one cycle (of the standard 14 frames) resulting in respective total on-source exposure times of 140 s per epoch and total AOR durations on the order of 690 s per epoch. The MIPS 24 μm flux of SN 1999bw was uncertain in the SINGS Cycle 1 data from December 2004, so the deeper 30 s frame time,

Table 3.5: Observation details and flux densities/upper limits for the *Spitzer* Cycle 2 GO programme, P20320: IRAC and MIPS observations, July 2005 – May 2006. Exposure times in the fifth column take the form $a \times b = c$, where a is equivalent to the effective on-source frame time, b is the number of frame repeats (usually as a result of dithering techniques), and c is the total on-source exposure time.

Target	SN type	UT date	Age [days]	Exp. time [s]	Flux density/upper limit [μJy]					8.0 μm flux density/ upper limit scaled to 50 kpc [Jy]
					IRAC				MIPS	
					3.6 μm	4.5 μm	5.8 μm	8.0 μm	24.0 μm	
***Host galaxy: NGC 3198, $V_h = 663$ km s^{-1}, $D = 13.7$* Mpc**										
SN 1999bw	IIn	2005-11-29	2420	26.8 × 12 = 321.6	2.6 ± 0.3	13.6 ± 0.6	53.5 ± 3.6	105 ± 8	···	7.9 ± 0.6
		2005-12-01	2422	30.0 × 28 = 840.0	···	···	···	···	≤ 650	···
		2006-05-03	2575	26.8 × 12 = 321.6	≤ 10	6.9 ± 0.6	43.3 ± 2.9	86.9 ± 6.1	···	6.5 ± 0.5
		2006-05-04	2576	30.0 × 28 = 840.0	···	···	···	···	≤ 650	···
***Host galaxy: NGC 6946, $V_h = 48$ km s^{-1}, $D = 5.9$* Mpc**										
SN 2002hh	II-P	2005-07-19	994	1.2 × 12 = 14.4	610 ± 50	690 ± 50	2730 ± 250	9680 ± 760	···	135 ± 11
		2005-09-17	1054	1.2 × 12 = 14.4	560 ± 40	640 ± 30	2470 ± 210	9090 ± 600	···	127 ± 8
		2005-12-30	1158	1.2 × 12 = 14.4	510 ± 40	650 ± 40	2800 ± 230	9170 ± 670	···	128 ± 9
SN 2004et	II	2005-07-19	300	1.2 × 12 = 14.4	726 ± 60.5	3151 ± 96.5	1291 ± 218	2162 ± 154	···	30.1 ± 2.1
		2005-08-03	315	10.0 × 14 = 140.0	···	···	···	···	832 ± 74.5	···
		2005-09-17	360	1.2 × 12 = 14.4	430 ± 70.5	1728 ± 88.2	935 ± 285	1731 ± 156	···	24.1 ± 2.2
		2005-09-24	367	10.0 × 14 = 140.0	···	···	···	···	735 ± 73.5	···
		2005-12-30	464	1.2 × 12 = 14.4	174 ± 67.1	656 ± 77.3	606 ± 293	952 ± 162	···	13.3 ± 2.3
		2006-01-11	476	10.0 × 14 = 140.0	···	···	···	···	686 ± 88.5	···

which is sensitive to 0.1 mJy sources with S/N of 3 was used. With 2 cycles of the 14 frames, this resulted in a total on-source exposure time of approximately 840 s per epoch and a total AOR duration of about 1230 s per epoch.

3.3.4 Cycle 3 GO program: 30494

11.7 hours were awarded in Cycle 3 for mid-IR monitoring of six Type II SNe. Due to time constraints, data from three of those SNe are presented in this thesis and details of the IRAC, IRS Peak-Up Imaging (PUI) and MIPS observations are listed in Table 3.6, together with the measured fluxes. All SNe were observed with *Spitzer* IRAC and MIPS in previous cycles. The IRS-PUI observing mode became available in Cycle 2 and its blue filter (16 μm) provided useful coverage in the wavelength gap between the IRAC and MIPS 24 μm data.

Three epochs of observations with IRAC, PUI at 16 μm and MIPS at 24 μm were taken to continue monitoring the mid-IR evolution of SN 2004et and SN 2004dj, although the third epoch of observations for SN 2004dj was scheduled late, overlapping with further observations awarded in Cycle 4 and are consequently not presented here. Multiple observations of a single target from a given instrument were separated by approximately 4–7 months, and observations from the different instruments were requested to be as close in time as possible (within 30 days of each other) to provide a temporally homogeneous data set, i.e., a single spectral energy distribution, for each of the 3 epochs. Just one observation in each band was required for SN 2003gd since it was relatively faint when detected in Cycle 1 (~ 0.2 mJy at 8 μm on day 495) and the trend from Cycle 2 archival observations indicated fading of the mid-IR emission, meaning detection of the SN at these late times (1200–1600 days after explosion) was uncertain. Exposure times were chosen based on the brightness from previous observations and/or the distance-scaled flux of SN 1987A entered into the EX-PET, to provide a minimum S/N of 10 in each imager.

IRAC was used in Full Array mode with a medium size 12-point Reuleaux dither pattern. Frames times of 2, 12, 30 and 100 s were chosen based on calculations with the EX-PET, with exposure times generally increased for each subsequent epoch of observations to account for fading of the source with time. Total AOR durations ranged from ~ 500 s for the shortest observations of SN 2004dj and SN 2004et, to ~ 2870 s for the longest observation of SN 2003gd.

Table 3.6: Observation details and flux densities/upper limits for the *Spitzer* Cycle 3 GO programme, P30494: IRAC, MIPS and IRS observations, August 2006 – July 2007. Exposure times in the fifth column take the form $a \times b = c$, where a is equivalent to the effective on-source frame time, b is the number of frame repeats (usually as a result of dithering techniques), and c is the total on-source exposure time.

Target	SN type	UT date	Age [days]	Exp. time [s]	Flux density/upper limit [μJy]						8.0 μm flux density/ upper limit scaled to 50 kpc [Jy]
					IRAC				IRS-PU	MIPS	
					3.6 μm	4.5 μm	5.8 μm	8.0 μm	16.0 μm	24.0 μm	
***Host galaxy: NGC 628, $V_h = 657$ km s^{-1}, $D = 9.3$* Mpc**											
SN 2003gd	II-P	2006-08-13	1245	96.8 × 12 = 1161.6	≤ 2.2	≤ 2.5	≤ 18	≤ 19	···	···	≤ 0.7
		2006-09-01	1264	30.0 × 14 = 420.0	···	···	···	···	···	≤ 55	···
		2006-09-08	1271	30.0 × 9 = 270.0	···	···	···	···	≤ 32	···	···
***Host galaxy: NGC 2403, $V_h = 130$ km s^{-1}, $D = 3.3$* Mpc**											
SN 2004dj	II-P	2006-10-31	843	1.2 × 12 = 14.4	839 ± 24	1089 ± 27	1622 ± 46	2097 ± 48	···	···	9.1 ± 0.2
		2006-11-15	858	6.0 × 9 = 54.0	···	···	···	···	1667 ± 40	···	···
		2006-12-01	874	10.0 × 14 = 140.0	···	···	···	···	···	1148 ± 21	···
		2007-03-24	987	14.0 × 9 = 126.0	···	···	···	···	1323 ± 57	···	···
		2007-04-02	996	10.4 × 12 = 124.8	455 ± 18	637 ± 16	1098 ± 24	1380 ± 27	···	···	6.0 ± 0.1
		2007-04-13	1007	10.0 × 14 = 140.0	···	···	···	···		857 ± 20	···
***Host galaxy: NGC 6946, $V_h = 48$ km s^{-1}, $D = 5.9$* Mpc**											
SN 2004et	II	2006-08-13	690	1.2 × 12 = 14.4	≤ 49	45.9 ± 53.0	115 ± 220	342 ± 132	···	···	4.8 ± 1.8
		2006-09-01	709	10.0 × 14 = 140.0	···	···	···	···	···	663 ± 77	···
		2006-09-10	718	6.0 × 9 = 54.0	···	···	···	···	264 ± 30	···	···
		2006-12-29	828	10.4 × 12 = 124.8	≤ 45	29.4 ± 12.4	≤ 87	145 ± 82	···	···	2.0 ± 1.1
		2007-01-21	851	30.0 × 14 = 420.0	···	···	···	···	···	513 ± 54	···
		2007-01-27	857	14.0 × 9 = 126.0	···	···	···	···	147 ± 30	···	···
		2007-06-26	1007	30.0 × 9 = 270.0	···	···	···	···	24.8 ± 28.7	···	···
		2007-07-03	1014	26.8 × 12 = 321.6	≤ 23	14.1 ± 17.5	≤ 83	113 ± 76	···	···	1.6 ± 1.1
		2007-07-10	1021	30.0 × 14 = 420.0	···	···	···	···	···	644 ± 48	···

PUI observations were carried out in the blue array (16 μm) only, with ramp (exposure) durations of 6, 14 or 30 s and a small scale 9-position random dither pattern. Total on-source integration times ranged from 54 to 270 s with equivalent AOR durations of ~ 460 to 690 s. MIPS 24 μm photometry used the small field size with a sky offset of 300'' for all observations. Exposure times of 10 and 30 s, with one cycle of the standard 14-frame dither pattern, resulted in total on-source exposure times of 140 s and 420 s, respectively.

3.3.5 Cycle 4 GO program: 40010

16.1 hours were awarded in Cycle 4 for photometry of ten Type II SNe. Multi-epoch data for four of the SNe, all previously observed with *Spitzer*, are presented in this thesis and details of the IRAC, IRS-PUI at 16 μm and MIPS 24 μm observations are listed in Table 3.7. As for Cycle 3, exposure times were chosen based on the previous *Spitzer* observations or the distance-scaled flux of SN 1987A at the relevant epoch entered into the EX-PET, to achieve a minimum S/N of 10 in each waveband.

Multi-epoch observations of SN 2003gd (×2), SN 2004dj (×2) and SN 2004et (×3) taken with each imager, were separated by 4–7 months per target. Observations expected to be equivalent to a single epoch (usually one from each of the 3 instruments) were carried out within 30 days. Only one observation in each imager was taken of the oldest supernova in the sample, SN 1999bw, which would be 3000–3300 days post-explosion (≥ 8 years old) during Cycle 4 and whose brightness was not expected to change substantially over the course of the year at this stage of its evolution. Whilst 2 epochs of observations with each instrument were taken for SN 2003gd, only the first epoch is presented in Table 3.7. The second set of observations (IRAC on 26 January 2008, equivalent to 1776 days post-explosion; PUI on 21 January 2008, day 1771; and MIPS on 14 February 2008, day 1795) were used by SEEDS collaborator Dr B. E. K. Sugerman as the reference frames for PSF-matched difference imaging of the data from previous epochs, since the SN had clearly faded beyond detection by this time.

IRAC observations used the Full Array readout mode with a medium scale 12-point Reuleaux dither pattern, except for SN 1999bw where the medium size 36-point Reuleaux dither sequence was effectively used to provide longer exposure times. A frame time of 30 s was used for all observations. Total on-source integration times were 321.6 s for SN 2003gd, SN 2004dj and SN 2004et, with an equivalent AOR duration of ~ 1160 s. For SN 1999bw the total on-source time of 964.8 s resulted in an AOR duration of ~ 3000 s.

Table 3.7: Observation details and flux densities/upper limits for the *Spitzer* Cycle 4 GO programme P40010: IRAC, MIPS and IRS observations, August 2007 – July 2008. Exposure times in the fifth column take the form $a \times b = c$, where a is equivalent to the effective on-source frame time, b is the number of frame repeats (usually as a result of dithering techniques), and c is the total on-source exposure time.

Target	SN type	UT date	Age [days]	Exp. time [s]	Flux density/upper limit [μJy]						8.0 μm flux density/ upper limit scaled to 50 kpc [Jy]
					IRAC				IRS-PU	MIPS	
					3.6 μm	4.5 μm	5.8 μm	8.0 μm	16.0 μm	24.0 μm	
***Host galaxy: NGC 628, $V_h = 657$ km s^{-1}, $D = 9.3$* Mpc**											
SN 2003gd	II-P	2007-08-16	1613	$26.8 \times 12 = 321.6$	≤ 3.0	≤ 3.7	≤ 27	≤ 20	···	···	≤ 0.7
		2007-08-24	1621	$30.0 \times 14 = 420.0$	···	···	···	···	···	≤ 56	···
		2007-09-04	1632	$30.0 \times 9 = 270.0$	···	···	···	···	≤ 30	···	···
***Host galaxy: NGC 2403, $V_h = 130$ km s^{-1}, $D = 3.3$* Mpc**											
SN 2004dj	II-P	2007-10-24	1201	$30.0 \times 14 = 420.0$	···	···	···	···	···	1046 ± 19	···
		2007-11-04	1212	$30.0 \times 9 = 270.0$	···	···	···	···	1110 ± 18	···	···
		2007-11-23	1231	$26.8 \times 12 = 321.6$	332 ± 13	425 ± 11	732 ± 17	992 ± 18	···	···	4.3 ± 0.1
		2008-04-12	1372	$26.8 \times 12 = 321.6$	297 ± 11	362 ± 11	630 ± 16	890 ± 17	···	···	3.9 ± 0.1
		2008-04-14	1374	$30.0 \times 14 = 420.0$	···	···	···	···	···	1148 ± 26	···
		2008-05-03	1393	$30.0 \times 9 = 270.0$	···	···	···	···		···	···
***Host galaxy: NGC 3198, $V_h = 663$ km s^{-1}, $D = 13.7$* Mpc**											
SN 1999bw	IIn	2008-05-13	3316	$26.8 \times 36 = 964.8$	≤ 10	4.0 ± 0.5	20.9 ± 2.4	46.3 ± 8.0	···	···	3.5 ± 0.6
		2008-05-17	3320	$30.0 \times 56 = 1680$	···	···	···	···	···	≤ 650	···
		2008-05-28	3331	$30.0 \times 18 = 540.0$	···	···	···	···	93.2 ± 15.8	···	···
***Host galaxy: NGC 6946, $V_h = 48$ km s^{-1}, $D = 5.9$* Mpc**											
SN 2004et	II	2007-08-02	1044	$30.0 \times 9 = 270.0$	···	···	···	···	66.9 ± 34.9	···	···
		2007-08-12	1054	$26.8 \times 12 = 321.6$	≤ 34	15.1 ± 14.0	≤ 78	115 ± 67	···	···	1.6 ± 0.9
		2007-08-27	1069	$30.0 \times 14 = 420.0$	···	···	···	···	···	610 ± 49	···
		2007-12-09	1173	$30.0 \times 9 = 270.0$	···	···	···	···	725 ± 32	···	···
		2007-12-27	1191	$26.8 \times 12 = 321.6$	52.5 ± 38.6	189 ± 10	345 ± 75	458 ± 73	···	···	6.4 ± 1.0
		2008-01-07	1202	$30.0 \times 14 = 420.0$	···	···	···	···	···	1276 ± 42	···
		2008-07-18	1395	$26.8 \times 12 = 321.6$	76.3 ± 22.6	258 ± 11	465 ± 49	578 ± 82	···	···	8.0 ± 1.1
		2008-07-29	1406	$30.0 \times 14 = 420.0$	···	···	···	···	···	1563 ± 54	···

PUI observations were carried out in the blue array (16 μm) only, with a small scale 9-position random dither pattern and a ramp duration of 30 s, resulting in total on-source integration times of 270 s and AOR durations of ∼690 s per target. For SN 1999bw, mapping was used to repeat the dither pattern, effectively doubling the exposure time for this object.

MIPS 24 μm photometry used the small field size with a sky offset of 300″ for all observations. Exposure times of 30 s, with one cycle of the standard 14-frame dither pattern for all targets, except SN 1999bw, resulted in total on-source exposure times of 420 s, equivalent to total AOR durations of ∼780 s per target. SN 1999bw was observed with 4 cycles of the 30 s × 14 dither pattern, yielding a total integration time of ∼1680 s.

3.4 *Spitzer* data reduction

3.4.1 Data retrieval

The SSC provides basic (pipeline) science data processing and quality assessment, and maintains a data archive that has been publicly accessible since May 2004. Pipeline-processed science data, as well as raw data and calibration files, are obtained via the Leopard software tool, which acts as the *Spitzer* Science Center Data Archive interface (*now superseded by the Spitzer Heritage Archive*[2]). Leopard was used to access proprietary data via a personal login to the archive, as well as public datasets, such as the Legacy Programs and other non-proprietary data (which do not require login to the archive). Most *Spitzer* data were downloaded via Leopard as and when they became available in the archive, typically within two to three weeks of being observed.

The SINGS Legacy team process their own data to produce enhanced data products and these data were downloaded from the Legacy Programs section of the SSC website[3], where all Legacy are staged. There have been various releases of the SINGS Enhanced Data Products since the program began in 2004, but most of the SINGS data presented in this thesis are the fifth and final version, delivered on 10 April 2007. Occasionally, the *Spitzer* pipeline version of the SINGS data was used in preference to the enhanced products and was retrieved using Leopard in the conventional way. The reason for this is discussed when such data is presented.

[2]http://sha.ipac.caltech.edu/applications/Spitzer/SHA/
[3]http://irsa.ipac.caltech.edu/data/SPITZER/docs/spitzermission/observingprograms/legacy/

3.4.2 The SSC data reduction pipelines and flux calibration

As previously mentioned, the SSC has its own pipelines for processing IRAC, IRS and MIPS data. For each instrument, the main processing of the raw science data takes place in the appropriate "Basic Calibrated Data (BCD) pipeline", which consists of a set of modules that work with inputs from calibration and pointing servers. One BCD image is generated by the pipeline for each science frame, or Data Collection Event (DCE), of an Astronomical Observation Request (AOR). An AOR is the fundamental unit of a *Spitzer* observation which can be specified by the user (also see Appendix D). The extended pipeline, known as the "post-BCD pipeline", combines the calibrated images (BCDs) from a full AOR , following pointing refinement and outlier rejection, to create a final coadded image, or mosaic. For *Spitzer* data presented in this thesis, this final stage was generally carried out manually with the SSC MOPEX (MOsaicker and Point source EXtractor) software (Makovoz et al. 2006) in order to improve the spatial sampling of the final mosaics over those of the standard *Spitzer* post-BCD pipeline. A summary of the processing steps with MOPEX are discussed in Section 3.4.4.

A brief outline of the basic processing steps and flux calibration for IRAC, IRS Peak-up Imaging and MIPS 24 μm data are described below. For a more detailed explanation of the SSC data reduction algorithms and flux calibration used to generate the BCD and post-BCD data products, please see the references given in the relevant sections.

The IRAC data pipelines

IRAC BCD pipeline The IRAC BCD pipeline performs standard imaging data reduction steps, such as bias and dark current subtraction using a laboratory dark, dark sky subtraction using in-flight calibration images of dark sky regions, linearisation to correct the response function of each pixel, flat fielding using calibration images of bright sky regions, and finally conversion from engineering to scientific image units.

Additional processing steps during the pipeline include initial validation of the data to ensure it is not corrupted, updating of image headers, corrections for pixel latency artifacts caused by electronic bandwidth limitations, subtraction of a timing-dependent bias offset (the "first-frame effect"), a correction for multiplexer-bleeding where the InSb arrays exhibit a similar effect to the electronic bandwidth artifact, subtraction of internal scattered light patterns, and image transposition for channels 1 and 2, such that they are

flipped to the same orientation as channels 3 and 4 (the dichroic beamsplitters used to redirect the incoming light for a given field of view through each of the two filters, e.g. channels 1 and 3, results in one detector seeing a mirror image of the other).

A full description of the IRAC BCD pipeline algorithms is provided in the IRAC Pipeline Description Document (version 1.0; Reach et al. 2005*b*).

IRAC flux calibration Flux calibration of IRAC data uses a system of primary and secondary standard stars, which are used to monitor the long- and short-term variations in the photometry respectively. A complete description of the absolute calibration (for IRAC pipeline versions S13 and greater) is provided in Reach et al. (2005*a*).

In brief, the absolute calibration was performed by comparing the observed to predicted brightness for a set of A-type main-sequence stars (Cohen et al. 2003). Fluxes of the standard stars were measured using aperture photometry, with an aperture radius of 10 native IRAC pixels (12 arcseconds) and a sky annulus over a 12 to 20 pixel radius centred on the source, chosen for optimised photometry of isolated, bright sources (Reach et al. 2005*a*). Consequently, measurements of IRAC data with other aperture sizes or sky annuli require appropriate aperture corrections (see Section 3.5 for details). The IRAC data are calibrated in units of MJy sr^{-1}, which was achieved during the BCD pipeline by multiplying the image by the appropriate flux conversion factor in units of [MJy/sr][DN/s]$^{-1}$, as determined by Reach et al. (2005*a*). The conversion factor is stored in the (P)BCD fits header keyword *FLUXCONV*.

Further information on the SSC IRAC pipelines can be found in the IRAC Data Handbook (version 3.0; Reach et al. 2006) and the SOM (version 8.0; 2007) – *both now superseded by the IRAC Instrument Handbook, version 1.0, February 2010*[4].

The IRS Peak-Up Imaging (PUI) data pipelines

PUI BCD pipeline Most of the basic data processing steps for the IRS-PUI data are the same as those for spectroscopy on the short-low detector. These include: updates to the image header, masking saturated pixels, gain corrections due to channel-dependent array readout differences, cosmic ray detection/flagging, droop corrections to rectify the signal on the arrays for the coupling of signal between pixels, dark current subtraction,

[4]http://irsa.ipac.caltech.edu/data/SPITZER/docs/irac/iracinstrumenthandbook/

linearisation of the signal ramps, and flat-fielding. Imaging-specific calibration files are used for the flat fields (generated from observations of high zodiacal background regions) and dark current subtraction (which includes removal of the detector bias voltage and some sky emission, in addition to the small amount of dark current during an exposure). After applying the flat field, PUI data are cropped into separate red and blue BCD frames (each 35×45 pixels), WCS information is updated in the header, and final flux calibration is performed. A detailed description of the IRS science pipeline modules can be found in the IRS S11 Pipeline Handbook (version 1.0; 2005).

PUI flux calibration Several different versions of the pipeline have to been used to the process the PUI data presented in this thesis and the flux calibration for the red and blue filters has changed over the course of the pipeline history. For pipeline versions S15-S16, the calibration is based on PUI observations of five standard stars, for which a few IRS spectra were also obtained to cross-calibrate the fluxes (instead of models). Aperture photometry of the standard stars was performed using aperture sizes of 12 PUI native pixels (21.6 arcseconds) for blue filter observations (sky annulus radii typically spanning 12-17 pixels) and 13 pixels for red (sky annuli at 13-18 pixels). The flux calibration factors of $0.0124 \pm 5\%$ MJy/sr/e$^-$/s for blue and $0.0136 \pm 5\%$ MJy/sr/e$^-$/s for red were tied to these fixed apertures, such that aperture corrections were required for measurements with other size apertures. Aperture corrections for PUI observations are discussed in Section 3.5.1. For pipeline version S17, the flux calibration was revised to reduce the uncertainties (Ardila 2008). It differs from the previous calibration in using observations of three A type stars with a larger number of spectroscopic observations, and includes the use of stellar models. The new calibration was based on an infinitely large aperture, derived using TinyTim V2.0, such that the flux calibration values, of 0.0117 ± 0.00020 MJy/sr/e$^-$/s for blue and 0.0118 ± 0.00018 MJy/sr/e$^-$/s for red, provide the true pixel surface brightness, and no aperture correction is necessary for the calibration of uniform extended sources.

Detailed descriptions of the data processing steps summarised here can be found in the IRS Data Handbook (version 3.2; Ardila et al. 2008) and the IRS section of the SOM (version 8.0; 2007) – *both now superseded by the IRS Instrument Handbook, version 1.0, February 2009*[5].

[5]http://irsa.ipac.caltech.edu/data/SPITZER/docs/irs/irsinstrumenthandbook/

The MIPS 24 μm data pipelines

MIPS 24 μm BCD pipeline The standard imaging data reduction steps of the MIPS 24 μm BCD pipeline are: subtraction of the (small: 0–3 DN/sec) dark current using an average dark generated with the scan-mirror in the dark position, correction for electronic non-linearity, flat-fielding using mirror position-dependent flat fields, image flux calibration and single outlier detection. Additional processing steps during the pipeline include: detection and replacement of saturated pixels, the "read-2" correction (an offset in the second read of the 24 μm array results in a gradient across the array that depends on the array position and background level; correction is $\ll 1\,\%$), slope desaturation and droop corrections (that remove an excess signal in each pixel that is proportional to the signal in the entire array). A full description of the MIPS 24 μm BCD pipeline algorithms is provided in Masci et al. (2005) and Gordon et al. (2005).

MIPS 24 μm flux calibration In summary, the flux calibration for the MIPS 24 μm data was based on the observed to predicted brightness for a sample of 22 A-type stars adopted from Rieke et al. (2008) that had already been carefully vetted to exclude sources that would bias the calibration, such as those exhibiting an infrared excess (e.g., debris disk systems). 24 μm flux densities were derived by Engelbracht et al. (2007) using extinction-corrected K magnitudes for the sample from Rieke et al. (2008), a $K - [24]$ colour difference of 0 mag, and the 24 μm zero-point, derived by Rieke et al. (2008), of 7.17 Jy. Kurucz models were extrapolated from 10.6 μm to predict the 24 μm zero-point for A stars. Engelbracht et al. (2007) performed aperture photometry on the observations of the sample using an aperture of radius 35″, with a background annulus from 40″ to 50″ in radius. Aperture corrections were derived from a MIPS 24 μm point-response function computed from a 10,000 K PSF for a blackbody (generated using the *Spitzer* TinyTim software) such that the absolute flux calibration was effectively scaled to the flux density in an infinite aperture. The final calibration factor was the weighted average of the ratio of the 24 μm predictions to the observed count rate. Its units are $[\mathrm{MJy/sr}][\mathrm{DN/s}]^{-1}$ and the value is stored in the (P)BCD fits header keyword *FLUXCONV*. A complete description of the flux calibration for the MIPS 24 μm data is provided in Engelbracht et al. (2007), with further information provided in Rieke et al. (2008).

Detailed descriptions of the data processing steps summarised here can be found in the

MIPS Data Handbook (version 3.3.1; MIPS Instrument Support Team (SSC) et al. 2007) and the MIPS section of the SOM (version 8.0; 2007) – *both now superseded by the MIPS Instrument Handbook, version 1.0, February 2010*[6].

3.4.3 The SINGS data pipelines

For the 11 SNe in galaxies observed as part of the SINGS Legacy program (Kennicutt et al. 2003), the IRAC and MIPS 24 μm images analysed in this thesis are generally the enhanced data products processed and delivered by the SINGS team in their fifth and final data delivery. These combine observations from two epochs, separated by ∼1–2 days, to best correct for transients and detector artifacts.

The fundamental data used to create the SINGS IRAC mosaics were the BCD images produced by the standard SSC pipeline (summarised in Section 3.4.2, the *IRAC BCD pipeline*). Additional processing by the SINGS team included correction for frame geometric distortion and rotation, residual flat fielding, cosmic ray rejection, frame alignment and bias drift correction. The individual images from both epochs were combined using a drizzle algorithm to produce a final mosaic of the galaxy in each IRAC channel, maximising the spatial resolution from the individual sub-sampled images. The final mosaics had a pixel scale of 0.″75 (compared to 1.″2/pixel for the standard SSC pipeline data), and were rotated to the conventional orientation of north up, east left. In addition, a constant background level for each mosaic was determined from the peak of a Gaussian fit to a histogram of the pixel levels in a region outside of the galaxy. The constant value subtracted from the mosaic was stored in the fits header keyword *BACKGRND*.

For the MIPS 24 μm data, the multiple images obtained from the 2 epochs of scan map observations were fully processed with the MIPS Data Analysis Tool (MIPS DAT, Gordon et al. 2005) version 3.06, along with additional customised processing software. The main processing steps included droop correction, non-linearity correction, dark current subtraction, flat fielding, latent image removal and correction for the "jailbar" pattern (caused by bright sources). Constant backgrounds were subtracted for each image and the subtracted value stored in the fits header keyword *BACKGRND*. This was achieved by finding background levels as a function of time for each scan leg in regions off-galaxy, avoiding bright sources and fitting a third order polynomial to these values. The function was then used to calculate the background for each frame, which was then subtracted.

[6]http://irsa.ipac.caltech.edu/data/SPITZER/docs/mips/mipsinstrumenthandbook/

Low-level scan mirror position-dependent scattered light was also subtracted from each image. Preliminary mosaicking of the individual frames for each of the two epochs, and the difference images of these, effectively filtered cosmic rays and other transients before final mosaics are drizzled together from the frames of both epochs. The final MIPS 24 μm mosaics had a pixel scale of 1.″5 (compared to 2.″45/pixel for the standard SSC pipeline data), chosen to adequately sample the PSF and at the same time be an approximate integer multiple of the IRAC mosaics' pixel scale. The mosaics were rotated to the conventional orientation of north up, east left. Finally, calibration factors were applied to convert the image units to MJy/sr (stored in the image header keyword *JANSCALE*).

For a more detailed description of the SINGS processing, see the *SINGS: The Spitzer Infrared Nearby Galaxies Survey Fifth Data Delivery April 2007 User's Guide*[7].

3.4.4 MOPEX

For *Spitzer* data presented in this thesis (generally excluding the SINGS Legacy data described previously), the final image processing stage was carried out manually with the SSC MOPEX software (Makovoz et al. 2006). This was primarily in order to improve the spatial sampling of the final mosaics over those of the standard *Spitzer* post-BCD pipelines and to have consistency with the SINGS enhanced data where initial SN detections were followed-up with observations from our own *Spitzer* GO programs.

MOPEX (MOsaicker and Point source EXtractor) is an astronomical image processing package developed at the *Spitzer* Science Centre for the automatic pipeline to process *Spitzer* data, although it can be applied to data from other telescopes. The package is implemented as a set of perl scripts each running a separate task, with each script running a number of individual modules written in C/C++. The software can be downloaded from the SSC website[8]. MOPEX version 16.2.5 was used to process the *Spitzer* data in this thesis. The perl scripts were run from the command line, with configuration files (known as "namelists") also supplied on the command line, although a graphical user interface for MOPEX is also available. The namelists were used to select the individual modules run by the script, provide the location of the input data (BCD images and mask files) and set the output directories. They were also used to set parameters for the individual modules.

[7] http://irsa.ipac.caltech.edu/data/SPITZER/SINGS/doc/sings_fifth_delivery_v2.pdf
[8] http://irsa.ipac.caltech.edu/data/SPITZER/docs/dataanalysistools/tools/mopex/mopexdownload/

The major tasks used in MOPEX for the post-BCD processing of the *Spitzer* data in this thesis were 1) background matching between overlapping frames, achieved with the overlap task, which applies an additive correction calculated for each image in the input stack in order to bring them to a common background level, 2) mosaicking with outlier detection of the individual BCD frames with the mosaic task, which performs interpolation and co-addition of the BCD images with a choice of outlier rejection modules to remove cosmic rays and bad pixels.

The default interpolation scheme was adopted to project the input images onto a 2D plane defined by the fiducial image frame (FIF) table that specifies a unified coordinate system for the output mosaic, with an output pixel size defined by the user. With the default interpolation, each output pixel is a linear weighted sum of input pixels with weights equal to the area overlap with the output pixel. The output pixel sizes adopted were generally the same as those used by the SINGS team for the enhanced processing of their Legacy data, i.e., 0.″75/pixel for the IRAC mosaics and 1.″5/pixel for the MIPS 24 μm mosaics. For comparison, the pixel scale of the final mosaics produced by the *standard* SSC pipeline was 1.″2/pixel for IRAC (for pipeline versions prior to S18.14) and 2.″45/pixel for MIPS 24 μm data. For the final IRS-PUI mosaics, a pixel scale of 1.″2 was used, which compares with 1.″8/pixel for the standard IRS-PUI pipeline data. Dual outlier rejection was adopted which uses both spatial and temporal filtering and is best suited for low-to-medium coverage data, such as the SNe data presented here. Finally, the interpolated images were averaged to combine them in a single mosaic.

For a thorough description of the MOPEX software and the modules associated with the tasks described here, please refer to the *MOPEX User's Guide*[9].

3.5 Flux density measurement: detections and upper limits

3.5.1 Detections – PSF-fitting (and aperture photometry)

Flux densities of the *Spitzer* SNe sample detections were generally measured by way of PSF-fitting with the `daophot` and `allstar` tasks in IRAF, the general procedure for which has been referred to previously in Section 2.6.2 of Chapter 2 and described in Appendix C.

[9] http://irsa.ipac.caltech.edu/data/SPITZER/docs/dataanalysistools/tools/mopex/mopexusersguide/

Due to the lack of suitable isolated, bright stars in the *Spitzer* images, semi-empirical over-sampled PSF images were downloaded from the SSC archive for each of the four IRAC channels, the MIPS 24 μm channel and the blue (16 μm) IRS-PUI channel. In each case, the PSFs were produced by the SSC with *Spitzer*'s version of Tiny Tim, which combines empirical observations with theoretical optics to generate 4-times oversampled point spread functions for each detector and channel. The resultant PSFs have negligible noise in the wings and are pre-normalised to unit flux. To produce the PSF model for use with IRAF `daophot`, these PSF images were first geometrically transformed to the appropriate pixel scale for each image using standard scaling with bicubic interpolation as implemented by the `geotran` task within IRAF. For the SINGS images that had been rotated from their observed orientation to a north-up, east-left orientation during the processing stage, the PSF images were similarly rotated with the `geotran` task by taking into account the average position angle of the observations. Once transformed, the PSF images were processed for use within IRAF `daophot` by using the `daopsf` task (written by B. E. K. Sugerman), as described in Appendix C. The aperture radius for the photometry used to set the magnitude of the PSF model within the `daopsf` task was chosen to be the same size as the PSF radius, i.e., the PSF should measure 100 % of the flux. A PSF radius of 13.5″ was typically used for the IRAC PSF models. This differs from the 12″ radius used for the absolute calibration of the IRAC bands, but aperture photometry of the PSFs with a 12″ aperture radius differed by as little as 1–2 % in all IRAC channels, which is well within the calibration errors described below (Section 3.5.3).

For PSF-fitting of the SN detections, the size of the fitting radius was chosen to be approximately equivalent to the FWHM of the stellar profile, but was occasionally varied by 1 or 2 pixels to optimise the fits. For example, for IRAC images this was found to be between 3 and 5 pixels, corresponding to angular sizes of 2.″25–3.″75 for mosaics with a pixel size of 0.″75×0.″75. The sky background was modelled during the PSF-fitting process, using sky annuli at appropriate distances around the SN, avoiding any contaminating sources. In most cases, the `allstar` task used to do the actual PSF-fitting was successful in centring on the SN profile via its centroiding algorithm. However, if the SN was quite faint, this algorithm was turned off such that the PSF-fitting was centred directly on the input coordinates corresponding to the SN position. The final PSF-fitted and subtracted images were inspected alongside the un-subtracted images to check the goodness of the fits. PSF-fitted flux densities for SN detections are detailed in Tables 3.3–3.7.

Aperture photometry was carried out in some cases where the source was isolated enough for comparison with the results from the PSF-fitting, using the IRAF `phot` task described in Section 2.6.1 of Chapter 2. For example, both techniques were used to measure SN 2004et, as described in Chapter 5. Aperture corrections were applied to the flux densities measured with `phot`. For IRAC data, aperture corrections for photometry using a variety of aperture sizes are given in Table 5.7 of the IRAC Data Handbook (version 3.0; Reach et al. 2006). Where different aperture sizes were needed to measure the SN data, aperture corrections were derived from measurement of a sample of IRAC calibration stars (Reach et al. 2005*a*), using the procedure described for SN 2004et in Section 5.5.2. The PUI 16 μm and MIPS 24 μm aperture corrections were derived by measuring the semi-empirical PSF images, as more fully described in Section 5.5.2. Whilst flux densities measured from aperture photometry are not listed, they were generally found to be consistent with results from PSF-fitting to within 15 %.

3.5.2 Non-detections – Upper limits to flux densities

For SNe not detected in the *Spitzer* data, upper limits to the flux densities were determined in a variety of ways depending on the nature of the background at the expected position of each source. Where there was clearly no source detected in the frames at the position of the SN (as reported in the literature from optical measurements, i.e., those listed in Table 2.1 of Chapter 2), the first approach was that adopted for the Gemini data, based on the background statistics in the region of the SN – see Section 2.6.3 of the previous chapter for a description of the method used to determine a 3-σ upper limit. However, the *Spitzer* data differs considerably from the Gemini data in that the background is much more complex with rapidly varying levels due to the location of the SNe, which often lie on the densely populated spiral arms of their host galaxies. To test the upper limits as determined from the background statistics in the immediate vicinity of the SN, a fake point source was constructed from the PSF images for each instrument/filter with a brightness set to the 3-σ limit previously determined. These were then added to the *Spitzer* images at the SN position to see if they could be confirmed as a robust detection by eye. For a few cases the fake stars were detected and the upper limits were considered to be reasonable, but for the majority of SNe the 3-σ upper limits were clearly not sufficient due to the confused background. For these SNe, the brightness of the fake PSF was increased until a clear detection was confirmed, and these were used as the final robust upper limits.

3.5.3 Error analysis

The flux density errors provided in Tables 3.3–3.7 are statistical errors computed by the PSF-fitting task `daophot`. The `daophot` error model includes readout noise from the detector; Poisson noise from the star and background; a photometric error term; and a profile error term that corrects for pixelization of a function. The photometric and profile errors were left as the the task's default values of 0.75 % and 5 % respectively, although in reality the photometric term should be considered to be much higher than this. A more realistic, but conservative photometric error is estimated to be 20 % which takes into account calibration errors, such as colour corrections for all instruments (which should be a maximum of ∼ 6 %) and further calibration corrections for IRAC described in Reach et al. (2005*a*), as well as accounting for differences between flux densities measured from PSF-fitting and aperture photometry.

Since the *Spitzer* images were calibrated in surface brightness units and converted to flux densities (μJy), the effective readout noise and gain of the detectors, required for an accurate noise model, were set as follows:

$$\textit{effective gain} = N \times (GAIN * EXPTIME)/(FlUXCONV * FAC)$$
$$\textit{effective readnoise} = \sqrt{N} \times READNOISE$$

where the following were keywords from the image headers: GAIN, in electrons/data number (DN); EXPTIME, the effective integration time in seconds; FLUXCONV, the *Spitzer* flux calibration factor in units of (MJy/sr)/(DN/s); and READNOISE, the detector readout noise in electrons. FAC was the conversion factor used to change flux units from MJy/sr to μJy and N was the number of frames (BCDs) on-source that were averaged to produce the final mosaic image.

3.6 Discussion of results

Mid-IR photometry of 18 SNe has been obtained with three different instruments on the *Spitzer Space Telescope* from 2004 to 2009. Five of the sample were detected from SINGS Legacy data in Cycle 1, and consequently monitored: SN 1999bw, SN 2002hh, SN 2003gd, SN 2004dj and SN 2004et.

Figure 3.7 shows the 8-μm flux densities and upper limits of the *Spitzer* SEEDS SNe sample, scaled to a distance of 50 kpc (measured as part of this work and presented in Tables 3.3–3.7), and plotted as a function of time (days) since explosion. The 8-μm data were obtained with IRAC channel 4 (λ_{eff} = 7.87 μm, $\Delta\lambda$: 2.91 μm). The distance-scaling allows for a comparison with the 8-μm flux densities of SN 1987A at similar epochs, which are also shown in the figure. The Bouchet et al. (1989) and Bouchet & Danziger (1993) data for SN 1987A, from days 14–1031, were taken with the narrow-band N1 filter (λ_{eff} = 8.36 μm, $\Delta\lambda$: 0.85 μm FWHM), on the IR photometer attached to the 1-, 2.2- and 3.6-m ESO telescopes in La Silla, Chile. The figure caption provides a further explanation of the symbols and labelling. (A similar figure was shown for the 11-μm SNe data obtained with the Gemini telescopes, in the discussion section of Chapter 2 – Figure 2.5). Panel (a) of Figure 3.7 shows the complete *Spitzer* sample for SN ages of 64 to 3316 days after explosion, including the exceptionally high 8-μm upper limit to the flux density derived for SN 2004C. The upper limit for SN 2004C was particularly high (about 3 orders of magnitude greater than the average upper limits for the sample), because the SN position was embedded in a bright unresolved emission region close to the centre of its host galaxy NGC 3683 at a Hubble distance, D, of ~23.5 Mpc. In this case, the upper limit provides an indication of how bright the SN would need to be for detection in the unresolved *Spitzer* images. Similarly, the high upper limits for the Type Ib/c supernovae SN 2003jg and SN 2002ji were due to their positions at the edge of the nucleus of their respective host galaxies NGC 2997 ($D \sim 15$ Mpc) and NGC 3655 ($D \sim 20$ Mpc). No conclusions can be drawn about the significance of their non-detections, as any thermal emission from dust in the vicinity of these SNe would clearly be swamped by the unresolved mid-IR emission from their host galaxies. For clarity, panel (b) of Figure 3.7 displays the same information for SN ages limited to 2000 days after explosion (the last 3 epochs of SN 1999bw are therefore excluded from this plot), and for scaled flux densities limited to 1000 Jy (therefore excluding the upper limit for SN 2004C previously discussed).

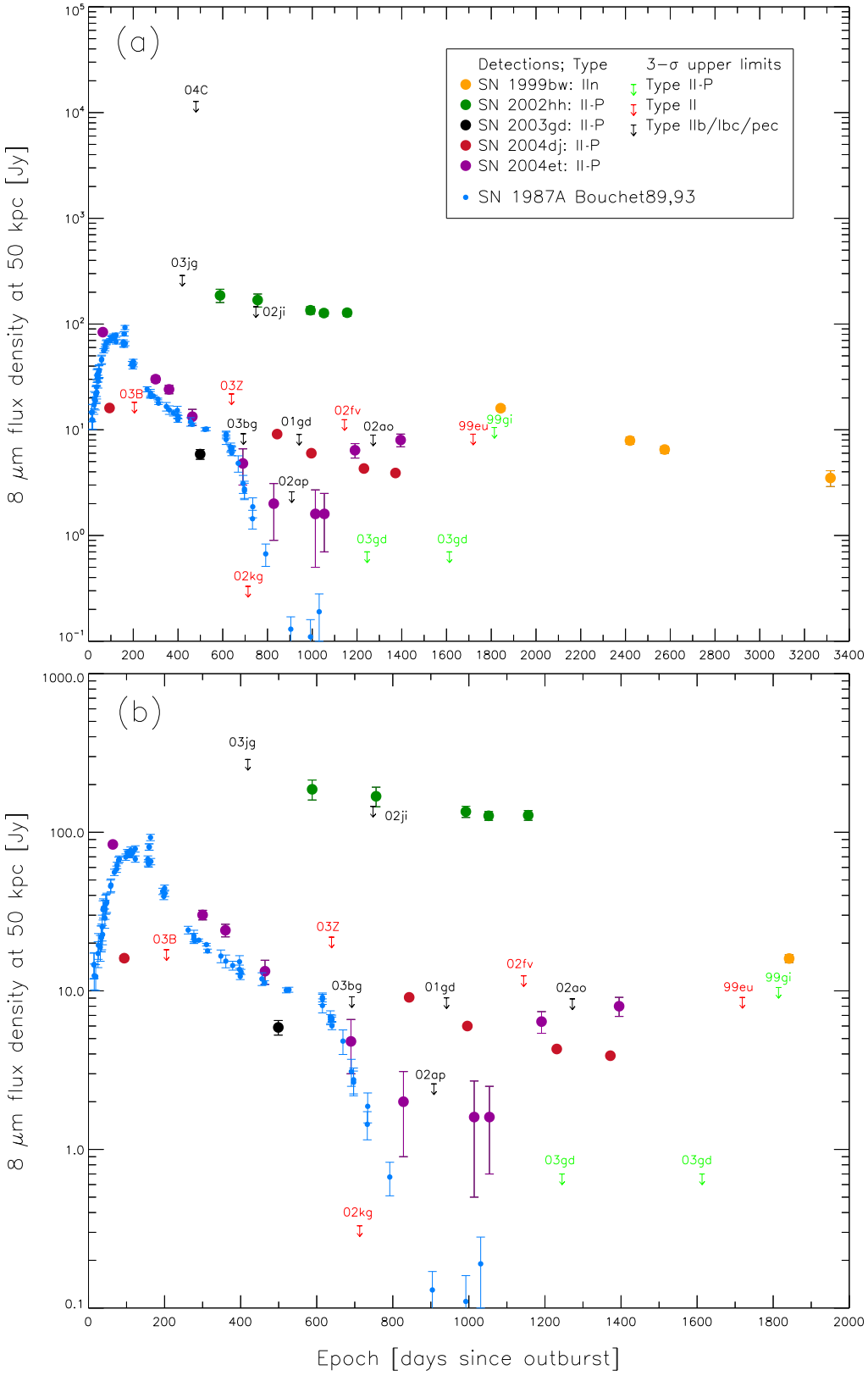

Figure 3.7: 8-μm flux densities and upper limits of the *Spitzer* SEEDS SNe, scaled to a distance of 50 kpc, as a function of time (days) since explosion. The distance-scaling allows for a comparison with the 8-μm flux of SN 1987A at similar epochs, indicated by the small blue, filled circles (Bouchet et al. 1989; Bouchet & Danziger 1993). Detections for the SEEDS sample are shown as filled coloured circles identified by the key in panel (a). For non-detections, the upper limits to the flux densities are shown as downward-pointing arrows and are labelled with the SN name, abbreviated to the last two digits of the year and the letter suffix. The upper limits are also colour-coded by SN type (see key, and Table 2.1 for a list of the individual SN types). Panel (a) shows the complete *Spitzer* sample, and panel (b) shows a slightly zoomed-in view for clarity.

The first *Spitzer* detections of the tentatively classified Type IIn SN 1999bw were made from SINGS Legacy observations of NGC 3198 ($D = 13.7$ Mpc; Freedman et al. 2001), at 1842 days (~ 5 years) after the SN had exploded. With a 50-kpc 8-μm flux density of 16 Jy at this time, its bright, late-time mid-IR detection was surprising, and is comparable to the much earlier 8-μm flux of SN 1987A at day 350. It was the only SN detected with *Spitzer* that was not also observed with Gemini. The SN clearly fades in all IRAC bands over the next three years, to day 3316, by a factor of ~ 4.5 at 8 μm, as shown in panel (a) of Figure 3.7. A summary of the *Spitzer* observations, including blackbody fits to the mid-IR spectral energy distribution over the four epochs, is presented in Chapter 4, Section 4.2, and includes a discussion of an IR echo as the likely source of emission and the possibility that the source was not a true supernova.

SN 2002hh is the brightest of the *Spitzer* detections at 8 μm. As found from the Gemini 10-μm observations, its mid-IR evolution was very slow, with the 8-μm flux declining by a factor of only ~ 1.5 between days 590–1158. At day 590, the SN was about 20 times brighter than SN 1987A at the same epoch, and by day 1000 was $\sim 1200\times$ as bright. As mentioned in Section 2.7, the mid-IR (and optical) evolution of SN 2002hh is most easily explained in terms of an IR echo from nearby pre-existing dust, although it has been argued that most of the strong mid-IR emission is actually from a cool, obscured star-formation region or molecular cloud along the line of sight (Meikle et al. 2006). The SN, clearly resolved in the Gemini images, occurred in a complex field and was confused with nearby sources in the *Spitzer* data, due to the comparatively lower spatial resolution of the 0.85-m space telescope. A comparison of the *Spitzer* and Gemini fields of view is shown in Figure 4.6 of Section 4.3, where a summary of the SEEDS analyses (Barlow et al. 2005; Welch et al. 2007) is presented.

The Type II-P SN 2003gd was detected with *Spitzer* IRAC and MIPS (24 μm) at day 499, with the distance-scaled 8-μm flux of 5.6 Jy a factor of only ~ 2 fainter than the coeval 8-μm flux of SN 1987A. Subsequent *Spitzer* observations at days 1245 and 1613 showed that the SN had faded beyond detection. The SN was observed at 10 μm with Gemini at days 781 and 784 but was not detected (to a 50-kpc 3-σ upper limit of 10–20 Jy). Archival *Spitzer* IRAC observations (GO program: 3248, PI: Meikle) on day 670 were also examined by the SEEDS team and showed the SN was still detected in the 8 μm channel only, at a 50-kpc flux of 2 Jy (not shown in Figure 3.7). Models to the SEDs of SN 2003gd by the SEEDS team indicated that the SN had formed up to 0.02 $M_\odot$ in its ejecta by day 678

(Sugerman et al. 2006) implying that CCSNe could be efficient dust producers, however this was disputed by Meikle et al. (2007). A summary of the SEEDS analysis of SN 2003gd is presented in Chapter 4 (Section 4.4).

SN 2004dj is another of the *Spitzer* SNe that was also observed with Gemini. Whilst its earliest Gemini 10 μm flux, at around day 600, was at similar levels to the coeval 10 μm flux of SN 1987A, the 8-μm flux of SN 2004dj at day 94 was a factor of 4.3 fainter than that from SN 1987A at similar times. During days 94–1372, the 8-μm light curve of SN 2004dj declined by a factor of 4.5, confirming the relatively slow mid-IR evolution implied by the Gemini observations at days 615 and 967, especially when compared to SN 1987A and SN 2004et (see discussion below). The 8-μm flux at day 850 was ∼30 times brighter than SN 1987A and ∼5 times brighter than SN 2004et for the same epoch. An IR echo from pre-existing grains is a likely cause of the relatively strong late-time mid-IR emission.

SN 2004et was the most-intensively observed SN of the sample, with one early SINGS IRAC observation on day 64 (plus a serendipitous SINGS pre-explosion IRAC image at day -75) and nine SEEDS IRAC observations from from days 300–1395. There was a comparable 10 epochs of MIPS 24-μm observations and five epochs of IRS-PUI 16-μm photometry. Difference imaging, using the pre-explosion SINGS images as the reference frames, was used to isolate the varying emission component attributed to the SN in the IRAC and MIPS images. Figure 3.7 shows that SN 2004et is the only SN of the sample whose 8-μm evolution closely resembles that of SN 1987A until almost 700 days. However, after this time their evolution is markedly different. Whilst SN 1987A continued to fade rather steeply from this time until at least 1000 days, the 8-μm light curve of SN 2004et appears to flatten after day 800 until day 1054, but after this time rises sharply to a distance-scaled 50-kpc flux of 8 Jy by day 1395. The large flux uncertainties for days 828–1054 occurred when the SN was very faint. The *Spitzer* observations also confirmed the Gemini 10-μm results that the SN had faded after day 300 and risen again by day 1395 (Section 2.7). The observations suggest that, similar to SN 1987A, SN 2004et also formed dust in its ejecta, possibly from as early as day 400 to around day 700 (Chapter 5). The late-time rise in the mid-IR has been attributed to thermal emission from dust formed in a cool dense shell behind the reverse SN shock, due to ejecta/CSM interaction (Kotak et al. 2009), although the SEEDS team are investigating the possibility that the mid-IR emission after ∼ day 1000 is caused by an IR echo from circumstellar dust. A thorough discussion of the mid-IR evolution of SN 2004et is presented in Chapter 5, together with analysis of

complementary SEEDS (and archival) optical and NIR data.

Also of note from Figure 3.7 is the flux upper limit for the peculiar Type IIc SN 2003bg which is reasonably close to the intrinsic 8-μm fluxes of SN 1987A and SN 2004et at ∼day 690. This was during the epoch of dust formation in both SNe, suggesting that SN 2003bg did not produce larger amounts of dust at similar epochs. It is significant that the majority of the non-detections (9 SNe, not including SN 2004C, SN 2003jg and SN 2002ji mentioned towards the beginning of this section), lie at similar intrinsic levels to, or below, the detections of SN 2004dj, SN 2004et and SN 1999bw, implying that they do not have larger amounts of ejecta-dust or pre-existing circumstellar dust present.

It is also interesting that whilst SN 2004dj in NGC 2403, at the closest distance of the sample, was detected, the Type IIn SN 2002kg was not detected in the same host galaxy to a particularly low 50-kpc 8-μm flux upper limit of 0.33 Jy. However, the nature of SN 2002kg is ambiguous – it is also known as the luminous blue variable (LBV) V37 (Weis & Bomans 2005).

3.7 Summary

This chapter has presented mid-IR observations of 18 CCSNe obtained with the *Spitzer Space Telescope* during the years 2004 to 2008. The description of the *Spitzer* data included a discussion of the space telescope and the instruments used, providing a contrast with the ground-based mid-IR observations with the Gemini telescopes presented in Chapter 2. The *Spitzer* reduction pipelines and flux calibration for the IRAC, IRS Peak-up Imaging module and MIPS instruments were described, including details of the SINGS Legacy team's own enhanced data pipeline. For the SEEDS data, further processing of the basic calibrated *Spitzer* pipeline data to higher spatial resolution with the MOPEX software was also carried out.

The methods for flux measurement of the SN detections via PSF-fitting were described in the previous chapter for the Gemini observations, but the parameters adopted for measuring the *Spitzer* data were provided in this chapter, together with a description of how the flux upper limits for non-detections were derived. The flux densities, and upper limits for non-detections, were then presented and discussed.

Five SNe were detected, and subsequently monitored, with *Spitzer*. The initial detections of all five of these Type II SNe, at distances ranging from 3.3–13.7 Mpc, were made

from SINGS Legacy data (programme ID: 159, PI: Kennicutt) obtained in the first cycle of *Spitzer* observations. This was not surprising as the SINGS project was a survey of 75 nearby galaxies ($D < 30$ Mpc), and included many of the host galaxies for SNe that had been on the original list of SEEDS targets for *Spitzer* observations. Four of the detected SNe (SN 2003gd, SN 2002hh, SN 2004dj and SN 2004et; all Type II-P) were also observed with Gemini, three of which were detected at 10-μm(the non-detection of SN 2003gd from Gemini observations occurred after the SNe had faded beyond detection with *Spitzer*). The unexpected fifth *Spitzer* detection was of SN 1999bw in NGC 3198, at the furthest distance of 13.7 Mpc, starting five years after explosion. SN 1999bw was classified as a Type IIn, although ambiguity surrounds the nature of this SN (which is discussed further in Chapter 4).

Our own SEEDS Cycle 1 program, yielded no detections from 7 SNe at distances of 10.3 to 23.5 Mpc. Observations in subsequent cycles were generally used for monitoring previous detections, although a few additional CCSNe observed during the SEEDS *Spitzer* programme have not been included in this work.

Five SNe observed with both *Spitzer* and Gemini were not detected with either telescope. An additional 8 SNe were not detected with *Spitzer* and another 12 SNe not detected with Gemini.

Despite the small sample, it is significant that the majority of the non-detections (9 SNe out of the total *Spitzer* sample of 18, not including SN 2004C, SN 2003jg and SN 2002ji whose host galaxy emission would swamp any thermal dust emission from the region of the SN), lie at similar intrinsic levels to, or below, those SNe that were detected, implying that there were not significant amounts of ejecta-dust or pre-existing circumstellar dust present for these 9 SNe.

Since the only detections with Gemini were also detected with *Spitzer* and lay at the closest distances of 3.3–5.9 Mpc, it is concluded that for likely detection with Gemini, SN targets should be limited to distances of about 10 Mpc, and for *Spitzer* to about 15 Mpc.

Chapter 4

Dust emission detected from Type II SNe in the SEEDS sample

4.1 Introduction

This chapter summarises the results from initial analysis of three supernovae detected and monitored in the mid-IR, mainly with the *Spitzer Space Telescope*, as part of the SEEDS program. These are: the unusual Type IIn SN 1999bw observed at four epochs with *Spitzer* from 5–9 years after outburst; and two Type II-P SNe whose Gemini and *Spitzer* mid-IR fluxes have been presented in Chapters 2 and 3, namely SN 2002hh and SN 2003gd. These last two SNe have been the subject of papers by the SEEDS team documenting initial results from our mid-IR observations: Barlow et al. (2005) for SN 2002hh and Sugerman et al. (2006) for SN 2003gd. Although I did not conduct the majority of the analysis for these two SNe, as co-author of both papers I was involved in the work, and it is instructive, at this point, to summarise the published results.

4.2 SN 1999bw in NGC 3198

The discovery of SN 1999bw at a magnitude of $\sim$17.8 was reported by Li (1999*a*) from unfiltered CCD images taken on 20 April 1999 with the 0.8-m Katzman Automatic Imaging Telescope (KAIT) as part of the Lick Observatory Supernova Search (LOSS). Li (1999*a*)

confirmed that KAIT images revealed the presence of this object as early as 15 and 19 April 1999 (~ 18.4 and 18.0 mag respectively), but that it was not seen in earlier observations on 3 April, or the 24 and 29 March 1999. For the purposes of this work, the earliest detection of this object from the LOSS images, on the 15 April 1999, is adopted as the explosion or outburst date to which all epochs are referenced. The reported position was 85.″8 east and 83.″8 south of the nucleus of its host galaxy, NGC 3198.

Ambiguity has surrounded the exact nature of SN 1999bw since its discovery. Filippenko et al. (1999*b*) noted that its absolute V magnitude at discovery ($M_V \approx$ -12.9 mag for an assumed distance to NGC 3198 of 13.7 Mpc; Freedman et al. 2001) was particularly subluminous for a Type II supernova, which have typical $M_V \lesssim$ -18 mag (Van Dyk et al. 2000). Optical spectra obtained by Garnavich et al. (1999) and Filippenko et al. (1999*b*,*a*), 6–9 days after the SN was first detected in the 15 April LOSS images, were dominated by narrow hydrogen Balmer emission lines (full width at zero intensity (FWZI) $\sim 600\,\mathrm{km\,s^{-1}}$) sitting on top of a broader component (FWZI $\sim 3000\,\mathrm{km\,s^{-1}}$). Filippenko et al. (1999*a*) likened the spectra to that of the Type IIn SN 1997bs in NGC 3627, which was similarly underluminous ($M_V \approx$ -13.8 mag; Van Dyk et al. 2000).

4.2.1 Evolution of the mid-IR emission

The region around SN 1999bw was first imaged in the mid-IR almost 5 years after discovery, via *Spitzer* SINGS Legacy IRAC and MIPS observations of NGC 3198 (program 00159, PI: Kennicutt). Following its detection in the IRAC images (Figure 4.1) (reported by members of our SEEDS team; Sugerman, Meixner, Fabbri & Barlow 2004), further time was awarded in *Spitzer* Cycles 2 and 4 (programs 20320, PI: Sugerman; and 40010, PI: Meixner) for continued monitoring of this object. Photometric observations spanned 4 years from May 2004 to May 2008, corresponding to 1843–3331 days after discovery, and included 4 epochs of IRAC and MIPS 24 μm observations, and one IRS-PUI 16 μm observation in Cycle 4. Dates and exposure times of the observations are detailed in Table 4.1. Full details of the SINGS and SEEDS observations can be found in Chapter 3 (Section 3.3). The SEEDS IRAC, PUI and MIPS BCD data from the *Spitzer* pipeline were further processed with MOPEX (Section 3.4.4) to create the final images with improved pixel scales (compared to the standard pipeline PBCD products) of 0.″75/pixel, 1.″2/pixel and 1.″5/pixel, respectively. The IRAC and MIPS pixel sizes were the same as those of the SINGS enhanced data, processed by the SINGS team.

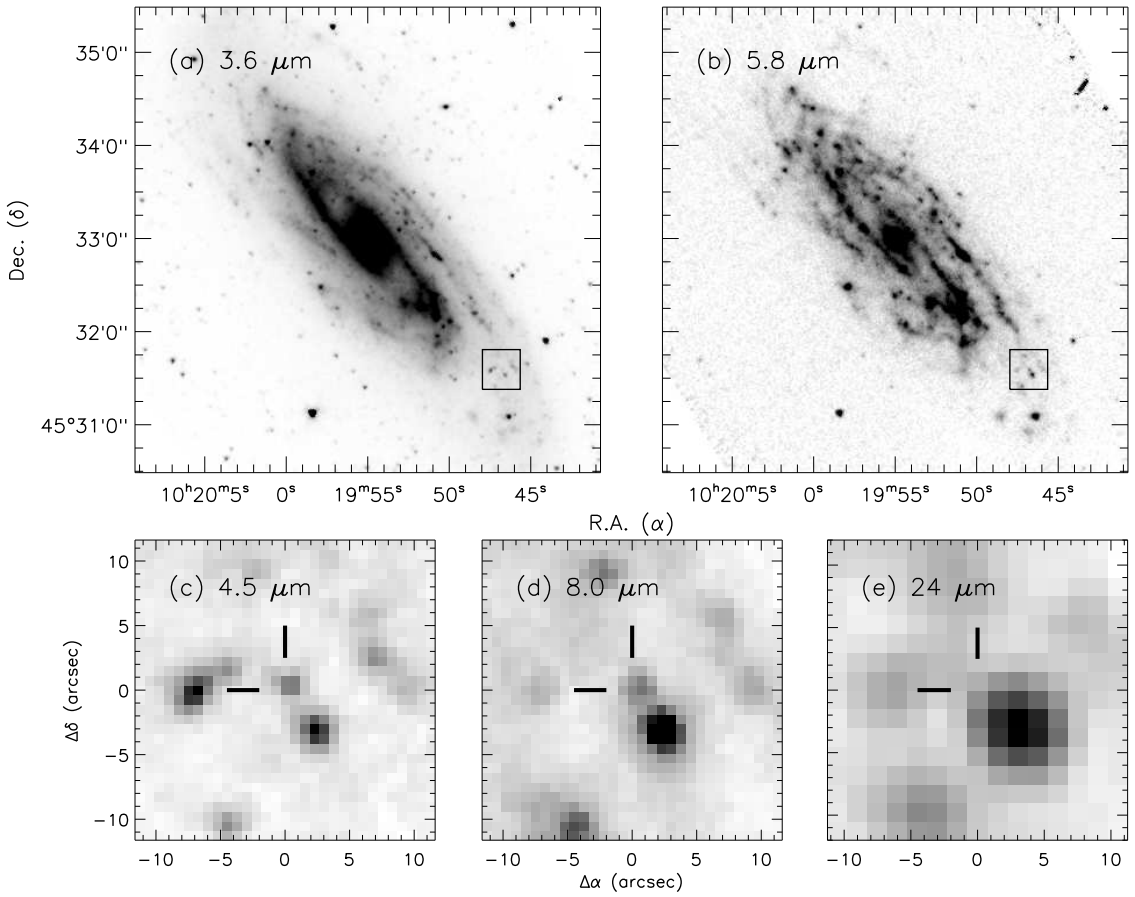

Figure 4.1: The position of SN 1999bw in *Spitzer* SINGS Legacy images of NGC 3198 observed in May 2004 (IRAC) and December 2004 (MIPS). Panels (a) and (b) show the whole galaxy in the IRAC 3.6 μm and 5.8 μm channels respectively. The ∼20″×20″ square is centred on the SN coordinates. Panels (c), (d) and (e) zoom in on the square region of the SN field at 4.5, 8.0 and 24 μm respectively, with the crosshairs indicating the SN position. The SN was detected in all four IRAC filters of the SINGS images which, although taken ∼5 years after discovery, were the first mid-IR observations of this object. The bright source to the south-west of the SN, "S2", dominates the SN position at 24 μm.

Table 4.1 summarises the *Spitzer* mid-IR flux densities and associated uncertainties of SN 1999bw, as well as the upper limits to the flux densities, from 1843–3331 days after discovery (previously presented in Chapter 3). A source coincident with the SN position was detected in most of the IRAC images at all epochs. Emission was also detected from a point source at the SN position in the IRS-PUI 16-μm image from the most recent Cycle 4 data at day 3331, the only observations at that wavelength. At 24 μm, a bright neighbouring source (∼4″ to the south-west of the SN position, and also seen in the IRAC images), dominated the field at this wavelength (panel *e* of Figure 4.1) and emission at the SN position was uncertain.

Table 4.1: *Spitzer* mid-IR fluxes of SN 1999bw from PSF-fitted photometry.

UT date	Age [days]	Exp. time [s]	Flux density / upper limits [μJy]					
			IRAC				IRS-PUI	MIPS[1]
			3.6 μm	4.5 μm	5.8 μm	8.0 μm	16 μm	24 μm
2004-05-01	1843	214.4	11 ± 1	39 ± 2	121 ± 6	213 ± 12	···	···
2004-12-07	2063	168.8	···	···	···	···	···	≤ 650
2005-11-29	2420	321.6	2.6 ± 0.3	14 ± 1	53 ± 4	105 ± 8	···	···
2005-12-01	2422	840.0	···	···	···	···	···	≤ 650
2006-05-03	2575	321.6	≤ 10	6.9 ± 0.6	43 ± 3	87 ± 6	···	···
2006-05-04	2576	840.0	···	···	···	···	···	≤ 650
2008-05-13	3316	964.8	≤ 10	4.0 ± 0.5	21 ± 3	46 ± 8	···	···
2008-05-17	3320	1650	···	···	···	···	···	≤ 650
2008-05-28	3331	534.8	···	···	···	···	93 ± 16	···

[1] The upper limits for the MIPS 24 μm data were estimated by measuring the flux density of the faint point source seen ∼6″ to the east of the SN position. This was found to have an average brightness of 657μJy with a standard deviation of 2.5 % over the four epochs, and this approximate value was used as a robust upper limit for the SN brightness at each epoch. See text for further details.

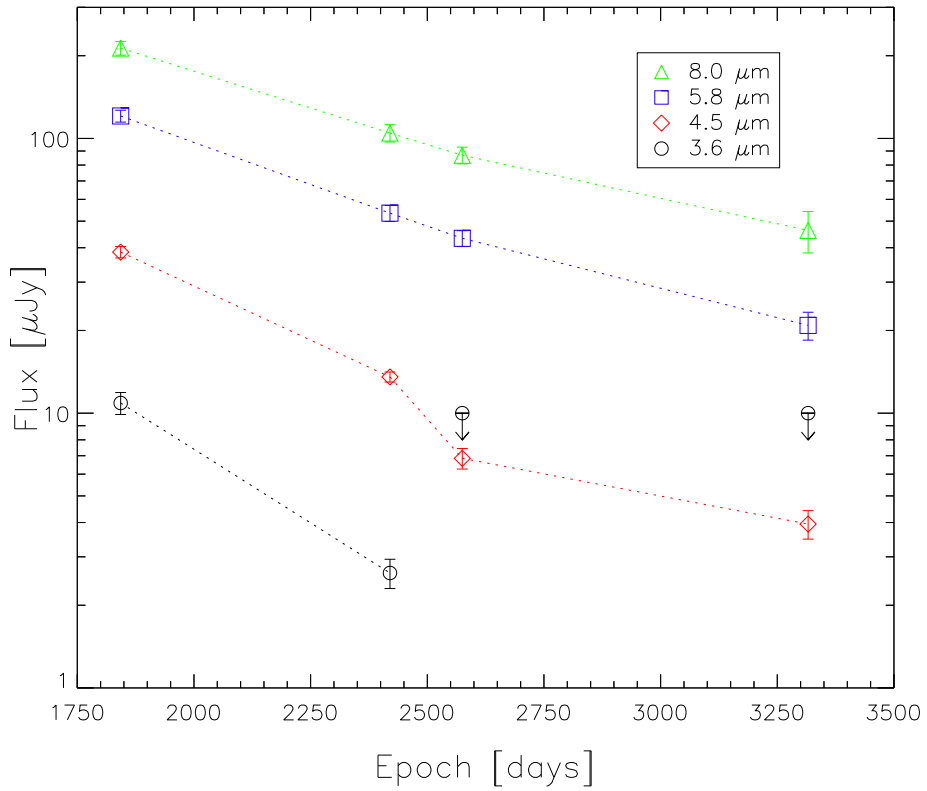

Figure 4.2: Mid-infrared light curves of SN 1999bw in the IRAC wavebands at 3.6, 4.5, 5.8 and 8.0 μm. Upper limits to the 3.6-μm flux densities are indicated by the downward-pointing arrows.

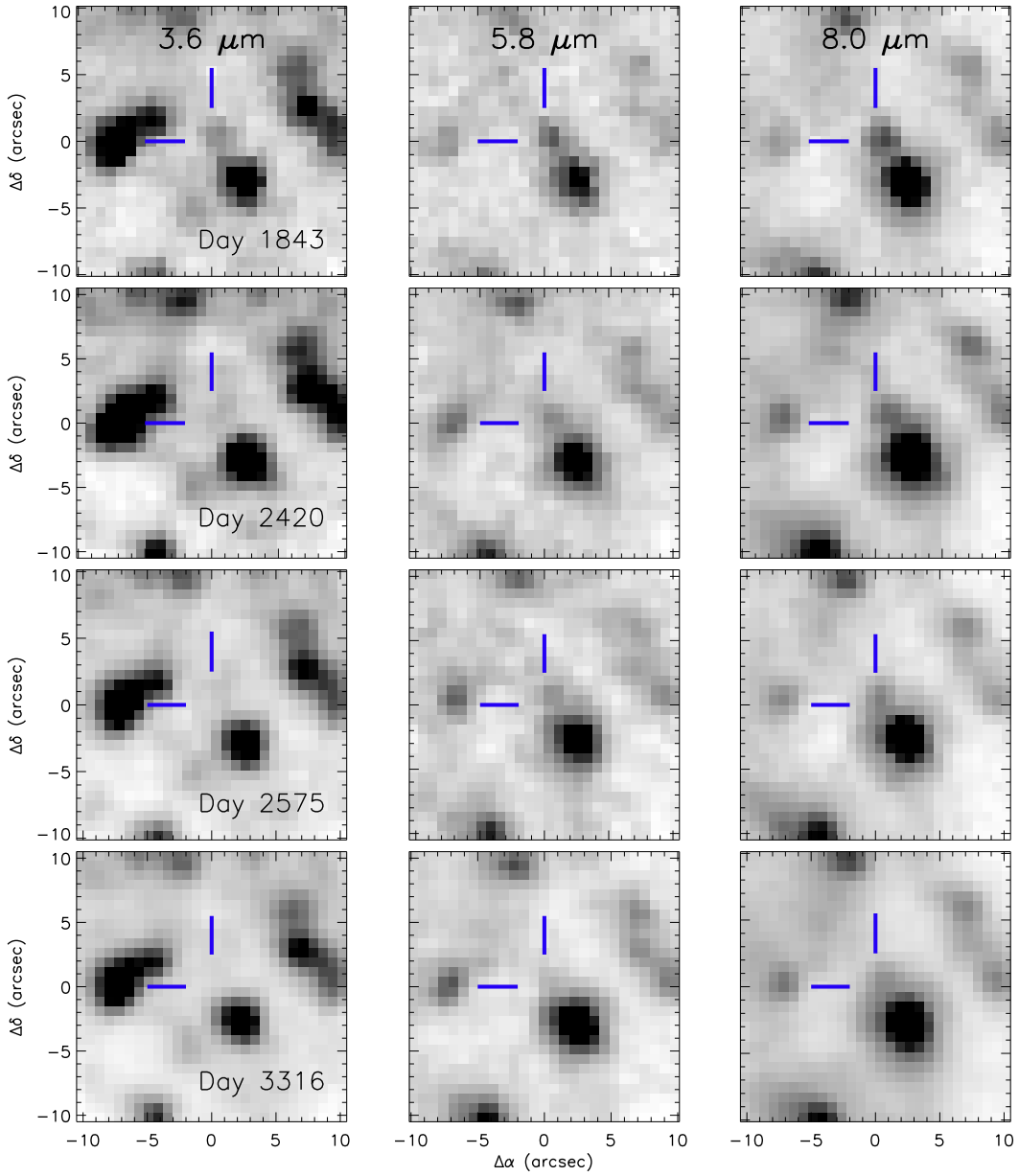

Figure 4.3: The position of SN 1999bw in *Spitzer* IRAC 3.6, 5.8 and 8.0 μm images, revealing the mid-IR evolution over the four epochs from days 1843–3316. The point source visible at the SN coordinates (centre of the frame, indicated by the cross-hairs) from day 1843 in all IRAC channels, clearly fades during the 4 years of observations. The 20″ by 20″ region around the SN, corresponds to an area of ∼1.3 sq. kpc for the adopted distance of 13.7 Mpc to SN 1999bw.

The fluxes were measured by way of PSF-fitting, as described in Section 3.5.1. Flux upper limits for the non-detections by days 2575 and 3316 at 3.6 μm were derived by adding a fake star of known brightness to the image at the expected position of the SN and increasing the flux until the point source was clearly detected by eye. The flux upper limits for the MIPS 24-μm data were estimated by measuring the flux density of the faintest point source in the region of the SN (∼ 6″ east of the SN position). The faint point source was found to have an average 24-μm flux density of 657 μJy with a standard deviation of 2.5 % over the four epochs, and this approximate value was used as an upper limit to the SN flux at each epoch. A fake star of this brightness was added to the image at the SN coordinates, confirming the presence of an additional source blended with the bright neighbouring star. Although the ability of PSF-fitting and subtraction to detect fake stars of lower brightness was not investigated, the values reported should provide robust upper limits to the 24-μm flux.

Figure 4.2 depicts the slow decline of the IRAC 3.6–8.0-μm light curves over the four epochs from days 1843–3316, equivalent to ∼ 4–9 years after outburst. The emission at 3.6 and 4.5 μm appears to evolve more quickly than that at the longer wavelengths, fading by factors of ∼ 4 and 3 respectively during the first 1.5 years, compared to the factor of ∼ 2 decline observed at 5.8 and 8.0 μm. The 3.6-μm source had faded completely by the third epoch of observations (day 2575 ≈ 7 years). The 4.5-μm emission continued to decline at a faster rate than the longer wavelength emission, by a factor of almost 10 over the course of the four years, compared to the decline in the 5.8- and 8.0-μm bands by factors of ∼ 6 and 4.5, respectively. The mid-IR evolution is also depicted in Figure 4.3, which shows a 20″ × 20″ field of view centred on the SN position (indicated by the cross-hairs) in the 3.6, 4.5 and 8.0 μm IRAC images for the four epochs.

4.2.2 SED analysis: Blackbody fitting

Blackbodies were fit to the mid-IR SEDs of SN 1999bw to investigate the limits of the physical properties of the SN at the various epochs. The blackbody fitting was carried out using the STARLINK software package DIPSO (Howarth et al. 2004). The `grid` and `bbody` commands were used to generate the blackbody curves at the required temperatures and the `atnorm` command was used to normalise the curves to the observed photometric flux densities.

Preliminary blackbody fits to the mid-IR energy distributions, generally normalised to

the 8-μm flux, are presented in Figure 4.4. The amount of reddening towards SN 1999bw is not known, so the fluxes were de-reddened using the Galactic foreground colour excess toward NGC 3627 of $E(B-V) = 0.013$ mag (Schlegel et al. 1998), with the extinction law of Cardelli et al. (1989) and $R_V = 3.1$. The IRAC 3.6-, 4.5- and 8.0-μm fluxes at days 1843 and 2420 were consistent with blackbodies cooling from 410 K to 370 K (solid lines), although these underestimated the 5.8-μm flux at both epochs. The alternative BB fits with marginally cooler temperatures (dotted lines) highlight that to match the 5.8-μm flux would be at the expense of over-estimating the shorter wavelength fluxes. A similar 5.8-μm excess is seen for the later epochs compared to blackbodies that provide a good match to the other fluxes. However, there is little data available to constrain the day 2575 SED, since there were no 3.6-μm detections from this time onwards. More realistic dust particles have $\lambda^{-\alpha}$ emissivities in the IR, with α typically between 1 and 2. Alternative fits shown for day 2575 show examples of these, but they do not manage to explain the 5.8-μm excess. The day 3316 SED is better constrained at longer wavelengths with the PUI 16-μm datum, although the PUI observations were obtained 15 days after the IRAC data.

The corresponding blackbody parameters (those for the solid curves only) are given in Table 4.2 and were calculated as follows. The blackbody luminosity, L, was calculated from the standard equation:

$$L = 4\pi D^2 F \tag{4.1}$$

where $4\pi D^2$ is the area of the spherical surface being illuminated at a distance D of the observer from the source, and F is the frequency-integrated flux of the source being approximated by the blackbody. F was obtained by integrating under the blackbody curve of the best-fit SED using the DIPSO command `integrate`, which uses simple trapezoidal integration. A distance (D) of 13.7 Mpc to the SN host galaxy NGC 3198 (Freedman et al. 2001) was adopted. The minimum emitting radius, R, indicated by the blackbody fit was calculated from $L = 4\pi R^2 \sigma T^4$, where the luminosity, L, was calculated previously, σ is the Stefan-Boltzmann constant ($5.67\times10^{-8} Wm^{-2}K^{-4}$), and T is the effective temperature of the blackbody representing the SN emission, i.e.:

$$R = \sqrt{\frac{L}{4\pi\sigma T^4}} \tag{4.2}$$

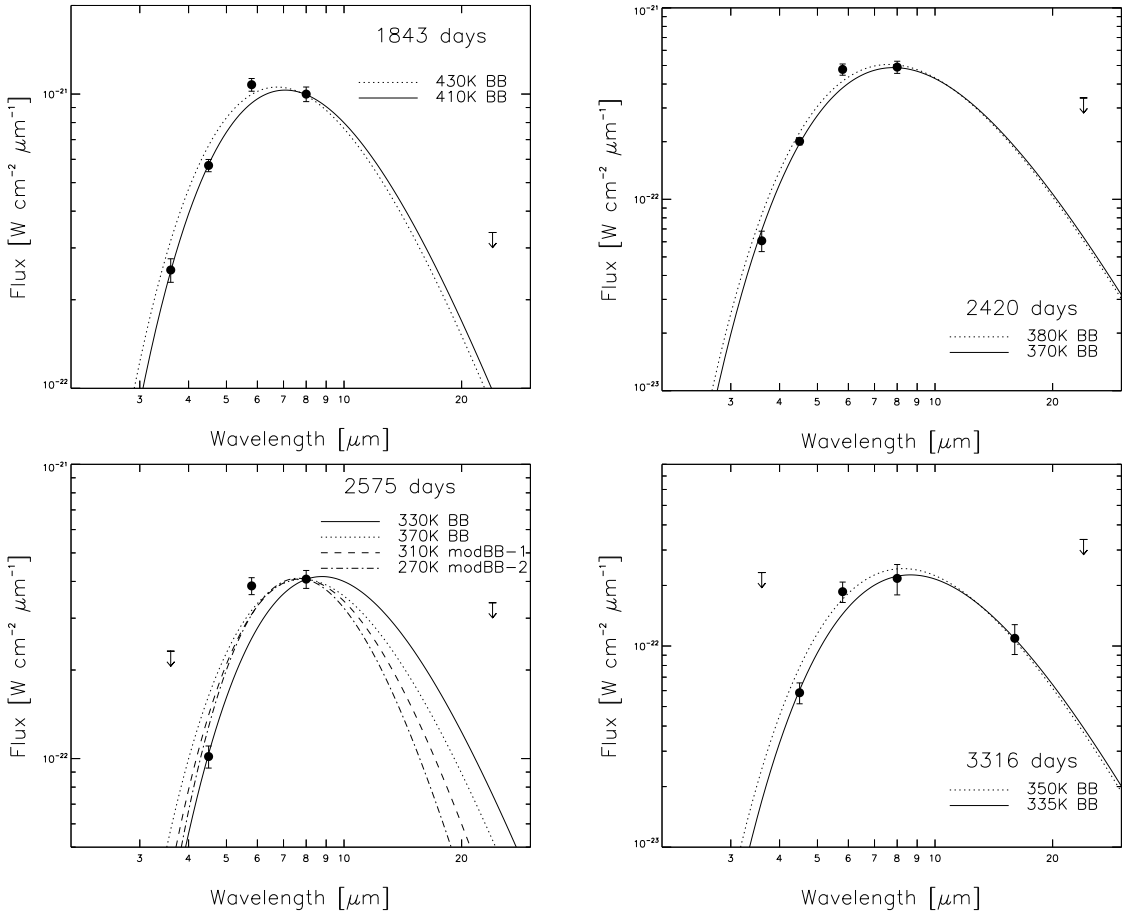

Figure 4.4: Blackbody fits to the mid-IR SEDs of SN 1999bw at IRAC epochs of 1843, 2420, 2575 and 3316 days. Upper flux limits to the 3.6- and 24-μm flux densities are indicated by the downward-pointing arrows. Where error bars are not shown, uncertainties are smaller than the symbol size. All fluxes were de-reddened using a foreground $E(B-V) = 0.013$ mag (Schlegel et al. 1998) and the extinction law of Cardelli et al. (1989) with $R_V = 3.1$.

Finally, the minimum ejecta velocity, v, implied by the emitting radius, R, was calculated simply from:

$$v = \frac{R}{t} \tag{4.3}$$

where t corresponds to the age of the SN when observed, i.e., the time since explosion, adopted to be 15 April 1999 for SN 1999bw.

The luminosity evolution of SN 1999bw determined from blackbody fitting to the mid-IR SEDs is depicted in Figure 4.5. The luminosities for SN 1999bw (black circles) have been scaled to the distance of SN 2004et at 5.9 Mpc for days 1843–3316, and compared with the mid-IR luminosity evolution of SN 2004et from days 1000–1400 (red triangles) (see Chapter 5).

Table 4.2: Blackbody-fit parameters to the mid-IR energy distributions of SN 1999bw.

Epoch [days]	T [K]	F [10^{-17} W m^{-2}]	R [10^{15} cm]	v [km s^{-1}]	L [10^5 L$_\odot$]
1843	410	11.1	11.1	698	6.5
2420	370	5.8	9.9	473	3.4
2575	330	5.6	12.2	546	3.3
3316	335	3.0	8.6	301	1.7

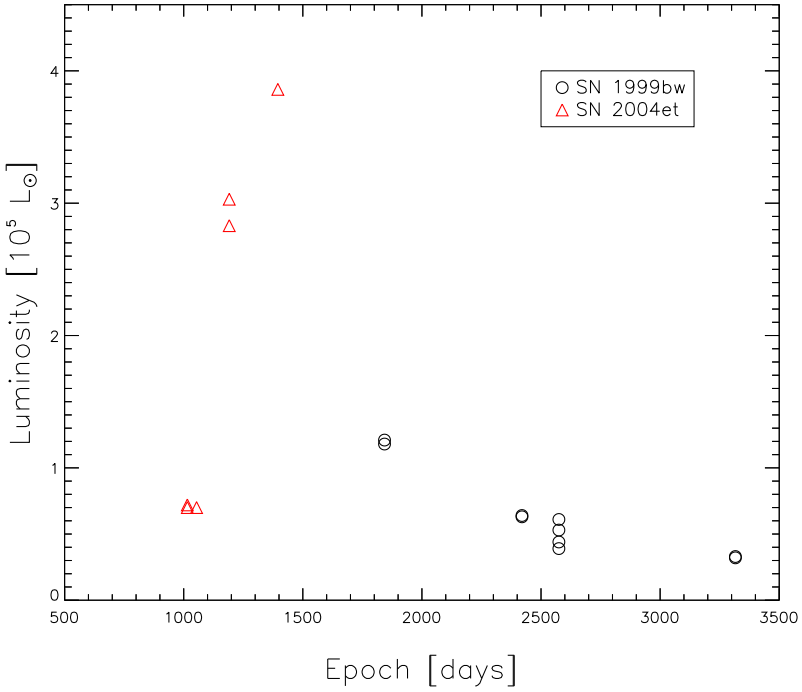

Figure 4.5: Luminosity evolution of SN 1999bw from blackbody fitting to the mid-IR SEDs scaled to the distance of SN 2004et at 5.9 Mpc for days 1843–3316, and compared with the mid-IR luminosity evolution of SN 2004et from days ~ 1000–1400 (see Chapter 5).

4.2.3 An unusual supernova or SN imposter?

Filippenko et al. (1999*a*) likened the early spectra of SN 1999bw to that of the Type IIn SN 1997bs. In the case of SN 1997bs, a progenitor star was associated with the SN by Van Dyk et al. (1999) from archival pre-discovery *HST* WFPC2 images of the host galaxy (*F*606*W* magnitude $\sim$22.9). The detection of the SN from similar *HST* WFPC2 images approximately 9 months (January 1998) after discovery at about 0.5 mag fainter than the progenitor, together with an apparent flattening of the *V*-band light curve from about 8 months post-discovery, led the authors to suggest the progenitor of SN 1997bs might have survived a "superoutburst" of an LBV star, analogous to η Carinae (Van Dyk et al. 2000). However, further *HST* WFPC2 observations by Li et al. (2002) in their "Snapshot Survey of Nearby Supernovae" seemed to provide evidence against the superoutburst interpretation for SN 1997bs, showing the SN continued to decline in the *V* and *I* bands after early 1998, inconsistent with the suggestion that the SN progenitor survived the explosion. Dust formation was ruled out by Li et al. (2002) as an explanation for the optical light curve decline of SN 1997bs based on its colour evolution, which became progressively bluer from early 1998 to early 2001. The nature of SN 1997bs, and by comparison that of SN 1999bw, remains unclear.

SN 1999bw was also imaged by Li et al. (2002) in their *HST* snapshot survey $\sim$635 days after discovery. Using pointing information from the image header and the reported discovery position of the SN (Li 1999*a*), they found a single source within a 0.″5 radius error circle which they concluded to be the supernova. Li et al. measured the WFPC2 *F*555*W* magnitude ($\approx V$) to be 24.08 $\pm$ 0.06 which, from comparison with several early-time (previously unpublished) KAIT observations, they showed had declined by 5.6 mag in the almost 2 years since maximum. In the same work, they estimated SN 1997bs had declined by about 7 mag in an equivalent period, concluding that the photometric evolution of these two objects seem to differ to some extent, despite their similar spectra and low peak luminosity.

SN 1999bw has also been compared (Thompson et al. 2009) to the luminous transients SN 2008S, NGC 300 and a similar object in M85. The discovery that SN 2008S (Prieto et al. 2008) and NGC 300 (Prieto 2008) had dust-enshrouded progenitors led Thompson et al. (2009) to propose a new classification of transient, formed when stars located near the upper mass limit for AGB evolution go through a self-obscured phase shortly before

exploding as electron capture SNe. These transients have progenitors with relatively low luminosities ($\sim 5 \times 10^4$ L$_\odot$) and low mid-IR variabilities, as well as being deeply dust embedded. The transients themselves have low luminosity (for SN 2008S and NGC 300, $M_V \approx -14 \pm 1$ mag, $\sim$2-3 mag fainter than normal CCSNe; Richardson et al. 2002), and spectra showing narrow Balmer lines (similar to low-luminosity Type IIn SNe and LBV-like SN imposters) with [Ca II] emission, as well as rapidly decaying light curves compared to Type II-P SNe.

With the luminosity and spectral features for SN 1999bw described previously, and its luminous mid-IR detection with *Spitzer* approximately 5 years after discovery (Sugerman et al. 2004; work presented herein), Thompson et al. (2009) likened SN 1999bw, and a similar transient in M85, to SN 2008S and NGC 300. However, because there was no progenitor information for these objects, no definite conclusions could be drawn.

The mid-IR observations pre- and post-outburst of NGC 300 and SN 2008S (Prieto 2008; Prieto et al. 2008; Botticella et al. 2009; Wesson et al. 2010) revealed the dusty environment of this type of transient and its progenitor, providing a potentially alternative source for the dust enrichment of galaxies.

SEEDS members Wesson et al. (2010) utilised pre- and post-outburst *Spitzer* images to investigate the optical and mid-IR SEDs of SN 2008S, the ninth supernova to be discovered in the spiral galaxy NGC 6946. Radiative transfer models constructed for the object before outburst and at two epochs post-outburst ($\sim$17 days and 6 months) provided a self-consistent fit to the SEDs with the same r^{-2} density distribution in a spherical shell of pre-existing amorphous carbon grains for all epochs, taking light time travel effects into account. The derived dust-mass-loss rate of 5.2×10^{-7}M$_\odot$ yr^{-1} implied an overall mass-loss rate from the progenitor star of 0.5–1.0 $\times 10^{-4}$M$_\odot$ yr^{-1} (for gas-to-dust mass ratios in the outflow of 100-200), consistent with mass-loss rates determined from a high-fraction of carbon-rich stars found amongst the most luminous AGB stars in the LMC (Matsuura et al. 2009). Their results indicated that super-AGB stars, of which the progenitor of SN 2008S appears to be an example, are only likely to contribute about 1.6 % of the 2×10^8 M$_\odot$ of dust observed in the $z = 6.4$ galaxy J114816.64+5251 (Dwek et al. 2007), potentially ruling out these objects as significant sources of dust in such galaxies.

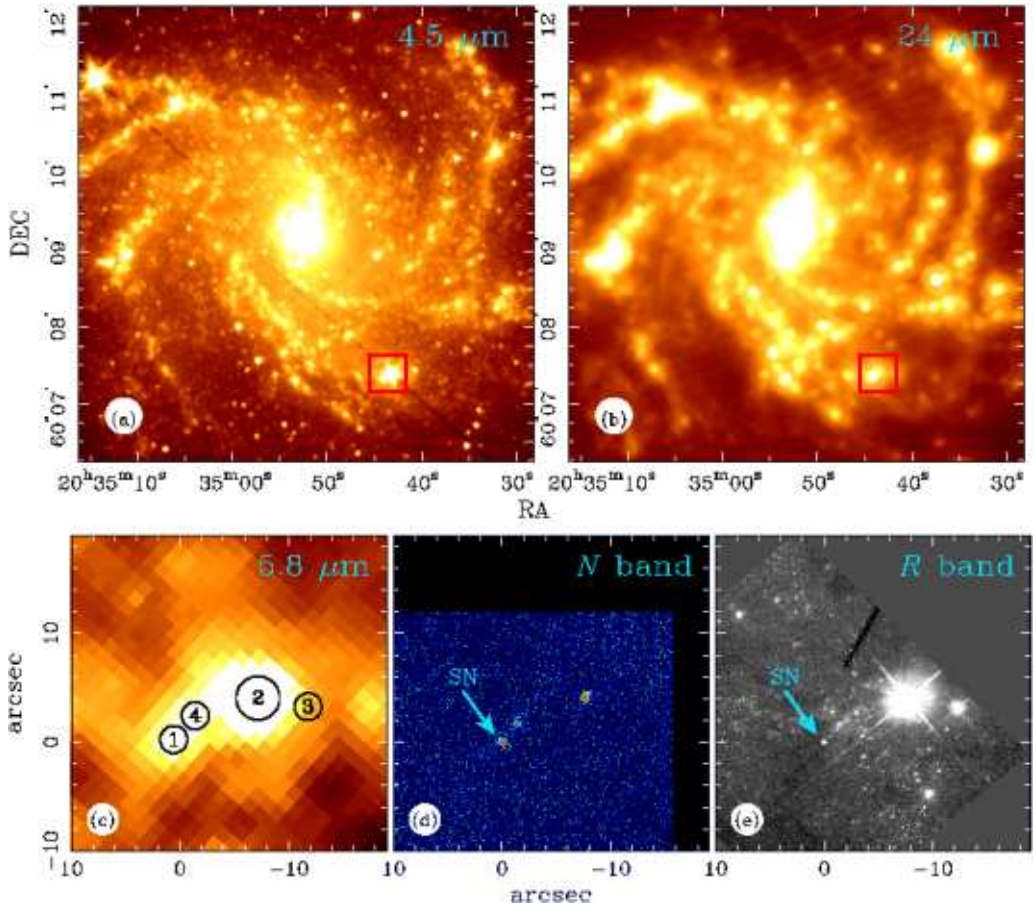

Figure 4.6: The complex field around SN 2002hh in NGC 6946: (a) *Spitzer*-IRAC 4.5 μm and (b) MIPS 24 μm images of NGC 6946 from SINGS Legacy observations, with the location of SN 2002hh marked inside the red box. (c) A 5.8 μm image of SN 2002hh (marked "1"), showing it is crowded with at least three other sources. *Spitzer* images taken at days 590 (IRAC) and 619 (MIPS). (d) Gemini *N*'-band image, confirming Star 4 is extended. (e) *HST*/ACS F606W observations resolving the crowded field.

4.3 SN 2002hh in NGC 6946

Early in the *Spitzer* mission, dust emission from the Type II-P SN 2002hh was detected in SINGS IRAC images of NGC 6946 (Barlow, Fabbri, Meixner & Sugerman 2004) and confirmed by higher angular resolution Gemini Michelle imaging (Barlow et al. 2005). Panels (a)-(c) of Figure 4.6 show the complex field around SN 2002hh in the SINGS IRAC (4.5 and 8 μm, day 590) and MIPS (24 μm, day 619) images. The region close to the SN is dominated by a bright adjacent field star (marked "2" in panel c). The Gemini-Michelle N'-band image and *HST*-ACS *F606W* image (~ *R*-band) resolve the crowded field.

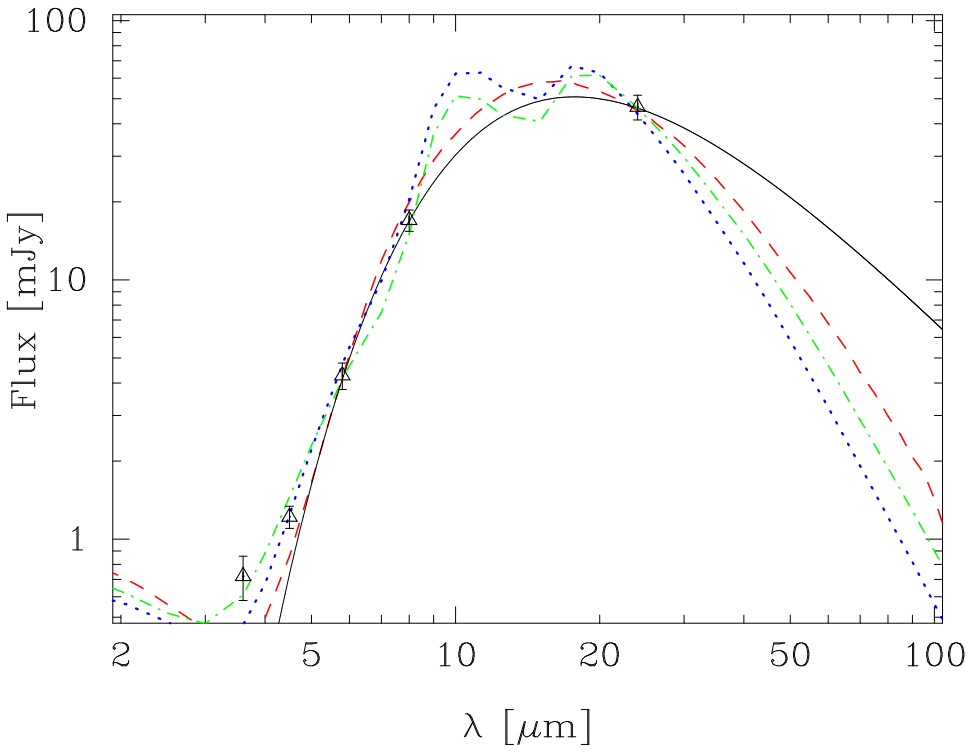

Figure 4.7: The measured day-600 *Spitzer* 3.6–24 μm fluxes for SN 2002hh are shown as open triangles. The solid black line is a 290 K blackbody normalised to the 8-μm flux density. The dashed, dotted, and dash-dotted lines correspond to radiative transfer dust models of differing input parameters, discussed in Barlow et al. (2005)

Barlow et al. (2005) found that the day 600 5.8–24μm flux distribution could be fitted by a 290 K blackbody (Figure 4.7), yielding a minimum emitting radius of $R_{min} \sim 10^{17}$ cm and a luminosity of $L = 1.6{\times}10^{7}$ $L_{\odot}$. A more realistic λ^{-1} grain emissivity gave $R_{min} = 5{\times}10^{17}$ cm, far too large for the emitting dust to have formed in the main ejecta (it would have taken > 10 years for material in the ejecta to reach this radius). It was therefore inferred that the emitting dust must have been pre-existing.

Using radiative transfer models (MOCASSIN, Ercolano et al. 2003, 2005; and 2-Dust, Ueta & Meixner 2003) with realistic dust grain parameters, fits to the observed day 600 5.8–24μm flux distribution (Figure 4.7) yielded total emitting dust masses in the range 0.10–0.15 $M_{\odot}$. SN 2002hh is a Type II-P (plateau) supernova, whose very extended optical light curve (Welch et al. 2007) appears explicable in terms of a just-resolved light echo that has been revealed from *HST* ACS/HRC images. Preliminary analysis indicated that the visible light echo occurred from a thick dust distribution that is located about 2–8 light years (2–8 $\times 10^{18}$ cm) in front of the supernova.

From an analysis of similar *Spitzer*-IRAC photometry from days 590–994, Meikle et al. (2006) concluded that most of the strong mid-IR emission was likely to have originated in a cool, obscured star-formation region or molecular cloud along the line of sight. Their work did reveal a declining component of the flux that was consistent with an IR echo due to circumstellar material illuminated by the SN flash, for which they estimated a dust mass of $\sim 0.04\,M_{\odot}$ using analytic models. Small contributions from newly-condensed ejecta dust and/or an ejecta-CSM interaction could not be ruled out, nor could the case that the IR echo could actually be due to the surrounding dense, dusty IS, rather than CS, material.

The observations of SN 2002hh presented in Chapter 3 showed that the emission at the position of the SN continued a slow decline until at least day 1158 (the 8-μm flux faded by a factor of ~ 1.5 between days 590–1158 - Section 3.6). Additional observations obtained in *Spitzer* cycles 3 and 4 (days 1383–2100; not presented here) show that emission at the SN position is still detected. Careful difference imaging is clearly required to isolate the declining component due to the SN within the complex field, to compare with the results of Meikle et al. (2006). The contribution of an IR echo to the declining emission can then be investigated, for example, with the 3D radiative transfer code, MOCASSIN, which has been updated since the work of Barlow et al. (2005) to only sum up the emission from an ellipsoidal region of the grid corresponding to the light travel time, as is necessary to model light echoes.

The minimum dust mass of $0.04\,M_{\odot}$ estimated from the analytic IR echo model of Meikle et al. (2006) to explain the declining component of the mid-IR emission for SN 2002hh, is considerably larger than the $\sim 10^{-3}\,M_{\odot}$ of directly observed ejecta dust inferred from studies of SN 1987A, SN 1998S and SN 1999em. If the $0.04\,M_{\odot}$ of dust corresponds to circumstellar dust that was formed in outflows of the CCSN progenitor in a previous mass-loss phase, then the massive-star progenitors of some CCSNe could make a significant contribution to the dust content of galaxies.

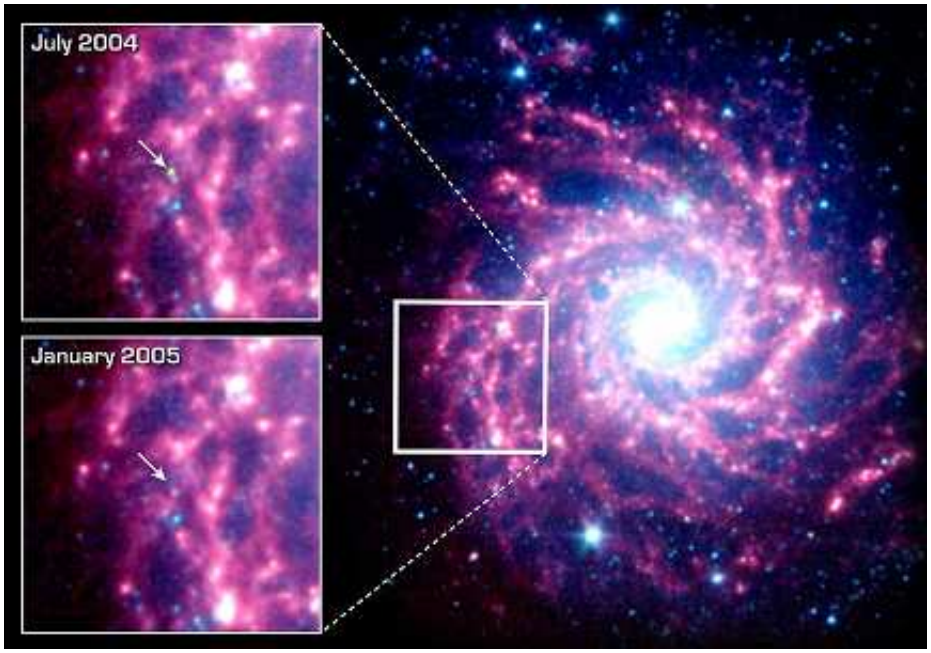

Figure 4.8: A *Spitzer* SINGS multi-band IRAC image of NGC 628, showing data from the 3.6-μm (blue), 4.5-μm (green), and 8-μm (red) channels. There was a clear detection of SN 2003gd on day 499 (upper inset; SN position indicated by the white arrow) relative to day 670 (lower inset). Image credit: NASA/JPL-Caltech/B.E.K. Sugerman, STScI.

4.4 SN 2003gd in NGC 628

Sugerman et al. (2006) detected the onset of dust emission from SN 2003gd in NGC 628 (Messier 74; Figure 4.8), utilising *Spitzer* SINGS and archival mid-IR data, together with SEEDS GMOS-N spectra, and archival optical photometry and spectroscopy. Unlike SN 2002hh, the emitting dust was inferred to have formed inside the supernova ejecta by the occurrence of three relatively contemporaneous phenomena: (1) an increase in optical extinction after day 500, as evidenced by the dip in its light curve from that date (Figure 4.9); (2) an IR excess, clearly evident from the *Spitzer* SINGS mid-IR data compared to the optical photometry at days 499 and 678 in Figure 4.10; and (3) asymmetric blue-shifted emission lines, attributed to dust forming in the ejecta preferentially extinguishing emission from receding (red-shifted) gas. Between days 157 and 521 the Hα feature in optical spectra of SN 2003gd developed an asymmetric profile, with a reduction in flux on the red side. All three phenomena had previously only been unambiguously observed in SN 1987A (Section 1.3.4 and references therein).

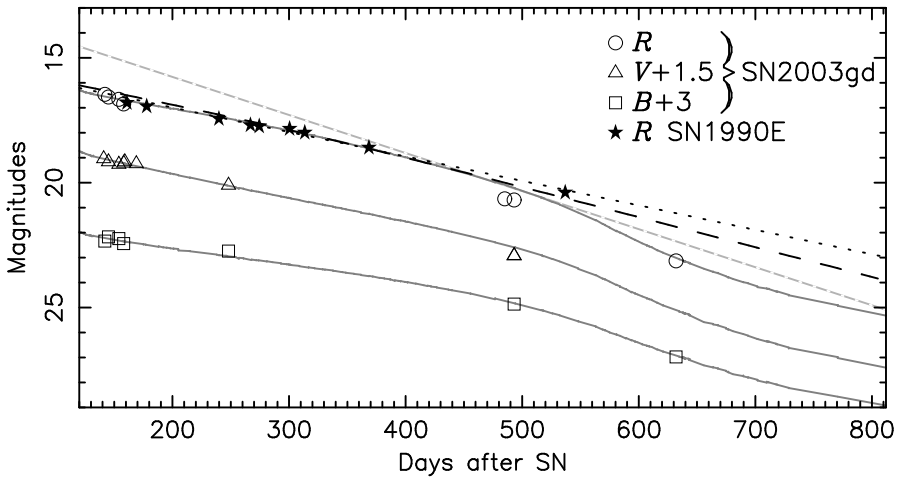

Figure 4.9: Optical *BVR* light curves of SN 2003gd (Hendry et al. 2005; Sugerman 2005), showing the increase of extinction with time. For comparison, the corresponding light curves of SN 1987A (Suntzeff & Bouchet 1990) are also shown as thick grey lines, and the *R*-band light curve of SN 1990E is shown as filled stars. Also plotted in black are the light curves expected from the energy deposition due to the radioactive decay of ^{56}Co with (dashed) and without (dotted) increased opacity to γ-rays. The dashed grey line shows a linear fit to SN 1987A from days 450 to 525 used by Lucy et al. (1991) (Sugerman et al. 2006).

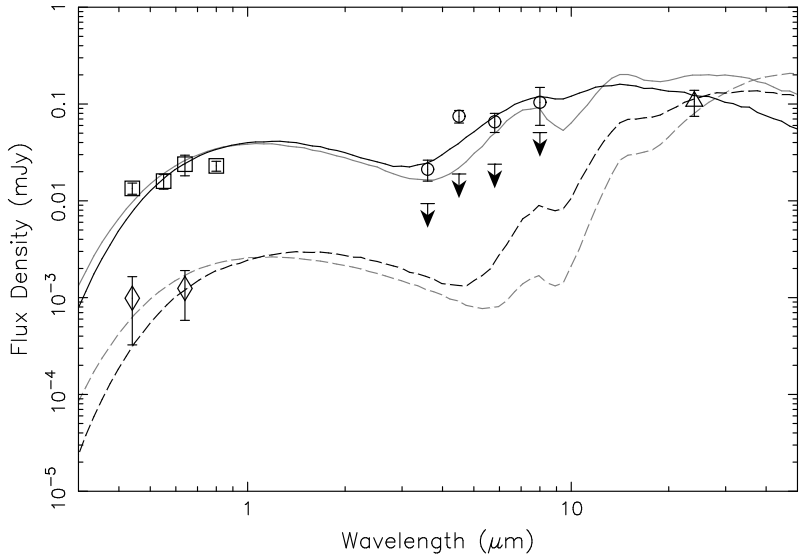

Figure 4.10: Optical–IR spectral energy distributions of SN 2003gd at ~499 and 678 days after explosion. The curves are MOCASSIN radiative-transfer model fits to the data at day 499 (solid lines) and 678 (dashed lines) based on smoothly distributed (black) and clumpy (grey) dust (Sugerman et al. 2006).

Both smooth and clumpy ejecta-dust model fits to the SN 2003gd observations were presented by Sugerman et al. (2006), using the 3D Monte Carlo radiative transfer code MOCASSIN (Ercolano et al. 2003, 2005; see Chapter 5, Section 5.9 for a brief overview of MOCASSIN and the dust model parameters in the context of those adopted for SN 2004et).

The radiative-transfer models were constructed under the initial assumption that the dust and source luminosity were mixed within a spherical, expanding shell with inner radius, $R_{\rm in}$ and outer radius $R_{\rm out} = YR_{\rm in}$. Initial values for the shell size, source luminosity, and temperature were guided by blackbody fits to the mid-IR data and by models of SN 1987A at similar epochs. A standard MRN $a^{-3.5}$ grain size distribution (Mathis et al. 1977) was adopted with $a_{\rm min}$=0.005 μm and $a_{\rm max}$=0.05 μm, and the adopted dust composition was 15 % amorphous carbon and 85 % silicates.

The smooth models adopted a dust distribution following an r^{-2} density profile, whereas the clumpy models had dense clumps existing in a less-dense interclump medium (ICM), where the ICM followed a smooth r^{-2} density distribution, with the local heating source located only in the ICM. The clumps had radius $\delta \times R_{out}$, a volume filling factor f, and density contrast $\alpha = \rho_c/\rho$, embedded in the ICM of dust density, ρ (defined above). Sugerman et al. (2006) explored the limiting case where all the dust was in clumps ($\alpha \rightarrow \infty$) to provide an upper limit to the dust mass, with the smooth models providing lower mass limits. As suggested from hydrodynamic simulations, they fixed $\delta = 0.025$.

To match both the optical–IR SEDs and the derived R-band extinction estimates for the SN ejecta, their day 499 data could be fitted with smoothly distributed dust having a dust mass of 2×10^{-4} M$_\odot$, whereas up to 2×10^{-3} M$_\odot$ of dust could be accommodated by a clumped dust model. For day 678, their best-fit smooth dust model required 3×10^{-3} M$_\odot$ of dust, while up to to 0.02 M$_\odot$ could be accommodated by a clumpy model, the latter implying heavy element condensation efficiency of about 10 %.

Meikle et al. (2007) also studied the mid-IR evolution of SN 2003gd from *Spitzer* observations, reanalysing the SINGS data from days 499 (IRAC) and 678 (MIPS 24 μm) studied by Sugerman et al. (2006), together with additional IRAC data from day 670 (PID: 3248, PI: Meikle) and MIPS data from day 1264 (PID: 30494, PI: Sugerman). From their analytic models, the authors concluded that by day 499 the mid-IR flux was consistent with emission from at least 4×10^{-5} M$_\odot$ of newly condensed dust in the ejecta. They also reported that the 24-μm emission at day 678 (with a flux $\sim 4\times$ larger than that measured by Sugerman et al. 2006) had faded beyond detection by day 1264. From consideration of the

SN ejecta velocities (implied by the size of the emitting region from a blackbody fit to the data) and the energy budget (the total bolometric luminosity of the SN compared to that expected from the radioactive decay deposition), Meikle et al. ruled out ejecta-condensed dust as the main source of the emission at days 670–678, concluding that the mid-IR observations of SN 2003gd did not support the presence of $0.02\,M_{\odot}$ of ejecta-condensed dust.

SEEDS analysis of the SN 2003gd data has continued, with two additional epochs of *Spitzer* observations (IRAC, PUI and MIPS) in Cycle 4. Collaborator B. E. K. Sugerman, has conducted precise difference imaging with the latest data (from which the SN had clearly faded beyond detection in all bands) confirming the results of Meikle et al. (2007) who concluded that the day 678 24-μm source had faded significantly by day 1264 and that the source was still detected by day 670 in IRAC 8-μm images. By day 1245, the 8-μm flux had also faded beyond detection. The most recent flux measurements, by B. Sugerman, for SN 2003gd were averaged results from difference images using the three most recent epochs of IRAC and MIPS data from cycles 3 and 4, and these, together with upper limits for the non-detections, were presented in Chapter 3 for epochs spanning 499–1632 days. The flux densities were consistent with my own measurements of the SN at days 499 and 670/678 from previous difference images (which used the IRAC and MIPS Cycle 3 data at days 1245–1264 as the reference frames) to within 5 %, and are reasonably consistent with the IRAC fluxes reported by Sugerman et al. (2006) and Meikle et al. (2007) for day 499 (to within 15 %), and with the 8-μm flux at day 670 (to within ∼ 20 %). Whilst investigating the discrepancy of the day 678 24-μm fluxes measured by both authors, a problem was discovered with the calibration of the enhanced SINGS data which showed incorrect exposure times in the FITS image headers. The MIPS BCD data was consequently downloaded from the *Spitzer* archive and reprocessed with MOPEX, by B. Sugerman. The average flux measurement from the three difference images was 543 μJy with an r.m.s. scatter of ∼ 4 %, much smaller than the 16 % calibration and statistical uncertainty quoted in Table 3.3. The new 24 μm flux at day 678, is a factor of 5 higher than that reported by Sugerman et al. (2006) and a factor of 1.4 higher than the value reported by Meikle et al. (2007), lending further weight to the energy budget argument of Meikle et al. that the 24-μm flux is unlikely to originate from ejecta-condensed dust. Circumstellar material causing the optical light echo detected around the SN (Sugerman 2005) was considered by Sugerman et al. (2006) to be an unlikely origin for the rapidly varying mid-IR fluxes,

however, this is now being revisited. With the revised fluxes, IR echo models are being investigated by the SEEDS team to quantify the possible contribution of a thermal IR echo from pre-existing CS material to the mid-IR emission detected at the earliest *Spitzer* epochs. It is emphasised that the day 499 observations of SN 2003gd are still consistent with the energy budget of the SN and with being due to ejecta dust.

It is concluded from the data presented by Sugerman et al. (2006) that there is strong evidence for dust formation in the ejecta of SN 2003gd by day 500, with dust mass estimates ranging up to $2 \times 10^{-3}\,M_{\odot}$ (Sugerman et al. 2006), although a contribution from an IR echo might reduce these estimates. This is similar to dust masses estimated for other CCSNe and suggests that Type II SNe are not significant producers of dust.

Chapter 5

SN 2004et in NGC 6946

5.1 Introduction

This chapter presents the analysis of multi-epoch observations of the Type II-P supernova SN 2004et. Mid-infrared imaging, with Michelle on Gemini-North and all three instruments of the *Spitzer Space Telescope*, was carried out over the years 2004 to 2008, supplemented by archival *Spitzer* data. The supernova's mid-IR detection was reported by Fabbri et al. (2005). The observations span 104 days prior to the supernova explosion to 1395 days post-explosion, providing a comprehensive picture of the evolution of this SN at these wavelengths. Further *Spitzer* photometry was obtained in IRAC channels at 3.6 and 4.5 μm in August 2009, January 2010 and August 2010 (days 1779, 1931 and 2151) during the observatory's 'warm' mission, and has been included for completeness. Section 5.2 provides a brief review of the literature to-date regarding this SN. Section 5.3 describes the Hα and [O I] 6300 Å line profiles obtained from a sequence of optical spectra for SN 2004et. Section 5.4 describes the mid-IR observations and data processing, and Section 5.5 details the photometric analysis techniques used. The resulting mid-IR fluxes are presented in Section 5.6, together with a discussion of the mid-IR light curve evolution.

Complementary photometric data, obtained by collaborators at optical and near-infrared (NIR) wavelengths using the *HST* and Gemini North telescopes, are presented in Section 5.7. The spectral energy distributions (SEDs) of SN 2004et at 12 epochs from days 64 to 1395 are discussed in Section 5.8, including blackbody fitting to the observed

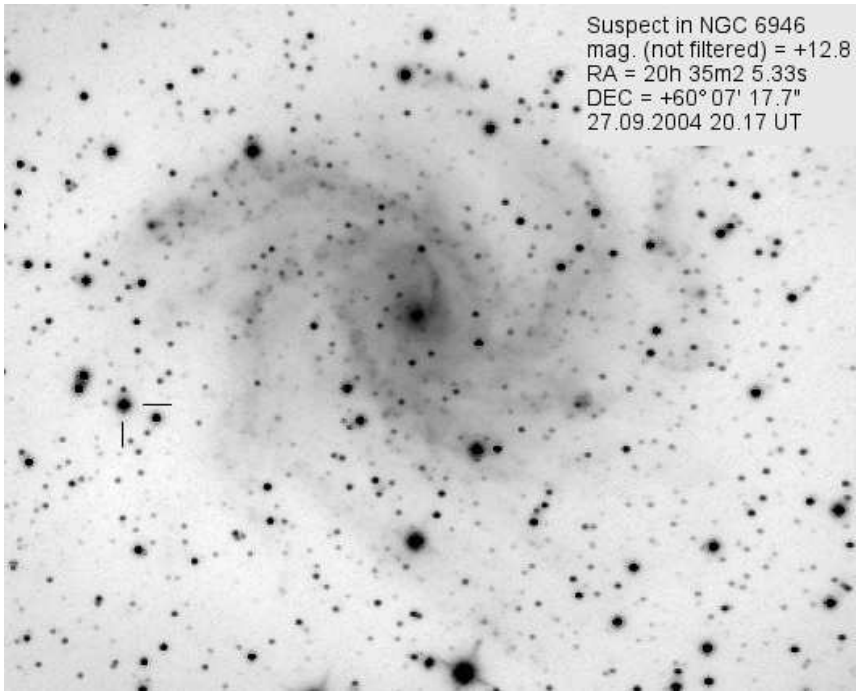

Figure 5.1: Discovery image of SN 2004et in NGC 6946 on 27 September 2004 by Stefano Moretti, taken with an unfiltered CCD on the 0.4-m ARAR telescope in Ravenna, Italy (adapted from http://www.supernovae.net/sn2004/n6946s1.jpg). The SN is seen south-west of the galaxy nucleus, marked by the cross-hairs.

SEDs, allowing limits to be placed on the physical properties of the SN at the various epochs. Section 5.9 describes the Monte Carlo radiative transfer models used to estimate how much new dust condensed in the ejecta between days 300 and 690. Finally, the results from the multi-epoch analysis of SN 2004et are summarised in Section 5.10. The implications for dust production by Type II SNe are also discussed. This work is the subject of a recently submitted paper (Fabbri et al. 2011).

5.2 Previous studies of SN 2004et

SN 2004et was the eighth supernova to be discovered in the nearby spiral galaxy NGC 6946 in the past century, and the second brightest (unfiltered magnitude 12.8) supernova detected in the year 2004.

5.2.1 Discovery and explosion date

The SN was discovered on 27 September 2004 by S. Morreti with a 0.4-m telescope (Zwitter et al. 2004). The reported position of $\alpha = 20^{\,h}35^{\,m}25^{\,s}.33$ and $\delta = +60^{\,h}07^{\,m}17^{\,s}.7$ (J2000.0) is 247.″1 east and 115.″4 south of the nucleus of its host galaxy. Figure 5.1 shows Moretti's discovery image of the supernova. Frequent survey imaging around this time by the robotic TAROT telescope at l'Observatoire de Haute Provence by Klotz and collaborators (Yamaoka et al. 2004) allowed the explosion date of SN 2004et to be well-constrained to within one day. Following Li et al. (2005*b*), an explosion date of 22.0 September 2004 (JD 2,453,270.5) is adopted as the day 0 epoch to which the observation dates herein are referenced.

5.2.2 Optical observations and SN type

High-resolution optical spectroscopy, taken with the echelle spectrograph on the 1.82-m telescope in Asiago on 28 September 2004, showed a relatively featureless spectrum with very broad, low-contrast Hα emission, suggesting SN 2004et to be a Type II event (Zwitter et al. 2004). This was subsequently confirmed by a low-resolution spectrum taken with the Shane 3-m telescope at the Lick Observatory on 1 October 2004 (Filippenko et al. 2004). The spectrum showed the P-Cygni profile of Hα to be dominated by the emission component, but the other hydrogen Balmer lines to have more typical P-Cygni profiles. The continuum was quite blue but dropped off dramatically shortwards of 4000 Å.

Further observations of the supernova were made in the Johnson-Cousins *U*BVRI system with the 0.76-m Katzman Automatic Imaging Telescope (KAIT) at the Lick Observatory, from day 8 after explosion to around day 25 (Li et al. 2005*b*). The *V*, *R* and *I*-band light curves showed SN 2004et to be a Type II-P (plateau) supernova, but it did exhibit some differences when compared with the typical Type II-P SN 1999em. Evolution was slower in the *U* and *B* bands, consistent with the $(U-B)$ and $(B-V)$ colour evolution, leading Li et al. (2005*b*) to conclude that SN 2004et seemed to evolve more slowly than SN 1999em, especially in the violet part of the spectrum.

Extensive photometric and spectroscopic monitoring in the optical was carried out by Sahu et al. (2006) from days 8 to 541 after explosion, with the 2-m Himalayan Chandra Telescope (HCT) of the Indian Astronomical Observatory. They confirmed the supernova to be of Type II-P based on the plateau observed in the *VRI* bands which lasted for ~ 110

days after the explosion. From their light curve analysis, they determined that the SN was caught at a very early stage soon after the shock breakout, reaching a maximum B-band magnitude ~ 10 days after explosion. They noted that SN 2004et was among the brighter Type II-P SNe based on the luminosity at maximum. They also confirmed the slower colour evolution of SN 2004et compared with other Type II-P SNe, particularly of the $(U-B)$ and $(B-V)$ colours, with the trend lasting until ~ 150 days after explosion, and the $(R-I)$ colour appearing bluer than that of SN 1999em even after day 200. They found that the decline rate of the light curve during the early nebular phase (~ 180–310 days) was similar to the radioactive decay rate of ^{56}Co, indicating that γ-ray trapping was efficient during this time (see Section 5.2.4). A steepening of the decline rate from around day 320 was interpreted by Sahu et al. (2006) as due to dust formation in the SN ejecta, after analysis of the emission lines at a similar epoch – see Section 5.2.8 for further discussion. Misra et al. (2007) also presented optical data from days ~ 14 to 470, with light curves and colour evolution similar to those presented in earlier studies (Li et al. 2005*b*; Sahu et al. 2006).

5.2.3 Distance and reddening

There are many estimates in the literature for the distance to the host galaxy NGC 6946. Sahu et al. (2006) summarised a few of these and included the result from their own analysis of SN 2004et using the standard candle method of Nugent et al. (2006) for Type II-P supernovae, deriving an average distance of 5.6 Mpc. Herrmann et al. (2008) estimated a distance of 6.1 ± 0.6 Mpc to NGC 6946 using the planetary nebula luminosity function. For consistency with previous studies of SN 2002hh (Barlow et al. 2005; Welch et al. 2007) and SN 2008S (Wesson et al. 2010) by the SEEDS collaboration, a distance of 5.9 Mpc to NGC 6946 is adopted for the analysis of SN 2004et in this thesis, as estimated by Karachentsev et al. (2000) from the brightest stars method.

From Schlegel et al. (1998), the foreground Galactic reddening towards SN 2004et is estimated to be $E(B-V) = 0.34$ mag. Zwitter et al. (2004) used the equivalent width of Na I D 2 lines from their high-resolution echelle spectra to estimate a total reddening (Galactic + host) towards the SN of $E(B-V) = 0.41$ mag. Sahu et al. (2006) used similar analysis with their lower-resolution spectra to obtain a comparable value of $E(B-V) = 0.43$ mag. A total reddening of $E(B-V) = 0.41$ mag is adopted for the analysis of SN 2004et in this thesis.

5.2.4 Ejected nickel mass

Three methods have been used in previous studies to estimate the amount of ^{56}Ni ejected during the explosion of SN 2004et, with generally consistent results: the tail phase bolometric luminosity method of Hamuy (2003), the steepness parameter method of Elmhamdi, Chugai & Danziger (2003*a*), and a comparison of the bolometric luminosity with that of SN 1987A.

From the first method, the ^{56}Ni mass can be estimated using the assumption that the early (150–300 days post-explosion) tail luminosity of Type II-P SNe is dominated by the radioactive decay of ^{56}Ni to ^{56}Co (Hamuy 2003). Using a bolometric correction of Hamuy et al. (2001) of 0.26 ± 0.06 mag and the V magnitudes during the nebular phase (250–315 days), Sahu et al. (2006) estimated that 0.06 ± 0.02 $M_\odot$ of ^{56}Ni was synthesised during the explosion of SN 2004et. In a similar way, Misra et al. (2007) estimated an ejected ^{56}Ni mass of 0.06 ± 0.03 $M_\odot$ for SN 2004et from two different points in the radioactive tail of the light curve. In recent work by Maguire et al. (2010), application of the same method with their own derived bolometric correction of 0.33 ± 0.06 mag, yielded a nickel mass of 0.06 ± 0.02 $M_\odot$, in good agreement with the previous studies.

For the second method, Elmhamdi et al. (2003*a*) showed a correlation between the rate of decline from the plateau to tail phase of the V-band light curve and the nickel mass, such that the smaller the mass of ^{56}Ni, the steeper the transition from plateau to tail. Despite the lack of good V-band data coverage at this light curve transition region for SN 2004et, Sahu et al. (2006) use this method to estimate a ^{56}Ni mass of 0.062 ± 0.02 $M_\odot$, compared to 0.056 ± 0.016 $M_\odot$ from Misra et al. (2007) and 0.057 ± 0.02 $M_\odot$ from Maguire et al. (2010).

Finally, Sahu et al. (2006) compared the bolometric light curve of SN 2004et with that of SN 1987A, assuming that the γ-ray deposition for both SNe was the same. They found the tail bolometric luminosity of SN 2004et between days ∼250–300 to be ∼1.6 times fainter than that of SN 1987A, implying a ^{56}Ni mass of 0.048 ± 0.01 $M_\odot$ for SN 2004et, for a nickel mass of SN 1987A of 0.075 ± 0.005 $M_\odot$ (Arnett 1996). However, they note that this should be a lower limit since their bolometric light curve did not include a NIR contribution. Maguire et al. (2010) adopted a similar method, comparing bolometric luminosities between days ∼ 120–250, which included NIR data, to estimate a ^{56}Ni mass of 0.057 ± 0.03 $M_\odot$.

5.2.5 Radio observations: ejecta asymmetry and interaction with CSM

SN 2004et was detected at radio frequencies (22.46 and 8.46 GHz) with the Very Large Array by Stockdale et al. (2004) on 5.128 October 2004 (day 13). The radio position of $\alpha = 20^{\rm h}35^{\rm m}25\overset{\rm s}{.}36$ and $\delta = +60^{\rm h}07^{\rm m}17\overset{\rm s}{.}7$ (J2000.0, $\pm$ 0.″1 in each coordinate) was in very close agreement with the reported optical position. Radio monitoring (at 4.99 and 6.04 GHz) was carried out from days 8 to 130 with the Multi-Element Radio Linked Interferometer Network (MERLIN) (Beswick et al. 2004; Argo et al. 2005).

Very-long-baseline-interferometric imaging (the first VLBI observations of a Type II-P supernova) at 8.4 GHz on 20 February 2005 (day 151) showed a clear asymmetry of the radio emitting structure, implying interaction with circumstellar material (Martí-Vidal et al. 2007). The preferred emission model was one of an underlying expanding shell with two hot spots, attributed to anisotropies of the circumstellar density distribution and/or anisotropies in the magnetic field.

Chevalier et al. (2006) modelled the radio light curve, comparing synchrotron and Compton cooling models with observations. They estimated a mass-loss rate of $\dot{M}_{-6}/v_{w1} = (9-10)T_{cs5}^{3/4}$, where $\dot{M}_{-6}$ is the mass-loss rate in units of $10^{-6}\,M_\odot\,{\rm yr}^{-1}$, v_{w1} is the wind velocity in units of $10\,{\rm km\,s}^{-1}$, and T_{cs5} is the circumstellar temperature in units of 10^5 K. Misra et al. (2007) reported one epoch of radio observations on day 102 (1.4 GHz) which had a flux in reasonable agreement with the models of Chevalier et al. (2006).

5.2.6 X-ray observations

Rho et al. (2007*b*) reported the X-ray detection of SN 2004et at days 30, 45 and 72 after explosion from archival *Chandra X-Ray Observatory* data. Rho et al. (2007*a*) modelled the emission in terms of the interaction of the supernova ejecta with a progenitor wind, arising from the reverse-shock region, with a pre-supernova mass-loss rate of (2–2.5) $\times 10^{-6}$ $M_\odot\,{\rm yr}^{-1}$ for a wind velocity of $10\,{\rm km\,s}^{-1}$. This is consistent with the mass-loss rate expected for a progenitor star of mass (15–20) $M_\odot$ (Chevalier et al. 2006). The same *Chandra* observations were also presented by Misra et al. (2007) who noted that the X-ray spectrum softens with time and demonstrated that its luminosity is well characterised by $L_X \propto t^{-0.4}$. Similarly to Rho et al. (2007*a*), they concluded that the majority of the detected X-ray emission was due to the reverse shock. They found that the hard (2–8 keV) X-ray band luminosity approximately followed the expected evolution of free-free emis-

sion from the reverse shock, but that the soft (0.5–2 keV) X-ray band luminosity stayed roughly constant. From the observed hard band X-ray luminosity they estimated a progenitor mass-loss rate of $\sim 2 \times 10^{-6}$ $M_\odot$ yr^{-1} for an assumed wind velocity of 10 km s^{-1}, in agreement with Rho et al. (2007*a*).

5.2.7 Properties of the progenitor star

Sahu et al. (2006) found that the [O I] 6300, 6363 Å luminosity before dust formation was comparable to that of SN 1987A at similar epochs, implying a progenitor mass of $\sim 20\,M_\odot$. Chevalier et al. (2006) also estimated a progenitor mass of $\sim 20\,M_\odot$ from their comparison of the radio light curve to Compton- and synchrotron-dominated cooling models.

Based on the plateau luminosity and duration, and the mid-plateau expansion velocity, Sahu et al. (2006), Misra et al. (2007) and Maguire et al. (2010) have estimated explosion energies for SN 2004et in the range (0.88–1.2)$\times 10^{51}$ erg. From these calculations of the explosion parameters, using the hydrodynamic models of Litvinova & Nadezhin (1985), Misra et al. (2007) also estimate a progenitor mass of $\sim 20\,M_\odot$, consistent with previous estimates.

A candidate progenitor star for SN 2004et was reported by Li et al. (2005*a*,*b*) from pre-explosion optical images with the Canada-France-Hawaii Telescope. Through comparison with stellar evolutionary models, Li et al. (2005*b*) identified the source as a *yellow* supergiant star with a zero-age main-sequence mass of 15^{+5}_{-2} $M_\odot$. This was unusual as progenitors of normal Type II-P were expected to be red, not yellow, supergiants. However, Crockett et al. (2009) found that the same candidate progenitor star was still visible ~ 3 years after explosion. Their late time high-resolution NIR imaging with Gemini-North adaptive optics, together with archival *HST*-WFPC2 and NICMOS data, revealed that the candidate progenitor star was comprised of at least 3 distinct sources. Crockett et al. (2009) reported the discovery of the unresolved progenitor as an excess of flux in a deep pre-explosion *i*′-band image of NGC 6946 with the Isaac Newton Telescope Wide Field Camera. After accounting for the late-time contribution of the SN using published optical spectra, they determined the progenitor was most likely to be a late K to late M-type supergiant with an initial mass of 8^{+5}_{-1} $M_\odot$, much lower than the previous mass estimates from hydrodynamical modelling.

5.2.8 Evidence for dust production

From their spectroscopic observations, Sahu et al. (2006) showed the temporal evolution of the oxygen doublet [O I] 6300, 6363 Å and Hα line profiles from days 277 to 465, highlighting a blueshift in the emission peak of both, and a flattening of the Hα emission peak, beyond day 300. This, together with a steepening of the light curve after day $\sim$ 320, they interpreted as indications of early dust formation in the ejecta of SN 2004et. Misra et al. (2007) also found that rate of decline in the optical light curves had accelerated between $\sim$ 320–386 days.

Fabbri, Sugerman & Barlow (2005) reported the day 64 detection of SN 2004et in all four *Spitzer* IRAC bands, from 3.6 to 8.0 μm, in SINGS Legacy program archival images of NGC 6946 (see Section 5.4).

At the time of completing the mid-IR studies of SN 2004et discussed in the following sections of this thesis, similar work was presented by Kotak et al. (2009). They presented their own and archival *Spitzer* mid-IR observations of SN 2004et obtained between days 64 and 1406, together with late-time optical spectra. They concluded that:

- For days 300–795, the spectral energy distribution was comprised of three components – hot, warm and cold – each respectively due to emission from: optically thick gas; newly-formed, ejecta-condensed dust; and an IR echo from the interstellar medium of the host galaxy.

- The mass of dust formed in the ejecta grew to a few times $10^{-4}\,M_{\odot}$, located in co-moving clumps of fixed size. From their *Spitzer* IRS spectra, they reported the first spectroscopic evidence of silicate dust formed in the ejecta of a supernova, supported by the detection of strong but declining molecular SiO emission in the 8 μm region.

- After about 2 years post-explosion, the appearance of broad, box-shaped optical emission line profiles was due to the impact of the ejecta on the circumstellar medium of the progenitor star, resulting in the formation of a cool, dense shell to which they attributed responsibility for a later rise in the mid-IR emission from SN 2004et.

The work of Kotak et al. (2009) is compared to our own as appropriate throughout this chapter.

Maguire et al. (2010) reported optical and NIR photometric and spectroscopic observations of SN 2004et carried out from just after explosion to +500 days. Their NIR spectrum at day 306 showed a clear detection of the first overtone band of CO at ~ 2.3 μm, which they interpreted as being a signature of dust formation. By analysing the optical light curves in the early nebular phase, they found that the *BVR* decline rates between days ~ 136 and 296 were consistent with those expected from light curves powered by the radioactive decay of ^{56}Co (assuming complete γ-ray trapping). However, between days ~ 296 and 414 they found that these decline rates had steepened. They also noted a significant blueshift in the peak of the Hα emission line from days ~ 300 to 464, in agreement with the results of Sahu et al. (2006). These results were interpreted as signatures of dust formation occurring post 300 days. Their presentation of very late time (> 1000 days) photometry showed a flattening of the optical and NIR light curves, which they mainly attributed to the interaction of the SN ejecta with the circumstellar medium (CSM), following the work of Kotak et al. (2009).

5.3 Optical spectroscopy of SN 2004et

In addition to the photometric data of SN 2004et presented in this chapter, optical spectroscopy was also obtained as part of the SEEDS program. The observations, data processing and measurements were carried out by SEEDS collaborator, J. Gallagher (University of Cincinnati), but interpretation of these data is my own work for this thesis. For clarity, my interpretation is noted as "*THIS WORK*" in the following section.

The Gemini Multi-Object Spectrograph on Gemini-North (GMOS-N) was used to observe SN 2004et as part of program GN-2005B-Q-54 (PI: G. Clayton), on 5 August and 31 October 2005, corresponding to 317 and 404 days after explosion. A log of these and the other Hα-region observations analysed here can be found in Table 5.1. The GMOS-N observations used a 0.″75 slit width and the B600-G5303 grating in long-slit mode with a position angle of 296°. Three spectra were obtained during each epoch with identical exposure times of 900 s. The central wavelength of the images were 5950, 5970, and 5990 Å, respectively, to allow for gap removal of the combined spectra. A 2×2 binning of the CCD pixels in the low gain setting was employed. All spectra were taken with adjacent GMOS baseline calibration flat exposures to correct for sensitivity gradients across the CCD, and CuAr spectra were utilised for the initial calibration of the dispersion solution.

Table 5.1: Log of optical spectroscopic observations of SN 2004et from the SEEDS collaboration (GMOS-N, PI: Clayton), from the authors Sahu et al. (2006) and from online archives (TNG and Subaru).

Date	Age [days]	Telescope/ instrument	Wavelength range [Å]	Exp. time	Program ID	Principal Investigator
2005-06-07	259	HCT HFOSC[a]	3500–7000; 5200–9200	1×900 s	–	S06
2005-08-01	314	HCT HFOSC[a]	3500–7000; 5200–9200	1×900 s	–	S06
2005-08-05	317	Gemini GMOS-N	3500–10000	3×900 s	GN-2005B-Q-54	G. Clayton
2005-08-29	336	TNG LRS[b]	3890-8000	1×1800 s	AOT12 CAT-G109	E. de la Rosa
2005-10-17	391	HCT HFOSC[a]	3500–7000; 5200–9200	1×900 s	–	S06
2005-10-31	404	Gemini GMOS-N	3500–10000	3×900 s	GN-2005B-Q-54	G. Clayton
2005-11-23	428	HCT HFOSC[a]	3500–7000; 5200–9200	1×900 s	–	S06
2006-06-30	646	Subaru FOCUS[c]	4670-8970	2×900 s	S06A-152	K. Kawabata

[a] Raw data, including calibration frames and flux standards, provided by the authors of Sahu et al. (2006, S06).
[b] Raw and calibration data were downloaded from the online TNG archive at http://ia2.oats.inaf.it/.
[c] Raw and calibration data downloaded from the online Subaru Mitaka Okayama Kiso Archive (SMOKA) at http://smoka.nao.ac.jp/index.jsp.

The GMOS-N spectra were reduced using the Gemini IRAF package. Pipeline processed calibration images were obtained from the Gemini Science Archive. The spectra were trimmed and then overscan, bias and flat-field corrected using the task `gsreduce`. Wavelength calibration solutions were determined from the CuAr lamp spectra using `gswavelength`, and the solution was applied to the SN 2004et spectra via `gstransform`. Object spectra were extracted using `gsextract`. The observations were not flux calibrated since the primary goal was to monitor the evolution of the line profiles.

Sahu et al. (2006) [hereafter S06] presented photometric and spectroscopic data for SN 2004et from approximately 8 to 541 days after the explosion. Their results showed a shift to the blue of the central peak of both Hα and [OI] 6300,6364 Å at late times. They concluded that this was indicative of new dust formed in the ejecta of SN 2004et. However, comparisons between the Hα profiles in our GMOS-N spectra and those at similar epochs in the archived calibrated spectra of S06, obtained from the *Online Supernova Spectrum Archive (SUSPECT)*[1], showed some inconsistencies, with their spectra showing clear blueshifting of the Hα emission line profile between days 314 and 391, while our own spectra showed little change between days 317 to 404. In order to rectify this discrepancy, the S06 authors generously provided their raw data for SN 2004et for several of the epochs presented in their paper. This allowed us to reduce the respective sets of data in the same way, with the exception that the standard routines within IRAF

[1] http://bruford.nhn.ou.edu/~suspect

(`ccdproc, apall, identify, dispcor`) were used rather than counterparts in the `gmos` package. The S06 data was obtained with the Himalaya Faint Object Spectrograph Camera (HFOSC) on the 2-m Himalayan Chandra Telescope (HCT) of the Indian Astronomical Observatory, Hanle, India. A description of the observational setup used by S06 can be found in their paper. We also obtained two archival spectroscopic observations of SN 2004et taken on days 336 and 646. The earlier epoch corresponds to an observation on 29 August 2005 taken with the DELORES (Device Optimized for the LOw RESolution; LRS for short) spectrograph on the 3.58-m Telecopio Nazionale Galileo (TNG) at Roque de Los Muchachos Astronomical Observatory in La Palma. The latter epoch corresponded to an observation on 30 June 2006 with the Faint Object Camera and Spectrograph (FOCUS) on the 8.2-m Subaru telescope on Mauna Kea in Hawaii. The reduction procedure matched that carried out by us for the GMOS-N and S06 spectra.

Since our goal was to self-consistently align a number of spectra taken with four different instrument/telescope setups, we did not rely solely on the initial wavelength calibrations. During the extraction of each SN spectrum, a sky spectrum was also extracted that was ultimately subtracted from the SN spectrum. Since the sky and SN spectra possessed identical wavelength calibrations, we derived corrections to the initial wavelength calibrations of each of the SN spectra using the strong and narrow [O I] 5577 Å and 6300 Å sky emission lines.

THIS WORK: The temporal evolution of the Hα profile between days 259 and 646, following the re-analysis of the combined set of spectra, is depicted in the left-hand panel of Figure 5.2. The spectra are displayed in velocity space, with the continua subtracted and the peaks of the emission line normalised to approximately unity. The dashed line at 0 km s^{-1} corresponds to the rest wavelength of Hα at 6562.8 Å (the radial velocity of the host galaxy NGC 6946 is +40 km s^{-1}, Epinat et al. 2008). The inset shows a close-up view of the earliest and latest Hα profiles, obtained just over a year apart at days 259 and 646, to highlight the overall blueshifting of the profile during this time. The dashed lines in the inset indicate the line peak centres measured (*by SEEDS collaborator J. Gallagher*) on days 259 and 646, with the blueshifting of the latter profile providing strong evidence for the formation of dust in the ejecta during the intervening period, as described by Lucy et al. (1989) for SN 1987A.

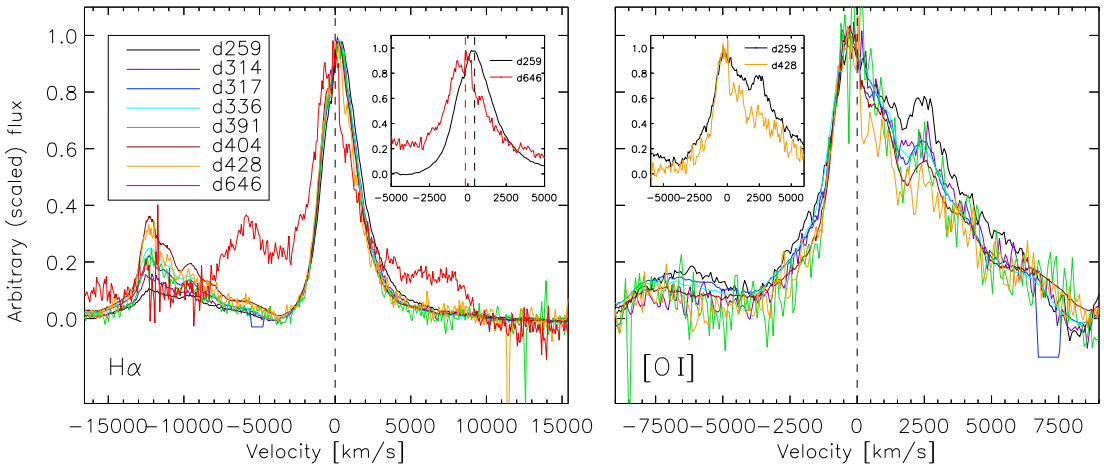

Figure 5.2: The Hα and [O I] profile evolution. The left-hand panel shows the Hα spectra from days 259–646, with the normalised continua subtracted to a zero-level and the peaks of the emission line normalised to unity. The dashed vertical line in the main plot corresponds to the rest wavelength of Hα (NGC 6946 has a radial velocity of +40 km s^{-1}). The inset shows a comparison of the earliest and latest Hα spectra, obtained just over a year apart, to highlight the blueshifting ($\sim$ 600 km s^{-1}) during this interval. The dashed lines in the inset plot indicate the measured line centres. The right-hand panel shows the evolution of the [O I] 6300 Å profile from days 259 to 428. The dashed line in the main plot indicates the rest velocity of the 6300 Å line. The emission feature in the red wing corresponds to the [O I] 6363 Å line. The spectra from days 259, 314, 391 and 428 are from S06 (raw data kindly provided by the authors and calibrated by us). The spectra from days 317 and 404 are SEEDS GMOS-N observations, and those from days 336 and 646 are archival TNG-LRS and Subaru-FOCUS spectra respectively. The earliest spectra have higher signal-to-noise and a lack of intrinsic structure, particularly compared to the Subaru-FOCUS spectra at day 646.

The Hα line profiles presented by Sahu et al. (2006) showed a significant blueshifting with time of the emission peak, amounting to a few hundred km s^{-1} with the largest shift appearing to occur between days 277 and 314. Sahu et al. (2006) did not quantify the shifts in their Hα profiles, beyond stating that a blueshift in the emission peak was clearly seen beyond day 300 in their day 277–465 Hα (and [O I] 6300,6364 Å) profiles. Kotak et al. (2009) confirmed this from their own analysis of the Sahu et al. (2006) spectra, reporting a shift of -400 km s^{-1} in the whole Hα profile between days 301 and 314, but little sign of a progressive blueshift in the subsequent day 314–465 period. Using the Sahu et al. (2006) spectra, along with additional spectra, Maguire et al. (2010) found that the peak of the Hα emission line was at $+280 \pm 50$ km s^{-1} between days 163 and 300, but from days 314 to 464 showed a constant blueshift to -137 km s^{-1}.

The recalibrated spectral dataset was used to measure the wavelength of peak Hα emission in each of the profiles plotted in panel (a) of Figure 5.2. The evolution of the peak wavelength is shown in Figure 5.3. The Hα line peaks show an overall blueshifting between days 259 and 646 of $\sim$ 13.2 Å, corresponding to a velocity shift of ~ -600 km s^{-1}.

Between days 259 and 314 we measured an initial blueshift of ~ 3 Å ($\approx 140\,\mathrm{km\,s^{-1}}$), not as large as the $400\,\mathrm{km\,s^{-1}}$ shift between days 301 and 314 measured by Kotak et al. (2009) from the Sahu et al. (2006) spectra in the *SUSPECT* archive. While we find little change between days 314/317 and day 391 in the measured emission line peaks in the recalibrated spectral dataset (Figure 5.3), between days 404 and 428 we measured a blueshifting of the emission peak by ~ 4 Å ($185\,\mathrm{km\,s^{-1}}$), followed by a further blueshifting of ~ 4.5 Å ($205\,\mathrm{km\,s^{-1}}$) between the spectra obtained at days 428 and 646. We therefore find that the majority of the blueshifting occurred after day 391.

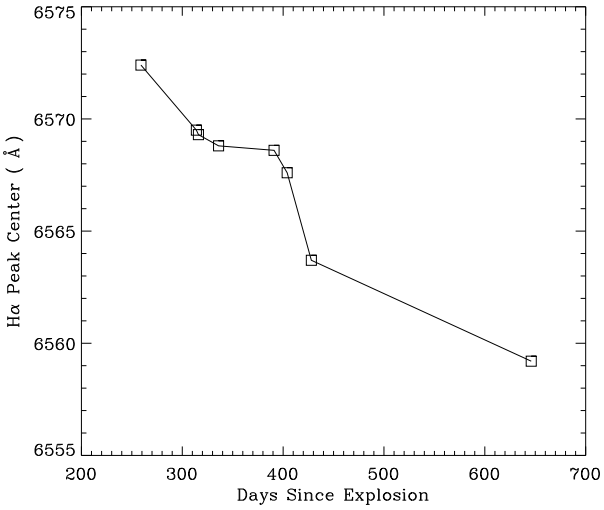

Figure 5.3: The evolution with time of the measured wavelength of the Hα emission peak of SN 2004et.

Whilst there is no strong evidence for a developing line asymmetry in the earlier epoch Hα profiles (Figure 5.2), a diminution of the red wing can be discerned by days 428 and 646. By day 646 a significant blueshifting (~ 4.5 Å) of the whole profile since day 428 is evident, with multiple peaks evident at the centre of the profile, although there are earlier inflections in the blue wing of the Hα profiles. Two broad features either side of the main emission line (at $\sim +7000$ and $-6000\,\mathrm{km\,s^{-1}}$) have appeared by day 646. Kotak et al. (2009) presented three later optical spectra of SN 2004et, obtained with the Keck telescopes on days 823, 933 and 1146, which show similarities to, and a development of, the Subaru day 646 Hα profile. They described the Hα profile from the late-time Keck spectra as having a steep-sided, box-like component, with a half width at zero intensity (HWZI) of $8500\,\mathrm{km\,s^{-1}}$ and noted that the characteristic ejecta profile of Hα seen in the S06 spectra may still be present at days 823 and 933, with a HWZI of $\sim 2000\,\mathrm{km\,s^{-1}}$, but that its presence at day 1146 is less certain.

The 6300 and 6363 Å lines of [O I] can be seen in emission on the blue side of the Hα profiles plotted in Figure 5.2. The right-hand panel of Figure 5.2 displays the [O I] 6300 Å velocity profiles for days 259–428 (the day 646 profiles had too low a signal to noise). The inset compares the day 259 and day 428 [O I] profiles, showing a clear diminution of the red wing of the day 428 profile relative to day 259.

5.4 Mid-infrared observations and data processing

5.4.1 Gemini-Michelle and *Spitzer* photometry

NGC 6946, the host galaxy of SN 2004et, was observed with the *Spitzer Space Telescope* by the SINGS Legacy program (Kennicutt et al. 2003) between June and November 2004, such that the region of the SN was serendipitously imaged pre- and post-explosion.

As explained in Chapter 3, Section 3.3.1, the SINGS Legacy program usually took two IRAC and MIPS images of each galaxy, separated by a minimum of 24 hours, in order to best correct for image artifacts. In the case of the IRAC observations of NGC 6946, the first of the two images was taken on 10 June 2004 (104 days prior to the SN explosion) but later that same day unforeseen problems caused the telescope to enter safe mode, ending observations scheduled for the rest of the week. These observations were re-scheduled and took place over 6 months later, with the second of the SINGS IRAC images of NGC 6946 being taken on 25 November 2004, 64 days after the explosion of the SN 2004et. Figure 5.4 shows the position of the SN in relation to its host galaxy NGC 6946 in the pre- and post-explosion SINGS IRAC images, together with a closer view of the SN region in the different IRAC wavebands. The first MIPS images of the galaxy were acquired by the SINGS program on 9 July 2004, 75 days before the SN exploded.

SN 2004et was clearly detected in the SINGS IRAC image at day 64 and was subsequently monitored with IRAC, MIPS and the IRS Peak-Up Imaging (PUI) module via our *Spitzer* GO programs during Cycles 2, 3, 4, 6 and 7. Cycle 6 was the beginning of the *Spitzer* 'warm' mission whereby, after cryogen depletion, the observatory operates using only the 3.6 and 4.5 μm IRAC channels. The sensitivity with these detectors was expected to remain unchanged from performance in the cryogenic mission. No other IRAC channels or *Spitzer* instruments were available for use in Cycles 6 or 7. Archival *Spitzer* data of the SN from Cycles 2 and 3 were also downloaded to provide a more complete time-sample of the SN's mid-IR evolution. In summary, post-explosion mid-IR observations

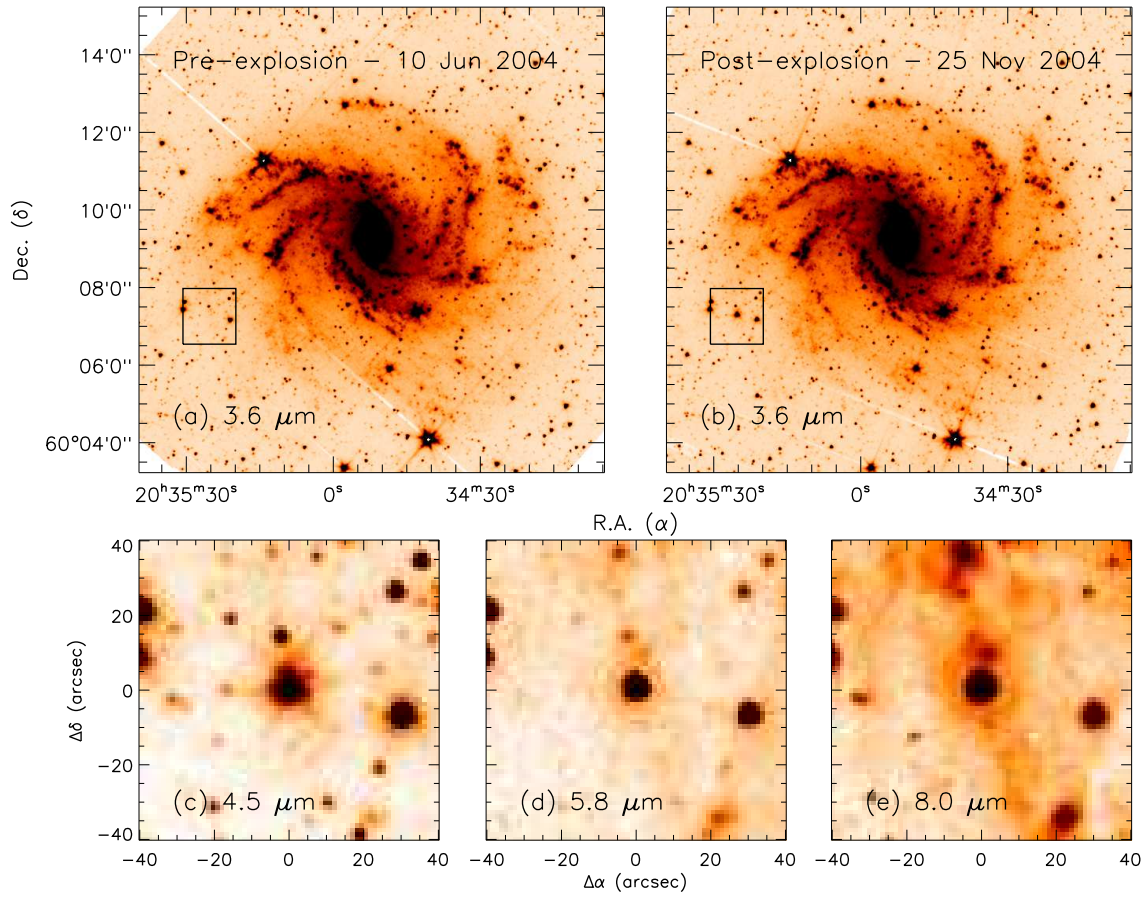

Figure 5.4: The position of SN 2004et in SINGS Legacy IRAC images of NGC 6946. Panels (a) and (b) show the whole galaxy at 3.6 μm pre- (day -104) and post-explosion (day 64) respectively. The square is centred on the SN coordinates, with the SN clearly evident at day 64. Panels (c), (d) and (e) zoom in on the square region of the SN field at 4.5, 5.8 and 8.0 μm respectively at day 64.

of SN 2004et were taken between November 2004 and August 2010, corresponding to an age range of 64 to 2151 days. With the *Spitzer Space Telescope*, there are 12 epochs of observations in each of the four IRAC wavebands, with a further three epochs of IRAC observations during the 'warm' mission in just the 3.6 and 4.5 μm channels. There are 8 epochs of IRS PUI observations at 16 μm, and 9 epochs of MIPS 24 μm observations. Of the 33 individual *Spitzer* observations listed in Table 5.2, the first 3 were obtained by the SINGS Legacy program, 5 were obtained by programs led by PIs Meikle and Kotak, and 25 were obtained by our SEEDS program.

In addition to the *Spitzer* mid-IR observations, complementary broad-band N' photometry at 11.2 μm was obtained with Michelle on Gemini-North during 2005, 2006, 2007 and 2008, consisting of 6 observations and corresponding to 4 epochs. A time-ordered list of all the *Spitzer* and Michelle mid-IR observations of SN 2004et is provided in Table 5.2.

Table 5.2: Summary of observations - Mid-infrared imaging of SN 2004et with the *Spitzer Space Telescope* and Gemini-North.

UT date	Age [days]	Detector	λ_{eff} [μm]	FoV [′ × ′]	Pixel scale [″/pixel]	Exp. time [s]	Ref.
2004-06-10	-104	IRAC	3.6/4.5/5.8/8.0	5.2 × 5.2	1.2	107.2	[1]
2004-07-09	-75	MIPS	24.0	5.4 × 5.4	1.5	161.5	[1]
2004-11-25	64	IRAC	3.6/4.5/5.8/8.0	5.2 × 5.2	1.2	107.2	[1]
2005-07-13	294	IRS-PUI	16.0	1.0 × 1.2	1.2	629.2	[2]
2005-07-19	300	IRAC	3.6/4.5/5.8/8.0	5.2 × 5.2	0.75	14.4	[3]
2005-07-30	311	Michelle	11.2 (N′)	0.5 × 0.4	0.1	1081.9	[4]
2005-08-03	315	MIPS	24.0	5.4 × 5.4	0.75	140.0	[3]
2005-09-17	360	IRAC	3.6/4.5/5.8/8.0	5.2 × 5.2	0.75	14.4	[3]
2005-09-24	367	MIPS	24.0	5.4 × 5.4	0.75	140.0	[3]
2005-11-02	406	IRAC	3.6/4.5/5.8/8.0	5.2 × 5.2	0.75	536.0	[2]
2005-12-22	456	IRS-PUI	16.0	1.0 × 1.2	1.2	629.2	[2]
2005-12-30	464	IRAC	3.6/4.5/5.8/8.0	5.2 × 5.2	0.75	14.4	[3]
2006-01-11	476	MIPS	24.0	5.4 × 5.4	0.75	140.0	[3]
2006-05-12	597	Michelle	11.2 (N′)	0.5 × 0.4	0.1	811.4	[5]
2006-05-14	599	Michelle	11.2 (N′)	0.5 × 0.4	0.1	376.3	[5]
2006-08-04	681	IRS-PUI	16.0	1.0 × 1.2	1.2	629.2	[6]
2006-08-13	690	IRAC	3.6/4.5/5.8/8.0	5.2 × 5.2	0.75	14.4	[7]
2006-09-01	709	MIPS	24.0	5.4 × 5.4	0.75	140.0	[7]
2006-09-10	718	IRS-PUI	16.0	1.0 × 1.2	1.2	56.6	[7]
2006-12-29	828	IRAC	3.6/4.5/5.8/8.0	5.2 × 5.2	0.75	124.8	[7]
2007-01-21	851	MIPS	24.0	5.4 × 5.4	0.75	420.0	[7]
2007-01-27	857	IRS-PUI	16.0	1.0 × 1.2	1.2	132.1	[7]
2007-06-26	1007	IRS-PUI	16.0	1.0 × 1.2	1.2	283.1	[7]
2007-07-03	1015	IRAC	3.6/4.5/5.8/8.0	5.2 × 5.2	0.75	321.6	[7]
2007-07-09	1020	Michelle	11.2 (N′)	0.5 × 0.4	0.1	1999.2	[8]
2007-07-10	1021	MIPS	24.0	5.4 × 5.4	0.75	420.0	[7]
2007-08-02	1044	IRS-PUI	16.0	1.0 × 1.2	1.2	283.1	[9]
2007-08-12	1054	IRAC	3.6/4.5/5.8/8.0	5.2 × 5.2	0.75	321.6	[9]
2007-08-27	1069	MIPS	24.0	5.4 × 5.4	0.75	420.0	[9]
2007-12-09	1173	IRS-PUI	16.0	1.0 × 1.2	1.2	283.1	[9]
2007-12-27	1191	IRAC	3.6/4.5/5.8/8.0	5.2 × 5.2	0.75	321.6	[9]
2008-01-07	1202	MIPS	24.0	5.4 × 5.4	0.75	420.0	[9]
2008-01-17	1212	IRS-PUI	16.0	1.0 × 1.2	1.2	1258.4	[10]
2008-06-21	1368	Michelle	11.2 (N′)	0.5 × 0.4	0.1	1928.6	[11]
2008-07-09	1386	Michelle	11.2 (N′)	0.5 × 0.4	0.1	2257.9	[12]
2008-07-18	1395	IRAC	3.6/4.5/5.8/8.0	5.2 × 5.2	0.75	321.6	[9]
2008-07-29	1406	MIPS	24.0	5.4 × 5.4	0.75	420.0	[9]
2009-08-06	1779	IRAC	3.6/4.5	5.2 × 5.2	0.75	1161.6	[13]
2010-01-05	1931	IRAC	3.6/4.5	5.2 × 5.2	0.75	1161.6	[13]
2010-08-13	2151	IRAC	3.6/4.5	5.2 × 5.2	0.75	1161.6	[14]

[1] *Spitzer* Cycle 1 SINGS Legacy program 00159, PI: Kennicutt.
[2] Archival data, *Spitzer* Cycle 2 GO program 20256, PI: Meikle
[3] This thesis, *Spitzer* Cycle 2 GO program 20320, PI: Sugerman.
[4] This thesis, Gemini semester 05A program GN-2005A-Q-20, PI: Barlow.
[5] This thesis, Gemini semester 06A program GN-2006A-Q-1, PI: Barlow.
[6] Archival data, *Spitzer* Cycle 3 GO program 30292, PI: Meikle.
[7] This thesis, *Spitzer* Cycle 3 GO program 30494, PI: Sugerman.
[8] This thesis, Gemini semester 07A program GN-2007A-Q-5, PI: Barlow.
[9] This thesis, *Spitzer* Cycle 4 GO program 40010, PI: Meixner.
[10] Archival data, *Spitzer* Cycle 4 GO program 40619, PI: Kotak.
[11] This thesis, Gemini semester 07B program GN-2007B-Q-4, PI: Barlow.
[12] This thesis, Gemini semester 08B program GN-2008B-Q-44, PI: Barlow.
[13] This thesis, *Spitzer* Cycle 6 GO program 60071, PI: Andrews. Cycle 6 took place during the *Spitzer* 'warm' mission following completion of the cryogenic mission. Only IRAC 3.6 and 4.5 μm channels were available, with expected sensitivity unchanged from performance in the cryogenic mission.
[14] This thesis, *Spitzer* Cycle 7 GO program 70008, PI: Andrews, *Spitzer* 'warm' mission.

The exposure time listed in the table is the total time spent observing on-source. The final column provides a key to the list of observing programs from which these data were obtained; the program number and principal investigator are detailed in a footnote to the table. Complimentary data retrieved from the archive are marked as such.

5.4.2 Data processing

The earliest *Spitzer* data of SN 2004et were those from the SINGS Legacy program. As described in Chapter 3, Section 3.4.2, the SINGS Legacy team produced enhanced data products which could be downloaded from the SINGS Legacy Data Deliveries section[2] of the SSC website.

The MIPS 24 μm mosaic of NGC 6946 (providing the pre-explosion image of SN 2004et at day -75) were downloaded from the SINGS fifth and final data delivery in this way. The mosaic was created from multiple *Spitzer* images obtained in scan-mapping mode over two days (75 and 73 days prior to the explosion of SN 2004et), and processed with the MIPS Data Analysis Tool version 3.06 (Gordon et al. 2005), along with additional custom processing by the SINGS team. An outline of the processing steps they carried out is given in Chapter 3, Section 3.4.3.

However, the enhanced SINGS IRAC data were not used due to the unusually long time span between the two observations of NGC 6946 (~ six months, compared to the usual one or two days) which were combined by the SINGS team to construct the final enhanced mosaic. Instead, the standard BCD pipeline data for each day (corresponding to the pre-explosion image at day -104 and the first mid-IR post-explosion image at day 64) were downloaded from the *Spitzer* archive and further processed with the rest of the *Spitzer* observations as described below.

The SEEDS and archival *Spitzer* data for the remaining epochs were downloaded from the SSC archive using the Leopard software as and when they became available. Various pipeline versions of the data have been looked at since inception of this work, but for the results presented in this chapter the *Spitzer* pipeline versions S14.0.0 to S18.0.2 (IRAC), S16.0.1 to S18.0.1 (MIPS) and S15.3.0 to S17.0.4 (PUI) have been used. An outline of the processing steps of the pipelines for the three instruments can be found in Chapter 3, Section 3.4.2.

[2]http://ssc.spitzer.caltech.edu/legacy/singshistory.html

The basic calibrated data (BCD) from the *Spitzer* pipeline were combined into final mosaic images using the *Spitzer* MOPEX software package (Makovoz et al. 2006), which includes outlying-pixel rejection, background matching, and mosaicking with drizzling to increase the sampling of the point-spread function (PSF), as described in Chapter 3, Section 3.4.2. The IRAC and MIPS data were re-drizzled to plate scales of 0.″75/pixel and 1.″5/pixel, respectively (compared to the standard *Spitzer* pipeline products with a spatial sampling of 1.″2/pixel for IRAC and 2.″45/pixel for MIPS), following the pixel sizes adopted by the SINGS team for producing their enhanced data products. The PUI data were re-drizzled to a plate scale of 1.″2/pixel (compared to the standard pipeline data with a spatial sampling of 1.″8/pixel). The final mosaic images for all three *Spitzer* instruments were calibrated in surface brightness units of MJy sr^{-1} during the BCD pipeline stage.

For the IRAC and MIPS 24 μm data PSF-matched difference images were produced, which use the pre-explosion SINGS mosaics as the reference images. A collaborator in the SEEDS project, Dr. B. E. K. Sugerman, provided the difference images which he produced in the following way. The final mosaics produced by MOPEX were geometrically registered to a common reference frame using matching point sources identified within the fields of view, with a 2nd-order general fit within the IRAF `geotran` task. In all cases, registration residuals were less than 0.1 pixels RMS in both the x and y dimensions. Once registered, the data were PSF-matched and differenced using the DIFIMPHOT package (Tomaney & Crotts 1996) as implemented and modified by Sugerman et al. (2005). Two approaches were taken to PSF-matching. In the first, an empirical PSF was built for each image using bright, isolated point sources combined using the `daophot` PSF-building tasks (Stetson 1987). In the second, these same tasks were run on a single theoretical PSF available for each *Spitzer* IRAC and MIPS 24 μm image from the archive, after that model had been rotated and scaled according to the data's particular plate scale and position angle. Images were PSF-matched separately using the empirical and theoretical PSFs, photometrically scaled by the median brightness of a number of matching point sources, and then subtracted to yield the final difference images. In general, the difference images made using the theoretical PSFs were of higher quality (i.e., smaller subtraction residuals and less background noise) since the shape of *Spitzer*'s PSFs have varied quite little during its mission. In practice, these techniques allow the reliable detection and measurement of changes in point sources that would be considered significant below the 1-σ level in direct, undifferenced images (Sugerman et al. 2002). Examples of IRAC direct images

are shown in Figure 5.6 for four epochs, while the corresponding difference images are shown in Figure 5.7. Figure 5.8 shows PUI 16 μm and MIPS 24 μm direct images for three and four example epochs respectively, together with the corresponding MIPS difference images.

The Gemini Michelle data were downloaded from the Gemini Science Archive and processed with the Gemini IRAF `midir` tasks and further cleaning procedures as described in Chapter 2, Section 2.5.2 and Appendix B, Section B.2. The flux densities, or upper flux limits, in counts measured from the final average-combined images were converted to $F(\nu)$ units by multiplying with the flux conversion factor derived by aperture photometry of standard stars as described in Chapter 2, Section 2.5.4.

5.5 Photometric analysis techniques

Flux densities of SN 2004et from the original Gemini and *Spitzer* PUI 16 μm images and from the *Spitzer* IRAC and MIPS difference images (where pre-explosion images were subtracted from each epoch of post-explosion data) were measured by way of PSF-fitting with the `daophot` and `allstar` tasks in IRAF. Aperture photometry was also carried out on most of the images to compare with the results from PSF-fitting.

The techniques and software used for the photometry are described more throughly in previous chapters (cross-referenced where relevant below) and are briefly discussed in this section together with analysis procedures specific to the mid-IR data of SN 2004et.

5.5.1 PSF-fitted photometry

PSF-fitted photometry was carried out using the `daophot` package (Stetson 1987) within IRAF as described more fully in Chapter 3, Section 3.5.1; and Appendix C.

Due to the lack of suitable isolated, bright stars in the *Spitzer* and Gemini images, alternative methods were used to obtain input images for building the PSF models. For the *Spitzer* IRAC, MIPS and IRS-PUI data, semi-empirical PSF images (with no noise in the wings and pre-normalised to unit flux) were obtained from the SSC archive and processed to the appropriate platescale for each SN image using the IRAF `geotran` task. The PSF models for the Gemini-Michelle observations were generated from the bright standard stars used to calibrate the data, after applying airmass corrections to the SN and standard star images as described in Chapter 2, Section 2.5.4. The final PSF models for each

Table 5.3: PSF-fitting parameters for fluxes presented in Table 5.6.

Instrument	Image pixel scale (″/pixel)	PSF model created from	PSF radius[a] (pixels)	Fitting radius[b] (pixels)	Sky annuli[c] (pixels)
SST-IRAC 3.6–8.0 μm	0.75	Semi-empirical PSFs from SSC website.	18	5	1,18
SST-PUI blue 16 μm	1.5		20	3	3,12
SST-MIPS 24 μm	1.5		20	2	1,20
Gemini-Michelle 11.2 μm	0.09	Standard stars	15–40	4	1,11

[a] The PSF radius is also known as the `daophot` **psfrad** parameter. As defined in Appendix C, this should contain nearly all of the light of the brightest star used to construct the PSF model, and is equivalent to the radius of the aperture used to set the magnitude of the PSF model.
[b] The fitting radius, also known as the `daophot/allstar` **fitrad** parameter, defines the extent of the PSF used for fitting a point source).
[c] The sky fitting region is defined by the starting radius (**sannulus**) and width (**wannulus**) of the sky annuli.

instrument/waveband were constructed using these input images and the PSF-building tasks within IRAF `daophot`. The magnitude of the PSF models was set by performing aperture photometry on the semi-empirical profiles for the *Spitzer* data and the standard stars for the Gemini data, with an aperture size set to contain approximately all of the stellar flux, as determined from growth-curve analysis via multi-aperture photometry.

For the PSF-fitting, the size of the fitting radius was chosen to be approximately equivalent to the FWHM of the stellar profile, with the sky background modelled during the PSF-fitting process using appropriate sky annuli. In most cases, the `allstar` task, used to do the actual PSF-fitting, was successful in centring on the SN profile via its centroiding algorithm. However, at some epochs when the SN was quite faint, this algorithm was turned off such that the PSF-fitting was centred directly on the input coordinates corresponding to the SN position in the optical reported by Zwitter et al. (2004). The final PSF-fitted and subtracted images were inspected alongside the un-subtracted images to check the goodness of the fits. Table 5.3 lists the main parameters used to obtain the final PSF-fitted flux densities presented in Table 5.6.

5.5.2 Aperture photometry

Aperture photometry of the SN in *Spitzer* and Gemini images was carried out for comparison with the results from PSF-fitting using the IRAF `phot` task, as described more generally in Chapter 2, Section 2.6.1. A circular aperture of radius 5″ was used for all of the *Spitzer* photometry, corresponding to a linear size of ∼143 pc at the adopted distance of 5.9 Mpc to SN 2004et. The theoretical diffraction limited angular resolution of *Spitzer*

at the longest wavelength data presented here of 24 μm is 7.″1. Based on the variability of the background in both the original and difference images, a smaller aperture might have been preferable for when the SN had faded substantially at later epochs, but the 5″ radius aperture was chosen as a compromise for maintaining consistency of the photometry and to minimise the size of the aperture correction required to determine the final flux. Sky background levels in the original images were measured and subtracted using a concentric sky annulus of inner and outer radii at 7.″5 and 10″ respectively, with a centroid sky algorithm. The centroid sky algorithm is recommended in `phot` as reasonably robust in rapidly varying and crowded regions. For the IRAC and MIPS difference images, the residual background was subtracted using the same size sky annulus, with a 2σ-clipped mean sky algorithm. At the earliest and latest epochs, when the SN was relatively bright in the mid-IR, the `phot` task was centred on the SN for the photometry via a centroiding routine. At epochs between days 690 and 1191, when the SN was quite faint, the aperture was manually centred using the image World Coordinate System (WCS) coordinates corresponding to the optical position of the SN as given by Zwitter et al. (2004).

The SN was quite faint where detected in the Gemini Michelle 11.2 μm data, so these were measured with the `phot` task using a relatively small aperture size. The aperture radius was of the order of 0.″4, corresponding to a linear size of ∼11.4 pc at the adopted distance of 5.9 Mpc to SN 2004et. The sky background was determined from sky annuli with radii between 0.″5 and 2″ using a mean sky algorithm, since the background was relatively smooth. Airmass corrections were applied as detailed in Section 2.5.4.

Aperture corrections to the flux densities output from `phot` were derived as follows:
IRAC: As mentioned in Chapter 3, Section 3.4.2, IRAC data are calibrated using aperture photometry on a set of stars with a calibration aperture radius of 10 native pixels (12″) in all 4 channels, such that photometry of science targets in smaller or larger apertures than the calibration size requires an aperture correction (Reach et al. 2005*a*). Since a smaller aperture was used for the photometry of SN 2004et it was necessary to correct the measured flux densities to match the absolute calibration. Aperture corrections for photometry using different aperture sizes are given in Table 5.7 of the IRAC Data Handbook (version 3.0; Reach et al. 2006), however, the table did not include the specific aperture size and sky annulus used for measuring SN 2004et, so the corrections had to be derived.

As advised by the *Spitzer* Help Desk, aperture corrections for the IRAC data were derived by measuring a sample of IRAC calibration stars used for the formal IRAC

Table 5.4: IRAC primary calibration stars (Reach et al. 2005*a*) used for deriving aperture corrections.

Star[a]	Type	R.A. (J2000.0)	Decl. (J2000.0)	8 μm flux density [mJy]	UT date of observations			Exp. time[b] [s]
NPM1p67.0536	K2 III	17 58 54.5	+67 47 37.4	185 ± 7	2004-04-05	2004-07-18	2005-03-31	0.2 × 5 = 1.0
KF09T1	K0 III	17 59 23.0	+66 02 56.0	38.8 ± 1.0	2004-06-28	2004-10-27	2005-05-06	1.2 × 10 = 12
HD165459	A1 V	18 02 30.7	+58 37 38.1	148 ± 4	2004-06-09	2004-12-21	2005-03-24	0.2 × 5 = 1.0
NPM1p64.0581	A0 V	19 12 47.2	+64 10 37.3	14.4 ± 0.3	2004-07-28	2004-10-12	2005-01-22	1.2 × 10 = 12

[a] The star names in this table are not the formal designations but those used by Reach et al. (2005*a*).
[b] Exposure times take the form $a \times b = c$, where a is equivalent to the effective on-source frame time, b is the number of frame repeats and c is the total on-source exposure time. The same exposure times were used for each epoch of observations.

calibration described by Reach et al. (2005*a*). Four of the eleven primary calibration stars were identified from the Reach et al. (2005*a*) paper and three randomly selected epochs of IRAC BCD data of each star were downloaded from the SSC archive. Table 5.4 provides details of the stars and observations used.

The multi-frame BCD data for each star were processed and combined into single mosaic images per epoch and filter with the *Spitzer* MOPEX software, in the same way as for the science data of SN 2004et (as described in Section 5.4.2). Images were converted from surface brightness units to flux density units of μJy/pixel by taking into account the pixel size in steradians. Aperture photometry of the calibration stars was then carried out with IRAF `phot` using the aperture size and sky background region used by Reach et al. (2005*a*) for the IRAC calibration (radius 12″ with a concentric sky annulus with inner and outer radii at 14.4″ and 24″ respectively), and also with the apertures used for the photometry of SN 2004et (radius 5″ with a concentric sky annulus with inner and outer radii at 7.5″ and 10″ respectively). The ratio of the flux measured in the large aperture (used for the IRAC flux calibration) to the flux measured in the smaller aperture (used for the measuring the SN) was calculated for each calibration star for each epoch. The average of these ratios was used as the aperture correction for each filter. A list of the aperture corrections applied to the IRAC aperture photometry is given in Table 5.5. Standard deviations from the average were less than 1% and the values derived are consistent with interpolation between those listed in Table 5.7 of the IRAC Data Handbook.

PUI and MIPS: The PUI 16 μm and MIPS 24 μm aperture corrections were derived using semi-empirical PSFs from the SSC website (these were used as the PSF stars for the PSF-fitted photometry). The PSF images were of unit flux with effectively zero background.

Table 5.5: *Spitzer* IRAC, PUI and MIPS aperture corrections derived for photometry of SN 2004et, using an aperture of radius 5″ with a concentric sky annulus of inner and outer radii 7.5″ and 10″ respectively.

Instrument	λ_{eff} [μm]	Ap. corr.
IRAC	3.6	1.08
IRAC	4.5	1.10
IRAC	5.8	1.09
IRAC	8.0	1.11
PUI	16	1.50
MIPS	24	2.16

Aperture photometry was used to measure the fractional flux of the PSF images in an aperture of radius 5″, the same size aperture as that used for the science photometry of SN 2004et. The ratios of the total unit flux to the fractional flux in the science aperture were used for the final aperture corrections, the values of which are listed in Table 5.5. The absolute calibration of the PUI 16 μm data processed with *Spitzer* pipeline version S15.3.0 was tied to a finite aperture of 12 PUI native pixels (equivalent to 21.″6) explained in the PUI flux calibration description of Section 3.4.2. A separate aperture correction factor of 1.51 was derived for this, but is not listed in Table 5.5, since it differs from the infinite-aperture calibration value by less than 1%.

For each *Spitzer* instrument/filter, the SN flux densities measured from the science data with IRAF `phot` were multiplied by the values given in Table 5.5 to obtain the final aperture-corrected flux densities. Errors introduced due to uncertainties in the aperture corrections are of the order of 5–10%.

Gemini-Michelle: The aperture corrections to the Michelle 11.2 μm flux densities were estimated in a similar way to the *Spitzer* PUI and MIPS corrections described above, using aperture photometry of the standard stars by taking the ratio of the number of counts in the large aperture (used for the flux calibration) to the number of counts in the smaller science aperture (used to do photometry on the SN). For an aperture of radius 4 pixels (= 0.″4), a multiplicative correction factor of $\sim$1.4 was applied. The airmass-corrected flux densities of the SN detections were then scaled by this aperture-correction factor to provide the final flux densities.

5.5.3 Pre-explosion images

The pre-explosion SINGS images of SN 2004et with IRAC and MIPS revealed the presence of spatially extended emission at and around the position of the supernova. Difference imaging techniques were used to subtract this emission from post-explosion observations, revealing a clearer evolution of the supernova's brightness with time. The emission at the location of the SN from the pre-explosion IRAC and MIPS images was measured using aperture photometry with the same size apertures and sky annuli as described above.

Whilst similar pre-explosion emission would be expected at IRS-PUI wavelengths, no such observations were available. Initially, the pre-explosion flux level at 16 μm was estimated by blackbody interpolation between the IRAC and MIPS pre-explosion flux densities. The best fit with a 410 K blackbody to the longest wavelengths (8 and 24 μm) gave a 16 μm pre-explosion flux estimate of ∼ 520 μJy, which was subtracted from the post-explosion 16 μm fluxes. However, blackbody fitting to the supernova SEDs (described in Section 5.8) indicated a significant over-estimation of the net 16 μm flux, especially at the later epochs, suggesting that the pre-explosion background estimate was too large. Since the nature of the spatially extended emission seen in the IRAC and MIPS pre-explosion images is unknown, possibly including unresolved stars and/or H II regions, it is unlikely that a simple blackbody would be representative of the emission. In fact, the 410 K blackbody could not fit the IRAC fluxes from 3.6–5.8 μm. An alternative method was adopted to estimate a pre-explosion 16 μm background flux, whereby blackbodies were fit to the day 1015 SED, where the 16 μm flux was particularly discrepant, with the 16 μm flux omitted. The flux at 16 μm was then obtained from the fit. Knowing the measured flux at this epoch and the flux indicated by the best blackbody fit, a pre-explosion 16 μm flux was estimated by subtracting the latter from the former, yielding a flux that was ∼ 40% of that estimated by blackbody fitting to the pre-explosion fluxes. All PUI data were corrected for this estimated pre-existing flux level. The results from the two methods obviously differ most when the SN is at its faintest levels (days 828–1054), with the flux at this time being as much as a factor of 12 brighter with the adopted 'boot-strap' method than that obtained from the blackbody interpolation of the pre-explosion IRAC and MIPS data. Consequently, there are larger uncertainties associated with the 16 μm flux densities from days 828–1054, in addition to the statistical errors presented in Table 5.6.

5.5.4 PSF-fitted photometry vs. aperture photometry

The PSF-fitting and aperture photometry of the SN in the original *Spitzer* IRAC images was generally consistent to within 5–15 %, with a larger discrepancy at epochs where the SN was very faint between days 690–1054. The two methods were slightly more consistent when working on the difference images, generally between 2 and 10 %, but again with larger discrepancies at the same epochs when the SN was faint.

The 16 μm PUI flux densities were measured from the original images only, since there were no pre-explosion 16 μm images and, therefore, no difference images. The results from both methods were consistent to within 8 %, except at day 718, when PSF-fitting resulted in a 30 % higher flux than that from aperture photometry.

The PSF-fitting and aperture photometry from the original and difference *Spitzer* MIPS 24 μm images were generally consistent to within 2–10 %, with a larger discrepancy at days 851 and 1069, when the SN was at its faintest levels.

5.5.5 Flux density uncertainty analysis and upper limits

The final flux densities presented in the following section (5.6) were measured via PSF-fitted photometry as described above (although see previous discussion of PSF-fitting vs. aperture photometry). Statistical uncertainties associated with the mid-IR flux densities were estimated using the noise models of the `daophot-allstar` routine within IRAF used for the PSF fitting. The `allstar` error model includes readout noise from the detector; Poisson uncertainty in the source and background flux; an extra photometric error term which was estimated to account for uncertainty in flat-fielding, bias-subtraction, photometric scaling and calibration; and a profile error term that corrects for pixelization of a function. The photometric error was estimated to be at the 10 % level and the profile error used the task's default value of 5 %.

For the photometry from the IRAC and MIPS difference images, uncertainties were measured with a custom implementation of an optimal photometry code written for the original version of DIFIMPHOT (Tomaney & Crotts 1996; used to produce the difference images as described in Section 5.4.2), which includes the full noise model of `allstar` described above as well as correct noise contributions from both input and reference images and the original sky values in each image prior to pipeline calibration.

For the IRAC data, during days 690 to 1054, when the SN is faint, the formal flux uncertainties obtained by this method are relatively large and, in some cases, *larger* than the measured flux density itself (see Table 5.6 in the following section for a list of the measured flux densities and their associated errors). As demonstrated in Sugerman et al. (2002), difference imaging can reliably detect point sources at less than the 1-σ formal uncertainty in direct, un-differenced images (which is what the uncertainties described above seek to represent), most simply because the position of the object is known ahead of time. The *detection* is unambiguous, but the flux measurement is not. The formal error is large due to the background pixel variations which, as explained previously, include noise contributions from the input and reference images. Without including these latter contributions, the errors output from the `allstar` task alone are much smaller, since the contribution of the background noise is relatively low (by definition, for a difference image). Therefore the flux densities appear much better than 3-σ detections using the `allstar` error model alone. In light of this, and because a negative flux is unrealistic for those cases where the formal error was larger than the measured flux, we decided to reduce the formal errors for the IRAC data, during days 690 to 1054, when the SN is faint, such that the fluxes are considered to be 3-σ detections. This is a compromise between both the `allstar` error model alone and the formal error described above, and these reduced errors have been used for the mid-IR light curves and SED analysis presented in the following sections.

Since the *Spitzer* images were calibrated in surface brightness units and converted to flux densities (μJy), the effective readout noise and gain of the detectors, required for an accurate noise model, were set as follows:

$$\textit{effective gain} = N \times (GAIN * EXPTIME)/(FlUXCONV * FAC)$$
$$\textit{effective readnoise} = \sqrt{N} \times READNOISE$$

where the following were keywords from the image headers: GAIN, in electrons/data number (DN); EXPTIME, the effective integration time in seconds; FLUXCONV, the *Spitzer* flux calibration factor in units of (MJy/sr)/(DN/s); and READNOISE, the detector readout noise in electrons. FAC was the conversion factor used to change flux units from MJy/sr to μJy and N was the number of on-source frames (BCDs) that were averaged to produce the final mosaic image.

For non-detections of the SN in the IRAC difference images, the formal uncertainty described above (that including the noise contributions from the input and reference images) was reported as the upper limit to the flux density for that epoch. It was empirically found that a point source with this flux density was marginally detectable, while a source with three-times this flux density was reliably detected; i.e., the upper limits should be considered significant at only the 1-σ level.

The upper limits for the non-detections in the Gemini data at days 598 and 1020 are 3-σ values based on the uncertainty of the background in the region of the SN position scaled to a diffraction-limited size aperture, as described more fully in Chapter 2, Section 2.6.3.

5.6 Evolution of the mid-IR emission

Table 5.6 lists the complete set of *Spitzer* and Gemini mid-infrared flux densities and associated uncertainties/upper-limits of SN 2004et from days 64 to 2151 as determined from the PSF-fitting techniques described in Section 5.5. *Spitzer* IRAC, MIPS and IRS-PUI data have had pre-explosion flux levels subtracted as discussed in Section 5.5.3. Measured (IRAC and MIPS) and estimated (PUI) pre-explosion flux densities at the position of the SN are summarised in the last row of the table.

The *Spitzer* IRAC, PUI 16 μm and MIPS 24 μm mid-IR light curves (with pre-explosion levels subtracted) are shown in Figure 5.5. For clarity, the 4.5 μm, 5.8 μm, 8.0 μm, 16 μm and 24 μm light curves have been arbitrarily shifted by the factors shown. Upper limits to the flux densities at 3.6 μm and 5.8 μm are indicated by the downward pointing arrows. Each waveband demonstrates the decline in brightness from the earliest epochs to around day 800 when the SN has faded or is fading to its faintest levels. At 3.6 μm and 5.8 μm, the upper limits measured from the difference images indicate that the SN faded to below background levels for $\sim$ 200 days. The distinctive rise in brightness after this time ($>$ 1000 days) is also evident in all wavebands. The latest *Spitzer* data at days 1779, 1931 and 2151 were obtained during the post-cryogenic phase of the mission, where only the shortest wavelength IRAC channels at 3.6 and 4.5 μm were available. They show that sometime between days 1395 and 1779, the mid-IR brightness of the SN at 3.6 and 4.5 μm began to decline again, continuing with a slower decline to day 2151. The 3.6 μm flux at day 2151 is about 9 % higher than the pre-explosion level, whilst the 4.5 μm flux at the latest epoch is a factor of 2.7 brighter than the pre-explosion level.

Table 5.6: Mid-infrared photometry of SN 2004et. The shaded rows indicate those fluxes across different wavebands to be considered as the same epoch.

UT date	Age [days]	Flux density[1]/ upper limits[2] [μJy]						
		IRAC[3]				Michelle N′	IRS-PUI[3]	MIPS[3]
		3.6 μm	4.5 μm	5.8 μm	8.0 μm	11.2 μm	16 μm	24 μm
2004-06-10	-104	83.8 ± 10.2	45.4 ± 8.3	178 ± 25	412 ± 51	···	···	···
2004-07-09	-75	···	···	···	···	···	···	376 ± 25
2004-11-25	64	17490 ± 532	13038 ± 745	10046 ± 179	6020 ± 91	···	···	···
2005-07-13	294	···	···	···	···	···	930 ± 33	···
2005-07-19	300	726 ± 61	3151 ± 97	1291 ± 218	2162 ± 154	···	···	···
2005-07-30	311	···	···	···	···	1700 ± 200	···	···
2005-08-03	315	···	···	···	···	···	···	832 ± 75
2005-09-17	360	430 ± 71	1728 ± 88	935 ± 285	1731 ± 156	···	···	···
2005-09-24	367	···		···	···	···	···	735 ± 74
2005-11-02	406	315 ± 21	1045 ± 21	707 ± 79	1500 ± 77	···	···	···
2005-12-22	456	···	···	···	···	···	890 ± 32	···
2005-12-30	464	174 ± 67	656 ± 77	606 ± 293	952 ± 162	···	···	···
2006-01-11	476	···	···	···	···	···	···	686 ± 89
2006-05-12/14	597/599	···	···	···	···	≤ 650	···	···
2006-08-04	681	···	···	···	···	···	670 ± 34	···
2006-08-13	690	≤ 49	45.9 ± 53.0	115 ± 220	342 ± 132	···	···	···
2006-09-01	709	···	···	···	···	···	···	663 ± 77
2006-09-10	718	···	···	···	···	···	562 ± 30	···
2006-12-29	828	≤ 45	29.4 ± 12.4	≤ 87	145 ± 82	···	···	···
2007-01-21	851	···	···	···	···	···	···	513 ± 54
2007-01-27	857	···	···	···	···	···	446 ± 31	···
2007-06-26	1007	···	···	···	···	···	324 ± 29	···
2007-07-03	1015	≤ 23	14.1 ± 17.5	≤ 83	113 ± 76	···	···	···
2007-07-09	1020	···	···	···	···	≤ 400	···	···
2007-07-10	1021	···	···	···	···	···	···	644 ± 48
2007-08-02	1044	···	···	···	···	···	366 ± 35	···
2007-08-12	1054	≤ 34	15.1 ± 14.0	≤ 78	115 ± 67	···	···	···
2007-08-27	1069	···	···	···	···	···	···	610 ± 49
2007-12-09	1173	···	···	···	···	···	1023 ± 33	···
2007-12-27	1191	52.5 ± 38.6	189 ± 10	345 ± 75	458 ± 73	···	···	···
2008-01-07	1202	···	···	···	···	···	···	1276 ± 42
2008-01-17	1212	···	···	···	···	···	1055 ± 31	···
2008-06-21	1368	···	···	···	···	1036 ± 212	···	···
2008-07-09	1386	···	···	···	···	1016 ± 224	···	···
2008-07-18	1395	76.3 ± 22.6	258 ± 11	465 ± 49	578 ± 82	···	···	···
2008-07-29	1406	···	···	···	···	···	···	1563 ± 54
2009-08-06[4]	1779	17.3 ± 7.6	113 ± 8	···	···	···	···	···
2010-01-05[4]	1931	14.4 ± 6.9	90.3 ± 16.8	···	···	···	···	···
2010-08-13[4]	2151	7.2 ± 3.0	76.7 ± 5.3	···	···	···	···	···
Pre-explosion		83.8 ± 10.2	45.4 ± 8.3	178 ± 25	412 ± 51	···	221 ± 22	376 ± 25

[1] All post-explosion flux densities were measured with PSF-fitted photometry (using IRAF `daophot`). Pre-explosion IRAC and MIPS fluxes were measured in an aperture of radius 5″ with sky annuli at inner radius 7.″5 and outer radius 10″ respectively, using a 2-σ clipped-mean sky algorithm (using IRAF `phot`).

[2] Upper flux limits for the non-detections in the Gemini-Michelle data are 3-σ values based on the standard deviation of the background in the region of the SN position scaled to a diffraction-limited size aperture. For the *Spitzer* IRAC data, upper limits were estimated from the adopted error model described in Section 5.5.5.

[3] *Spitzer* IRAC, MIPS and IRS-PUI data have had pre-explosion flux levels subtracted: IRAC and MIPS by use of difference imaging techniques to subtract pre-explosion SINGS images, and IRS-PUI by estimating the pre-explosion level from blackbody fits to the SED at day 1015 (see text). Measured (IRAC and MIPS) and estimated (IRS-PUI) pre-explosion fluxes at the position of the SN are summarised in the last row of the table.

[4] Observations at days 1779, 1931 and 2151 were obtained during the *Spitzer* 'warm' mission, where only IRAC 3.6 and 4.5 μm channels were available.

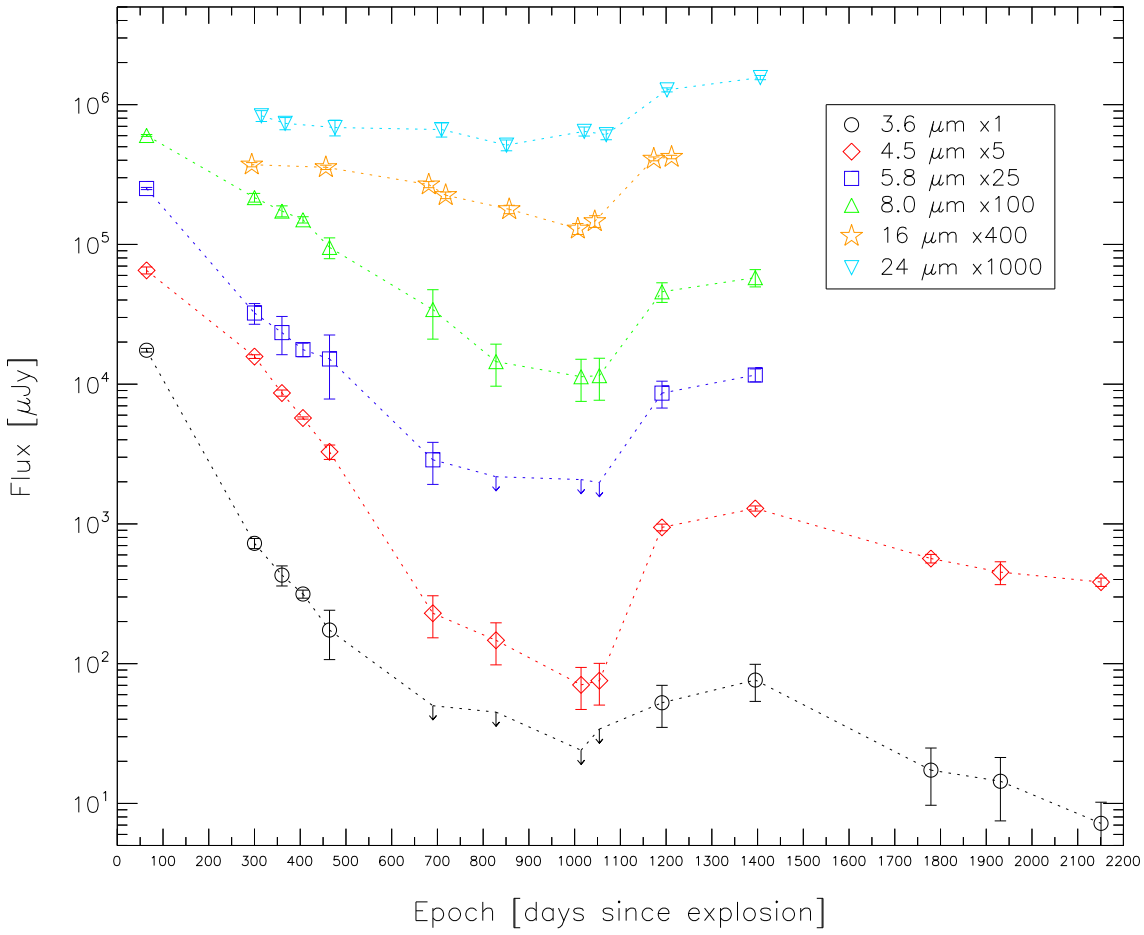

Figure 5.5: *Spitzer* mid-infrared light curves of SN 2004et: 3.6, 4.5, 5.8 and 8.0 μm (IRAC), 16 μm (IRS Peak-Up Imaging) and 24 μm (MIPS). The IRAC and MIPS flux densities are from PSF-fitted photometry carried out on difference images which use the pre-explosion image (day -104 for IRAC and day -75 for MIPS) as the reference image. The 16 μm flux densities are from PSF-fitted photometry of the original images from which an estimated pre-explosion flux was subtracted (see text for details). For non-detections, upper limits to the flux densities are indicated by the downward-pointing arrows. See Section 5.5.5 for a discussion of the IRAC flux uncertainties for days 690–1054 when the SN was faint. For clarity the light curves have been shifted vertically by the factors indicated.

Whilst the 3.6 μm flux densities at days 1779 to 2151 are lower than the upper limits between days 690 and 1015, the on-source integration times for the latter observations were between factors of 3 and 80 longer than those for the earlier observations. The corresponding increase in signal-to-noise for the IRAC 'warm' images, together with difference imaging techniques, allowed the SN to be reliably detected at deeper levels than for previous observations with shorter exposure times when the SN was also faint.

A selection of pre- and post-explosion IRAC images at 4.5 μm, 5.8 μm and 8.0 μm are shown in Figure 5.6, depicting the mid-infrared evolution of SN 2004et. The supernova position is shown in the pre-explosion SINGS images at day -104 revealing evidence of extended emission in this region. The first mid-IR images of the SN, obtained 64 days after explosion (second row of figure) by the SINGS Legacy survey, showed the SN to be very bright. This was during the photospheric plateau phase which characterises Type II-P supernovae, where hot blackbody emission dominates the optical emission and its Rayleigh-Jeans tail extends into the infrared. By day 1015 (third row), it can be seen that the SN has faded to almost pre-explosion levels, but a late rise in brightness is clearly evident by day 1395. Comparable difference images depicting the net mid-IR emission at the SN position for the same epochs are shown in Figure 5.7. The first row again shows the pre-explosion images at day -104, which were used as the reference images for subtraction from the post-explosion images, to yield the difference images shown in the remaining panels. At day 1015 when the SN has faded to its faintest levels, a detection at 4.5 μm can just be discerned. For the same epoch at 5.8 μm, whilst there is positive emission coincident with the position of the SN, this is at a similar level to the average noise levels in the residual background of the difference image and is therefore considered to be a non-detection for which an upper limit to the flux is derived. The SN is much more clearly detected in the 8.0 μm difference image at day 1015, although the irregular residual background, seen as diagonal bands across all of the difference images at this wavelength, creates relatively large uncertainties in the final measured flux.

Figure 5.8 shows similar example IRS-PUI 16 μm and MIPS 24 μm images, with the same field of view as for the IRAC images in Figures 5.6 and 5.7. The first column shows the 16 μm data, while the second and third columns show the respective direct and difference 24 μm images. The first image in the second column shows the pre-explosion SINGS image of the SN position at 24 μm observed 75 days before the SN exploded. This was the reference image used to create the MIPS difference images shown in the

third column. The post explosion data are shown in rows 2–4. In the second row, the images show the first observations with PUI and MIPS taken ~10 months after the SN had exploded, during the nebular phase when the SN was still quite bright. The third row shows the observations almost 2 years later when the SN had faded substantially. The last row shows the final epoch observations at 16 and 24 μm, between 3 and 4 years after explosion, from which it is evident that the SN had increased in brightness again, mirroring the mid-IR evolution seen in the IRAC wavebands.

For the 16 μm *Spitzer*-PUI data, the pre-explosion flux estimated by Kotak et al. (2009) was ~56 % higher than that from this work and, as expected, my results yield generally higher post-explosion fluxes than those presented by Kotak et al. (2009). The factor by which the post-explosion fluxes exceed those of Kotak et al. (2009) varies from ~1.1 to 3.3. The largest differences in the photometry occur for days 1007–1044 when the SN was close to its faintest levels in this waveband. During the final epochs observed (days 1212–1173), when the rebrightening was strongest, the fluxes agree to within 10 %.

For the 24 μm *Spitzer*-MIPS data, Kotak et al. (2009) measured the flux in the two SINGS pre-explosion images observed at days -75 and -73, as processed with the standard *Spitzer* pipeline. They found the flux at day -75 to be a factor of almost 1.3 higher than that at day -73. From these they measured an average pre-explosion flux which is almost 40 % lower than the pre-explosion flux measured in this work. As discussed in Section 5.4.2, the pre-explosion MIPS image used here for the analysis of SN 2004et was the SINGS enhanced mosaic from their 5th data delivery, which combined data from both days. Investigating the two separate images, I found a flux consistent with that of Kotak et al. (2009) at day -73 but at day -75 I found the flux to be about a factor of 1.7 higher. I also measured the fluxes of a number of nearby isolated point sources that were present in both images. No systematic offset was found, with the photometry differing by no more than 1–10 %. Large and small scale differences in the background were noticeable between the images, likely in part due to artifacts resulting from the scan mapping mode employed by the SINGS team to image the whole galaxy. Differences in the photometry of the isolated point sources in these two separate images are most likely due to the varying background levels. The SINGS enhanced 24 μm mosaic used in this work was processed by the SINGS team with steps that go beyond the standard pipeline to improve data quality. The flux measured at the position of the SN in this pre-explosion image which combines the data from both days is consistent with the flux of the pre-explosion standard pipeline image

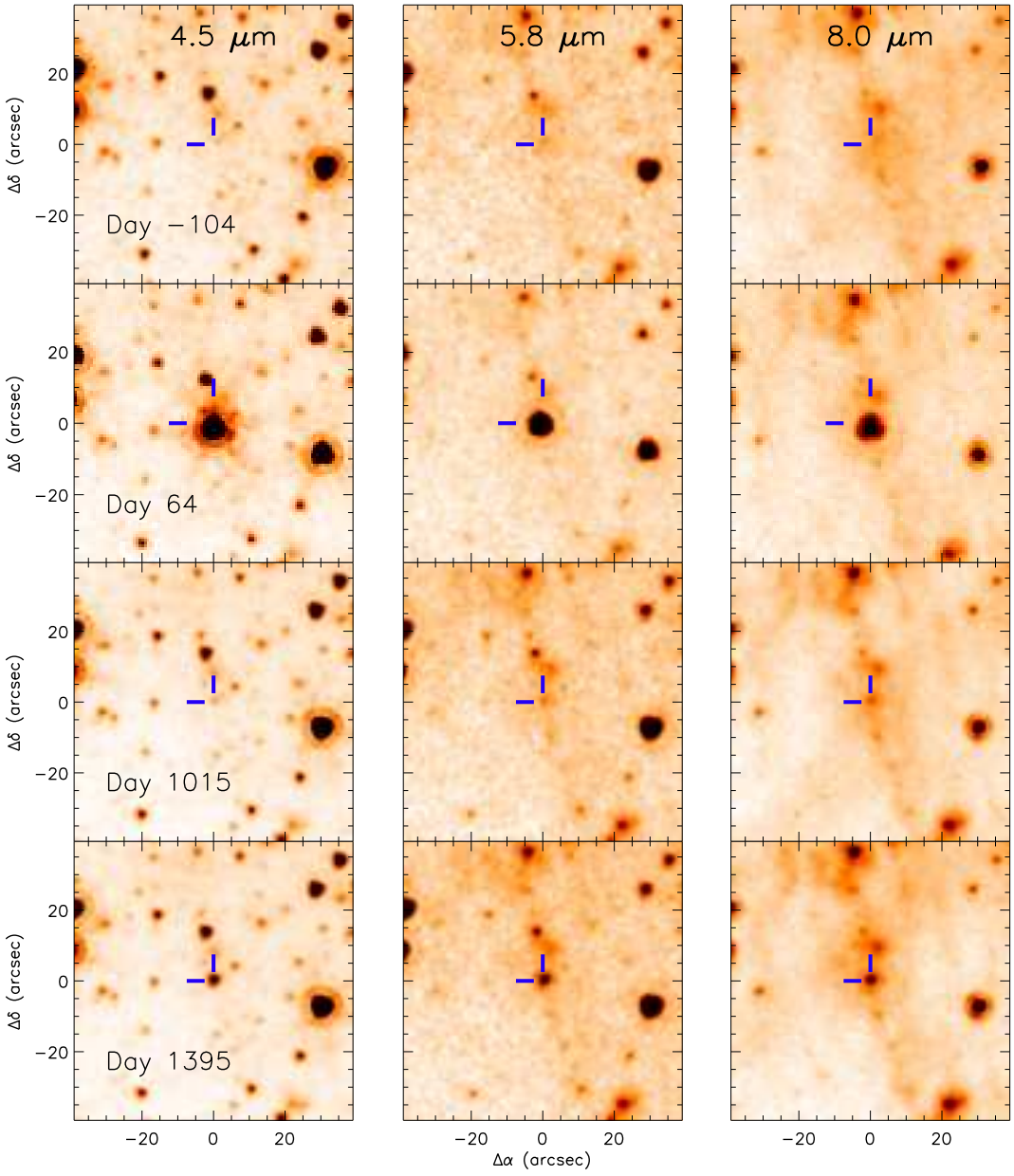

Figure 5.6: The SN position in *Spitzer* images at select epochs, revealing the mid-IR evolution in IRAC bands 4.5, 5.8 and 8.0 μm. The first row shows the SN field in the pre-explosion SINGS images at day -104. The first mid-IR detections were obtained 64 days after explosion when the SN was still very bright (second row). The third row shows that the SN had faded to almost pre-explosion levels by day 1015, yet by day 1395 the SN has brightened again (fourth row). Equivalent difference images (i.e., at the same wavelengths and epochs as those in this figure), whereby the pre-explosion data is registered to and subtracted from the post-explosion data, are shown Figure 5.7.

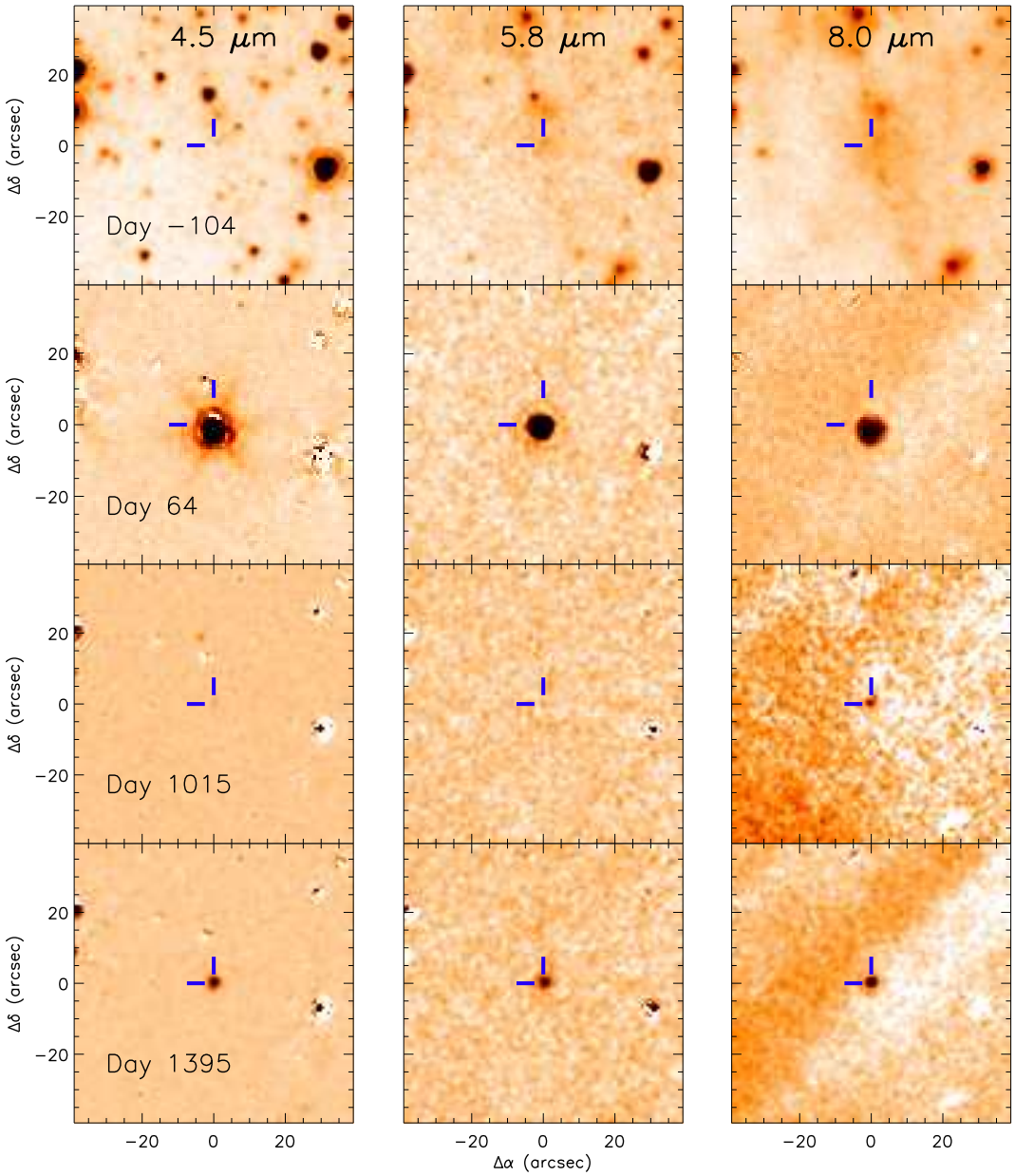

Figure 5.7: Example difference images in *Spitzer* IRAC bands 4.5, 5.8 and 8.0 μm at equivalent epochs to those images shown in Figure 5.6. The pre-explosion images at day -104 (first row) have been registered to, and subtracted from, the post-explosion images using PSF-matched difference imaging techniques (see Section 5.4.2). Note the strong, uneven background residuals at 8.0 μm.

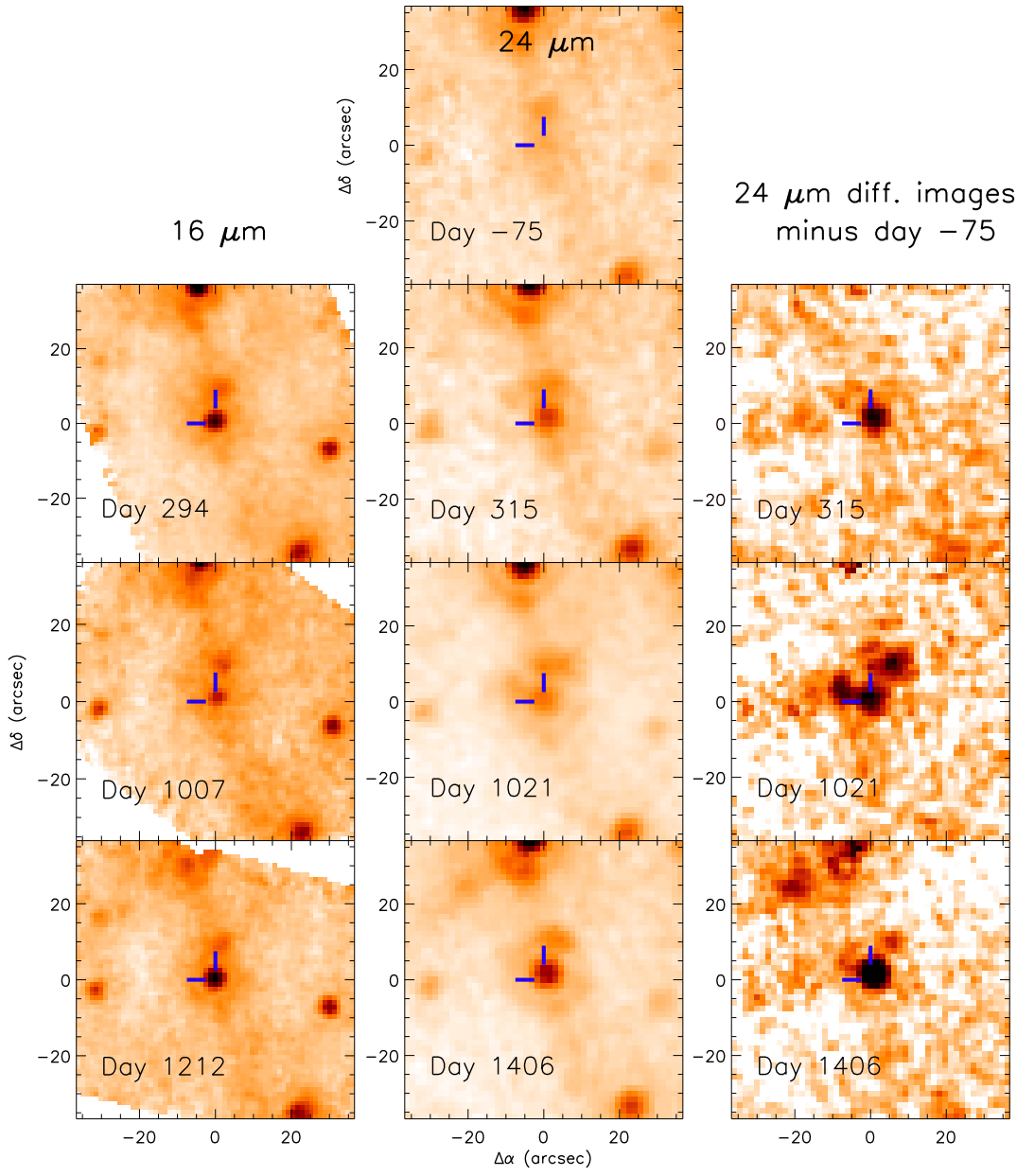

Figure 5.8: Example *Spitzer* PUI 16 μm and MIPS 24 μm images showing similar evolution to that observed with IRAC. Three epochs of post-explosion data are shown in the direct images for each instrument. These are comprised of the first observations with PUI and MIPS ~ 10 months after the SN had exploded, when the SN was still quite bright; followed by observations almost 2 years later when the SN had faded substantially; to the final epoch observations for each, between 3 and 4 years after explosion, showing the late-time rise in brightness of SN 2004et. The first image in column 2 shows the pre-explosion SINGS MIPS 24 μm image of the SN position observed 75 days before the SN exploded. The third column shows the 24 μm difference images at the corresponding epochs to those in column 2, which use the day -75 SINGS image as the reference.

at day -75 to within ∼2 %. Further investigation of the differences between the standard pipeline data and the combined enhanced data is beyond the scope of this work.

Despite measuring a higher pre-explosion flux than Kotak et al. (2009) at 24 μm, we find that photometry from our difference images yields generally *higher* post-explosion fluxes than theirs. There are a number of different methods employed in our respective analyses that might result in the differences seen in the photometry at 24 μm, and those at other wavelengths. In the case of the 24 μm data, it is unclear which of the two (standard pipeline) pre-explosion images Kotak et al. (2009) used as a reference for their difference imaging, whereas this work uses the data from both nights as combined in the final mosaic delivered by the SINGS team. Differences between the background levels in all three of these images have just been discussed. More generally, different techniques/software were used to produce the final difference images, which is likely to result in different background residuals affecting the photometry. In addition, Kotak et al. (2009) used aperture photometry to measure their fluxes, whereas this work uses results from PSF-fitting. Any differences in the photometry itself would be compounded by the possibly different techniques used to interpolate the 16 and 24 μm data to the IRAC epochs.

5.7 Optical and near-infrared photometry

This section summarises and discusses the optical and NIR (NIR) data of SN 2004et obtained by the SEEDS project in order to help constrain, together with the mid-IR data discussed in the previous section, the evolution of the spectral energy distribution of the supernova (Sections 5.8 and 5.9). In general, the observations, data processing and flux measurements were carried out by SEEDS collaborators, but collation and interpretation of these data is my own work for this thesis with their permission. For clarity, where analysis of the optical and NIR data is my own work, it is noted as "*THIS WORK*" in the following paragraphs.

5.7.1 The observations

Optical and NIR photometric observations of SN 2004et were obtained as part of the SEEDS program over the years 2004 to 2009, spanning 79–1803 days after explosion. Table 5.7 provides a complete log of the optical and NIR photometric observations of SN 2004et taken as part of the SEEDS project.

Table 5.7: Log of optical and near-infrared photometric observations of SN 2004et from the SEEDS collaboration.

Date	Age [days]	Telescope/ instrument	Filters	Exp. time	Program ID	Principal Investigator
2004-12-10	79	Tenagra II 32″	*VRI*	9×100 s	–	D. Welch
2004-12-20	89	Tenagra II 32″	*VRI*	9×100 s	–	D. Welch
2005-06-17	268	Bok 2.3-m 256×256 IR cam	*JHK*	20×30 s	–	K. Gordon
2005-08-05	317	Gemini GMOS-N	$g'r'i'$	1×60 s	GN-2005B-Q-54	G. Clayton
2005-08-05	317	Gemini NIRI	*JHK*	22×30 s	GN-2005B-Q-54	G. Clayton
2005-10-17	390	Gemini NIRI	*JHK*	10×30 s	GN-2005B-Q-54	G. Clayton
2005-10-31	404	Gemini GMOS-N	$g'r'i'$	1×60 s	GN-2005B-Q-54	G. Clayton
2006-07-06	652	Gemini NIRI	*JHK*	22×30 s	GN-2006A-Q-52	G. Clayton
2006-07-18	664	Gemini GMOS-N	$g'r'i'$	1×60 s	GN-2006A-Q-52	G. Clayton
2007-07-08	1019	*HST* WFPC2	F606W,F814W	4×400 s	GO11229	M. Meixner
2007-07-08	1019	*HST* NICMOS2	F110W,F205W	5×128 s	GO11229	M. Meixner
2007-07-08	1019	*HST* NICMOS2	F160W	4×128 s	GO11229	M. Meixner
2008-01-20	1215	*HST* WFPC2	F606W,F814W	4×400 s	GO11229	M. Meixner
2008-01-20	1215	*HST* NICMOS2	F110W,F205W	5×128 s	GO11229	M. Meixner
2008-01-20	1215	*HST* NICMOS2	F160W	4×128 s	GO11229	M. Meixner
2008-08-04	1412	Gemini GMOS-N	$g'r'i'$	2×600 s	GN-2008B-Q-44	M. Barlow
2009-08-30	1803	WIYN WHIRC	*H*	4×180 s	2009B-0516	M. Otsuka

The first two epochs of optical photometry were obtained during the plateau phase of the SN at days 79 and 89 with the 32″ Tenagra II telescope in Arizona. A further three epochs of optical photometry were obtained during the nebular phase between days 317 and 664 with the Gemini Multi-Object Spectrograph on Gemini-North (GMOS-N) in Hawaii. In addition, an archival flux-calibrated Subaru spectrum was used to obtain optical photometry at day 646 by integrating over the *BVRI* filter transmission curves. Two epochs of late-time, high resolution observations of the SN field were obtained with the *HST* Wide Field Planetary Camera 2 (WFPC2) around three years after explosion at days 1054 and 1215. A final epoch of optical photometry, almost 4 years after explosion, was obtained with GMOS-N at day 1412.

The first epoch of NIR photometry was obtained at day 268 with the 2.3-m Bok telescope, part of the Steward Observatory at Kitt Peak, Arizona. This was followed by three epochs of data from the Near InfraRed Imager (NIRI) on Gemini-North at dates close in time to the optical images taken with GMOS-N during the nebular phase. Late-time, high-resolution data was obtained with the *HST* Near Infrared Camera and Multi-Object Spectrometer 2 (NICMOS2), at epochs corresponding to those of the optical WFPC2 data. A final *H*-band image was taken approximately 5 years (day 1803) after explosion with the WIYN High-resolution InfraRed Camera (WHIRC; Meixner et al. 2010), on the WIYN 3.5-m telescope at Kitt Peak, Arizona.

5.7.2 Data processing

In the following paragraphs I briefly describe the processing steps *carried out by SEEDS collaborators* for the data presented in this section.

Gemini/GMOS-N On days 317, 404, and 664, 60 s images were taken with GMOS-N in the g', r', and i' broad-band filters. Longer exposures of 2×600 s in the same filters were taken at day 1412 when the SN was expected to have faded. The images were reduced using the Gemini IRAF package. Pipeline processed bias and flat field images were obtained from the Gemini Science Archive. Object images were trimmed, corrected for overscan and bias, and flat-fielded using the `gsreduce` task. Finally, `gmosaic` was used to mosaic the three GMOS CCDs into a single image. PSF-fitted photometry was performed on the SN and a sample of standard stars from the photometric V, R, and I sequence of Pozzo et al. (2006) to establish the nightly zeropoint. The GMOS Sloan Digital Sky Survey (SDSS) magnitudes were transformed into Johnson V, R, and I magnitudes using the transformation equations given by Welch et al. (2007). These linear transformations were derived from the photometric V, R, and I sequence presented by Pozzo et al. (2006).

Gemini/NIRI In order to ensure a consistent sky background between exposures, individual exposures of 30 s in each of the broad-band *JHK* filters were taken, with the total number being dictated by the anticipated decline of the SN NIR light. A 5″ dither pattern was employed to ensure efficient removal of point sources while making sky images. Data reduction for each night was performed using the standard NIRI routines within the Gemini IRAF package. `nprepare` and `niflat` were used to derive the normalized flat field and the bad pixel mask while `nisky` was used to create the final sky image. `nireduce` was used to subtract this sky image from and apply the flat field correction to the processed object images. Finally, the individual images in each filter were coadded using the GEMTOOLS routine `imcoadd`. PSF-fitted photometry was performed on SN 2004et and three standard stars present within the field. The *JHK* magnitudes of the standard stars are contained within the 2MASS all-sky catalogue and were used to derive the nightly zeropoint in each filter. The photometric uncertainty is dominated by the standard deviation of the zeropoint derived from the three standard stars.

Tenagra and Steward/Bok These early optical and NIR data were reduced, calibrated and measured in a similar manner to the GMOS-N and NIRI observations described above using standard routines within IRAF. The data were bias and dark subtracted, flat-fielded, and the multiple exposures were combined to form the final image.

HST WFPC2 and NICMOS2 For the WFPC2 observations, imaging with the broadband *F606W* and *F814W* filters was used to measure the *V*- and *I*-band flux densities. For the NICMOS2 observations, imaging was carried out with the *F110W*, *F160W*, and *F205W* filters, most closely representing the standard *JHK*-bands. Small-scale dithering was employed for both instruments to improve S/N, remove cosmic rays and to improve the pixel-scale of the final images by drizzle techniques. The WFPC2 observations used a 4-point dither × 400 s exposure for each band. The NICMOS2 observations used a 5-point dither × 128 s in the *F110W* and *F205W* filters and a 4-point dither × 128 s for *F160W*.

The data were reduced and calibrated using the IRAF external package `stsdas` (version 3.8) and included the removal of cosmic rays and other artifacts, as well as linearity corrections. High-resolution images were created using the `stsdas/drizzle` package and additional distortion correction and alignment was performed using background stars. The point spread functions of these reference background stars were fit by Gaussian profiles to obtain accurate positions, and then instrumental distortions were corrected with the IRAF tasks `xyxymatch`, `geomap`, and `geotran`. The resultant pixel scale is ∼0.02″ pixel^{-1} in the WFPC2 images and ∼0.04″ pixel^{-1} in the NICMOS2 images. The FWHM of the PSFs was ∼3 pixels. Flux measurements were performed using the IRAF `daophot` tasks.

For the WFPC2 data, *HST* magnitudes were converted to the Johnson-Cousins system using the transforms of Dolphin (2000, 2009), which include charge transfer efficiency (CTE) corrections.

THIS WORK: Whilst the broad band NICMOS filters, *F110W*, *F160W* and *F205W*, are roughly equivalent to the *J*, *H* and *K* filters respectively, colour transformations are not well constrained for late-time SN spectra at NIR wavelengths, and consequently magnitudes were not converted to the standard *JHK* photometric system. The late-time *HST*-NICMOS magnitudes listed in Table 5.9 are for the *HST* filters in the Vegamag system, which uses an estimate of the flux density of Vega, from synthetic spectra integrated over

the NICMOS bandpasses, as a photometric zeropoint. For each filter and epoch, the measured count rate (*CR*, in units of $\mathrm{DN\,s^{-1}}$) at the position of the SN was converted to flux by multiplication with the *PHOTFNU* ($\mathrm{Jy\,s\,DN^{-1}}$) conversion factor given in the fits header, where *PHOTFNU* is the bandpass-averaged flux density for a source that would produce a count rate of $1\,\mathrm{DN^{-1}}$. An approximate Vega-normalised magnitude was then calculated from the following equation (NICMOS data handbook; Thatte et al. 2009):

$$m = ZP(Vega) - 2.5\log_{10}(PHOTFNU \times CR \times \langle F_\nu(Vega)\rangle^{-1})$$

where $\langle F_\nu(Vega)\rangle$ is the bandpass averaged flux density (in Jy) for the NICMOS filters using a model reference spectrum of Vega[3] (Bohlin 2007) and $ZP(Vega)$ is the magnitude of Vega, which is defined to be 0.00 mag under the California Institute of Technology (CIT) infrared photometry scale.

WIYN/WHIRC The WHIRC (Meixner et al. 2010) has a 2048×2048 HgCdTe VIRGO detector with a pixel scale of $\sim 0\farcs1\,\mathrm{pixel^{-1}}$. Sky conditions during the observation were fair, with a seeing of $\sim 0\farcs8$. To minimise the effects of high background levels and pixel-to-pixel variations on the array, dithering techniques were employed whereby the source was offset in each frame of a series of exposures. The offset images were used for sky level corrections. Data reduction was carried out using standard IRAF tasks. The array linearity correction was performed using the WHIRC task `wprep` and a distortion correction was applied using files downloaded from the WIYN-WHIRC web page[4]. A selection of 2MASS stars close to SN 2004et were used for final flux calibration. The WIYN *H*-band observation of SN 2004et on day 1803 was the last of our NIR observations of the SN, some 5 years after explosion. The SN was not clearly detected due to the contribution from neighbouring stars that were resolved in the high-resolution *HST*-NICMOS observations (on days 1019 and 1215; see the following section). Consequently, an upper limit to the magnitude was derived. The magnitude in an aperture of radius $0\farcs6$ (~ 17 pc, for the adopted distance of 5.9 Mpc) was measured using the IRAF `daophot` tasks. Estimated contributions from 3 neighbour stars resolved in the high-resolution NICMOS *F160W* filter ($\simeq H$ band) were measured from the NICMOS data and subtracted from the WIYN magnitude to provide the final upper limit presented in Table 5.9.

[3]Taken from the NIC2 table of Photometric Keywords and Vegamag Zeropoints at

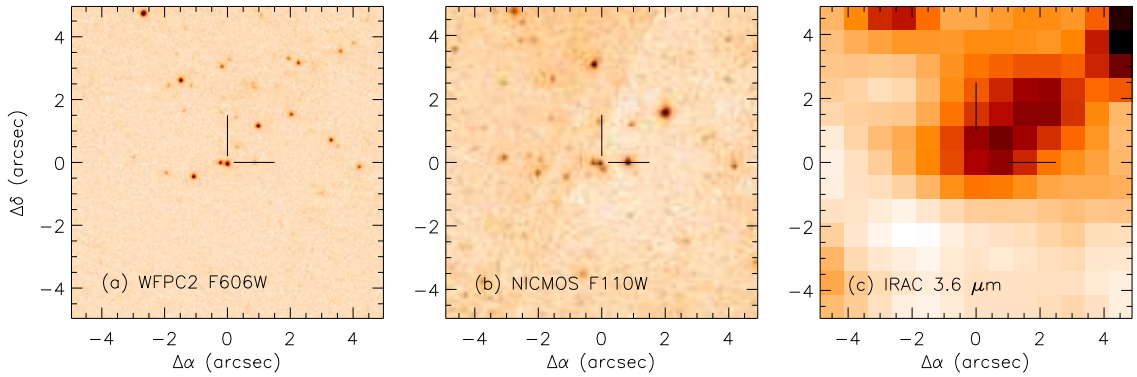

Figure 5.9: Late-time high-resolution *HST* images reveal a complex field compared with *Spitzer* IRAC data. Panel (a) shows the WFPC2 *F606W* image at day 1019 with a 5″×5″FOV centred on the SN position. A source assumed to be the SN is located at the centre of the image (indicated by the cross-hairs), with a close companion to the east ("star 2") which is detected in both WFPC2 filters. Panel (b) shows the equivalent field in the NICMOS *F110W* filter at the same epoch. Star 2 is detected in all 3 NICMOS filters together with an additional red object just south of the SN position. For comparison, panel (c) shows the *Spitzer* IRAC 3.6 μm image at day 1054.

5.7.3 Late-time high resolution *HST* images

The late-time high resolution *HST* images reveal that the single point source seen at the SN position in the *Spitzer* images is actually a complex field comprised of at least 3 sources. Figure 5.9 shows example *HST* WFPC2 *F606W* ($\approx V$) and NICMOS *F110W* ($\approx J$) images from July 2007 (day 1019) compared to the *Spitzer* IRAC 3.6 μm image from August 2007 (day 1054). Each field of view is centred on the position of the SN and a source is located at this position indicated by the cross-hairs. The star to the east ("star 2") was detected in both WFPC2 filters and all three NICMOS filters at days 1019 and 1215. The third star to the south of the SN position ("star 3") was detected in all three NICMOS bands but was not detected in the WFPC2 filters at either epoch. The magnitude of star 2 was measured from the WFPC2 images and transformed to V and I_c band magnitudes as described previously for the SN.

THIS WORK: The V and I_c magnitudes of star 2 were de-reddened using $E(B-V) = 0.41$ mag (Zwitter et al. 2004) and adopting the extinction law of Cardelli et al. (1989) with $R_V = 3.1$, corresponding to $A_V = 1.27 \pm 0.22$ mag. The intrinsic $(V-I)_c$ colour was then used to estimate an R_c band magnitude using a table of intrinsic colours as a function of

http://www.stsci.edu/hst/nicmos/performance/photometry/postncs_keywords.html
[4]http://www.noao.edu/wiyn/

spectral type compiled by the Space Telescope Science Institute (STScI)[5] based on the work of Fitzgerald (1970) and Ducati et al. (2001). The derived colour index of $(V - I)_c = 0.8$ indicated star 2 was a K1.0 star with an intrinsic R_c magnitude of ~22.5. The equivalent reddened R_c magnitude of 23.53 ± 0.50 was in reasonable agreement (within the errors) with a magnitude estimated from fitting two PSFs to the blended 'SN plus star 2' in the R_c-band GMOS-N image at day 1412. This PSF-fitted measurement (made by collaborator Ben Sugerman) gave an R_c-band magnitude for star 2 of 23.63 ± 0.19. A B-band magnitude for star 2 of 25.46 ± 0.50 was estimated in the same way.

The estimated reddened B and R_c magnitudes of star 2, together with the measured V and I_c magnitudes, were subtracted from the optical magnitudes of SN 2004et obtained from the Subaru-FOCUS and GMOS-N observations from day 646 onwards. During this time the SN had faded substantially such that the neighbouring star 2 made a significant contribution to the brightness measured at those epochs. At day 646, the estimated contribution from star 2 was ~ 8 % in the V band and ~ 10 % in the I_c band, whilst by day 1412, the contribution was almost half that of the total flux in both bands. For epochs earlier than day 500, the brightness contribution from star 2 was ≤ 1 %.

The late-time Gemini-NIRI *JHK* photometry at day 652 have not been corrected for contamination by stars 2 and 3. As previously explained, the NICMOS magnitudes are listed in the *HST* Vegamag system, and were not converted to the standard *JHK* photometric system since colour transformations are not well constrained for late-time SN spectra at NIR wavelengths. It is possible that these neighbouring stars made a small but significant (~ 10 %) contribution to the brightness measured in the NIRI observations at day 652, so the uncertainties on the day 690 interpolated flux densities in Table 5.9 have been increased to reflect this, by adding a further 10 % error in quadrature to the original flux uncertainty.

5.7.4 Photometry and light curve evolution

THIS WORK: The final optical *VRI* magnitudes for SN 2004et are presented in Table 5.8, including those of neighbouring star 2 discussed previously. The magnitudes for epochs from day 646 onwards have been corrected for the contribution from star 2, but this was not necessary for earlier epochs when the SN brightness dominated. The B-band magnitude at day 646, corrected for the contribution from star 2, is detailed in the notes

[5] http://www.stsci.edu/ inr/intrins.html

Table 5.8: Optical photometry of SN 2004et.

UT date	Age [days]	Magnitudes V	R_c	I_c	Source
2004-12-10	79	13.09 ± 0.04	12.38 ± 0.03	11.93 ± 0.03	Tenagra II
2004-12-20	89	13.21 ± 0.03	12.45 ± 0.03	11.98 ± 0.03	Tenagra II
2005-08-05	317	17.35 ± 0.02	16.52 ± 0.03	15.91 ± 0.04	Gemini GMOS-N
2005-10-31	404	18.28 ± 0.04	17.69 ± 0.03	16.87 ± 0.04	Gemini GMOS-N
2006-06-30	646*	21.59 ± 0.55†	21.00 ± 0.55†	20.63 ± 0.56†	Subaru FOCAS
2006-07-18	664	22.13 ± 0.06†	21.56 ± 0.09†	21.37 ± 0.11†	Gemini GMOS-N
2007-07-08	1019	23.20 ± 0.20‡	···	22.70 ± 0.20‡	*HST* WFPC2
2008-01-20	1215	23.40 ± 0.30‡	···	23.00 ± 0.30‡	*HST* WFPC2
2008-08-04	1412	23.80 ± 0.40†	22.87 ± 0.28†	22.80 ± 0.70†	Gemini GMOS-N
Star 2		24.2 ± 0.3	23.5 ± 0.5	22.9 ± 0.4	*HST* WFPC2
Zero-magnitude flux [Jy]		3670.3	2972.3	2402.1	Evans (1993); Glass (1999)
λ_{eff} [μm]		0.55	0.64	0.80	

* Optical photometry at day 646 was estimated from an archival Subaru-FOCAS spectrum by integrating over the *BVRI* filter transmission curves. The *B* band magnitude of SN 2004et at this time was 22.47 ± 0.22, corrected for an estimated *B*-band contribution from star 2 of 25.46 ± 0.50 (see text).

† The SN magnitudes at these late epochs have been corrected for contamination by star 2 (whose magnitudes measured from the high-resolution *HST* data are listed in the final table entry).

‡ Since the SN and star 2 were resolved in the day 1019 and day 1215 *HST* images, the magnitudes given for these epochs are for the SN alone.

to the table. The NIR *JHK* magnitudes of the supernova are given in Table 5.9, although the magnitudes measured from the NICMOS images at days 1019 and 1215 are *HST* Vegamags (as previously explained). The optical and NIR light curves are presented in Figures 5.10 and 5.11 respectively.

Figure 5.10 combines the *BVRI* data of Sahu et al. (2006) with the SEEDS data described above to provide optical light curves (open symbols) from a few days after the explosion to almost 4 years later. The light-curves are well-sampled until at least day 400, but less-so beyond this time. This is generally found to be the case for Type II SNe, since very few have been observed beyond ∼500 days. However, SN 1987A, the closest supernova to have occurred in the past century, has been well-studied for over 2 decades and provides detailed light curves for comparison. The broad-band *BVRI* light curves of SN 1987A (Hamuy & Suntzeff 1990; Walker & Suntzeff 1991)[6] are plotted as solid curves in Figure 5.10, normalised to the data of SN 2004et at around 200 days. The light curve evolution of both supernovae is quite similar from the early nebular phase (∼160 days) to around day 650, although beyond this time, their evolution is markedly different. The brightness of SN 2004et clearly levels off from around day 1000 in the *VRI* bands (the last *B*-band measurement was at day 646), while SN 1987A continued to fade. Interestingly,

[6] Hamuy & Suntzeff (1990) data downloaded from the NOAO FTP archive: ftp://ftp.noao.edu/sn1987a/ubvri.txt

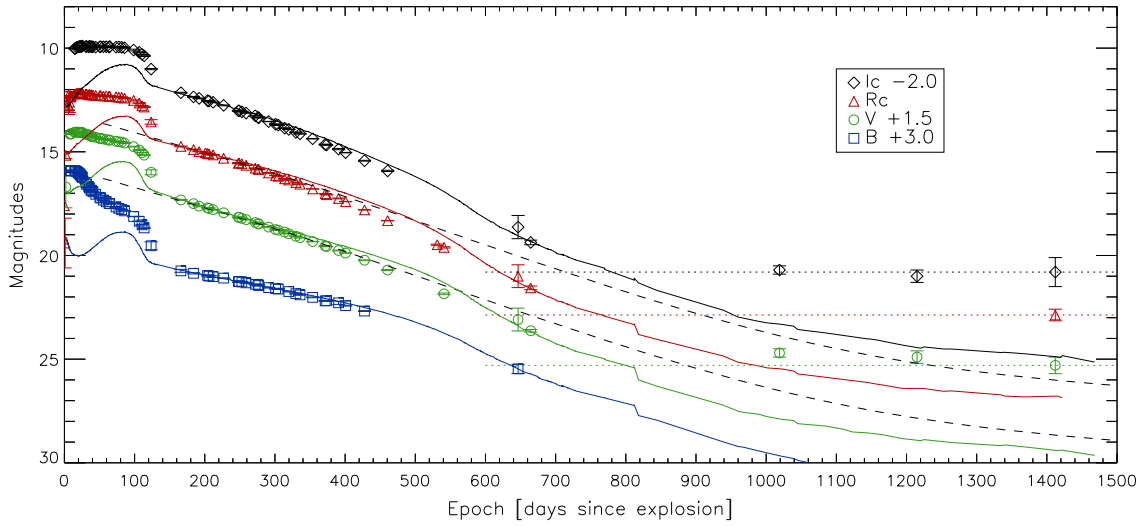

Figure 5.10: *BVRI* light curves of SN 2004et. For clarity, the plots have been vertically shifted by the amounts shown in the legend. The black dashed lines are the expected light curve based on the decay of ^{56}Co and other isotopes (Woosley et al. 1989) normalised to the *V* and *R* band magnitudes of SN 2004et during the early nebular phase (between ~160–260 days). The solid lines are the corresponding light curves of SN 1987A (Hamuy & Suntzeff 1990; Walker & Suntzeff 1991) normalised to those of SN 2004et at ~ 200 days. Dotted lines are only to guide the eye along the horizontal or "flat" parts of the light curve. These curves are typical for SNe that show a light echo, in that the light curve levels off or "flattens" once the SN flux drops below that of the echo.

the slope of the radioactive decay curves resemble those of SN 1987A between days ~ 720 and 800, around the time when dust production for SN 1987A was assumed to have ended (day 775; Wooden et al. 1993).

For the first few years during the nebular phase, the light curve of Type II SNe is predominantly powered by γ-rays from the radioactive decay of ^{56}Co to ^{56}Fe, at a rate corresponding to the *e*-folding time of the ^{56}Co decay (τ_{56} = 111.3 days). For example, the *R*-band photometry of the Type II SN 1990E (Benetti et al. 1994) closely follows this evolution through to ~ 540 days post-explosion, suggesting that simple ^{56}Co decay provides a good estimate of the unextinguished *R*-band light curve for at least that long. The expected decay rate is γ (mag per 100 days) = 0.98 for complete γ-ray trapping (Patat et al. 1994). For SN 2004et, Sahu et al. (2006) found that the decay of the broad band *BVRI* light curves in the early nebular phase (180–310 days) was linear, with decay rates of γ_B ~ 0.64, γ_V ~ 1.04, γ_R ~ 1.01 and γ_I ~ 1.07. Maguire et al. (2010) found similar results from their own data (~ 136–300 days), with $\gamma_B = 0.64 \pm 0.02$, $\gamma_V = 1.02 \pm 0.01$, $\gamma_R = 0.92 \pm 0.01$ and $\gamma_I = 1.09 \pm 0.01$. With the exception of the *B* band, the decay rates were close to that of ^{56}Co decay, suggesting that γ-ray trapping was efficient during this phase.

However, both authors found that the optical decay rates of SN 2004et steepened beyond ~300 days, suggesting that either the supernova had become transparent to γ-rays and hence γ-rays as a source of energy were escaping, or that dust was forming within the ejecta and causing localised optical extinction, or possibly was due to both phenomena.

To investigate this further we can look again at the radioactive deposition. As previously mentioned, as the ejecta expand, their opacity to γ-rays is expected to decrease, which results in a modified light curve of the form (Woosley et al. 1989):

$$L_{56}^{\gamma}(t) \propto e^{-t/\tau_{56}} [1 - e^{-\kappa_{56}\,\phi_0\,(t_0/t)^2}], \tag{5.1}$$

where the term in the brackets is the deposition function, i.e., the fraction of γ-rays deposited in the envelope; $\kappa_{56,\gamma} = 0.033$ cm^2 g^{-1} is the average opacity to ^{56}Co-decay γ-rays, and $\phi_0 = 7{\times}10^4$ g cm^{-2} is the column depth at the fiducial time $t_0 = 11.6$ days chosen to match the bolometric light curve of SN 1987A.

After this first source of decay energy has become sufficiently weak, other energy sources which could become important in powering the very late time light curves are γ-rays, positrons and electrons from the radioactive decay of ^{57}Co, ^{44}Ti and ^{22}Na. The equations that describe the energies from all these isotopes, including ^{56}Co, are summarised by Li et al. (1993), following the work of Woosley et al. (1989), to describe the deposition behaviour of SN 1987A. Adopting the same deposition behaviour for SN 2004et, the radioactive decay curve attributable to the energy sources from these isotopes, including a term to account for the decrease in opacity to γ-rays as the ejecta expands, has been plotted in Figure 5.10 (dashed line) over both the *V* and *R* band magnitudes of SN 2004et, normalising to the early nebular phase data (~160–260 days). As expected, with the exception of the *B* band, the decay rates during the early nebular phase closely follow those of the radioactive decay deposition. However, from about 400 days the *R* band light curve has clearly begun to decline more rapidly than the expected light curve from radioactive decay deposition. The *I* band follows a similar trend, whereas the steepening of the decline rate appears to occur slightly later in the *V* band, having clearly begun sometime between 460 and 540 days. In comparison with the expected radioactive decay deposition behaviour of SN 1987A, as modelled by Li et al. (1993), there is evidence for a steepening decline of the light curves, indicative of dust formation in the ejecta of SN 2004et from

around 400 days, and possibly earlier (Sahu et al. 2006; Maguire et al. 2010). From the V-band light curve (Figure 5.10), the difference between the observed and predicted light curves was estimated to be 0.8 mag by day 690, if allowance is made for the effective opacity term for ^{56}Co γ-rays, or 1.5 mag if the term is neglected.

It is clear that the elevated brightness of SN 2004et after 1000 days cannot be explained by the inclusion of isotope decays, such as ^{57}Co and ^{44}Ti, which could be important at these late times. The plateauing of the optical light curves above the expected radioactive decay suggests an additional energy source has come into play by at least day 1000 and is consistent with the late rise observed in the mid-IR observations after this time. Similar phenomena observed in other SNe have been attributed to light echoes (e.g., SN 2007od; Andrews et al. 2010) and this scenario is investigated for SN 2004et by Sugerman et al. (in preparation).

Figure 5.11 presents the late-time NIR light curves (open symbols) of SN 2004et based on the SEEDS data described previously. The *JHK* light curves of SN 1987A (solid lines; Bouchet & Danziger 1993) have been arbitrarily scaled to the early nebular phase data of SN 2004et for comparison. The NIR light curves of SN 2004et are not well-sampled but clearly deviate from those of SN 1987A by day 646, after which time SN 2004et is systematically higher. The NIR light curve evolution reflects that of the optical, with a relative plateau in brightness occurring from around 1000 days, consistent with a light echo hypothesis. However, by day 1803 (see inset in Figure 5.11), the *H*-band brightness has faded to beyond a clear detection with the WHIRC detector on the 3.5-m WIYN telescope. The derived upper limit of 22.6 mag accounts for contamination by neighbouring stars (as described in Section 5.7.2). It is possible that the SN has faded sometime after day 1215, which would be contemporaneous with the fading of the SN seen in the mid-IR with the *Spitzer*-IRAC 3.6 and 4.5 μm observations between days 1395 and 2151, where the steepest decline occurred between days 1395 and 1779.

For an assumed light echo scenario to explain to the post-1000 day data, it is plausible that the fading which possibly occurs sometime after day 1215 in the NIR and after day 1395 in the mid-IR, is a consequence of an echo moving into the furthest regions of the CS material, where a much smaller volume of material would be illuminated. These latest data are useful for constraining the geometry of any proposed echoing material. See Section 5.10 for a summary of initial results for light echo models to explain the post-1000 day optical, NIR and mid-IR data for SN 2004et (Sugerman et al., in preparation).

Table 5.9: Near-infrared photometry of SN 2004et.

UT date	Age [days]	Magnitudes J	H	K	Source
2005-06-17	268	15.14 ± 0.05	15.15 ± 0.03	···[a]	Steward/Bok IR Camera
2005-08-05	317	16.01 ± 0.03	15.84 ± 0.03	15.18 ± 0.04	Gemini NIRI
2005-10-17	390	16.96 ± 0.03	16.62 ± 0.03	16.23 ± 0.04	Gemini NIRI
2006-07-06	652	20.09 ± 0.05	19.52 ± 0.06	19.19 ± 0.07	Gemini NIRI
2007-07-08	1019	22.25 ± 0.13[b]	22.61 ± 0.36[b]	21.91 ± 0.28[b]	*HST* NICMOS
2008-01-20	1215	22.55 ± 0.14[b]	22.69 ± 0.43[b]	21.44 ± 0.18[b]	*HST* NICMOS
2009-08-30	1803	···	≤ 22.6	···	WIYN WHIRC
Zero-magnitude flux [Jy]		1656.3	1070.9	672.8	Glass (1999)
λ_{eff} [μm]		1.25	1.65	2.20	

[a] There is no K band magnitude at day 268 as unusual image artifacts compromised the photometry.
[b] *HST* Vegamags in NICMOS2 filters $F110W$ (≃ J band), $F160W$ (≃ H band) and $F205W$ (≃ K band) for days 1019 and 1215. For each filter and epoch, the measured count rate (CR, in units of DN s^{-1}) at the position of the SN was converted to flux by multiplication with the $PHOTFNU$ (Jy s DN^{-1}) conversion factor given in the fits header, where $PHOTFNU$ is the bandpass-averaged flux density for a source that would produce a count rate of 1 DN^{-1}. $PHOTFNU = 1.21 \times 10^{-6}$, 1.50×10^{-6} and 9.69×10^{-7} Jy s DN^{-1} for $F110W$, $F160W$ and $F205W$ respectively.

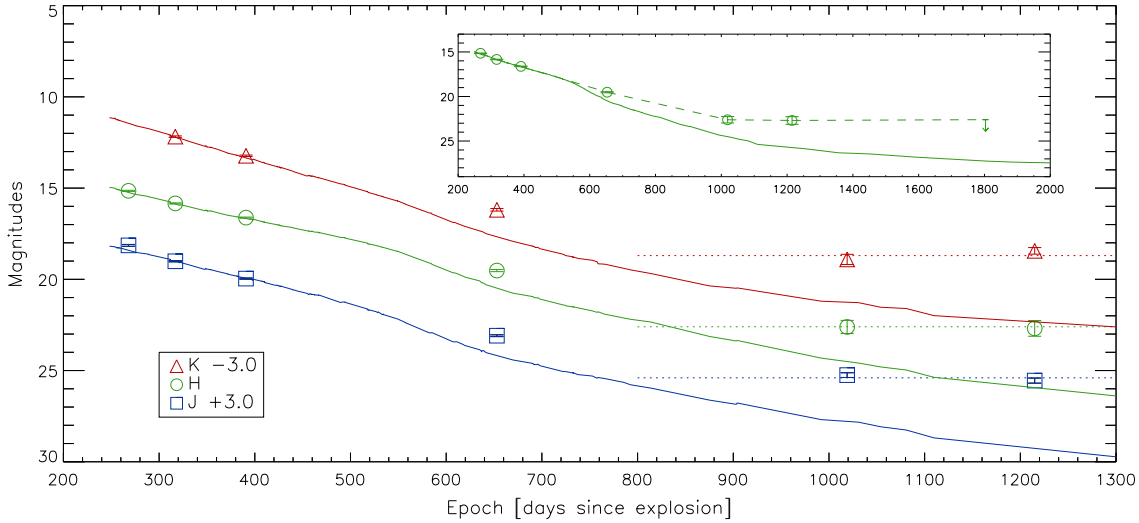

Figure 5.11: Late-time NIR light curves of SN 2004et, based on the SEEDS photometry listed in Table 5.9. For clarity, the plots have been vertically shifted by the amounts shown in the legend. The solid lines are the corresponding light curves of SN 1987A (Bouchet & Danziger 1993) normalised to the light curves of SN 2004et at day 317, during the early nebular phase. Dotted lines are only to guide the eye along the horizontal or "flat" parts of the light curve. The inset shows the H-band light curve only for the extended period to day 1803, the final SEEDS NIR observation, taken with the WIYN-WHIRC in August 2009. Contamination from neighbouring sources observed in the high-resolution NICMOS images at days 1019 and 1215 resulted in an ambiguous detection of the SN with the WHIRC at day 1803, for which an upper limit (downward pointing arrow) has been derived.

5.8 Optical–IR SED analysis via blackbody fitting: Days 64-1395

The mid-infrared photometry listed in Table 5.6, along with the optical and NIR photometry listed in Tables 5.8 and 5.9 and the optical photometry of Sahu et al. (2006), have been used to construct the spectral energy distributions (SEDs) of SN 2004et at each of the 12 IRAC observation epochs from days 64 to 1395.

To investigate the physical processes that determine the observed optical and infrared continuum emission and their evolution, blackbodies were matched to each of the SEDs. Where necessary, the light curves of the optical, NIR, PUI 16 μm and MIPS 24 μm data were used to interpolate their measured flux densities to the epochs of the IRAC data. It should be noted that to extrapolate the last B magnitude obtained on day 646 to the closest IRAC epoch at day 690, the better-sampled V-band decline rate during this period was adopted in order to account for the gradual flattening of the light curve. A simple extrapolation from previous epochs of B-band observations with earlier steeper decline rates would likely result in under-estimated fluxes at this epoch. Similarly, the JHK magnitudes from day 652 were extrapolated to the closest IRAC epoch of day 690 assuming the decline rate observed in the I_c-band during this period. Gemini Michelle flux densities at 11.2 μm were not interpolated due to insufficient data, but where available they are compared with the closest IRAC epoch.

The interpolated optical data were converted from the standard Johnson-Cousins BVR_cI_c magnitudes to flux densities using the zero-magnitude flux densities given in Evans (1993) and Glass (1999) (see Table 5.8). The interpolated Steward and Gemini NIR data were converted from standard JHK magnitudes to flux densities using the zero-magnitude flux densities from Glass (1999) based on the work of Bessell et al. (1998) (see Table 5.9). The late-time *HST*-NICMOS flux densities were obtained by multiplying the count rate measured for the SN by the *PHOTFLAM* (erg cm^{-2} Å^{-1} DN^{-1}) conversion factor from the fits image headers, where *PHOTFLAM* is the bandpass-averaged flux density in F_λ for a source that would produce a count rate of 1 DN s^{-1}.

All flux densities were de-reddened using $E(B-V) = 0.41$ mag (Zwitter et al. 2004) and assuming the extinction law of Cardelli et al. (1989) with $R_V = 3.1$, corresponding to $A_V = 1.27 \pm 0.22$ mag. Note that Kotak et al. (2009) found it was impossible to obtain a match to their dereddened optical continua without significantly overproducing the mid-IR flux, and so adopted $A_V = 1.0$ mag with the same extinction law and $R_V = 3.1$.

Blackbody fitting was carried out using the STARLINK software package DIPSO (Howarth et al. 2004). The `grid` and `bbody` commands were used to generate the blackbody curves at the required temperatures and the `atnorm` command was used to normalise the curves to the photometric flux densities. Blackbody parameters were calculated as discussed in Section 4.2.2.

A more detailed explanation of the fitting procedures and comments on individual epochs follow below. Interpretation of the results are discussed in Section 5.8.4.

5.8.1 Day 64

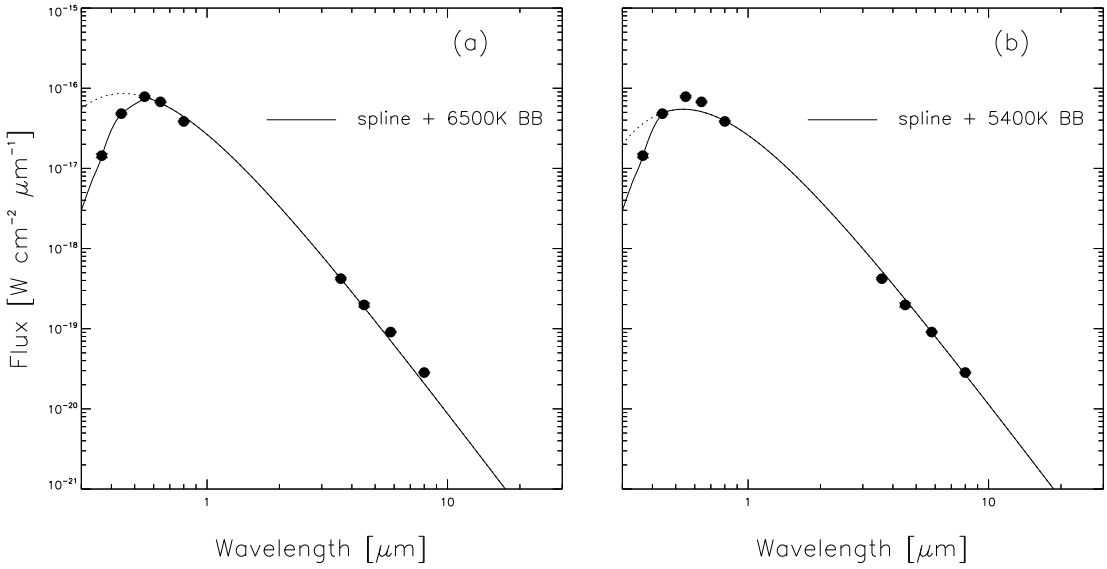

Figure 5.12: Two alternative blackbody fits to the SED of SN 2004et as defined by the optical and mid-IR observations at day 64 (wavelength range plotted: 0.3–30 μm). In panel (a) the solid line represents the fit from a blackbody of 6500 K at wavelengths greater than 5500 Å, combined with a spline curve fit to the *UBV* photometry extrapolated to shorter wavelengths. In panel (b) the solid line represents the fit from a blackbody of 5400 K at wavelengths greater than 4400 Å combined with a spline curve fit to the *UB* photometry extrapolated to shorter wavelengths. Flux densities have been de-reddened using $E(B-V)$ = 0.41 mag (Zwitter et al. 2004) and the extinction law of Cardelli et al. (1989) with R_V = 3.1. Statistical flux uncertainties are smaller than the symbol size.

Figure 5.12 shows two alternative fits to the SED at day 64, during the photospheric plateau phase of SN 2004et. As seen in panel (a), a single hot blackbody of temperature 6500 K, normalised to the IRAC flux at 3.6 μm, was found to be a good approximation to the optical *VRI* and mid-IR photometry. Panel (b) shows an alternative fit with a cooler blackbody of 5400 K, normalised to the IRAC 5.8-μm flux, which was found to better fit the longest mid-IR wavelengths and the *B*-band flux, but under-estimated the *V*- and

R-band fluxes. Whilst the 6500 K blackbody appears to provide a better match to the *V*–*I* band fluxes, there is likely to be a significant contribution from emission lines in the 5400–7000 Å wavelength region (Sahu et al. 2006; Kotak et al. 2009), which could explain the elevated *V* and *R* band fluxes compared to the 5400 K blackbody, since the blackbodies should mainly represent the continuum emission from the source.

Both blackbodies clearly over-estimate the flux at the shortest wavelengths (3400–4400 Å). A similar blue flux deficit relative to a blackbody fitted at longer wavelengths was seen at around this time for SN 1987A (Danziger et al. 1987; Wooden et al. 1993) and the phenomenon is briefly discussed below. A spline curve fitted to the *UB*(*V*) photometry was therefore used to estimate the effect of this blue deficit to the total flux. For the 6500 K blackbody, the spline curve extrapolated from the *UBV* fluxes was combined with the hot blackbody truncated at wavelengths $\leq V$ (5500 Å), yielding a total integrated flux of $5.8{\times}10^{-13}$ W m^{-2} (with a corresponding luminosity of $6.4{\times}10^{8}$ L$_{\odot}$) that was about 77% of the total integrated flux/luminosity from the hot blackbody alone. At wavelengths $\leq V$, the total flux corresponding to the spline fit constituted about 44% of that from the hot blackbody. For the 5400 K blackbody, the spline curve extrapolated from the *UB* fluxes was combined with the hot blackbody truncated at wavelengths $\leq B$ (4400 Å), yielding a total integrated flux of $4.5{\times}10^{-13}$ W m^{-2} (with a corresponding luminosity of $4.9{\times}10^{8}$ L$_{\odot}$) that was about 93% of the total integrated flux/luminosity from the hot blackbody alone. At wavelengths $\leq B$, the total flux corresponding to the spline fit constituted about 49% of that from the 5400 K blackbody fit.

In Figure 5.12, the solid lines in each plot represent the combined spline and truncated blackbody fit, whilst Table 5.10 lists the parameters for the single blackbodies only (see notes to the table for reference to the combined spline and truncated blackbody fits).

It is well known that all Type I SNe show a pronounced early-time deficit at ultraviolet (UV) wavelengths relative to a blackbody fitted at longer wavelengths (e.g., Panagia 2003). This has been explained as being due to strong line blanketing by the many low excitation lines of Fe II and other resonance lines shortwards of ~4000 Å (e.g., Branch & Venkatakrishna 1986). The situation for Type II SNe seems to be less clear. In his review of optical spectra of supernovae, Filippenko (1997) summarised that most Type II SNe do not show this feature, with the early-time spectra approximating a single-temperature Planck function from UV through to IR wavelengths, and occasionally even showing a slight UV excess. However, Fransson et al. (1987), from their studies of the peculiar

Type II SN 1987A, concluded that supernova atmospheres with a normal (solar) chemical composition can give rise to line blanketing effects, such as those seen in the UV spectra of SN 1987A. They proposed that the differences in UV spectra of supernovae may instead be due to differences in the density of the CSM. The earliest IUE (1150–3200 Å) spectra of SN 1987A ($\sim$ 6 days after explosion) showed a strong UV deficit in the wavelength range $\sim$ 1250–3200 Å, relative to the 6000 K blackbody curve defined at optical and infrared wavelengths (Danziger et al. 1987). This was still present at day 60, and possibly as late as day 260, as shown by the best-fit SEDs of Wooden et al. (1993).

The apparent UV drop-off relative to the blackbody fit to the photometric SED of SN 2004et at days 64 and 300 (the only IRAC epochs for which *U* band data was available) suggests that a similar effect is present in this Type II-P SN. Li et al. (2005*b*) noted from a spectrum of SN 2004et at day 9 that "there is a peculiar decline blueward of 4000 Å not commonly observed in the spectra of normal SNe II-P".

5.8.2 Days 300-828

The blackbody fits to the SEDs at days 300 to 828 are shown in Figure 5.13. The corresponding blackbody parameters are listed in Table 5.10. For the fluxes which were interpolated to the IRAC epochs (open circles), the uncertainties plotted are taken to be the largest of the uncertainties of the fluxes that were interpolated between, or extrapolated from, and do not include an estimate of the uncertainty associated with the interpolation itself.

For blackbody fits to the epochs from day 300 to day 828, more than one component was required to obtain a reasonable fit to the optical, NIR and mid-IR photometry. These were comprised of (i) a hot blackbody, with temperatures during the period 300–828 days ranging from 7100–10000 K, representing the optical and NIR continuum emission from the optically thick hot gas of the ejecta, (ii) a warm blackbody (420–650 K) representing the emission at mid-infrared wavelengths, and (iii) from day 464 onwards, a cooler (200–250 K) blackbody to account for emission at the longest mid-IR wavelengths (typically 16–24 μm). Excess emission is also present on days 300–406, but at a relatively constant level (see Figure 5.13 and discussion below).

Fits to the optical and NIR data with a hot component were made first, adjusting the fit by-eye to best match the fluxes within the errors. The NIR fluxes were found to be important in constraining the fits and the blackbodies were often normalised to the *J*, *H* or *K* fluxes. The contribution of the hot blackbody to the mid-IR emission was then accounted for by subtracting the normalised hot component from the observed fluxes. The residual IR fluxes were then fit with a second warm component in a similar manner, normalising where possible to the longer wavelength fluxes (5.8-8.0 μm), which are more sensitive to the warm dust emission, although see comments below regarding SiO band emission at 8 μm. Finally, where necessary, a cooler component was used to fit the excess at the longest mid-IR wavelengths, after subtracting the contribution from the warm blackbody component.

As was found for day 64, the *U* and *B* band fluxes at day 300 were significantly over-estimated by the hot blackbody that best matched the SED at longer wavelengths. The effect of this UV deficit was estimated by extrapolating a spline curve to the *UBV* data and combining this with the hot blackbody truncated at wavelengths $\leq V$ (5500 Å). The 'spline + truncated-hot blackbody + warm blackbody' yielded an integrated flux of 11.7×10^{-15} W m^{-2} (with a corresponding luminosity of 12.8×10^{6} L$_{\odot}$) that was about 73% of the integrated flux/luminosity from the hot + warm blackbodies alone. The total flux corresponding to the spline fit constituted about 40% of that from the hot blackbody at wavelengths $\leq V$. In panel (a) of Figure 5.13, the solid line represents the combined spline, truncated hot blackbody and warm blackbody fit, whilst Table 5.10 lists the parameters for the two-component blackbody fit only (although see notes to the table for reference to the combined spline and truncated blackbody fit).

During days 300 to 464, the optical *RI* fluxes were found to be in excess of the hot blackbody that best matched the *BV* and *JHK* fluxes. This is consistent with the results of Kotak et al. (2009) who demonstrated using the spectra of Sahu et al. (2006) that whilst the emission in the *BV* region was dominated by the continuum, strong emission lines in the *RI* region could account for their elevated photometric fluxes. After day 464, the excess in the optical *R* and *I* bands was no longer apparent and the hot blackbody components were a reasonable match to the interpolated optical and NIR data at days 690 and to the interpolated optical data at day 828. It should be noted that the optical light curves were not very well-sampled during this time and as a result the interpolated fluxes and corresponding blackbody parameters are subject to greater uncertainty.

From days 300 to 464, the mid-IR emission demonstrated a clear excess at 4.5 μm, as noted by Kotak et al. (2009). A similar feature has been seen in mid-IR photometry of other Type II SNe, such as the Type II-P SN 2003gd at day 499 (Sugerman et al. 2006), and SN 2007it at day 340 (Andrews et al. 2010). This can be attributed to emission from the carbon monoxide (CO) fundamental band at 4.65 μm which was directly observed in the infrared spectra of the Type IIpec SN 1987A from as early as 100 days after explosion (Suntzeff & Bouchet 1990) and stayed visible until at least day 615 (Wooden et al. 1993). The red wing of the same emission line was detected in the *Spitzer*-IRS spectra of the Type II-P SN 2004dj at days 109 and 129 (Kotak et al. 2005). Together with the detection of the first overtone of CO at ∼ 2.3 μm from NIR spectra of SN 2004et by Maguire et al. (2010) and in the NIR spectra of several other Type II SNe (Gerardy et al. 2002 and references therein), these observations indicate that strong CO emission is common in Type II SNe.

Kotak et al. (2009) also noted an excess at 8.0 μm compared to blackbodies matched to the mid-IR continuum emission from days 300 to 690. They found this to be consistent with a broad emission feature between 8–14 μm seen clearly in *Spitzer*-IRS spectra until at least days 450–481 and attributed this to silicate emission, with a contribution from the silicon oxide (SiO) fundamental band in the 7.7–9.5 μm region. SiO has previously been detected in other Type II SNe (e.g., in the spectra of SN 1987A at days 260 and 415, disappearing by day 615, Wooden et al. 1993; and in the *Spitzer*-IRS spectra of SN 2005af at day 214, Kotak et al. 2006). Kotak et al. (2009) noted that whilst the IRS spectra closest in time (day 823) to the IRAC epoch at day 690 showed little evidence for strong SiO emission, the 8.0 μm flux at day 690 was still under-predicted by the blackbody that best matched the continuum emission, indicating that the SiO emission, whilst diminishing, was still quite prominent at that time. These observations were used to help guide the fitting presented here during these epochs, such that the warm blackbody component was normalised to the 3.6 or 5.8 μm fluxes that best represented the continuum emission during these times. For the best-fit SED at day 300 (panel (a) in Figure 5.13), the Gemini 11.2 μm flux from day 311 is also under-estimated by the warm blackbody component. This excess could be attributable to the broad silicate emission feature seen at its strongest in the IRS spectra at days 294 and 349 presented by Kotak et al. (2009). The 8.0 μm excess is no longer evident after day 690, consistent with the IRS spectrum at day 823 presented by Kotak et al. (2009). Panel (f) of Figure 5.13 shows that by day 828 the observed 8.0 μm flux is well-matched by the blackbody fits.

As previously mentioned, a cooler blackbody component was only included for SED fits at epochs from days 464 onwards. However, from Figure 5.13 it can be seen there is a slight excess in the photometry at the longest wavelength of 24 μm between days 300 and 406. Model fits to the optical-IR SEDs of SN 1987A by Wooden et al. (1993) during a similar period (comparable epochs for SN 1987A are at days 260 and 415) included free-bound and free-free H I continuum emission components. It can be seen from their work that the predicted free-free continuum emission dominated the total flux at wavelengths $\gtrsim 30$ μm during this period. After this time, the contribution from free-free radiation declined significantly relative to the dust emission, which dominated the observed IR continuum of SN 1987A from days 615 to 775 at wavelengths longwards of 3 μm. A similar free-free emission component might explain the 24 μm excess seen for SN 2004et between days 300 and 406. However, Kotak et al. (2009) estimated that free-free emission could account for only ~ 20% of their total 24 μm flux at day 301, with the contribution declining to less than 1% by day 796. Instead they fitted a cold blackbody component to their fluxes at all epochs from day 300 onwards.

By day 464 the 16 μm flux was also in excess of the warm blackbody fit to the IRAC mid-IR fluxes and a cooler blackbody component was clearly required to fit the longest wavelength (16–24 μm) fluxes (Figure 5.13).

5.8.3 Days 1015–1395

Best fits to the SEDs at epochs of days 1015, 1054, 1191 and 1395 are shown in Figure 5.14 and the corresponding blackbody parameters are listed in Table 5.10. Hot (10000 K), warm (350–520 K) and cool (120–170 K) blackbody components were matched to the optical, NIR and mid-IR photometry. For days 1015 and 1191, the adopted NIR fluxes were those measured in the *F110W*, *F160W* and *F205W* NICMOS2 filters at the reasonably contemporary epochs of days 1019 and 1215.

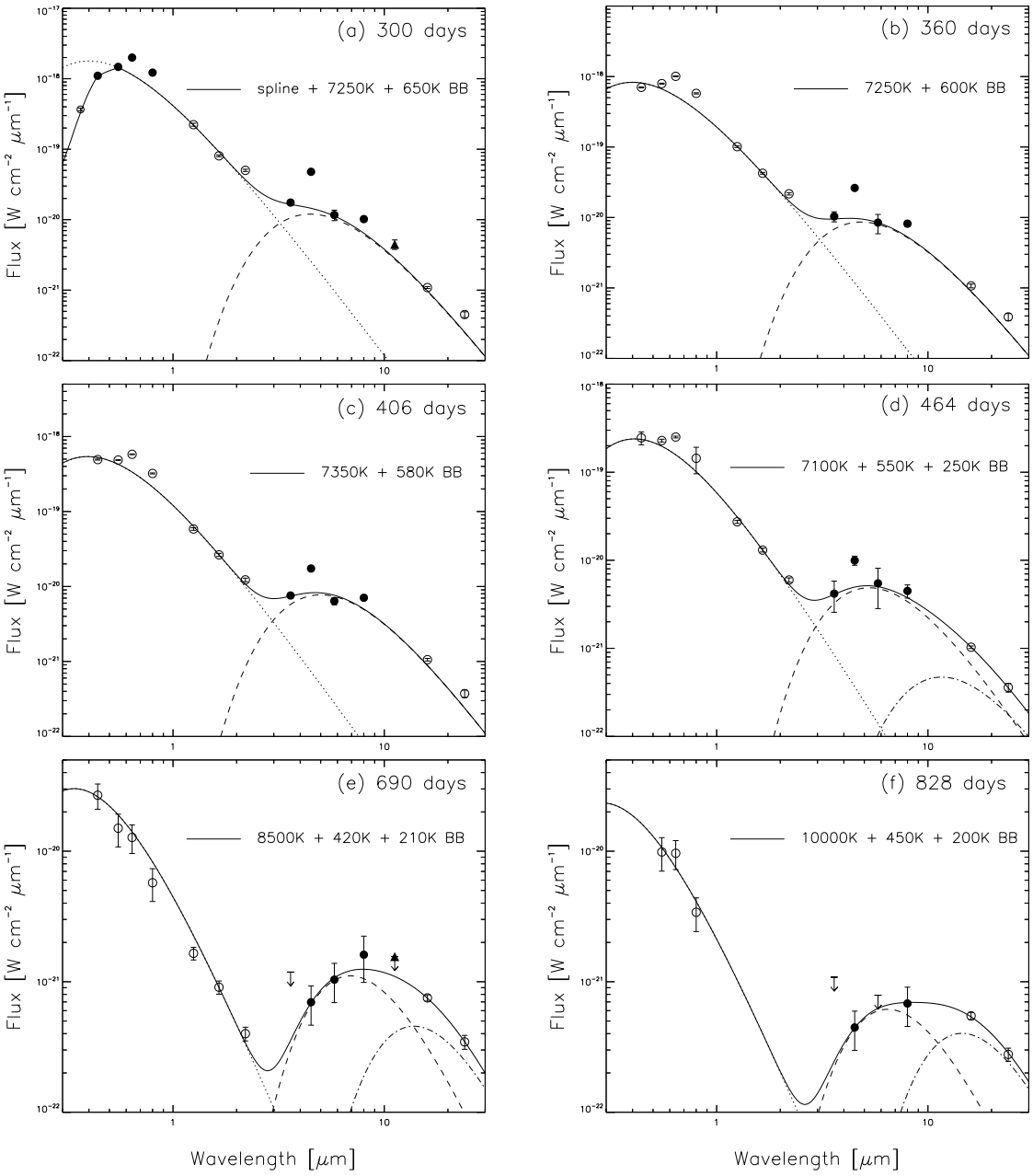

Figure 5.13: Blackbody fits to the day 300 to 828 SEDs of SN 2004et as defined by the optical-IR observations (wavelength range plotted: 0.3–30 μm). Filled circles indicate fluxes observed at the epoch of the IRAC observations. Open circles indicate optical, NIR and mid-IR photometry which has been interpolated or extrapolated to the epochs of the IRAC observations. Filled triangles indicate the closest epoch Gemini-Michelle N′-band photometry, which has not been interpolated (see Table 5.2 for epochs of the Michelle observations). Upper flux limits for non-detections are indicated by the downward-pointing arrows. Where error bars are not shown, uncertainties are smaller than the symbol size. All flux densities were de-reddened using $E(B-V)$ = 0.41 mag (Zwitter et al. 2004) and the extinction law of Cardelli et al. (1989) with R_V = 3.1.

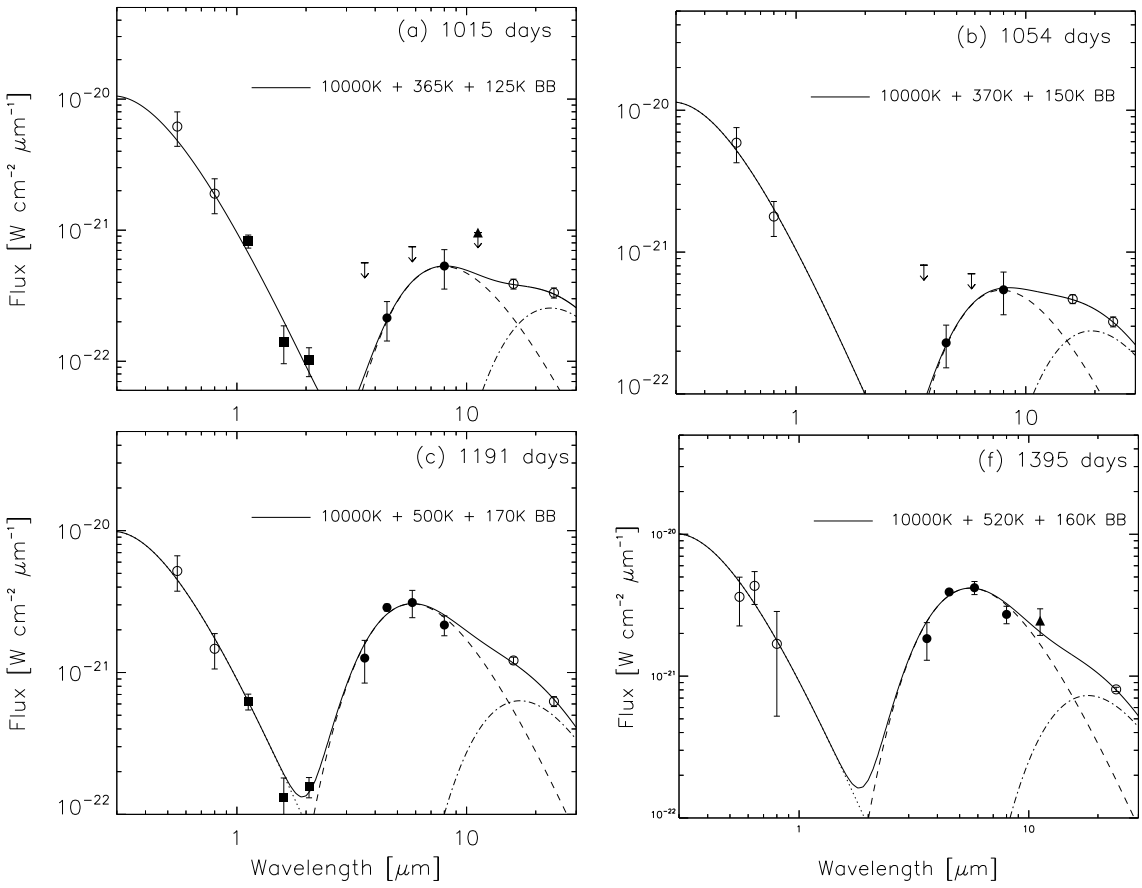

Figure 5.14: Blackbody fits to the day 1015 to 1395 SEDs of SN 2004et as defined by the optical-IR observations (wavelength range plotted: 0.3–30 μm). Filled circles indicate fluxes observed at the epoch of the IRAC observations. Open circles indicate optical, NIR and mid-IR photometry which has been interpolated or extrapolated to the epochs of the IRAC observations. Filled squares indicate the closest epoch (i.e., not interpolated) *HST*-NICMOS photometry and filled triangles indicate the closest epoch Gemini-Michelle N′-band photometry (see Table 5.2 for epochs of the Michelle and NICMOS observations). Upper flux limits for non-detections are indicated by the downward-pointing arrows. Where error bars are not shown, uncertainties are smaller than the symbol size. All flux densities were de-reddened using $E(B-V)$ = 0.41 mag (Zwitter et al. 2004) and the extinction law of Cardelli et al. (1989) with R_V = 3.1.

Table 5.10: Blackbody-fitted parameters to the SEDs of SN 2004et. Up to three components – hot, warm and cool – were used to fit the continuum emission of the SEDs (see text). For each component, R is the blackbody radius corresponding to the best fit temperature, T; v is the expansion velocity corresponding to the radius R; and L is the luminosity for an adopted distance to the SN of 5.9 Mpc.

Epoch [days]	T_{hot} [K]	F_{hot} [10^{-15} W m^{-2}]	R_{hot} [10^{15} cm]	v_{hot} [km s^{-1}]	L_{hot} [10^6 L$_\odot$]	T_{warm} [K]	F_{warm} [10^{-15} W m^{-2}]	R_{warm} [10^{15} cm]	v_{warm} [km s^{-1}]	L_{warm} [10^6 L$_\odot$]	T_{cool} [K]	F_{cool} [10^{-15} W m^{-2}]	R_{cool} [10^{15} cm]	v_{cool} [km s^{-1}]	L_{cool} [10^6 L$_\odot$]	F_{tot} [10^{-15} W m^{-2}]	L_{tot} [10^6 L$_\odot$]
64[1,2]	6500	584	1.38	2501	637	...	...	...	...	...	...	...	...	...	...	584	637[2]
64[1,3]	5400	446	1.75	3167	485	...	...	...	...	...	...	...	...	...	...	446	487[3]
300[4]	7250	10.9	0.15	59	11.9	650	0.81	5.16	1989	0.89	...	...	...	...	...	11.7	12.8[4]
360	7250	5.04	0.10	33	5.50	600	0.63	5.34	1718	0.69	...	...	...	...	...	5.67	6.19
406	7350	3.24	0.081	23	3.54	580	0.59	5.51	1570	0.68	...	...	...	...	...	3.83	4.18
464	7100	1.48	0.058	15	1.62	550	0.39	4.99	1246	0.42	250	0.083	11.15	2782	0.091	1.96	2.13
690	8500	0.16	0.013	2.2	0.17	420	0.12	4.67	784	0.13	210	0.096	16.96	2845	0.10	0.37	0.40
828	10000	0.10	0.0078	1.1	0.11	450	0.060	2.93	409	0.065	200	0.089	17.99	2515	0.096	0.25	0.27
1015	10000	0.047	0.0052	0.60	0.051	365	0.064	4.59	523	0.069	125	0.090	46.36	5286	0.098	0.20	0.22
1054	10000	0.050	0.0054	0.60	0.055	370	0.064	4.47	491	0.070	150	0.082	30.72	3374	0.089	0.20	0.21
1191	10000	0.044	0.0050	0.49	0.047	500	0.27	5.02	487	0.29	170	0.16	33.87	3291	0.18	0.48	0.52
1395	10000	0.045	0.051	0.42	0.049	520	0.35	5.32	441	0.39	160	0.20	42.33	3512	0.22	0.60	0.65

[1] Blackbody parameters from two alternative fits to the SED of SN 2004et at day 64 are detailed. The first entry in the table indicates the results of fitting a single-component 6500 K blackbody to the optical and mid-IR data, whilst the second entry in the table details an alternative fit with a 5400 K blackbody.

[2] As the 6500 K blackbody at day 64 over-estimated the U and B band fluxes, a spline curve fit to the UBV fluxes and extrapolated to shorter wavelengths was combined with the 6500 K blackbody fit to the longer wavelength data, where the blackbody was truncated at wavelengths shorter than the V-band – see panel (a) of Figure 5.12. The total integrated flux and corresponding luminosity of this "spline + 6500 K blackbody" fit are about 77% of those values for the pure 6500 K blackbody fit shown in this table.

[3] Similarly the 5400 K blackbody at day 64 over-estimated the U band flux. A spline curve fit to the UB fluxes and extrapolated to shorter wavelengths was combined with the 5400 K blackbody fit to the longer wavelength data, where the blackbody was truncated at wavelengths shorter than the B-band – see panel (b) of Figure 5.12. The total integrated flux and corresponding luminosity of this "spline + 5400 K blackbody" fit are about 93% of those values for the pure 5400 K blackbody fit shown in this table.

[4] At day 300, it was found that the hot component blackbody still over-estimated the fluxes at the shortest wavelengths. A spline curve fit to the UBV fluxes and extrapolated to shorter wavelengths was combined with the two-component blackbody fit to the longer wavelength data, as shown in panel (a) of Figure 5.13, where the 7250K blackbody component was truncated at wavelengths shorter than the V-band. The total integrated flux and corresponding luminosity of this "spline + 7250K + 650K blackbody" fit are about 73% of those values for the combined 7250K + 650K blackbody fit shown in this table.

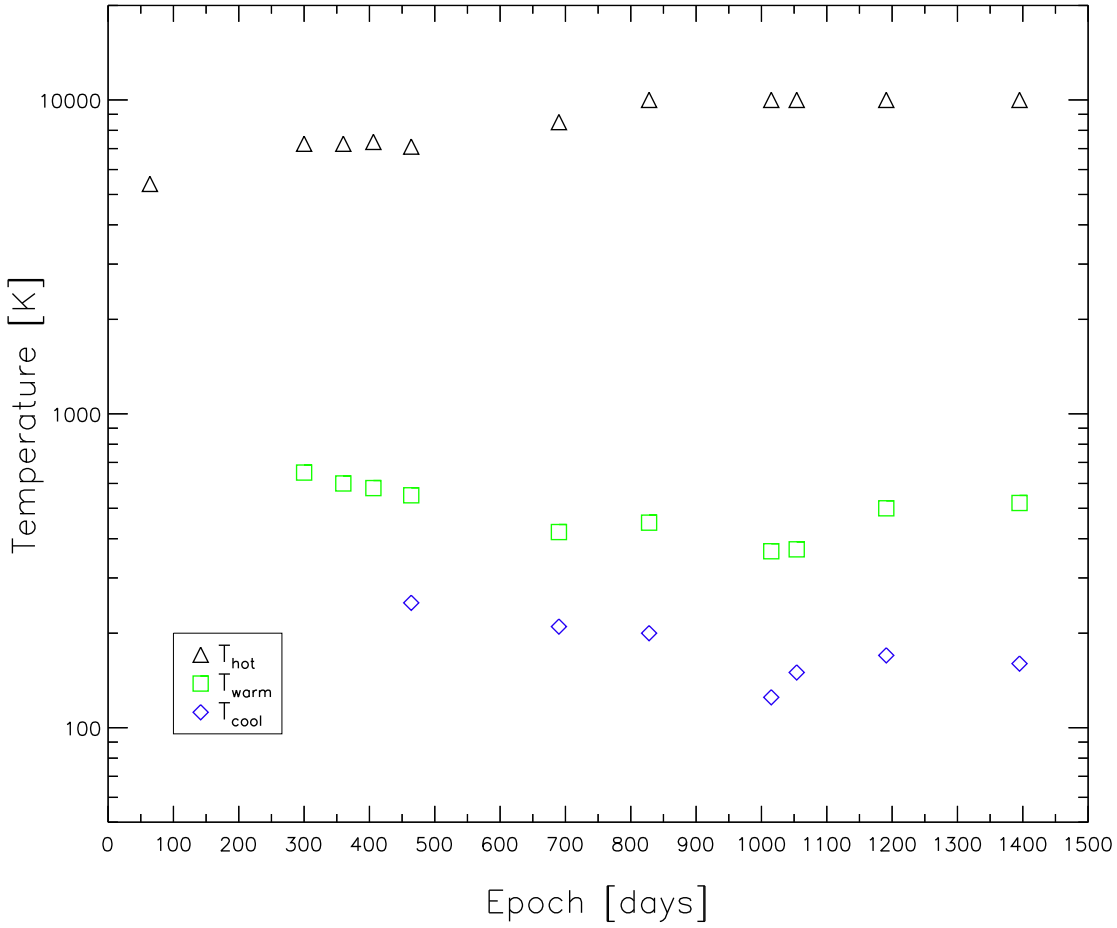

Figure 5.15: Temperature evolution from multi-component blackbody fitting to the SEDs of SN 2004et.

5.8.4 Discussion of results from blackbody fitting

The complete set of parameters from the blackbody fits to the photometry from days 64 to 1395 are listed in Table 5.10. The temperature evolution of the best fit multi-component blackbodies is shown in Figure 5.15.

Figure 5.16 shows the evolution of the luminosities of each of the blackbody components, and their sum, compared with the theoretical luminosity due to the radioactive deposition of ^{56}Co, ^{57}Co, and other isotopes, adopting the deposition behaviour of SN 1987A as modelled by Li et al. (1993) and Woosley et al. (1989). The radioactive decay deposition curve for SN 1987A was scaled by a factor of 0.69 to normalise it to the total luminosity of SN 2004et between days 300–464. It should be noted that the blackbody fits to the photometry mainly trace the continuum emission of the SN (known optical and mid-IR emission line features were deliberately not matched by the blackbodies as

discussed in the previous sections). As a consequence, the luminosities listed in Table 5.10 slightly underestimate the total luminosities.

Evolution of the hot component

Two alternative blackbody temperatures were found to explain the SED of SN 2004et at day 64. The first was a 6500 K blackbody which provided a good match to the V–I band fluxes, but slightly under-estimated the mid-IR fluxes at the longest wavelengths. The second was a cooler 5400 K blackbody which provided a good match the mid-IR fluxes and the B- and I-band fluxes but under-estimated the V- and R-band fluxes. The lower temperature blackbody can be considered a reasonable fit to the continuum emission of the SN at this time, since the excess V and R band fluxes are likely to be due to the significant emission-line contribution in the 5400–7000 Å wavelength region seen from the spectra of Sahu et al. (2006).

The hot blackbody is consistent with the continuum emission from the optically-thick gas of the ejecta photosphere during the plateau phase, with the Rayleigh-Jeans tail of the corresponding blackbody extending into the infrared. As the ejected envelope adiabatically expands and cools, the hydrogen ionised by the initial SN shock approaches the temperature for recombination (~ 5000 K) and a recombination wave recedes through the envelope. The recombination front defines the photosphere and as such the temperature of the photosphere is characterised by the recombination temperature of hydrogen. Wooden et al. (1993) found that a hot component of 5000-5500 K was a good match to the SED of SN 1987A from days 60 to 777, which they find to be in agreement with observations of other Type II supernovae by Kirshner et al. (1973). At a similar temperature, the 5400 K blackbody fit shown in panel (b) of Figure 5.12 appears to be most representative of the photospheric continuum emission at this time. Additional support for the lower temperature fit comes from the ejecta velocity of 3167 km s^{-1} implied by the emitting radius of the 5400 K blackbody, which is in reasonable agreement with the velocity of ~ 3500 km s^{-1} found by Sahu et al. (2006) for SN 2004et in the plateau phase, estimated from the minimum of weak, unblended absorption lines of Fe II at 4924, 5018 and 5169 Å. For these reasons, the 5400 K blackbody was adopted as the most representative fit to the SED at day 64 for this work. In comparison, Kotak et al. (2009) obtained a reasonable fit to the day 64 SED of SN 2004et with a single blackbody of temperature 5300 K, concluding there was little sign of thermal emission from dust.

As expected, the corresponding luminosity at day 64 exceeds that from radioactive decay deposition, which only begins to dominate the light curve during the nebular phase from ~ 130 days (Maguire et al. 2010) following the sharp decline from the plateau at ~ 110 days (Sahu et al. 2006). For the 5400 K blackbody fit the day 64 luminosity exceeds that from radioactive deposition by a factor of 4.9, or by a factor of 4.5 if considering the spline plus truncated blackbody fit which is a better match to the *U* band data. This compares to the factor of 3.8 found by Kotak et al. (2009).

By day 300, the estimated temperature of the hot blackbody component had increased to 7250 K and then remained relatively constant (± ~ 150 K) until day 464 (Figure 5.15), whilst its luminosity faded quite rapidly (by a factor of ~ 7) during this time (Figure 5.16). Note that at day 300, the blackbody fit significantly over-estimates the fluxes at the shortest wavelengths in the *U* and *B* bands, as also seen at day 64 (see discussion in Section 5.8.1). By day 690 the temperature had increased again to 8500 K and to 10,000 K by day 828, whilst the luminosity continued to decrease (by a factor of ~ 15). For epochs beyond 1000 days, the temperature of the hot component appears to remain constant. The luminosity of the hot component during these latest epochs appears to decrease much more slowly, possibly levelling off, and reflects the evolution of the optical and NIR light curves seen in Figures 5.10 and 5.11.

Evolution of the warm component

The warm component cooled monotonically from 650–420 K between days 300 and 690 (Figure 5.15). This is consistent with the fading of SN 2004et observed in the mid-IR during this time. The sum of the luminosities of the hot and warm components is less than or comparable to the radioactive deposition until at least day 690. On day 828 however, the sum of the hot and warm component luminosities is a factor of 1.7 higher than the predicted radioactive deposition luminosity. It should be noted that by this epoch the supernova had faded at shorter wavelengths such that it was not detected at 3.6 and 5.8 μm, resulting in a greater uncertainty in the blackbody fitting.

The presence of a mid-IR excess from day 300, demonstrated by the requirement of a warm component to match the SEDs from this time, and the evolution of this warm component from 300 to 828 days, are consistent with emission from dust freshly synthesised in the supernova ejecta, and agrees with the results of Kotak et al. (2009) from their interpretation of similar data.

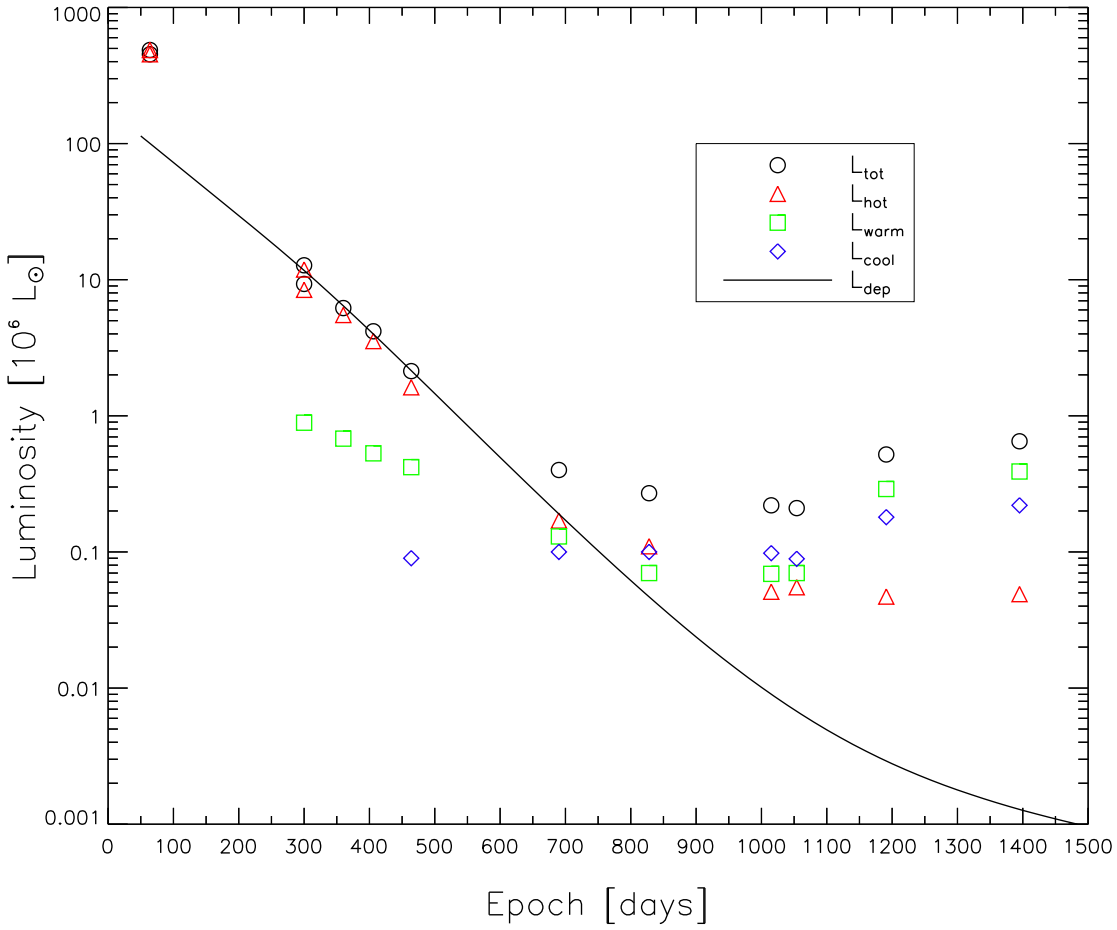

Figure 5.16: Luminosity evolution from multi-component blackbody fitting to the SEDs of SN 2004et compared to the luminosity due to radioactive deposition as scaled from the models of Li et al. (1993) for SN 1987A (see text for details).

It also supports the conclusions of Sahu et al. (2006) and Maguire et al. (2010) that dust formation occurred in the ejecta of SN 2004et after ~ 300 days based on their analysis of optical data, which showed signatures of dust formation such as a blueshift in the emission line profiles of Hα and [O I], as well as a steepening of the light curve around this time. Our independent analysis of these two optical signatures, discussed in sections 5.7.4 and 5.3, is consistent with the onset of dust condensation in the ejecta of SN 2004et between 300–500 days after explosion.

After 1000 days, the temperature of the warm component initially decreased (to ~ 360 K at days 1015 and 1054), followed by a clear rise again in temperature, to 500 K and 520 K at days 1191 and 1395 respectively, corresponding to the late rise in the mid-IR fluxes observed at this time. The approximately constant luminosity of the warm component between days 828 and 1054 corresponded to the lowest reached, since at day 1191 the

warm component luminosity had increased by a factor of 4.3. From day 1015 the warm component luminosity clearly exceeds that of the radioactive deposition (by a factor of ~ 8) and at day 1191 by a factor of over 100. The evolution of the warm component beyond 1000 days requires an additional energy source to explain the late rise in luminosity. Kotak et al. (2009) found similar results and from further modelling interpreted the late rise in the mid-IR flux as due to ejecta-CSM interaction, resulting in and the subsequent formation of a cool, dense shell of dust behind the reverse shock of the supernova. An alternative explanation of a light echo from pre-existing CSM dust has been investigated by Sugerman et al. (in preparation).

If the anomalously low day 828 value is omitted, then the radius of the warm blackbody component given by the fits to the 11 other epochs between days 300 and 1395 appears constant, with a value of $(5.0\pm0.3)\times10^{15}$ cm.

Evolution of the cool component

The cool dust component, required to the fit the mid-IR fluxes longwards of 16 μm from day 464 onwards, showed a monotonic decline in temperature from 250 K at day 464 to ~ 120 K at day 1015, but then increased slightly and remained around 160 K between days 1054 and 1395. Its luminosity stayed roughly constant from days 464 to 1054, but had increased by a factor of ~ 2 by days 1191–1395. The velocities implied by the minimum emitting radii of these cooler blackbodies ranged from ~ 2500–$6000\,\mathrm{km\,s^{-1}}$, consistent with an origin in the SN ejecta.

Kotak et al. (2009), on the other hand, found that the temperature of the cold component remained approximately constant at 120 ± 10 K for all epochs from day 300–1395, with minimum blackbody radii corresponding to velocities as large as $12000\,\mathrm{km\,s^{-1}}$, so they ruled out ejecta-condensed dust as a source of the emission.

The differences between our results for the cool component with those of Kotak et al. (2009) are most likely due to differences in the mid-IR data at the longest wavelengths, 16 and 24 μm, discussed in Section 5.6. Our 16 and 24 μm fluxes required generally higher temperature blackbodies to fit them than those of Kotak et al. (2009). Since our luminosities for the cool component are generally consistent with those of Kotak et al., the higher temperatures that we obtain resulted in lower minimum radii and therefore lower minimum outflow velocities.

5.9 Radiative transfer modelling: Days 300–690

The modelling described in this section was carried out in conjunction with SEEDS collaborators Dr Masaaki Otsuka (STScI) and Dr Roger Wesson (UCL).

In agreement with previous investigators (Sahu et al. 2006; Kotak et al. 2009), our blackbody fits to the optical and IR photometric data strongly support the inference that dust formed within the ejecta of SN 2004et from about 300 days after explosion. However, the total luminosity from the observed SED exceeds the estimated radioactive deposition luminosity, L_{dep}, by a factor of 4 on day 828 (Figure 5.16), indicating that an additional component dominates by that date. Consequently, epochs later than day 690, when the thermal IR emission can no longer be solely attributed to newly-formed dust in the ejecta, will not be discussed further.

To further investigate the time evolution of dust formation from the outflow in SN 2004et and to estimate the mass of dust present, a number of dust shell models were built to match the observed SEDs at the epochs between days 300 and 690 (Table 5.12). The models were calculated using the three-dimensional Monte Carlo radiative transfer (RT) code MOCASSIN (Ercolano et al. 2003, 2005) which accounts for the primary and secondary components of the radiation field in a fully self-consistent manner through absorption, re-emission and scattering of photons. The photon paths are followed from a specified source through a given composition, grain-size distribution, density and geometry of dust. The particular choices of these parameters are either constrained a priori or are varied until the model emission and extinction match the observations.

For the day 300–690 models we assumed that the observed IR emission originated from dust formed in the SN ejecta. Heating is due to γ-rays from the decay of ^{56}Co, which are reprocessed to optical and UV wavelengths through interaction with the gas. It is assumed that this leads to a local radiation field whose strength is proportional to the local ejecta density. Based on these assumptions, and following the previous modelling of SN 2003gd by Sugerman et al. (2006) and of SN 1987A by Ercolano et al. (2007), the RT models were constructed such that the dust and source luminosity were mixed within a spherical expanding shell of inner radius R_{in} and outer radius $R_{out} = YR_{in}$. For the dust density distribution, two cases were considered: (i) a smooth model with a dust distribution following an r^{-2} density profile, and (ii) a clumpy model where dense clumps exist in

Table 5.11: The contribution from line emission to the *VRI*-bands.

Epoch (days)	*V* (%)	*R* (%)	*I* (%)
336	21	75	68
417	20	58	60
454	26	58	57
649	26	60	27

a less-dense interclump medium (ICM), where the ICM follows a smooth r^{-2} density distribution, with the local heating source located only in the ICM. For each case, the observed SEDs were compared with those reproduced by the models to determine which gave the best fit to the observations.

Before running the models, the contribution from line emission to the *VRI*-bands was estimated using day 417 and day 454 optical spectra downloaded from the *SUSPECT* archive, plus day 336 TNG and day 646 Subaru spectra, along with the Subaru/FOCAS *VRI*-band filter transmission curves[7] because these have similar band centres and widths to the standard Johnson filters. The percentage line contributions in each band are listed in Table 5.11. When evaluating the fitting accuracy of the SED modelling, the *R* and *I* bands on days 300, 360, 406, and 464 were excluded because both bands were dominated by line emission at those epochs. The IRAC 4.5-μm data-points were also omitted from the fitting, due to the potentially very large CO line emission contributions in that band (Kotak et al. 2009). Although our modelling took into account potential emission from the broad silicate 10-μm band, the SiO fundamental vibrational band can also contribute to the IRAC 8-μm band – from *Spitzer* IRS spectra its contribution was deduced by Kotak et al. (2009) to be significant on days 300-464.

5.9.1 Smooth dust distribution models

Both amorphous carbon (AC) and silicate dust grains were considered. Optical constants were taken from Zubko et al. (1996) for amorphous carbon (their ACH2), and from Draine & Lee (1984) for the silicates. To investigate the dust composition, models were run with amorphous carbon:silicate mixtures of (100-x):x %, for x=0,20,40,60,80,100. It was found that the case of 20 % amorphous carbon and 80 % silicate (by mass) best matched the observed SEDs at all epochs, and this composition was adopted for all subsequent models.

[7]See http://www.naoj.org/Observing/Instruments/FOCAS/camera/filters.html

A standard MRN $a^{-3.5}$ distribution (Mathis et al. 1977) with $a_{\rm min}$=0.005 μm and $a_{\rm max}$=0.25 μm could not reproduce the steepness of the observed SED in the *JHK*-bands before day 690, nor the 16- and 24-μm flux densities. An improved fit was found using an MRN distribution with $a_{\rm min}$=0.1 μm and $a_{\rm max}$=1.0 μm and this was subsequently adopted for all epochs.

The density distribution in SN ejecta can range from approximately flat, to very steep in the layers that had formed the photosphere of the progenitor. Here, a r^{-2} law was adopted. It was found that distributions steeper than r^{-3} led to too much emission in the 1.6-3.6-μm spectral region at the earlier epochs, as a result of the high densities and high heating rates at the inner edge of the ejecta. As a first guess, initial values for R_{in} were adopted from the blackbody fitting (Section 5.8), and then varied to match the observations. Models were calculated with shell size scaling parameters $Y = R_{out}/R_{in}$ = 3.0, 3.2, 3.5, 4.0, 4.5. The adopted heating luminosities were the total luminosities measured from the blackbody fitting at each epoch, as listed in the final column of Table 5.10.

Table 5.12 lists the parameters of the best-fitting models for each epoch, including derived dust masses, M_d, and visual optical depths $\tau_{0.55}$. The variation in derived dust masses when parameters such as R_{in}, Y, L and T are varied from their best-fitting value allows us to estimate that the uncertainty in the derived dust mass is ≤50%. Figure 5.17 plots the emergent SEDs (red solid lines) and the observations, where the plotted flux densities have been corrected for foreground extinction.

The observed SEDs were best fitted using diffuse field radiation temperatures of 7000-8000 K, a little higher than the best-fitting hot blackbody temperatures listed in Table 5.10. This might be attributable to the effects of internal dust extinction on the emergent optical energy distribution in the radiative transfer models. The best-fitting models for the different epochs were not homologous, in that the $R_{\rm in}$ and $R_{\rm out}$ values did not increase linearly with time (Table 5.12). Since the derived dust masses increased by a factor of four between days 300 and 464, indicating ongoing dust formation, the dominant dust-emitting regions could in principal change with time. However, homologous models were also investigated for the different epochs, taking the day 300 value of Y = 4.0 from Table 5.12 and keeping it the same for subsequent epochs, adjusting only the total dust mass to obtain a best fit. These models are plotted as the blue solid lines in Figure 5.17. They produced slightly improved fits to the day 406 and 464 24-μm data-points, although they failed to match the observed SED on day 690 (Figure 5.17).

Table 5.12 shows that the smooth model dust masses increased from $0.4{\times}10^{-4}\,M_{\odot}$ on day 300 to $1.1{\times}10^{-4}\,M_{\odot}$ on day 464 and $4.4{\times}10^{-4}\,M_{\odot}$ on day 690. The inner and outer radii of the day 300 dust model correspond to expansion velocities of 2700 and 10,800 km s^{-1}, respectively, while those for the day 406 and 464 models correspond to expansion velocities of 2000 and 8000 km s^{-1} respectively. The above inner radii velocities are consistent with line absorption minimum velocities measured in optical spectra obtained at these epochs, e.g. Sahu et al. (2006) measured Fe II absorption minimum expansion velocities of $\sim$2000 km s^{-1} after day 150. Since absorption line optical depths scale as $\int ndr$, where n is the density, then for $n \propto r^{-2}$ or steeper density distributions, line optical depths are strongly weighted to the inner radii, where velocities are lowest, as are emission lines, whose emissivities typically scale as $\int 4\pi r^2 n^2 dr$. At the earliest epochs however, when ejecta densities are much higher, line optical depths of unity do not penetrate very deep into the outermost layers of the ejecta, where expansion velocities are much higher, e.g. the day 25 spectrum of Sahu et al. (2006) showed Hα and Hβ absorption minima at expansion velocities of $\sim$8000 km s^{-1} (their Fig. 9), consistent with the outer radius expansion velocities of our dust models, while Hα absorption was even detectable out to $-$14,500 km s^{-1} on day 25.

5.9.2 Clumpy dust distribution models

For the Type II SN 2003gd, Sugerman et al. (2006) demonstrated that smooth dust models could underestimate the dust mass by an order of magnitude or more compared to models that allow for clumping. Ercolano et al. (2007) showed that both smooth and clumpy dust models could fit the observed SEDs of SN 1987A at late epochs, with clumpy models able to accommodate significantly larger dust masses. Clumpy models were constructed for SN 2004et, employing a similar modelling strategy to that used for SN 1987A and SN 2003gd.

For the clumpy models, it is assumed that dense homogeneous clumps are embedded in a less-dense interclump medium (ICM) with an r^{-2} density distribution. The clumps have radius $\delta{\times}R_{out}$ and a volume filling factor, f. The same $\delta = 1/30$ and $f = 0.01$ were adopted for all epochs. The density contrast between the clumps and the smooth ICM is defined by $\alpha = N_{clump}(R_{in})/N_{smooth}(R_{in})$, where $N_{clump}(R_{in})$ and $N_{smooth}(R_{in})$ are the densities of the clumps and the smooth ICM at the inner radius, respectively. $\alpha = 55$ was set for all epochs. For the other parameters, the adopted source luminosity, temperature, dust

Table 5.12: Parameters for radiative transfer dust shell models.

			diffuse source					smooth		clumpy	
Epoch (day)	R_{in} (10^{15} cm)	R_{out}/R_{in}	L (10^6 $L_\odot$)	T (K)	AmC:Sil (%)	a_{min}–a_{max} (μm)	n(a)∝a^{-p} p=	$\tau_{0.55}$	M_d (10^{-5} $M_\odot$)	$\tau_{0.55}$	M_d (10^{-5} $M_\odot$)
300	7.0	4.0	12.8	8000	20:80	0.1–1.0	3.5	0.11	3.8	0.07	7.6
360	6.0	4.5	6.19	7000	20:80	0.1–1.0	3.5	0.20	5.6	0.12	10.0
406	7.0	4.0	4.18	8000	20:80	0.1–1.0	3.5	0.18	6.5	0.24	22.4
464	8.0	4.0	2.13	8000	20:80	0.1–1.0	3.5	0.38	11.1	0.39	50.0
690	6.0	3.5	0.40	8000	20:80	0.1–1.0	3.5	1.30	43.9	1.31	150

composition and size distribution were the same as those used for the smooth dust models. Similar SEDs to those from the smooth dust models were obtained for the clumpy models (red dashed curves in Figure 5.17). Compared to the variable-Y smooth dust models, the counterpart clumpy models produced an improved fit to the 3.6-μm photometry on days 300–360 and to the 24-μm photometry on days 300–406.

Compared to the smooth dust distribution models, the clumped dust models were able to accommodate two to five times larger dust masses without increasing the effective dust optical depths in the visible region of the spectrum. The smooth and clumpy dust models for day 690 both predict an effective optical depth of 1.3 in the V band, consistent with our estimate from the observed light curve of 0.8–1.5 magnitudes of internal extinction at this epoch (Section 5.7.4). The clumped dust model for day 690 listed in Table 5.12 had a total dust mass of 1.5×10^{-3} $M_\odot$, but it was found that up to 4×10^{-3} $M_\odot$ of dust could be accommodated in clumps at that epoch without seriously reducing the goodness of fit to the observed SED.

5.10 Discussion

A range of new and archival optical and infrared data have been used to investigate the formation of dust in the ejecta of the Type II-P SN 2004et, focusing in particular on the mid-IR observations, obtained with the *Spitzer Space Telescope* and Gemini-North telescope. New NIR and optical data obtained by SEEDS collaborators were incorporated, enabling a comprehensive photometric study of this core-collapse SN from the mid-plateau phase (day 64) to almost 4 years post explosion.

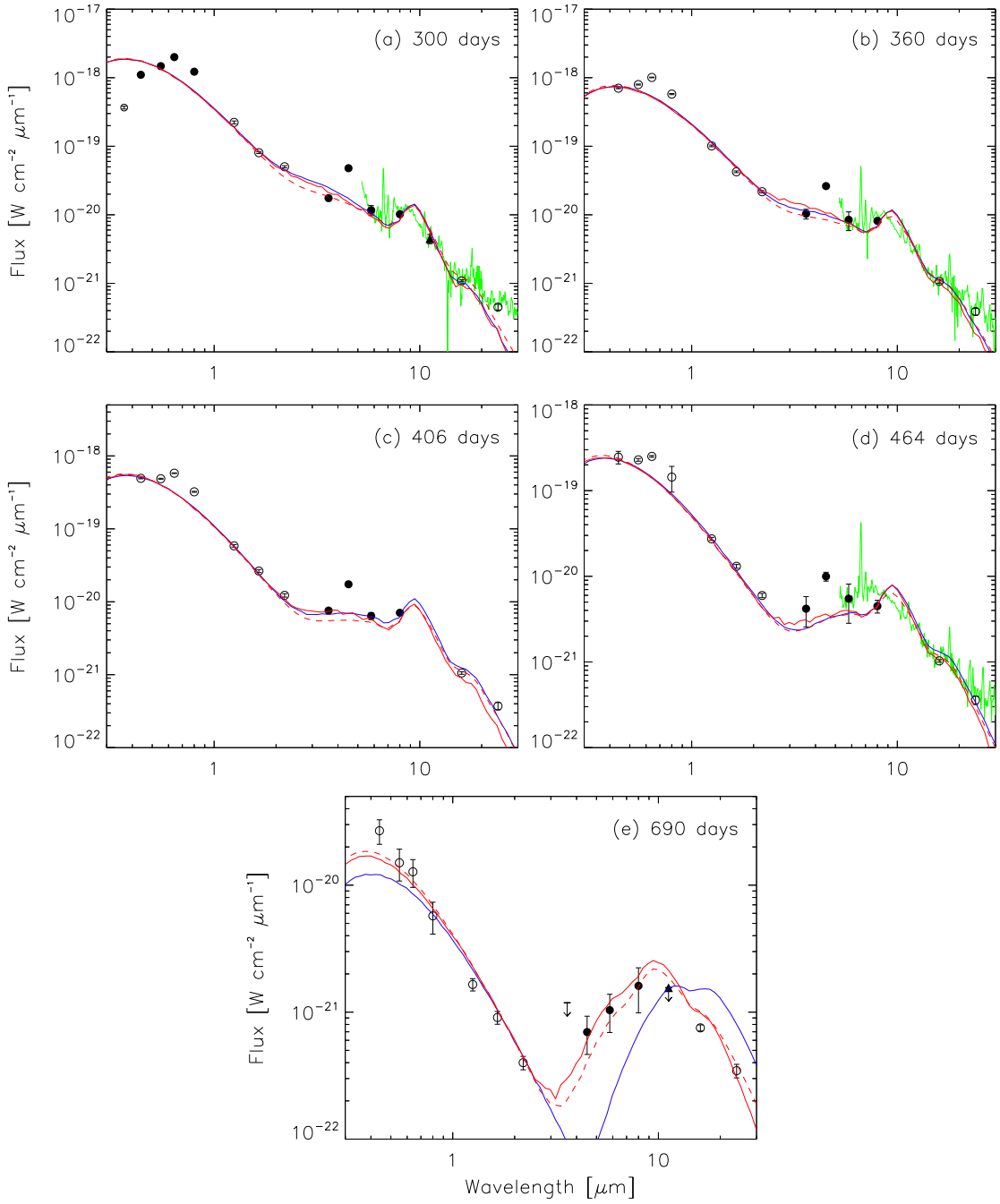

Figure 5.17: Monte Carlo radiative transfer dust model fits to the optical–IR (0.3–30 μm) SEDs of SN 2004et between days 300 and 690. Filled circles indicate fluxes observed at the epoch of the IRAC observations, whereas open circles indicate optical, NIR and mid-IR photometry which has been interpolated/extrapolated to the epochs of the IRAC observations. The filled triangles indicate the Gemini-Michelle N′-band observations, and upper limits to the flux densities are shown as downward-pointing arrows. *Spitzer* IRS spectra at epochs close to the IRAC observations (on days 294, 348 and 480, respectively: green solid line) are in good agreement with the mid-IR photometry. Model fits to the data are indicated by the blue solid curves (smooth dust distribution, fixed Y = 4.0), red solid curves (smooth dust distribution, varying Y) and the red dashed curves (clumpy dust distribution, varying Y). All models adopt a composition of 20:80 per cent amorphous carbon:silicates by mass. See text for further details.

As discussed in Chapter 1, Section 1.3.7, there are three distinct signatures of dust formation in the ejecta of core-collapse SNe. These are (1) the appearance of asymmetric blue-shifted emission lines caused by dust preferentially extinguishing emission from the receding (redshifted) gas; (2) a drop in visual brightness due to increased extinction by the newly formed dust; accompanied by (3) a mid-IR excess due to thermal dust emission. Previously all three signatures had been found in only two cases, that of the unusual Type II(-P) SN 1987A (Lucy et al. 1989) and the Type II-P SN 2003gd (Sugerman et al. 2006, also see Section 4.4). SN 2004et is the third Type II supernova that has shown evidence for all three of these phenomena, as demonstrated in this chapter (summarised below), and as found by previous studies (Sahu et al. 2006; Kotak et al. 2009; Maguire et al. 2010).

From an analysis of new and recalibrated spectra, we showed that between days 259 and 646 the peak of the Hα emission line shifted to the blue by 600 km s^{-1} (Figure 5.3). The optical light curve of SN 2004et declined more rapidly than that expected from radioactive deposition, with the onset of ejecta dust formation estimated to have occurred $\sim$300–400 days after explosion (Figure 5.10). The same light curves allowed us to estimate that by day 690 the additional extinction in the V band, attributable to newly formed ejecta dust, was between 0.8 and 1.5 magnitudes. From day 300 onwards the SN 2004et SEDs exhibit clear excess mid-IR emission relative to blackbodies extrapolated from the optical. The day 300, 360 and 406 SEDs could each be fitted by two blackbody components: (i) a hot component attributed to emission from optically thick gas, and (ii) a warm component attributed to dust freshly synthesised and radioactively heated in the SN ejecta (Figure 5.13). While these two-component fits provided adequate matches to the observed SEDs out to 16 μm, they did underpredict the 24-μm fluxes, which remained relatively constant between days 315 and 709 (Figure 5.5). The day 294, 348 and 480 *Spitzer* IRS spectra (Figure 5.17) also confirm the presence of relatively steady excess emission longwards of 20 μm at these epochs. By day 464 a cool third component was definitely required to fit an increasing excess seen in the 16-μm photometry.

Kotak et al. (2009) attributed the coolest component of their own SED fits to an IR echo from ISM dust in the host galaxy. With the requirement that the ISM gas density should not exceed 1 cm^{-3}, and an assumed dust/gas mass ratio of $\sim$0.006, their model match implied a dust-free cavity of radius 8–16 pc, which they suggested as possibly caused by winds from the SN progenitor and other nearby stars. With a single echo model they were able to account for the longest-wavelength fluxes ($\lambda > 20$ μm) from days 300–1395.

In support of the hypothesis that the day 300–690 mid-IR emission was due entirely to dust synthesised in the ejecta, our ejecta dust radiative transfer modelling was able to match the observed day 300–690 SEDs out to 20 μm (Figure 5.17), longwards of which the relatively invariant excess emission discussed above was present. The observed rise in mid-IR fluxes after 1000 days coincided with a flattening of the optical and NIR light curves at around this time. This, coupled with the fact that the minimum luminosities estimated from blackbody fitting exceeded those expected from radioactive decay from *c.* day 690 onwards, implies that an additional emission source is required after that date. One possibility, discussed by Kotak et al. (2009), is that this emission source was due to the formation of a cool dense shell of dust as a result of ejecta-CSM interaction. Another, discussed by Sugerman et al. (in preparation) is that this emission was due to a light echo from pre-existing CSM dust.

The silicate dust masses derived from our smooth dust models (Table 5.12) match those derived by Kotak et al. (2009) for days 300, 360 and 406, but our dust masses increase faster than their values from day 464 onwards and are a factor of 5 larger by day 690. The clumped dust models of Kotak et al. (2009) had similar masses to their unclumped dust models, while our clumped models have dust masses that are factors of 2–4 larger than for our smooth dust models (Table 5.12). The dust mass derived from our day 464 clumped model was $5{\times}10^{-4}$ $M_{\odot}$, increasing to $1.5{\times}10^{-3}$ $M_{\odot}$ by day 690. This mass of newly formed dust is similar to, or larger than, values derived for a number of other recent Type IIP SNe at similar epochs, e.g. SN 1987A (Wooden et al. 1993; Ercolano et al. 2007), SN 2003gd (Sugerman et al. 2006; Meikle et al. 2007), SN 2004dj (Szalai et al. 2011; Meikle et al. 2011), SN2007it (Andrews et al. 2011) and SN2007od (Andrews et al. 2010). It is also a factor of 100 or more smaller than the ejecta dust masses per CCSN needed to account for the large quantities of dust observed in some high redshift galaxies (Kozasa et al. 1989; Todini & Ferrara 2001; Nozawa et al. 2003; Bianchi & Schneider 2007; Dwek et al. 2007; Dwek & Cherchneff 2011).

5.10.1 Evolution after day 1000 - IR echoes

As discussed in Section 5.6, the most recent *Spitzer* observations of SN 2004et at 3.6–24 μm showed a mid-IR brightening starting after day 1000. Combined with a strong excess of unresolved optical flux found in *HST* imaging from around the same epoch, this suggests we are recording echoes of the SN pulse through pre-existing circumstellar

material. The latest *Spitzer* 'warm' data, from days 1779–2151, shows that the 3.6- and 4.5-μm emission has begun to fade again, which may be consistent with an echo moving into the furthest regions of the CS material, where a much smaller volume of material would be illuminated. Preliminary results from light echo models are summarised below and will be presented in a forthcoming paper, Sugerman et al. (in preparation).

A thermal IR echo from heated, pre-existing CS material will be dominated by the short (2.3 days) early UV pulse from the SN shock breakout. Using an analytic approximation for the UV pulse (Chevalier & Fransson 2008), and the time-integrated observed optical spectra from the SN, a wide variety of circumstellar geometries and dust compositions to match the observed optical and mid-IR fluxes from day 1000 onwards have been explored. It has been found that the IR-to-optical flux ratios are best explained by small dust grains with sizes ∼0.035 μm, while the shapes of the day 1015–1395 SEDs (for which we have 3.6–24 μm data) suggest that the dust can be, at most, 50 % silicate. Reasonable fits to all epoch SEDs from day 1000 have been obtained with models of a wind-compressed disk (Bjorkman & Cassinelli 1993) with uniform density, extending from 3–7 light years, with an opening angle of ∼ 13°, and an inclination to the line of sight of ∼ 8°.

5.11 Summary

A comprehensive optical–IR photometric study of the Type II-P SN 2004et has been presented, demonstrating clear evidence for dust production in the SN ejecta. A remarkable late rise in its mid-IR emission indicate that an additional luminosity component is required after day 1000, possibly attributable to an IR echo from pre-existing circumstellar grains (Sugerman et al., in preparation), or alternatively, from dust forming in a cool dense shell behind the reverse shock following ejecta-CSM interaction (Kotak et al. 2009).

The largest dust mass estimated to have condensed in the ejecta of SN 2004et, of $1.5{\times}10^{-3}\,M_{\odot}$ by day 690 (this work, and Fabbri et al. 2011; *submitted*), is similar to, or larger than, values derived for other Type II-P SNe at similar epochs, and falls far short of the 0.1–1 $M_{\odot}$ of dust required to explain the dust abundance seen in high-z galaxies. The current data and models imply that SNe of this type cannot make a significant contribution to the dust enrichment of galaxies, unless their dust masses continue to grow at later epochs than have typically been observed in the mid-IR.

Chapter 6

Conclusions and Future Work

The aim of this thesis was to help clarify the potential contribution of core-collapse supernovae to the dust-enrichment of galaxies via sensitive mid-infrared surveys with the *Spitzer Space Telescope* and Gemini telescopes. The motivation for this work stemmed from dust formation models (Kozasa et al. 1991; Clayton et al. 2001; Todini & Ferrara 2001; Nozawa et al. 2003) that predicted that CCSNe should be a major source (0.1–1 $M_{\odot}$/SN) of dust in galaxies; coupled with the discovery of very dusty ($M_d \sim 10^8\,M_{\odot}$), IR luminous galaxies at high-redshifts ($z \gtrsim 6$) (e.g., Bertoldi et al. 2003), which suggested massive-star SNe, arising from the starbursts that power these galaxies, were a plausible source for the prompt dust enrichment necessary to explain the observations, if CCSNe had similar condensation efficiencies to those implied by the previous models (e.g., Morgan & Edmunds 2003; Dwek et al. 2007), and produced at least 0.1 $M_{\odot}$ of dust per event.

Despite the assumption that SNe should synthesise dust, there had been surprisingly little observational evidence to support this. The most relevant evidence came from intensive multi-wavelength studies of SN 1987A, which in the LMC at a distance of ~ 50 kpc was the closest Type II SN to have been observed in the past 400 years. Optical–infrared photometry and spectroscopy from explosion to beyond 800 days post-outburst, revealed three clear signatures of dust formation within the ejecta of SN 1987A from at least day 530, models of which implied that a few $\times 10^{-4}\,M_{\odot}$ of clumpy dust had been produced by day 615 (Wooden et al. 1993; Ercolano et al. 2007). Whilst clearly not in the range to explain the dust observed in high-z galaxies, SN 1987A was an unusual Type II

SN with a rare blue supergiant progenitor, and so was felt to not rule out a more significant contribution from other Type II SNe.

The availability of 8-m class ground-based telescopes, such as Gemini, followed by the launch of the *Spitzer* provided the opportunity to search for mid-IR signatures of dust in a larger sample of these extragalactic SNe with greater sensitivities than previously possible, in order to seek evidence for dust formation and evolution in supernova ejecta. Work began on this project with OSCIR on Gemini-North in 2001, and continued in 2004 with both Gemini and *Spitzer*. The SEEDS (Survey for the Evolution of Emission from Dust in Supernovae) collaboration was formed and my involvement has been from the inception of the main programme in 2004.

The mid-IR observations with Gemini and *Spitzer* of 30 core-collapse SNe have been presented and discussed in this thesis. The conclusions drawn are summarised in the following paragraphs.

6.1 Detected supernovae

Of the 30 SNe observed, only *five* were robustly detected. These were comprised of four of Type II-P: SN 2002hh, SN 2003gd, SN 2004dj and SN 2004et, which at distances of 3.3–9.3 Mpc were among the closest of the sample. Three of these were detected and monitored with both Gemini and *Spitzer*. The fifth detection was of SN 1999bw, at a distance of 13.7 Mpc. SN 1999bw was classified as a Type IIn supernova, but the nature of this object is ambiguous, having been compared to LBV-like outbursts (Van Dyk et al. 2000) and the transient objects NGC 300 and SN 2008S, which were proposed to be a new class of electron capture SNe (Thompson et al. 2009).

6.1.1 Conclusive evidence for ejecta dust formation: SN 2003gd and SN 2004et

Of the detected SNe, only SN 2003gd (Section 4.4) and SN 2004et (Chapter 5) have provided unambiguous confirmation of dust production in their ejecta, by exhibiting all three of the following signatures: (1) the appearance of asymmetric blue-shifted emission lines caused by dust preferentially extinguishing emission from the receding (redshifted) gas; (2) a drop in visual brightness due to increased extinction by the newly formed dust, accompanied by (3) a mid-IR excess due to thermal dust emission (Sugerman et al. 2006; Kotak et al. 2009; Fabbri et al. 2011, *submitted*). Previously all three signatures had only

Table 6.1: Ejecta dust yields of core-collapse supernovae – a review.

Name	Type	D (Mpc)	M_{prog} ($M_\odot$)	Age (days)	M_d ($M_\odot$)	Refs[†]
SN 1987A	II(-P)	0.05	16–22	615–775	$(3–5)\times10^{-4}$	1
SN 1987A	II(-P)	0.05	16–22	615–775	$\lesssim 1.3\times10^{-3}$	2
SN 1999em	II-P	~ 11	≤ 15	510	$\sim 10^{-4}$	3
SN 2003gd	II-P	9.3	6–12	499	$\leq 1.7\times10^{-3}$	4
SN 2003gd	II-P	9.3	6–12	499	$\geq 4\times10^{-5}$	5
SN 2004dj	II-P	3.3	12–20	$\sim$270–1000	$\sim 8\times10^{-4}$	6
SN 2004et	II-P	5.9	13–20	300–795	1.5×10^{-4}	7
SN 2004et	II-P	5.9	13–20	300–690	4×10^{-5}–1.5×10^{-3}	8
SN 2005ip	IIn	~ 30	unknown	~ 940	$\sim 5\times10^{-4}$	9
SN 2006bc	II-L	20.3	unknown	~ 550	In prep.	10
SN 2006jc	Ib/c pec	~ 26	LBV/WR?	~ 200	$\sim 3\times10^{-4}$	11
SN 2006jc	Ib/c pec	~ 26	LBV/WR?	~ 200	$\sim 7\times10^{-5}$	12
SN 2007it	II-P	11.7	20–27	350–560	$\sim 10^{-4}$	13
SN 2007od	II-P	24.5	unknown	120–230	4×10^{-4}	14

[†] References for dust masses: 1. Wooden et al. (1993); 2. Ercolano et al. (2007); 3. Elmhamdi et al. (2003*b*); 4. Sugerman et al. (2006); 5. Meikle et al. (2007); 6. Szalai et al. (2011); 7. Kotak et al. (2009); 8. Fabbri et al. (*submitted*) – the lower and upper limits of the dust mass range for this reference correspond to the day 300 smooth and day 690 clumpy dust distribution models respectively (Section 5.9).; 9. Fox et al. (2010); 10. Gallagher et al.(*in prep.*); 11. Mattila et al. (2008); 12. Sakon et al. (2009); 13. Andrews et al. (2011); 14. Andrews et al. (2010).

been observed for SN 1987A (Lucy et al. 1989). The current estimates imply that less than $2\times10^{-3}\,M_\odot$ of dust condensed in the ejecta of these SNe (Table 6.1).

6.1.2 Ejecta and 'cool dense shell' dust in SN 2004dj

A detailed analysis of the mid-IR evolution of SN 2004dj was not conducted for this thesis, but most of the *Spitzer* data available for this SN has been the subject of a recent study by Szalai et al. (2011). From their analysis of available *Spitzer* photometric and spectroscopic data from days 98 to 1381 after outburst, and archival *HST* polarimetry data, Szalai et al. found evidence of dust formation in the SN ejecta in the form of a significant brightening of the mid-IR light curves from $\gtrsim 400$ days, and detection of $\sim 0.5\,\%$ polarisation from the SN ejecta in the optical at 425 days. Their best-fit analytic and 3D radiative-transfer models to the observed mid-IR SEDs yielded dust masses in the range $1.4–7.6\times10^{-4}\,M_\odot$, although only smooth dust density distributions were considered. They estimated that the dust mass could be an order of magnitude higher ($\sim 10^{-3}\,M_\odot$) with clumpy dust models following the work of Sugerman et al. (2006) and Ercolano et al. (2007).

The *Spitzer* fluxes for SN 2004dj that have been measured and presented in this thesis

are generally in good agreement with those of Szalai et al. (2011) and the same trend of a brightening of the mid-IR light curves from ∼400 days was observed. However, the relatively slow decline of the 8- and 10-μm light curves compared to those of SN 1987A and SN 2004et led to my suggestion (in the conclusions of Chapters 2 and 3) that perhaps a more plausible source for the strong late-time mid-IR emission of SN 2004dj was an IR echo caused by thermal radiation from pre-existing circumstellar (CS) or interstellar (IS) dust that was re-heated by the initial UV-optical SN flash.

The ejecta dust models of Szalai et al. (2011) were able to explain the *Spitzer* IRAC mid-IR emission but it is worth noting the following limitations of their analysis. Late-time optical photometry of SN 2004dj was dominated by the flux from the host cluster Sandage-96, so were not included in the SED analysis by Szalai et al. (2011). Consequently, further signatures of ejecta dust production, such as increased optical extinction and blue-shifting asymmetric emission line profiles, could not be confirmed. (A strong early blueshift of the Hα line profile of SN 2004dj observed during days 127–359 was interpreted by Chugai et al. (2005) as the result of an asymmetric ^{56}Ni ejection in an otherwise spherically symmetric envelope.)

Gamma rays from the radioactive decay of ^{56}Ni and its daughter products are known to power the light curve during the nebular phase of SNe (this "radioactive tail" typically occurs after ∼100 days in Type II-P SNe when the plateau phase has ended), where such gamma rays are downscattered, absorbed, and eventually reprocessed into optical emission. This provides a simple but useful energy budget test for ejecta dust during this time, since dust condensed within the SN ejecta merely reprocesses the optical photons to longer wavelengths and must satisfy the overall bolometric luminosity determined by radioactive decays, which are dominated by ^{56}Co. Such an analysis nicely supported the considerable other evidence for dust formation in the ejecta of SN 1987A (Whitelock et al. 1989; Suntzeff & Bouchet 1990) and was used in the analysis of SN 2004et to disentangle ejecta dust from late-time emission due to alternative dust sources (Chapter 5; Kotak et al. 2009). Szalai et al. (2011) found that the luminosity of the warm dust component of SN 2004dj significantly exceeded the luminosity due to radioactive ^{56}Co-decay from ∼850 days onwards, although the source of the additional energy from this time was not discussed by them. SED model fits to the IRAC and IRS Peak-up 16-μm fluxes of SN 2004dj at epochs of (477–510) days and (631–662) days would have been useful to investigate its energy budget for ejecta dust prior to 800 days. At late times ($\gtrsim$800 days) other

potential sources of energy could include contributions from a "freeze-out" phase where energy is released by nebulous matter ionised during the original explosion recombining on timescales longer than the expansion time (Fransson & Kozma 1993); radioactive deposition from other longer-lived isotopes, such as ^{57}Co with a half-life of 270 days (see Section 5.7.4); light echoes from pre-exisiting CS or IS dust (e.g., for SN 2004et see Section 5.10.1, and for SN 2007od, Andrews et al. 2010); and, shock interactions between the SN ejecta and any pre-existing circumstellar material.

Interestingly, Szalai et al. (2011) found that a "cold" dust component, required to explain the persistent excess flux longward of 10 μm for SN 2004dj, was located at $v \sim 6400\,\mathrm{km\,s^{-1}}$, close to the region between the forward and reverse shocks where a cool dense shell (CDS) is expected to form during the interaction of the SN ejecta and a pre-existing CSM. The CDS can provide a suitable environment for grain condensation, and this was Szalai et al.'s preferred explanation for the late-time cold dust component.

CDS dust has also been invoked to explain the observations of a number of other CCSNe, including SN 2004et (Kotak et al. 2009); SN 2005ip (Smith et al. 2009*b*); SN 2006jc (Mattila et al. 2008; Smith et al. 2008); and SN 2007od (Andrews et al. 2010). In the case of SN 2006jc and SN 2007od, the dust masses from the CDS models of Mattila et al. (2008) and Andrews et al. (2010) respectively, are listed in Table 6.1 for comparison with the ejecta dust masses of other CCSNe. It is shown that the amount of dust estimated to have condensed in these CDS regions (a few $\times 10^{-4}\,\mathrm{M_\odot}$) is comparable to current estimates for dust freshly-synthesised in the expanding SN ejecta.

6.1.3 IR echoes: SN 1999bw and SN 2002hh

For the remaining two mid-IR detected SNe from this work (SN 1999bw and SN 2002hh) it is likely that an IR echo was responsible for the mid-IR emission, caused by SN flash-heating of pre-existing dust in the circumstellar or local interstellar medium, possibly formed in the pre-explosion mass-loss phase of the progenitor star. However, since it has been suggested that SN 1999bw was not a true core-collapse event (Van Dyk et al. 2000; Thompson et al. 2009) its interpretation is difficult, especially due to the paucity of earlier data for this object.

In the case of SN 2002hh, the echo hypothesis has been supported by optical observations (Pozzo et al. 2006; Welch et al. 2007). A large mass (0.1–0.15 $\mathrm{M_\odot}$) of CSM dust was derived by Barlow et al. (2005) to explain the mid-IR SEDs, although difference imaging

by Meikle et al. (2006) revealed that some of the strong mid-IR emission might be attributable to nearby ISM material. A small declining component of the mid-IR emission was considered likely to be due to an IR echo from the SN, and the minimum dust mass of $0.04\,M_{\odot}$ estimated from models is considerably larger than the $\sim 10^{-3}\,M_{\odot}$ of directly observed ejecta dust inferred from studies of other SNe. If the $0.04\,M_{\odot}$ of dust corresponds to circumstellar dust that was formed in outflows from the CCSN progenitor in a previous mass-loss phase, then the massive-star progenitors of some CCSNe might still make a significant contribution to the dust content of galaxies.

There is also evidence of late-time IR echoes from CS material around SN 2003gd and SN 2004et (as discussed in Sections 4.4 and 5.10.1 respectively), and a number of other CCSNe, including SN 2006bc (Gallagher et al., *in prep.*); SN 2006jc (Mattila et al. 2008); SN 2007it (Andrews et al. 2011); and SN 2007od (Andrews et al. 2010), indicating that the outflows of massive-star progenitors can potentially be a common source of dust.

As briefly discussed in Section 4.2.3, IR echoes from a dusty CS shell around SN 2008S were modelled self-consistently from pre- to post-outburst by Wesson et al. (2010). Their results indicated that super-AGB stars, of which the progenitor of SN 2008S may be an example, could provide a total dust injection into the interstellar medium of up to $0.01\,M_{\odot}$ over the suggested duration of the self-obscured phase. Wesson et al. (2010) further considered the potential contribution of objects like SN 2008S to the dust enrichment of galaxies by considering the case of the dusty $z = 6.4$ galaxy J114816.64+5251. Accounting for modest dust destruction (70 % grain survival), they found that super-AGB stars (initial mass range of 6–10 $M_{\odot}$) were likely to contribute only about 1.6 % of the total $2 \times 10^{8}\,M_{\odot}$ of dust observed in J114816.64+5251, compared to 2.1 % from CCSNe (progenitor initial mass $> 8\,M_{\odot}$), and a further 2.3 % from AGB stars (initial mass 4–6 $M_{\odot}$).

6.2 Upper limits to dust masses for non-detected SNe

The majority of SNe observed (25 out of the 30) were not detected with either Gemini or *Spitzer*. Despite the small sample, it is significant that many of the non-detections (not including SN 2004C, SN 2003jg and SN 2002ji whose host galaxy emission swamps any thermal dust emission from the region of the SN), lie at similar intrinsic levels to, or below, those SNe that were detected, implying that there were not large amounts of ejecta-dust or pre-existing circumstellar dust present for at least 22 of the SNe.

To investigate this further, dust-mass upper limits for 16 of the non-detected SNe (those observed at typical dust-forming ages, ∼300–1000 days post explosion), were approximated by calculating flux to ejecta dust mass ratios, $\mathcal{R}$ (Jy/10^{-3} $M_{\odot}$), for several Type II SNe for which ejecta dust masses had been derived – listed in Table 6.2. $\mathcal{R}$ values were calculated for both 8- and 10-μm flux densities, in order to derive dust mass upper limits for the non-detected *Spitzer* and Gemini SNe samples respectively. Measured 8- and 10-μm flux densities of SN 1987A at days 615 and 775 were taken from Bouchet & Danziger (1993) and dust masses were those derived from the smooth and clumpy models of Ercolano et al. (2007), for which carbon-rich (amorphous carbon or graphite) grains provided the best fits. The 8-μm data for SN 2003gd at day 499 were obtained from Sugerman et al. (2006) and for SN 2004et at days 464 and 690 from Chapter 5 and Fabbri et al. (2011; *submitted*), with the authors' best-fitting models for these SNe requiring oxygen-rich (silicate) grain compositions. The fraction of amorphous carbon ("AC"), graphite ("Gr") and silicate ("Sil") grains for the adopted dust models are indicated as a percentage by mass in Table 6.2. All measured fluxes were scaled to a SN 1987A-equivalent distance of 50-kpc. Finally, the relevant 8- or 10-μm $\mathcal{R}$ value was divided into the 50-kpc *Spitzer* 8-μm or Gemini 10-μm flux upper limit for the non-detected SNe (Chapters 2 and 3), in order to estimate upper limits to their dust masses, as listed in Table 6.3.

The $\mathcal{R}$ values shown in bold font in Table 6.2 for the clumpy dust distributions were chosen as conservative values to provide the highest dust mass upper limits for the two general cases of carbon-rich or oxygen-rich grain compositions listed in Table 6.3. The 8-μm $\mathcal{R}$ values for the case of silicate dust composition (derived from data for SN 2003gd and SN 2004et) were also applied to the 10-μm sample, since no measured 10-μm data was available for SN 2003gd and SN 2004et at the appropriate epochs. This is a reasonable approximation since the 8- and 10-μm fluxes lie on a relatively flat region of the mid-IR SEDs, around the peak of the warm dust emission. For each of the *Spitzer* and Gemini samples, the dust mass upper limits were split into two groups, those observed before day 650 and those observed at or after this time, using $\mathcal{R}$ values calculated from data at appropriate epochs.

Due to the increased sensitivity of *Spitzer* over the Gemini telescopes and because the distances of the *Spitzer* SNe sample were, on average, lower than those from the Gemini sample, the intrinsic flux upper limits, and therefore the dust mass upper limits

Table 6.2: Mid-IR flux to ejecta dust mass ratios, $\mathcal{R}$, for deriving dust mass upper limits for the sample of non-detected SNe.

Name	Age (days)	Grain composition	$\mathcal{R}$ (Jy/10^{-3} $M_\odot$) Smooth	Clumpy[†]
Spitzer 8-μm sample:				
SN 1987A	615	100 % AC	43	40
SN 1987A	615	100 % Graphite	27	13
SN 1987A	**615**	**15:85 % Sil:Gr**	···	**6.7**
SN 1987A	775	100 % AC	2.9	2.1
SN 1987A	**775**	**100 % Graphite**	1.9	**1.2**
SN 2003gd	**499**	**15:85 % AC:Sil**	30	**3.5**
SN 2004et	464	20:80 % AC:Sil	120	26
SN 2004et	**690**	**20:80 % AC:Sil**	11	**3.1**
Gemini 10-μm sample:				
SN 1987A	615	100 % AC	37	33
SN 1987A	615	100 % Graphite	18	11
SN 1987A	**615**	**15:85 % Sil:Gr**	···	**5.7**
SN 1987A	775	100 % AC	3.8	2.7
SN 1987A	**775**	**100 % Graphite**	2.5	**1.5**

[†] Entries in bold font for the clumpy dust distributions were conservatively chosen to provide the highest range of dust mass upper limits in Table 6.3 below (see text).

are correspondingly lower for the 8-μm sample.

SN 2002ji has the largest dust mass upper limit of $\sim 0.1\,M_\odot$ for the 8-μm sample, although the approximations for this SN and SN 2003jg ($M_d \lesssim 0.04\,M_\odot$) are merely illustrative, as the location of these SN meant that the host galaxy mid-IR emission dominated the region of both SNe leading to significantly larger upper limits. For the 10-μm sample, the largest dust mass upper limit of $\sim 0.5\,M_\odot$ corresponds to the most distant supernova, SN 1999ac at almost 40 Mpc. The lowest dust mass upper limits are $\sim 10^{-4}\,M_\odot$ for the 8-μm sample and $\sim 10^{-3}\,M_\odot$ for the 10-μm sample, in line with dust mass estimates for detected Type II SNe (Table 6.1).

It was not possible to confirm the ambiguous 10-μm detection of SN 1999D in NGC 3690, but at a distance of ~ 42 Mpc, it would be unusually bright at any epoch, and is therefore considered as a non-detection.

Since the only detections with Gemini were also detected with *Spitzer* and lay at the closest distances (3.3–5.9 Mpc), it is concluded that for detection with current Gemini mid-IR instruments, most detectable SNe are likely to be limited to distances of less than 10 Mpc. For the *Spitzer* observations the distances for non-detections ranged from ~ 3.3–

Table 6.3: Dust mass upper limits for non-detected supernovae.

Name	Type	D (Mpc)	Age (days)	50-kpc flux (Jy)	M_d ($M_\odot$) if C-rich	M_d ($M_\odot$) if O-rich
Spitzer 8-μm sample:						
SN 2001gd	IIb	12.0	941	$\lesssim 9.0$	$\lesssim 7.8 \times 10^{-3}$	$\lesssim 2.9 \times 10^{-3}$
SN 2002ap	Ib/c pec	9.3	908	$\lesssim 2.6$	$\lesssim 2.2 \times 10^{-3}$	$\lesssim 8.3 \times 10^{-4}$
SN 2002ji	Ib/c	20.0	748	$\lesssim 145$	$\lesssim 1.2 \times 10^{-1}$	$\lesssim 4.6 \times 10^{-2}$
SN 2002kg	IIn	3.3	713	$\lesssim 0.33$	$\lesssim 2.8 \times 10^{-4}$	$\lesssim 1.0 \times 10^{-4}$
SN 2003bg	IIb	18.1	692	$\lesssim 9.2$	$\lesssim 7.9 \times 10^{-3}$	$\lesssim 2.9 \times 10^{-3}$
SN 2003jg	Ib/c	10.3	419	$\lesssim 288$	$\lesssim 4.3 \times 10^{-2}$	$\lesssim 8.3 \times 10^{-2}$
SN 2003Z	II	17.4	639	$\lesssim 21.8$	$\lesssim 3.3 \times 10^{-3}$	$\lesssim 6.3 \times 10^{-3}$
Gemini 10-μm sample:						
SN 1999ac	Ia pec	39.0	800	$\lesssim 730$	$\lesssim 4.8 \times 10^{-1}$	$\lesssim 2.3 \times 10^{-1}$
SN 1999an	II	20.6	791	$\lesssim 187$	$\lesssim 1.2 \times 10^{-1}$	$\lesssim 6.0 \times 10^{-2}$
SN 1999el	IIn	18.2	564	$\lesssim 225$	$\lesssim 4.0 \times 10^{-2}$	$\lesssim 6.5 \times 10^{-2}$
SN 1999gq	II	13.0	500	$\lesssim 115$	$\lesssim 2.0 \times 10^{-2}$	$\lesssim 3.3 \times 10^{-2}$
SN 2002ao	IIb/Ic	21.1	776	$\lesssim 146$	$\lesssim 9.7 \times 10^{-2}$	$\lesssim 4.7 \times 10^{-2}$
SN 2002ap	Ib/c pec	9.3	980	$\lesssim 20.4$	$\lesssim 1.4 \times 10^{-2}$	$\lesssim 6.5 \times 10^{-3}$
SN 2002ds	II	31.1	626	$\lesssim 298$	$\lesssim 5.3 \times 10^{-2}$	$\lesssim 8.6 \times 10^{-2}$
SN 2002ed	II-P	38.9	647	$\lesssim 454$	$\lesssim 8.0 \times 10^{-2}$	$\lesssim 1.3 \times 10^{-1}$
SN 2003B	II	17.4	304	$\lesssim 136$	$\lesssim 2.4 \times 10^{-2}$	$\lesssim 3.9 \times 10^{-2}$
SN 2005cs	II	8.4	628	$\lesssim 10.7$	$\lesssim 1.9 \times 10^{-3}$	$\lesssim 3.1 \times 10^{-3}$

20 Mpc, while the detected SNe were mainly at distances < 12 Mpc, although SN 2007od (Andrews et al. 2010) lies at a distance of 24.5 Mpc.

6.3 Overall conclusions

The derived dust masses for SN 2003gd, SN 2004dj and SN 2004et are in line with estimates for other CCSNe from the literature, as summarised in Table 6.1, including those determined by the SEEDS team for SN 2007it (Andrews et al. 2011) and SN 2007od (Andrews et al. 2010). The upper range to the measured dust masses of a few $\times 10^{-3}\,M_\odot$ for the SNe detected in the mid-IR suggests that Type II SNe are not major producers of dust, where the dust mass upper limits in Table 6.3 are almost all below $0.1\,M_\odot$ per SN (except for the most distant SN of the sample), and six are below $10^{-2}\,M_\odot$.

In conclusion, the set of observations presented here argue that the ejecta of core-collapse supernovae do not produce sufficient dust to explain the masses of dust derived for some galaxies in the early Universe. It remains possible that the progenitors of these massive stars may form larger (~by an order of magnitude) amounts of dust in their stellar winds during a preceding mass-loss phase. However, the quantities of dust inferred may

still not account for the dust seen at high redshifts, and it is not certain how much of any dust produced would survive further processing by the SN shocks. Therefore, the ultimate source of the dust in these distant dusty galaxies remains an open question.

It should however be noted that although Type II SNe are the most common type of CCSN their progenitor initial masses are estimated to be less than $20\,M_\odot$ (Smartt 2009). More massive stars are believed to produce hydrogen-deficient Type Ib and Ic SNe following a Wolf-Rayet phase. The dust formation properties of these SNe have still to be characterised, very few having been observable by *Spitzer*. In addition, the young supernova remnant Cas A – the product of a Type IIb SN (Krause et al. 2008*a*) – has been found from *Herschel* far-IR and sub-mm observations to contain $0.075\,M_\odot$ of cool dust (Barlow et al. 2010), interestingly close to the $0.1\,M_\odot$ minimum dust mass per SN required by dust evolution models for high-z galaxies.

Recent work by Cherchneff & Dwek (2010) predicts that only $\sim 0.15\,M_\odot$ of dust is created by a Population III $20\,M_\odot$ SN, which may be a typical yield for Population II SNe of similar masses, and compares to the range of 0.1–1 $M_\odot$ previously predicted by classical nucleation theory. From their modelling of the hyper-luminous quasar SDSS J1148+5251, Dwek & Cherchneff (2011) suggest that AGB stars, already established as efficient producers of dust in local galaxies, could produce the large quantities of dust inferred in the galaxy at $z = 6.4$, but that the final mass of surviving dust depends on the galaxy's star formation history.

Alternative sources of dust at high-z that have been proposed include quasar winds. Elvis, Marengo & Karovska (2002) suggested that the environment of these winds could provide temperatures and pressures similar to those found around cool dust-forming stars and that up to $10^7\,M_\odot$ of dust could be formed over a nominal 10^8-year lifetime. From *Spitzer* IRS spectra of the $z = 0.466$ broad absorption line QSO PG 2112+059, Markwick-Kemper et al. (2007) detected mid-IR emission features which they attributed to amorphous and crystalline silicates formed in the quasar wind. It is not yet clear whether all dust-emitting high-z galaxies posses such AGN central engines.

6.4 Future work

The SEEDS team are in the process of creating a grid of SN dust shell models with MOCASSIN to enable a consistent modelling approach for the objects studied, and to provide

a detailed exploration of the broad parameter space constrained by the observations.

Another area for future study is the role of massive stars in producing dust at late stages of their evolution, which has been highlighted by the discovery of light echoes around CCSNe and other mid-IR transient objects. Luminous late-type supergiants, or 'hypergiants' (> few $\times 10^5\,L_\odot$) can have high mass loss rates (up to > $10^{-4}\,M_\odot\,yr^{-1}$) and are often self-obscured by their own circumstellar dust at optical wavelengths, such as the red hypergiants VY CMA, VX Sgr and NML Cyg, (e.g., Smith et al. 2009*a*; Schuster et al. 2009). Similarly high mass-loss rates are exhibited by some yellow hypergiants, e.g., ρ Cas, IRC+10 420 and HR 8752 (Humphreys 2010). Such objects could potentially make a significant contribution to the dust enrichment of galaxies but such estimates are difficult whilst uncertainties remain about the duration of the yellow/red hypergiant phase and the total population of such objects in our Galaxy. Better statistics from current optical and near-IR surveys, together with distances from ESA's Galactic Gaia survey and more precise mass-loss rate determinations using improved wind modelling techniques, should contribute to a greater understanding of the role of these objects in the dust and gas evolution of galaxies.

The ejecta nebulae around luminous blue variables (LBVs) can also contain large masses of dust, as in the cases of η Car and AG Car, with the 1840's outburst of η Car estimated to have produced 0.2 $M_\odot$of dust (Morris et al. 1999). A rotating 'pinwheel' plume of dust emission has been discovered around several Wolf-Rayet star systems, including that of WR104, which was explained by Tuthill et al. (2002) as being formed in the compressed shock interaction region (hotspot) between the stellar winds of a WC9 primary and an OB secondary star in a binary system, whose relative motions create an Archimedean spiral. The M 1-67 ejecta nebula around the WN8 Wolf-Rayet star WR124 also contains large quantities of dust and is thought to have originated from the outburst of an LBV precursor (Grosdidier et al. 1998). The overall contribution of late WC-type Wolf-Rayet stars to the dust enrichment of galaxies is currently extremely uncertain. Future observations by ALMA can help to quantify their overall production rates, and search for emission from the hot-spot shocked wind compression region.

For point source imaging, *Spitzer*'s IRAC is 135× more sensitive at 8 μm than mid-IR instruments of ground-based 8-m telescopes, such as Gemini, due to *Spitzer*'s vastly lower thermal backgrounds. For point source imaging, the Mid-IR Instrument (MIRI) on the *James Webb Space Telescope* (*JWST*), is expected to be ∼ 40× more sensitive at 8 μm

than IRAC [1]. In addition to these sensitivity gains, the 8× higher angular resolution of *JWST*-MIRI compared to *Spitzer*-IRAC will greatly reduce point source confusion effects in dense starfields, such as encountered when observing galaxies. MIRI's much greater sensitivity and angular resolution should enable SNe out to nearly 200 Mpc to be detected at mid-IR wavelengths, corresponding to a volume ∼1000 times larger than for *Spitzer*. So MIRI will be able to quickly observe large numbers of new SNe of all classes, both photometrically and spectroscopically, enabling the dust contribution by each class to be accurately assessed, in particular the contribution from the Type Ib and Ic SNe produced by very massive stars.

[1] http://www.stsci.edu/jwst/instruments/miri/sensitivity/

Appendix A

Defining queue-mode observations with the Gemini Observing Tool

The Gemini Phase I process refers to the proposal preparation and submission stage using the Phase I Tool (PIT). Both classical and queue mode observations can be applied for, although queue mode observations are only offered with facility instruments. For classical scheduling, programmes are assigned to specific nights on the telescope, whereas in queue mode observing, observations are expressly defined by the investigators and carried out on their behalf by Gemini scientific staff.

Since the majority of Gemini data described in this thesis were obtained in queue mode, it is worth outlining the procedure of defining the observing schedules during the Phase II stage with the Gemini Observing Tool (OT). The OT is the software used for detailed planning and definition of observations from approved proposals. It also serves as a high-level interface for on-site observers, capable of configuring and sequencing the telescope and instrument motions, and integrating the processes of data taking and pipeline reduction.

During the Phase II process, the OT is used to access a database at the Gemini Observatory and download an outline of the approved science program as defined in the Phase I stage. From this skeleton program, observations are defined in detail. At a general level, this involves refining target coordinates, selecting appropriate guide and calibration stars, defining telescope motion sequences and instrument configuration, including

orientation, chop throw and angle, filters and exposure times.

Guide stars. Setting the wavefront sensors (WFS) forms an integral part of the guide star definition. The design of the Gemini telescopes is such that their lightweight structures are very sensitive even to light winds. It is therefore a requirement that all science data be collected with at least one WFS locked onto a guide star to provide image motion compensation and/or higher order correction. This is achieved by tip-tilt articulation of the secondary mirror, active optic manipulation of the primary mirror, and/or adaptive optics (AO). Neither OSCIR, T-ReCS or Michelle have on-board sensors and must therefore use one of the telescopes' two peripheral wavefront sensors, PWFS1 and PWFS2, which form part of the Acquisition and Guidance system located within the instrument support structure. Mounted on rotary stages, the PWFSs patrol an annulus of sky around the science field of view. They are positioned upstream of the science instruments and will vignette the science field unless positioned at sufficient distance.

The OT contains a display feature known as the Position Editor, providing a graphical view of the observation, which can then be modified interactively. The Position Editor was used to ensure the instrument field of view and the regions of PWFS vignetting did not overlap. Figure A.1 shows a screenshot of the Position Editor in the OT indicating the target position, the Michelle science field of view, and the PWFS field of view and vignetting regions for one of our Gemini SN observations. PWFS stars were selected from the brightest, true point-sources within the usable annulus, having R-band magnitudes of typically 11 – 13 mag for PWFS1 and 13 – 15 mag for PWFS2. By displaying background images of the field of view from online catalogues, the Position Editor was also used to select the best orientation of the instrument detectors and chop angles in order to avoid potential contamination from other sources.

"User1 astrometry". For the SNe programmes, the targets were too faint to see immediately on the array (for example, during acquisition), so to ensure good pointing accuracy, it was necessary to adopt a blind off-setting procedure referred to as "User1 astrometry". Briefly, this entails defining a short observation of a designated "astrometric" star on which to centre the Michelle "hot-spot". The astrometric star, found from the Hipparcos Catalogue, is chosen to be bright enough in the N' (11.2 μm)-band and within a few degrees of the SN target. The telescope is then slewed to an offset ("User1") star, visible only with the acquisition camera. The offset star has accurate coordinates (e.g. from The Second U.S. Naval Observatory CCD Astrograph Catalog [UCAC2] or The Guide Star

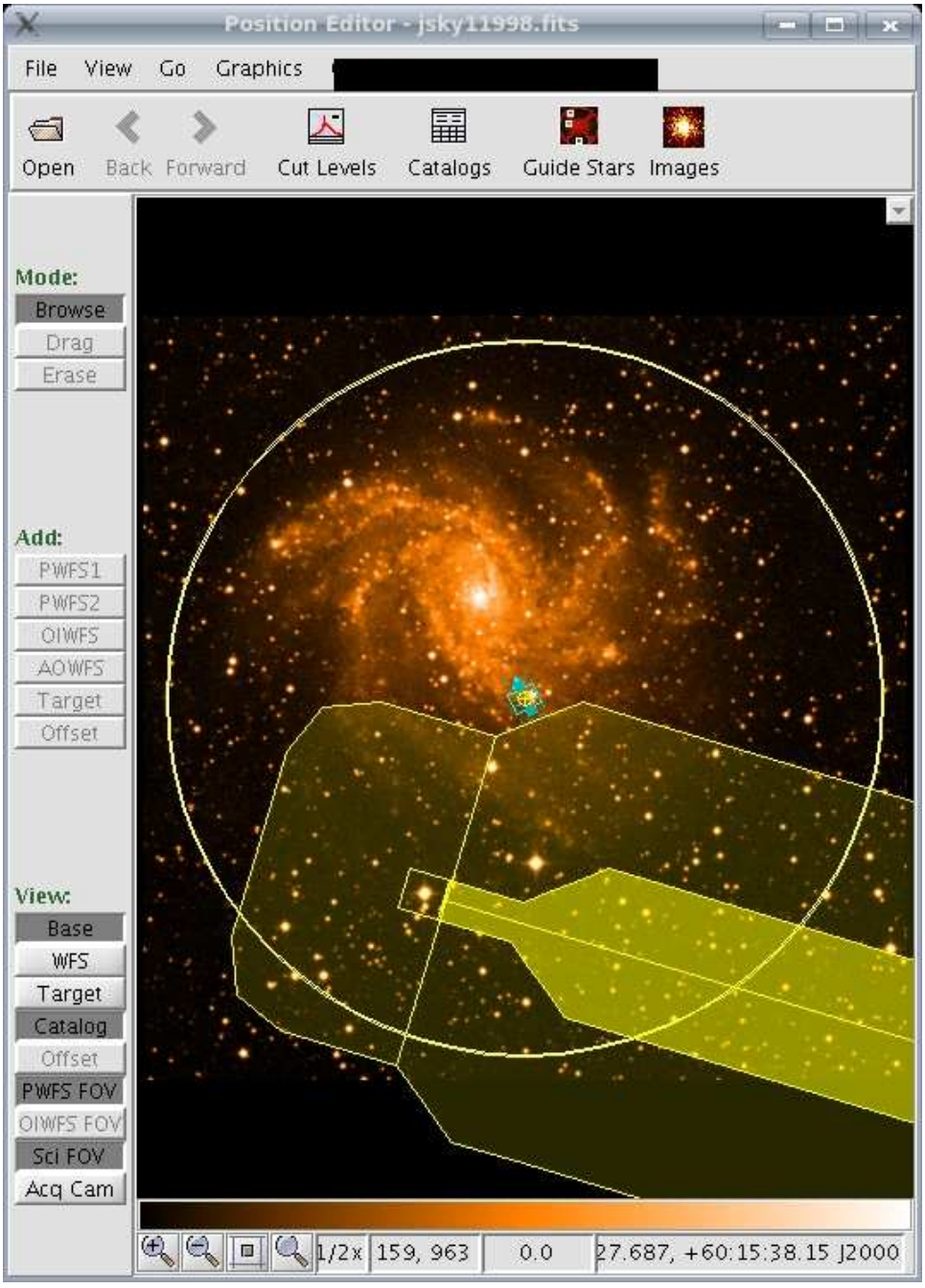

Figure A.1: Screenshot of the Position Editor in the Gemini Observing Tool for one of our Gemini observations of SN 2002hh in NGC 6946. The science target position is indicated by the small yellow circle with a cross in it at the centre of the frame; the Michelle science field of view and chop throw positions are indicated by the blue box immediately around the science target; and the field of view of the PWFS2 probe is indicated by the large circle. The vignetting pattern of the PWFS arm is also displayed and it is important that this does overlap with the science field of view.

Catalog Version 2.2.01 [GSC2.2] catalogues) and has the same guide star as the target SN, so that offsetting directly from the User1 star to the SN is possible without opening up the guide loops. This generally achieves a pointing accuracy within a 0.5 arcsecond radius of the nominal position.

Standard stars. A set of "baseline" calibrations are taken for all queue observations, which includes observations of standard stars for flux calibration of mid-IR images. Additional calibration observations can be requested but, unlike baseline calibrations, are charged to the program. All calibrations, baseline or additional, are defined with the OT at the Phase II stage. Baseline calibration observations of flux standards were used for the data presented herein. The main standard stars used for T-ReCS and Michelle observations are those presented in Cohen et al. (1999), and a library of these "Cohen" standards can be fetched from the Gemini database via the OT. Over the course of the various SNe observing programmes, the procedure for defining standard star observations was refined by Gemini and is now explicitly described in their web pages[1]. Two photometric standards were defined, one before and one after the science target observations, each chosen to match the airmass of the target as closely as possible. The elevation plot facility in the OT was used to check that the chosen standard stars were appropriately matched in airmass to the SN. For observations taking longer than about two hours, both standards should be observed. Photometric accuracy is limited to ~10% by the uncertainty in the airmass correction and in the fluxes of the standards themselves.

Liaison with Gemini staff ensures the schedules are complete and correct before remote submission to the queue via the OT, whereupon the schedules are activated for observation. Several combined factors dictate which observation is chosen for execution at a given time but prime are the scientific ranking and closeness of match to the observing conditions.

[1]The Baseline Calibrations section of http://www.gemini.edu/sciops/instruments/midir-resources

Appendix B

Gemini mid-IR imaging data reduction

B.1 OSCIR data reduction

The OSCIR data files, like those of other Gemini instruments, are Multi-Extension FITS (MEF) files, which differ somewhat from "regular" FITS files. A regular, or single-extension, FITS file has a one 2-dimensional image stored in it with all the header information, representing a single readout of the detector. By contrast a MEF file contains a number of images each with some of its own header information, each of which is analogous to a normal FITS file. This is basically a consequence of the telescope chopping and nodding techniques discussed at the beginning of this chapter. In summary, since the OSCIR detector is read out at several tens or hundreds of Hertz in synchronisation with the chopping secondary, frames are coadded into two hardware buffers: one for each chop position. The buffers are written to disk periodically (generally every few seconds), forming a 'saveset'. After several such savesets are recorded, data collection stops as the telescope nods, then resumes. A cycle during which the telescope nods to a new position and back is called a 'nodset'. Consequently, the file format of the raw data products from OSCIR is a 6-dimensional MEF file, consisting of the following dimensions:

Dim.	Name	Size
1	X dimension of array	128
2	Y dimension of array	128
3	Chop position	Number of chop positions (1 or 2)
4	Savesets	Number of savesets per nod position
5	Nod position	Number of nod positions (1 or 2)
6	Nodsets	Number of nodsets

The following tasks in Gemini IRAF package were used to process the OSCIR SN data presented in Chapter 2:

- OHEAD

  Prints header information for OSCIR files.

- OVIEW

  Allows quick inspection of the individual raw data frames. Interactive mode can be set where an IRAF IMEXAM session is started with each frame displayed and can be used to determine frame statistics.

- OBACKGROUND

  Is specifically used to calculate and plot statistics of reference frames, in order to analyse the background level and identify bad savesets or nodsets. It can identify saveset and nodset values for any frames outside some sigma of the average mean level (default sigma=4).

- OREDUCE

  This is the basic data reduction task which applies the usual method of differencing the image chop pairs (compute [beam A - beam B] or [beam B - beam A] for each saveset, depending on the nod position), then averages these differences to form a final image. The input image is a raw OSCIR data file, the output image is a 2-dimensional image which is the average of the chop and nod differences.

B.2 T-ReCS and Michelle data format and reduction

B.2.1 Format of the T-ReCS and Michelle raw data files

The basic file format for the T-ReCS and Michelle raw data is a multi-extension FITS (MEF) file with the primary header – containing information common to all the images - stored in extension '0', and one or more image extensions containing coadded data frames.

For the chop/nod observations detailed here, there is one image extension per nod position. As well as the image itself, each image extension contains a small FITS header with details specific to that individual image, such as the start and end UT times and the airmass. Each image contained in an extension is usually comprised of multiple coadded raw frames, each of which is a [320,240] array of data values of type long (T-ReCS) or double (Michelle). The format of the images in the extensions depends on the mode of the observation (stare, chop, chop/nod or nod) and on which instrument (T-ReCS or Michelle) was used to obtain the data.

For Michelle data obtained in chop/nod mode, each image extension is three dimensional: [320,240,3], where frames from each chop position are combined to form *chop_A* and *chop_B* position images, and these are subtracted to form a *difference* frame. It is these three images which are referenced in the third data dimension of each image extension. In turn, the *chop_A* and *chop_B* images are each the result of stacking a number of frames with typical exposure times of 25 milliseconds. This very short "frame time" is set to avoid saturation of the array caused by the high level of mid-IR background radiation. Michelle stacks these raw frames internally during the time at each nod position.

For T-ReCS data obtained in chop/nod mode, each image extension is four-dimensional: [320,240,2,N], where frames from each chop position are combined to form *chop_A* and *chop_B* position images. It is these two images where are referenced in the third data dimension of each image extension. As with Michelle, the *chop_A* and *chop_B* images are, in turn, each an accumulation of frames coadded in T-ReCS's internal buffers, with individual frame times of typically 25 milliseconds. A pair of coadded frames from each chop position is called a saveset, and there are 'N' number of savesets in each image extension for a single nod position (described in the fourth data dimension). At the end of the specified saveset time (normally 10 seconds) the stacked images are written out to the FITS extension.

B.2.2 Data reduction with the Gemini IRAF package

The MIDIR suite contains tasks for processing the mid-IR imaging data from the Michelle and T-ReCS instruments. There are tasks specific to each instrument, and tasks which are common to both. Table 2.7 in Chapter 2 provides a brief description of the tasks available in the MIDIR package and indicates which of the these were used for reducing the data discussed in this chapter. A more detailed description of each task follows:

- TVIEW and TBACKGROUND can be run on raw T-ReCS images to respectively view/examine, and determine background statistics for, each chop saveset. Bad savesets can be flagged so that they are not coadded with the TPREPARE task.

- TCHECKSTRUCTURE examines the structure of a T-ReCS raw data file to ensure that it has the correct number of extensions and the correct image dimensions in the extensions.

- MVIEW, like TVIEW, can be used to view and interactively examine (with IRAF's IMEXAMINE) each image of the Michelle raw data and flag any bad nods.

- MCHECKHEADER is a recent addition to the MIDIR package and is only useful for data which has been aborted during execution. It is used to repair incomplete FITS headers of Michelle raw data so that they can comply with the Gemini Science Archive (GSA) standard at the Canadian Astronomical Data Center (CADC).

- TPREPARE and MPREPARE are used to collapse and reorganise the raw T-ReCS and Michelle data respectively into the same data structure. For chop/nod observations, the format of the "prepared" files follows the format of the Michelle raw data such that the primary header information is contained in extension 0, and the remaining extensions contain one image each per nod position in a three-dimensional format of size [320,240,3]. As previously described for the raw Michelle data format, the three "planes" correspond to the on-source coadded image in image section [*,*,1], the off-source coadded image in image section [*,*,2,], and the difference image [*,*,1] - [*,*,2] in image section [*,*,3]. Specifically for T-ReCS, TPREPARE collapses the raw data to the same format as the Michelle raw images by averaging the savesets for each chop position of a given nod position, to give a mean on-source image and mean off-source image which are differenced in the third data plane as described

previously. The tasks endeavour to harmonise the T-ReCS and Michelle keywords in the FITS headers.

- MIVIEW can be used to view and examine the data from either instrument once it has been processed with T/MPREPARE. As with the T/MVIEW tasks, statistics can be derived for each nod frame and frames can be flagged as bad for exclusion from the final data coaddition.

- MIFLAT combines two T-ReCS or Michelle stare mode images of the sky which have been T/MPREPARE'd into a flat field frame. However, the Gemini web pages state that there is, so far, no satisfactory method of creating imaging flats without significantly increasing the noise level in the data and that since the detector response appears to be intrinsically fairly flat over the field of view, flat-fielding of T-ReCS and Michelle images is not recommended. No flat field observations were taken for the any of the T-ReCS/Michelle data presented herein.

- MISTACK and MIREGISTER collapse the nod sets of the chop/nod data into a single [320,240] image. Both routines require that the input frames have been prepared with either TPREPARE or MPREPARE.

  MISTACK averages (or sums, if the combine task parameter is changed to "sum" from the default of "average") each frame by coadding the signal from each nod position and dividing by the number of frames (nods). MISTACK was used for the processing of the data herein with the default setting of averaging the images. In this case, the effective exposure time remains the same as for a individual image in the raw data: the on-source time per saveset for T-ReCS and the on-source time per nod position for Michelle. The effective exposure time for the averaged frames is determined from information in the primary FITS header. For T-ReCS it is the product of the keywords: FRMCOADD, CHPCOADD and FRMTIME, i.e., the number of frames coadded per chop position multiplied by the number of chop cycles per saveset, multiplied by the exposure time per frame in milliseconds. For Michelle, it is the product of the NUMEXPOS and EXPOSURE keywords, where NUMEXPOS is the number of exposures per chop position per nod and EXPOSURE is the duration of one exposure in seconds.

MIREGISTER combines the nod frames using cross-correlation techniques with the XREGISTER task in IRAF to shift the frames before they are averaged (or summed if combine is set to "sum").

- MIREDUCE is a task which calls the main tasks from the aforementioned reduction steps for each T-ReCS or Michelle raw data file. By default, the task identifies if a file is from T-ReCS or Michelle, runs TPREPARE or MPREPARE as appropriate, and, for chop/nod data, combines the nod positions using MISTACK. The 'fl-view' and 'fl-background' keywords can be set to interactively view and examine the images (with T/M/MIVIEW), or investigate background statistics (T-ReCS only, with TBACKGROUND). The 'stackoption' parameter can be changed from the default of "stack", which uses MISTACK, to "register" which calls MIREGISTER to first register and then combine the data. Multiple raw data files can be reduced, with MIREDUCE or the individual tasks, using a list format for the 'inimages' parameter, i.e., "@in.lis", where in.lis is the list of images to be reduced. The output filenames can be defined simply with an output prefix added to the input file name, defined specifically for single images, or be provided in a list format for multiple images (i.e., "@out.lis").

B.3 Final image cleaning

As discussed in Chapter 2, Section 2.5.3, the reduced mid-IR images often showed broad horizontal and/or vertical striping. The custom IDL routines used to clean the data — 'NOISE_MASKH.PRO' which removes the horizontal banding, and 'NOISE_MASKV.PRO' which removes the vertical striping — are described here.

Essentially, both routines apply a standard IDL task MEDIAN.PRO to determine the median background value, within defined threshhold limits, of single rows (NOISE_MASKH.PRO) or columns (NOISE_MASKV.PRO) of data, each a pixel high/wide, for the entire height/width of the array. The median value of each row (or column) is assigned as the value for each pixel in that row (column) in order to build up a horizontal (or vertical) noise pattern for the entire 320×240 array. The noise pattern is then subtracted from the original data to return a cleaned image in one-dimension.

The threshhold limits are set as follows: The user supplies a threshhold value in the call to the appropriate cleaning routine, signifying how many standard deviations above or below the sky level to mask out before determining the noise pattern. The default is 2,

unless set otherwise. The mode and standard deviation of the background on which to apply the user-defined threshhold limit, are determined by calling another IDL routine, MMM.PRO, from within the main NOISE_MASKH.PRO and NOISE_MASKV.PRO programmes. Values above the higher limit of the threshhold or below the lower limit of the threshhold are effectively masked for the purposes of calculating the median by setting them to 'NaN's.

For the vertical cleaning with NOISE_MASKV.PRO, there is also an input option to "split" the cleaning so that sections of the array above and below a bright source are cleaned separately. This is really only desired when a very bright source in the field (for example, a primary flux standard) causes a channel offset effect above and below the source, such that the column containing the source becomes supressed in brightness in the top half of the array, yet appears brighter in the bottom half of the array, referred to as the "hammer effect". When using this option, the threshhold should be increased from the conservative default of 2 to a level that includes the "hammered" pixels, e.g.,threshhold= 50 or more. The hammer effect can also result in a depressed response in every channel of the array at the same row as the bright source (seen in Figure 2.4 in Chapter 2), although this is not so easily removed from the images. Photometry radii used for standards displaying this effect, were small enough such that the ghost images along the same row as the source could be ignored.

The cleaning routines are designed for data where the majority of the field is sky emission, which is the case for the Gemini T-ReCS and Michelle data presented herein.

The IDL scripts were run on both the science and calibration data using a wrapper IDL script, written with the UNIX command AWK, which does the following:

- Compiles the main routines NOISE_MASKH.PRO and NOISE_MASKV.PRO.
- Uses standard IDL routine MRDFITS.PRO to read the data FITS files with the header information into the IDL arrays.
- Executes NOISE_MASKH.PRO and NOISE_MASKV.PRO routines for each array in that order, where the input for the vertical cleaning is the output of the horizontal cleaning, to produce an array cleaned in both dimensions.
- Uses standard IDL procedure MRWFITS.PRO to write out the cleaned arrays and header information into a simple FITS file format.

A default threshhold of 2 was used as the mask for most of the science data and the calibration data, except where the hammer effect was noticeable. In which case, the "split" option of NOISE_MASKV.PRO was used with a threshhold of 50. Figure 2.4 in Chapter 2 shows before and after cleaning with the NOISE_MASKH.PRO and NOISE_MASKV.PRO routines.

Appendix C

PSF-fitted photometry with IRAF `daophot` - summary of process

1. *Identifying sources for PSF-fitted photometry.* Whilst there is an in-built task (`daofind`) to identify stars on the frame for PSF-fitting, for the SN data there were only a few sources per frame at most requiring photometry. Consequently, it was simpler to identify them manually using `imexamine` to obtain the image coordinates (keystroke 'a' or 'x') and copy these to a text file for input to the remaining tasks. For the Gemini data, coordinates were also acquired in the same way for the standard stars since these were used to construct the semi-empirical PSF model.

2. *Initial aperture photometry of sources.* `phot` was used to perform aperture photometry on the identified stars to compute sky backgrounds and initial magnitudes.

3. *Defining the PSF.* This is the most critical step of the method. The model is usually constructed in an iterative manner using a selection of suitable stars (usually between three and five stars, which are ideally isolated, well-sampled and unsaturated) from the image frame. Each of the PSF-stars is scaled according to its magnitude (estimated from aperture photometry) and the weighted average is fit with a suitable analytical function, with optional look-up table(s) of the residuals computed. Advice for selecting good candidate PSF-stars and a detailed explanation of the PSF-building process can be found in section 4.7 of "A User's Guide to

Stellar CCD Photometry with IRAF" by Massey & Davis (1992). However, creating the PSF was far simpler in the case of the Gemini data, in that the standard star was the only suitable star available.

A task called `daopsf`, written by Dr. B. E. K. Sugerman[1], was used to simplify the process of generating the PSF. `daopsf` first calls the `phot` task to determine sky backgrounds and initial magnitudes of the candidate PSF-stars. The task then calls existing `daophot` package tasks `pstselect` and `psf`, where `pstselect` is used to select suitable candidate stars from the photometry output file for input to the PSF modelling task `psf`. It also contains an option (**gensee**) to call the `seepsf` task which creates an image of the final PSF model (at the pixel scale of the image from which it was created). This can be examined to ensure that the final model looks reasonable (i.e., that is not contaminated with faint neighbouring stars). Critical parameters for the `daopsf` task include:

- **aperture** – This is the aperture radius, in pixels, used for the initial photometry of the candidate PSF-stars with the `phot` task. The sky-fitting parameters, **salgorithm**, **annulus** and **dannulus**, were defined within `daopsf` in the same way as for the `phot` task as previously described in Section 2.6.1. As only one star was available to create the PSF model, and this was a bright, isolated standard star, the aperture size was set to be the same as the **daorad** parameter described below.

- **daorad** – *Equivalent to the* **psfrad** *parameter in the* `daophot` *package*. This is the radius, in pixels, of the PSF, which should contain "nearly all" of the light from the brightest star of interest. This was investigated for the standard stars in the same way as when choosing an aperture size from which to determine the flux conversion factor for the aperture photometry, i.e., using multi-aperture photometry to determine which aperture size contained most of the flux by inspecting plots of counts versus aperture radius and noting the aperture size at which the counts levelled off.

- **fitrad** – This is the radius, in pixels, that defines the size of the PSF used for fitting a star. For suitable PSF stars, it is the data within this radius that is

[1]Private communication, 2005

used in computing the analytic component of the PSF model specified by the **function** parameter.

- **function** – There are several options for the form of the analytic function, including a 2-D elliptical Gaussian, Moffat and Lorentz functions and higher-order Gaussian/Lorentz combinations. But this option was generally set to "auto", whereby each of the six available functions were tried in turn and the one with the smallest scatter in the fit was selected.

- **varorder** – This is the order of the empirical component of psf model. This was set to zero, representing an empirical constant PSF model composed of an analytic component and a single look-up table. In this case, it is assumed that the PSF model has the same shape everywhere in the image frame.

A typical call to the `daopsf` task to create the semi-empirical PSF model is as follows:

```
 ecl> daopsf input=gemini_standard_image.fits \\
>>> psf=gemini_standard_image.coo nmin=1 gensee+ daorad=25 \\
>>> fitrad=4 salgorithm="mode" annulus=30 dannulus=10 \\
>>> aperture=25 function=auto varorder=0
```

4. *PSF-fitting.* `allstar` was used for simultaneous PSF-fitting of the relevant stellar sources in the frame, and to produce a PSF-subtracted image from which the goodness of the fit was examined by eye. The task uses a weighted, non-linear, least-squares fitting procedure to shift and scale the PSF model to fit each stellar source, using the centroid of the stellar source as the profile centre, and the sky level as determined from aperture photometry. The scaling yields the magnitude estimate. `allstar` also outputs a goodness of fit statistic, chi, given by the ratio of the observed pixel-to-pixel scatter in the fitting residuals to the expected scatter.

   Critical parameters of the `allstar` task include the name of the PSF model (**psfimage**) as created with the `daopsf` task; the fitting radius (**fitrad**) which, as previously defined, is the pixel radius that limits the extent of the PSF used in fitting a stellar source - this was generally set to be the same size as the aperture radius for aperture photometry, i.e., the FWHM of the stellar profile + 1 or 2 pixels.; the effective **readnoise** and gain (**epadu**) were defined to ensure an appropriate estimation

of the magnitude errors and PSF-fitting weights; the sky values were generally re-computed at this stage by setting the **fitsky** parameter to "yes" and using the annulus defined by the `daopars` parameters **sannulus** and **wsannulus**; finally, the **function** and **psfrad** parameters were set to reflect the values defined in the `daopsf` task for the PSF model.

A typical call to the `allstar` task for carrying out psf-fitted photometry of a SN detection is as follows:

```
 ecl> allstar image=gemini_sn_image.fits photfile=default \\
>>> psfimage=gemini_standard_image.psf allstarfile=default \\
>>> rejfile=default subimage=default readnoise=24250 epadu=24000 \\
>>> function=moffat25 psfrad=25 fitrad=4 \\
>>> fitsky=yes sannulus=5 wsannulus=10
```

As previously mentioned, the magnitudes output from `allstar` were scaled from the PSF model, whose own magnitude was determined from aperture photometry of the brightest PSF star. The zero-point of the magnitude scale for the aperture photometry was set with the **zmag** parameter within the `phot` task. However, as only relative magnitudes were required, **zmag** was left at the default, and arbitrary, value of 25 mag, corresponding to a unit flux. The magnitudes of the SN detections as output by `allstar` were then converted to image units (which for the Gemini data was in counts) using the standard form of the flux-magnitude equation:

$$F_{SN} = F_0 \times 10^{0.4(m_0 - m_{SN})},$$

where F_{SN} is the flux in counts of the SN detection; F_0 is the zero-point flux in counts, equivalent to 1.0 count; m_{SN} is the magnitude of the SN detection; and m_0 is the zero-point magnitude of 25 mag.

Appendix D

Defining *Spitzer* observations

Defining AORS with the Spitzer Planning Observations Tool (SPOT)

This section provides an overview of the Spitzer Planning Observations Tool (SPOT) and, more specifically, the parameters used to set up the *Spitzer* observations described in this thesis. For a more detailed discussion of the capabilities and functions of SPOT see the SPOT User's Guide, Spitzer Planning Observations Tool v18.0 (June 18, 2008)[1].

SPOT is a software tool used by potential and approved *Spitzer* observers for planning and modifying observations, and is also used for electronic submission of observing proposals. The multi-platform JAVA-based software uses a Graphical User Interface (GUI), and is available to download from the Proposal Kit section of the SSC webpages[2].

For each science target to be observed, an Astronomical Observation Template (AOT) must be selected to define a distinct *Spitzer* observing mode. Table D.1 outlines the eight AOTs which correspond to the eight possible observing modes available with the three *Spitzer* science instruments.

SPOT is used to enter the target information and define observation details for a selected AOT. The complete target and instrument information results in an Astronomical Observation Request (AOR), which is the fundamental unit of a *Spitzer* observation. An AOR contains three categories of information: the astronomical target, the AOT-specific parameters (e.g., instrument configuration, exposure time etc) and the timing

[1]http://ssc.spitzer.caltech.edu/documents/SPOT /SPOT_UserGuide_v18.pdf
[2]http://ssc.spitzer.caltech.edu/propkit/spot/

Table D.1: The eight Astronomical Observation Templates (AOTs) corresponding to the eight *Spitzer* observing modes.

AOT (*Spitzer* observing mode)	Description
IRAC Mapping/Photometry	Simultaneous imaging at wavelengths of 3.6, 4.5, 5.8 and 8.0 μm, over the two 5.′2 × 5.′2 fields of view.
MIPS Photometry and Super-Resolution Imaging	Imaging photometry and high-resolution imaging at 24, 70 and 160 μm.
MIPS Scan Mapping	For large field maps at 24, 70 and 160 μm. Maps are constructed from 5′-wide (2.5′-wide for full coverage at 70 μm) strips between 0.5° and 6° in length. The slow telescope scanning is combined with motion compensation using a cryogenic scan mirror.
MIPS Spectral Energy Distribution (SED)	Very low-res. (R = 15 – 25) spectroscopy in the wavelength range 55 –95 μm using the 70 μm Ge:Ga array.
MIPS Total-Power Measurement	Provides zero-level-reference observations for absolute brightness of extended sources.
IRS Staring-Mode Spectroscopy	Low-res. long-slit spectroscopy (R = 60 – 120) from 5.3 to 40 μm and high-res. spectroscopy (R = 600) from 10 to 37 μm. Also, peak-up array imaging in two filters covering wavelengths of 13.5 – 18.5 and 18.5 – 26 μm, over a field of view of ∼ 1 arcmin^2. Raster mapping is also supported in this mode.
IRS Spectral Mapping	Slit scanning spectroscopy for fields up to a few arcminutes in extent.
IRS Peak-Up Imaging	Peak-up array imaging only, in two filters over wavelengths 13.5 – 18.5 μm and 18.5 – 26 μm and a field of view of ∼ 1 arcmin^2.

and relational constraints (e.g., specify a window when an AOR should be executed, or how one AOR relates to others in a group).

In addition to its main function of allowing the construction and editing of AORs, SPOT also includes useful visualization tools for checking the position of proposed observations on the sky. SPOT can also be used to estimate the total observing time (including telescope overheads) for each AOR in a proposed program, as well as provide target visibility information, focal plane position angle for a selected observation date, and estimates of the zodiacal and cosmic infrared background at the target position.

Potential observations can be planned and developed in an iterative manner until AORs are ready for submission along with the observing proposal. For successful proposals, the complete AORs are uploaded to the *Spitzer* database for expansion into

activities and uplink sequences for transmission to the spacecraft.

The AOTs used for the *Spitzer* observations presented in this thesis were those for IRAC Mapping/Photometry, MIPS Photometry/Super-Resolution, MIPS Scan Mapping, and IRS Peak-Up Imaging. A brief description of each of the observing modes adopted and the corresponding AOT parameters follows. However, where relevant, specific parameter values selected for the observing programs/individual targets may also be given in Chapter 3, Section 3.3.

IRAC Mapping/Photometry. This observing mode was used in the SINGS Legacy program and all GO programs in *Spitzer* Cycles 1, 2, 3 and 4.

The IRAC AOT consists of imaging with an optional dither pattern superposed on an optional rectangular-grid raster for mapping. Imaging was carried out in all four IRAC channels by selecting both the 3.6/5.8 μm and 4.5/8.0 μm fields of view in the AOT.

Several imaging modes are available, including Full Array mode, High Dynamic Range (HDR) mode, Subarray mode, and Stellar mode. The Full Array readout mode was used for IRAC imaging of SNe with our *Spitzer* GO programs. Archival SINGS Legacy data, used to supplement our *Spitzer* sample of SNe, uses IRAC in its HDR mode. The Full Array and HDR imaging modes are discussed here.

In Full Array readout mode there are four exposure, or "frame", times to select from: 2, 12, 30 and 100 seconds, which correspond to effective exposure times per frame of: 1.2, 9.86, 26.8 and 96.8 seconds. A 30 s frame time was used for each image of the SINGS galaxies. For the first GO program a common frame time of 100 s was selected for all sources, but thereafter frame times were chosen specifically for each target based on desired sensitivities.

HDR mode is used where it is possible that bright sources will saturate the array in the frame time required to achieve the desired sensitivity. Selecting the HDR option in the IRAC AOT results in one or more short-duration frames being taken along with the longer-duration frames, allowing high dynamic range through the recovery of photometry of bright sources without loss in sensitivity. In HDR mode, frames are executed in order of shortest to longest without repositioning of the telescope. With the dither option selected, as was the case for the SINGS observations, the entire frame set in HDR mode is repeated at each dither position.

There are also mapping options within the IRAC AOT. The SINGS IRAC observations

required complete mapping of their sample galaxies. This was done in array coordinates which centres the map on the position directly between the two IRAC fields of view and images both fields simultaneously. Care must be taken with the AOT set-up to ensure the map centre is imaged and that there is equal field coverage in all four arrays. Celestial coordinate mapping is preferred for highly elongated regions and this mode was used in one case for our Cycle 2 GO program, where two SNe present in one galaxy (SN 2002hh and SN 2004et in NGC 6946) were separated by $\sim 5'$ in an east-west direction. For a celestial coordinates map, the AOT performs the map grid once with the 4.5/8.0 μm field of view centred on each map grid position, and then repeats the map grid steps with the 3.6/5.8 μm field of view. For either map type, the map grid is specified within the AOT by choosing the number of rows and columns and the map step size, and for celestial coordinate mapping, the position angle. Mapping was not necessary for subsequent GO programs. When "no mapping" is selected, the map grid consists of a single position at the coordinates specified in the target section of the AOT, viewed first by the 4.5/8.0 μm field of view and then by the 3.6/5.8 μm field of view.

Whilst there is an option in the IRAC AOT to set the number of in-place frame repeats (successive frames taken at the same position), this observing method is not encouraged by the SSC for a number of reasons (see section 6.2.4.1.1 of the SOM), and dithers are recommended for providing higher quality data. Dithered observations involve small shifts in pointing between multiple frames which provides a good way of removing array-dependent and transient (e.g., cosmic rays) image artifacts and reduces noise from the effects of pixel-to-pixel errors in the flat-field. The sub-pixel dithering that is available can be used to recover some level of information which would otherwise be lost through under-sampling of the array. Combined with the drizzle technique (Fruchter & Hook 2002) to reconstruct the images, sub-pixel dithering can improve the sampling to provide spatially enhanced final IRAC image mosaics. See Chapter 3, Section 3.4.2 for a further discussion of the processing used to achieve this result for the IRAC data presented here. Single observations per pointing together with dithering techniques were employed for all IRAC observations presented here.

At either the single position defined in the target section of the AOT or each of the positions defined by the map grid, the telescope is pointed to a series of offset positions that define the dither pattern. There are several dither patterns available to choose from. In Full Array mode there are five fixed pattern types which are performed identically at

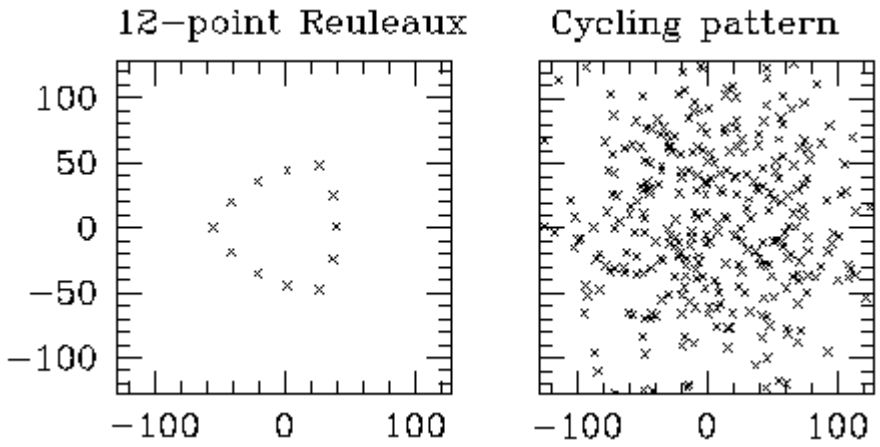

Figure D.1: The 12-point Reuleaux and Cycling IRAC dither patterns for the "large" scale factor. Axes are in pixels. Taken from IRAC Chapter 6 of the SOM.

each mapping position. Alternatively, the cycling pattern can be used, which is where a different subset of dither positions is performed at each mapping position. Each of the dither patterns is available in large, medium, and small scale sizes. Medium scale dither patterns were used for pointed observations to better protect against image artifacts and small-scale patterns were selected where mapping was carried out. Sub-pixel dithering is maintained for all dither patterns at all scales.

The small scale cycling and the fixed medium scale 12-point Reuleaux dither patterns were used for the IRAC observations presented in this thesis. Sub-pixel sampling to half a pixel is achievable in these modes (compared with the quarter pixel sub-pixel sampling limit, determined by the telescope pointing accuracy and IRAC image distortion). For the cycling dither pattern, the number of dithers to perform at each map grid position and the starting point in the cycling dither table were specified in the AOT. Figure D.1 shows the IRAC large-scale 12-point Reuleaux and cycling dither patterns.

MIPS Photometry/Super-Resolution Imaging. The MIPS photometry mode is for multi-band observations of reasonably compact sources. At 24 μm super-resolution imaging is automatically achieved from the standard dither sequence which provides thorough sampling of the point spread function, allowing the final image to be processed to higher angular resolution than the native detector pixel size. This observing mode at 24 μm was used for all programs in *Spitzer* Cycles 1, 2, 3 and 4.

For the 24 μm data, a "small" or "large" field size is selected in the AOT. The large field

size is generally used for larger (> 2″) sources, but it was used for the Cycle 1 observations since the original target list contained a couple of host galaxies which contained two SNe and this way both SNe could be observed with one pointing. For the subsequent GO programs, a small field size was used.

Dithering on the array is achieved by a combination of scan mirror motions and spacecraft small offsets. For the small field size, one cycle of basic 24 μm observations equates to a 14-position dither sequence. The nominal pattern for these observations is a column of 7 images on the left-hand side of the array dithered using the scan mirror, followed by a 25.5 pixel offset to right-hand side of the array, where a further column of 7 images are obtained (see section 8.2.1.2.1 of the SOM for more details). For the large field size, a 10-position dither sequence is comprised of a column of 5 images each separated by 1.5 pixels, followed by a spacecraft offset across the array of 4.5 pixels and a repeat of the column of 5 images. For the large field size, a sky image is obtained by slewing the telescope to a sky offset position specified by the user and repeating the dither sequence (see section 8.2.1.2.2 of the SOM for more details). The sky offset was set to be 10″ for the Cycle 1 observations.

The use of raster maps for coverage of a small area in photometry mode is an option that can be set in the AOT, but this was not necessary for the *Spitzer* GO programs presented in this chapter.

There are three exposure times to select from in the MIPS photometry AOT: 3, 10 and 30 seconds. For the first GO program a common exposure time of 10 s was selected for all sources, but thereafter exposure times were chosen specifically for each target based on desired sensitivities. The observer also specifies the number of observation cycles, which is the number of times to execute the basic observing sequence or full map sequence. This was set to 10 cycles for the GO Cycle 1 program and generally kept to one cycle for the remaining programs, except in a few cases where deeper exposures were desired for the older, and most probably fainter, SNe 1998S, 1999bw and 1999em.

MIPS Scan Mapping. The MIPS scan map mode provides efficient large-area coverage of the sky at 24 μm, 70 μm and 160 μm. This observing mode was used for the SINGS Legacy MIPS observations of nearby galaxies in *Spitzer* Cycle 1.

Coverage is achieved by scanning the telescope at a constant rate across the sky, whilst using a reverse sawtooth (ramp) motion of the scan mirror to effectively freeze the

images on all three arrays for a set integration time, before jumping forward for the next integration (Rieke et al. 2004). The ramp motion of the scan mirror avoids the need to re-point and stabilise the telescope between exposures.

The three constant scan rates available in the AOT are slow (∼ 2.″6/s), medium (∼ 6.″5/s) and fast (∼ 17″/s). The medium scan rate was used for the SINGS Legacy observations for all three MIPS arrays.

The map grid is specified in the AOT by the following parameters: the map centre offset, the cross-scan step, the number of scan legs and the scan leg length.

The map centre offset is specified in the cross-scan and in-scan directions in arcseconds. The map itself is comprised of essentially linear scans of the sky in the forward and reverse directions, with each direction defined as a "scan leg". The length of a scan leg can be between 0.5° and 6° depending on the scan rate. The SINGS observations presented in this thesis used a "scan leg length" of 0.5°. The scan leg offsets in the cross-scan direction (the "cross-scan step") set how much overlap there is between scan legs. The SINGS observations used a cross-scan step of 148″ (approximately one-half the array width) in both the forward and reverse directions, with a range of 3 to 11 scan legs for the data presented in this thesis.

A single scan leg provides multiple redundancy at 24 and 70 μm, but only single redundancy at 160 μm for slow and medium scan rates (and only half-coverage at the fast scan rate). For a single-pass, or scan leg, the scan map integration time per pixel is ∼ 40 s at 24 μm and 70 μm for the medium scan rate, since each point source is imaged around 10 times in a single scan leg with individual frame times of just under 4 s. At 160 μm the total single-pass scan map integration time per pixel is ∼ 4 s with the medium scan rate since each source appears in just one frame.

The SINGS MIPS observations were obtained using the scan-mapping mode in two separate visits to each galaxy. Due to the redundancy inherent in the scan-mapping mode, each pixel in the final mosaic core map area was effectively observed 40, 20, and 4 times at 24, 70 and 160 μm respectively, resulting in respective integration times per pixel of ∼ 160 s, 80 s, and 16 s. For example, for the MIPS 24 μm data, each point is imaged approximately 10 times in a single scan leg, which is then doubled due to the half-array width overlap with each scan direction. Since there are two visits to each galaxy, this results in an effective coverage of around 40 observations for the final core mosaic, with individual frames times of ∼ 4 s, resulting in a total integration time per pixel of ∼ 160 s.

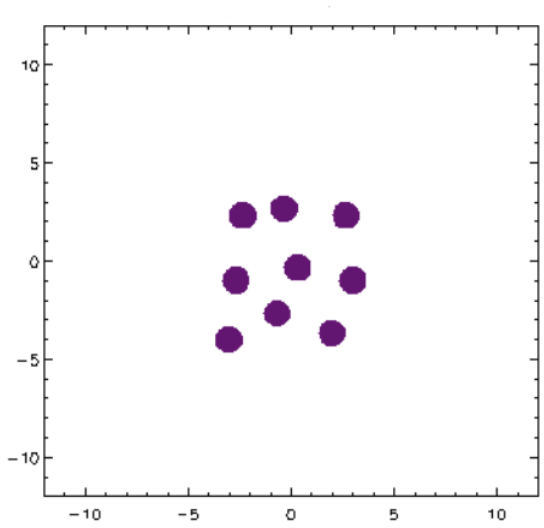

Figure D.2: The 9-point random IRS PUI dither pattern for the "small" scale factor. Axes are in pixels. Taken from IRS Chapter 7 of the SOM.

IRS Peak-Up Imaging. The peak-up arrays in the short-low module of the IRS provide science-quality imaging capabilities at 16 and 22 μm. This observing mode was used for the GO programs in *Spitzer* Cycles 3 and 4.

Within the IRS Peak-up imaging (PUI) AOT, observations can be selected in both the blue (16 μm) and red (22 μm) arrays, or both. The PUI observations presented in this thesis were carried out with just the blue peak-up array. The integration parameters selected in the AOT are the ramp (exposure) time and number of cycles. There is an option of three ramp times: 6, 14 and 30 seconds. The ramp times were chosen specifically for each SN based on desired sensitivities. For the Cycle 4 data, this resulted in the longest exposure time of 30 seconds for all sources except SN 2002hh, which was still bright enough to use the shortest exposure of 6 seconds. Exposure time can be increased via multiple ramps by selecting an appropriate number of cycles but this was not employed for the Cycle 3 and 4 GO observations. Instead, dithering was used to provide multi-pixel sampling of a given sky position. As highlighted previously in the case of the IRAC observations, dithering-techniques help to improve final image quality, and sub-pixel dithering can be used to recover additional spatial information (though the improvement is not pronounced in the critically-sampled blue peak-up array).

Random and cycling dither patterns are available. The small-scale, nine-position random pattern was used for the PUI observations, as shown in Figure D.2. The small

pattern has a minimum step size of 2 pixels (equivalent to the FWHM of point sources in the blue peak-up array) and allows for an area of full-overlap in the final mosaic image which is about twice that of the large patterns. With the 9-point patterns, sub-pixel sampling to a third of a pixel is achieved with offsets in multiples of a third of a pixel.

Bibliography

Amari, S., Hoppe, P., Zinner, E. & Lewis, R. S., 1992, *ApJ*, **394**, L43

Amari, S. & Lodders, K., 2007, *Highlights of Astronomy*, **14**, 349

Andrews, J. E., Gallagher, J. S., Clayton, G. C., Sugerman, B. E. K., Chatelain, J. P., Clem, J., Welch, D. L., Barlow, M. J., Ercolano, B., Fabbri, J., Wesson, R. & Meixner, M., 2010, *ApJ*, **715**, 541

Andrews, J. E., Sugerman, B. E. K., Clayton, G. C., Gallagher, J. S., Barlow, M. J., Clem, J., Ercolano, B., Fabbri, J., Meixner, M., Otsuka, M., Welch, D. L. & Wesson, R., 2011, *ApJ*, **731**, 47

Ardila, D., 2008, *Calibration of the IRS Peak-Up Arrays*, Spitzer Science Center, California Institute of Technology, Pasadena, USA, version 2.0 edition

Ardila, D., Chary, R. & IRS IST, 2008, *Infrared Spectrograph Data Handbook*, Spitzer Science Center, California Institute of Technology, Pasadena, USA, version 3.2 edition

Arendt, R. G., Dwek, E. & Moseley, S. H., 1999, *ApJ*, **521**, 234

Argo, M. K., Beswick, R. J., Muxlow, T. W. B., Pedlar, A., Fenech, D. & Thrall, H., 2005, *Memorie della Societa Astronomica Italiana*, **76**, 565

Arnett, D., 1996, *Supernovae and nucleosynthesis. an investigation of the history of matter, from the Big Bang to the present*

Arnett, W. D., Bahcall, J. N., Kirshner, R. P. & Woosley, S. E., 1989, *Ann. Rev. Astr. Astrophys.*, **27**, 629

Barlow, M., Fabbri, J., Meixner, M. & Sugerman, B., 2004, *IAU Circ.*, **8400**, 2

Barlow, M. J., 1978, *MNRAS*, **183**, 367

Barlow, M. J., Krause, O., Swinyard, B. M., Sibthorpe, B., Besel, M., Wesson, R., Ivison, R. J., Dunne, L., Gear, W. K., Gomez, H. L., Hargrave, P. C., Henning, T., Leeks, S. J., Lim, T. L., Olofsson, G. & Polehampton, E. T., 2010, *A&A*, **518**, L138+

Barlow, M. J., Sugerman, B. E. K., Fabbri, J., Meixner, M., Fisher, R. S., Bowey, J. E., Panagia, N., Ercolano, B., Clayton, G. C., Cohen, M., Gledhill, T. M., Gordon, K., Tielens, A. G. G. M. & Zijlstra, A. A., 2005, *ApJ*, **627**, L113

Beelen, A., Cox, P., Benford, D. J., Dowell, C. D., Kovács, A., Bertoldi, F., Omont, A. & Carilli, C. L., 2006, *ApJ*, **642**, 694

Benetti, S., Cappellaro, E., Turatto, M., della Valle, M., Mazzali, P. A. & Gouiffes, C., 1994, *A&A*, **285**, 147

Bertoldi, F., Carilli, C. L., Cox, P., Fan, X., Strauss, M. A., Beelen, A., Omont, A. & Zylka, R., 2003, *A&A*, **406**, L55

Bessell, M. S., Castelli, F. & Plez, B., 1998, *A&A*, **333**, 231

Beswick, R. J., Muxlow, T. W. B., Argo, M. K., Pedlar, A. & Marcaide, J. M., 2004, *IAU Circ.*, **8435**, 3

Bianchi, S. & Schneider, R., 2007, *MNRAS*, **378**, 973

Bjorkman, J. E. & Cassinelli, J. P., 1993, *ApJ*, **409**, 429

Blair, W. P., Ghavamian, P., Long, K. S., Williams, B. J., Borkowski, K. J., Reynolds, S. P. & Sankrit, R., 2007, *ApJ*, **662**, 998

Bode, M. F. & Evans, A., 1980, *MNRAS*, **193**, 21P

Bohlin, R. C., 2007, in C. Sterken (ed.), *The Future of Photometric, Spectrophotometric and Polarimetric Standardization*, volume 364 of *Astronomical Society of the Pacific Conference Series*, pp. 315–+

Botticella, M. T., Pastorello, A., Smartt, S. J., Meikle, W. P. S., Benetti, S., Kotak, R., Cappellaro, E., Crockett, R. M., Mattila, S., Sereno, M., Patat, F., Tsvetkov, D., van Loon, J. T., Abraham, D., Agnoletto, I., Arbour, R., Benn, C., di Rico, G., Elias-Rosa, N.,

Gorshanov, D. L., Harutyunyan, A., Hunter, D., Lorenzi, V., Keenan, F. P., Maguire, K., Mendez, J., Mobberley, M., Navasardyan, H., Ries, C., Stanishev, V., Taubenberger, S., Trundle, C., Turatto, M. & Volkov, I. M., 2009, *MNRAS*, **398**, 1041

Bouchet, P. & Danziger, I. J., 1993, *A&A*, **273**, 451

Bouchet, P., Slezak, E., Le Bertre, T., Moneti, A. & Manfroid, J., 1989, *A&AS*, **80**, 379

Boulanger, F., Cox, P. & Jones, A. P., 2000, in F. Casoli, J. Lequeux, & F. David (ed.), *Infrared Space Astronomy, Today and Tomorrow*, pp. 251–+

Branch, D., Livio, M., Yungelson, L. R., Boffi, F. R. & Baron, E., 1995, *PASP*, **107**, 1019

Branch, D. & Venkatakrishna, K. L., 1986, *ApJ*, **306**, L21

Cardelli, J. A., Clayton, G. C. & Mathis, J. S., 1989, *ApJ*, **345**, 245

Cernuschi, F., Marsicano, F. & Codina, S., 1967, *Annales d'Astrophysique*, **30**, 1039

Cherchneff, I. & Dwek, E., 2010, *ApJ*, **713**, 1

Chevalier, R. A. & Fransson, C., 2008, *ApJ*, **683**, L135

Chevalier, R. A., Fransson, C. & Nymark, T. K., 2006, *ApJ*, **641**, 1029

Chevalier, R. A. & Klein, R. I., 1978, *ApJ*, **219**, 994

Chugai, N. N., Fabrika, S. N., Sholukhova, O. N., Goranskij, V. P., Abolmasov, P. K. & Vlasyuk, V. V., 2005, *Astronomy Letters*, **31**, 792

Clayton, D. D., 1979, *Ap&SS*, **65**, 179

Clayton, D. D., Amari, S. & Zinner, E., 1997, *Ap&SS*, **251**, 355

Clayton, D. D., Deneault, E. A.-N. & Meyer, B. S., 2001, *ApJ*, **562**, 480

Cohen, M., Megeath, S. T., Hammersley, P. L., Martín-Luis, F. & Stauffer, J., 2003, *AJ*, **125**, 2645

Cohen, M., Walker, R. G., Carter, B., Hammersley, P., Kidger, M. & Noguchi, K., 1999, *AJ*, **117**, 1864

Colgate, S. A. & McKee, C., 1969, *ApJ*, **157**, 623

Crockett, R. M., Smartt, S. J., Pastorello, A., Stephens, A. W., Maund, J. R. & Mattila, S., 2009, *ArXiv e-prints*

Danziger, I. J., Fosbury, R. A. E., Alloin, D., Cristiani, S., Dachs, J., Gouiffes, C., Jarvis, B. & Sahu, K. C., 1987, *A&A*, **177**, L13

Danziger, I. J., Gouiffes, C., Bouchet, P. & Lucy, L. B., 1989, *IAU Circ.*, **4746**, 1

Davis, L. E., 1994, *A Reference Guide to the IRAF/DAOPHOT Package*, IRAF Programming Group, National Optical Observatories, Tuscon, Arizona 85726, USA

Dolphin, A. E., 2000, *PASP*, **112**, 1397

Dolphin, A. E., 2009, *PASP*, **121**, 655

Douvion, T., Lagage, P. O., Cesarsky, C. J. & Dwek, E., 2001*a*, *A&A*, **373**, 281

Douvion, T., Lagage, P. O. & Pantin, E., 2001*b*, *A&A*, **369**, 589

Draine, B. T., 2003, *Ann. Rev. Astr. Astrophys.*, **41**, 241

Draine, B. T. & Lee, H. M., 1984, *ApJ*, **285**, 89

Ducati, J. R., Bevilacqua, C. M., Rembold, S. B. & Ribeiro, D., 2001, *ApJ*, **558**, 309

Dunne, L., Eales, S., Ivison, R., Morgan, H. & Edmunds, M., 2003, *Nature*, **424**, 285

Dunne, L., Maddox, S. J., Ivison, R. J., Rudnick, L., Delaney, T. A., Matthews, B. C., Crowe, C. M., Gomez, H. L., Eales, S. A. & Dye, S., 2009, *MNRAS*, **394**, 1307

Dwek, E., 1983, *ApJ*, **274**, 175

Dwek, E., 1988, *ApJ*, **329**, 814

Dwek, E., 1998, *ApJ*, **501**, 643

Dwek, E., 2004, *ApJ*, **607**, 848

Dwek, E., A'Hearn, M. F., Becklin, E. E., Brown, R. H., Capps, R. W., Dinerstein, H. L., Gatley, I., Morrison, D., Telesco, C. M., Tokunaga, A. T., Werner, M. W. & Wynn-Williams, C. G., 1983, *ApJ*, **274**, 168

Dwek, E. & Cherchneff, I., 2011, *ApJ*, **727**, 63

Dwek, E., Galliano, F. & Jones, A. P., 2007, *ApJ*, **662**, 927

Dwek, E. & Scalo, J. M., 1980, *ApJ*, **239**, 193

Elias, J. H., Matthews, K., Neugebauer, G. & Soifer, B. T., 1986, in *Bulletin of the American Astronomical Society*, volume 18 of *Bulletin of the American Astronomical Society*, pp. 1016–+

Elmhamdi, A., Chugai, N. N. & Danziger, I. J., 2003*a*, *A&A*, **404**, 1077

Elmhamdi, A., Danziger, I. J., Cappellaro, E., Della Valle, M., Gouiffes, C., Phillips, M. M. & Turatto, M., 2004, *A&A*, **426**, 963

Elmhamdi, A., Danziger, I. J., Chugai, N., Pastorello, A., Turatto, M., Cappellaro, E., Altavilla, G., Benetti, S., Patat, F. & Salvo, M., 2003*b*, *MNRAS*, **338**, 939

Elvis, M., Marengo, M. & Karovska, M., 2002, *ApJ*, **567**, L107

Engelbracht, C. W., Blaylock, M., Su, K. Y. L., Rho, J., Rieke, G. H., Muzerolle, J., Padgett, D. L., Hines, D. C., Gordon, K. D., Fadda, D., Noriega-Crespo, A., Kelly, D. M., Latter, W. B., Hinz, J. L., Misselt, K. A., Morrison, J. E., Stansberry, J. A., Shupe, D. L., Stolovy, S., Wheaton, W. A., Young, E. T., Neugebauer, G., Wachter, S., Pérez-González, P. G., Frayer, D. T. & Marleau, F. R., 2007, *PASP*, **119**, 994

Epinat, B., Amram, P. & Marcelin, M., 2008, *MNRAS*, **390**, 466

Ercolano, B., Barlow, M. J. & Storey, P. J., 2005, *MNRAS*, **362**, 1038

Ercolano, B., Barlow, M. J., Storey, P. J. & Liu, X., 2003, *MNRAS*, **340**, 1136

Ercolano, B., Barlow, M. J. & Sugerman, B. E. K., 2007, *MNRAS*, **375**, 753

Evans, A., 1993, *The dusty universe.*

Fabbri, J., Otsuka, M., Gallagher, J., Barlow, M. J., Sugerman, B. E. K., Wesson, R., Meixner, M., Clayton, G. C., Andrews, J. & Ercolano, B., 2011, *MNRAS, submitted*

Fabbri, J., Sugerman, B. & Barlow, M., 2005, *IAU Circ.*, **8489**, 1

Fassia, A., Meikle, W. P. S., Vacca, W. D., Kemp, S. N., Walton, N. A., Pollacco, D. L., Smartt, S., Oscoz, A., Aragón-Salamanca, A., Bennett, S., Hawarden, T. G., Alonso, A., Alcalde, D., Pedrosa, A., Telting, J., Arevalo, M. J., Deeg, H. J., Garzón, F., Gómez-Roldán,

A., Gómez, G., Gutiérrez, C., López, S., Rozas, M., Serra-Ricart, M. & Zapatero-Osorio, M. R., 2000, *MNRAS*, **318**, 1093

Fazio, G. G., Hora, J. L., Allen, L. E., Ashby, M. L. N., Barmby, P., Deutsch, L. K., Huang, J.-S., Kleiner, S., Marengo, M., Megeath, S. T., Melnick, G. J., Pahre, M. A., Patten, B. M., Polizotti, J., Smith, H. A., Taylor, R. S., Wang, Z., Willner, S. P., Hoffmann, W. F., Pipher, J. L., Forrest, W. J., McMurty, C. W., McCreight, C. R., McKelvey, M. E., McMurray, R. E., Koch, D. G., Moseley, S. H., Arendt, R. G., Mentzell, J. E., Marx, C. T., Losch, P., Mayman, P., Eichhorn, W., Krebs, D., Jhabvala, M., Gezari, D. Y., Fixsen, D. J., Flores, J., Shakoorzadeh, K., Jungo, R., Hakun, C., Workman, L., Karpati, G., Kichak, R., Whitley, R., Mann, S., Tollestrup, E. V., Eisenhardt, P., Stern, D., Gorjian, V., Bhattacharya, B., Carey, S., Nelson, B. O., Glaccum, W. J., Lacy, M., Lowrance, P. J., Laine, S., Reach, W. T., Stauffer, J. A., Surace, J. A., Wilson, G., Wright, E. L., Hoffman, A., Domingo, G. & Cohen, M., 2004, *ApJSS*, **154**, 10

Feldmeier, J. J., Ciardullo, R. & Jacoby, G. H., 1997, *ApJ*, **479**, 231

Filippenko, A. V., 1997, *Ann. Rev. Astr. Astrophys.*, **35**, 309

Filippenko, A. V., Foley, R. J., Treu, T. & Malkan, M. A., 2004, *IAU Circ.*, **8414**, 1

Filippenko, A. V., Li, W. D. & Modjaz, M., 1999*a*, *IAU Circ.*, **7152**, 2

Filippenko, A. V., Matheson, T., Guhathakurta, P. & Szomoru, A., 1999*b*, *IAU Circ.*, **7150**, 2

Filippenko, A. V. & Moran, E. C., 1998, *IAU Circ.*, **6830**, 2

Fitzgerald, M. P., 1970, *A&A*, **4**, 234

Fox, O. D., Chevalier, R. A., Dwek, E., Skrutskie, M. F., Sugerman, B. E. K. & Leisenring, J. M., 2010, *ApJ*, **725**, 1768

Fransson, C., Gilmozzi, R., Groeningsson, P., Hanuschik, R., Kjaer, K., Leibundgut, B. & Spyromilio, J., 2007, *The Messenger*, **127**, 44

Fransson, C., Grewing, M., Cassatella, A., Wamsteker, W. & Panagia, N., 1987, *A&A*, **177**, L33

Fransson, C. & Kozma, C., 1993, *ApJ*, **408**, L25

Freedman, W. L., Madore, B. F., Gibson, B. K., Ferrarese, L., Kelson, D. D., Sakai, S., Mould, J. R., Kennicutt, Jr., R. C., Ford, H. C., Graham, J. A., Huchra, J. P., Hughes, S. M. G., Illingworth, G. D., Macri, L. M. & Stetson, P. B., 2001, *ApJ*, **553**, 47

Fruchter, A. S. & Hook, R. N., 2002, *PASP*, **114**, 144

Gallagher, J. S., Clayton, G., Andrews, J., Sugerman, B., Clem, J., Barlow, M., Ercolano, B., Fabbri, J., Wesson, R., Otsuka, M. & Meixner, M., 2011, *in prep.*

Garnavich, P., Jha, S., Kirshner, R., Calkins, M. & Brown, W., 1999, *IAU Circ.*, **7150**, 1

Gehrz, R. D. & Ney, E. P., 1987, *Proceedings of the National Academy of Science*, **84**, 6961

Gerardy, C. L., Fesen, R. A., Höflich, P. & Wheeler, J. C., 2000, *AJ*, **119**, 2968

Gerardy, C. L., Fesen, R. A., Nomoto, K., Garnavich, P. M., Jha, S., Challis, P. M., Kirshner, R. P., Höflich, P. & Wheeler, J. C., 2002, *ApJ*, **575**, 1007

Glass, I. S., 1999, *Handbook of Infrared Astronomy*

Glasse, A. C., Atad-Ettedgui, E. I. & Harris, J. W., 1997, in A. L. Ardeberg (ed.), *Proc. SPIE Vol. 2871, p. 1197-1203, Optical Telescopes of Today and Tomorrow, Arne L. Ardeberg; Ed.*, pp. 1197–1203

Gomez, H. L., Dunne, L., Ivison, R. J., Reynoso, E. M., Thompson, M. A., Sibthorpe, B., Eales, S. A., Delaney, T. M., Maddox, S. & Isaak, K., 2009, *MNRAS*, **397**, 1621

Gordon, K. D., Rieke, G. H., Engelbracht, C. W., Muzerolle, J., Stansberry, J. A., Misselt, K. A., Morrison, J. E., Cadien, J., Young, E. T., Dole, H., Kelly, D. M., Alonso-Herrero, A., Egami, E., Su, K. Y. L., Papovich, C., Smith, P. S., Hines, D. C., Rieke, M. J., Blaylock, M., Pérez-González, P. G., Le Floc'h, E., Hinz, J. L., Latter, W. B., Hesselroth, T., Frayer, D. T., Noriega-Crespo, A., Masci, F. J., Padgett, D. L., Smylie, M. P. & Haegel, N. M., 2005, *PASP*, **117**, 503

Graham, J. R. & Meikle, W. P. S., 1986, *MNRAS*, **221**, 789

Graham, J. R., Meikle, W. P. S., Selby, M. J., Allen, D. A., Evans, A., Pearce, G., Bode, M. F., Longmore, A. J. & Williams, P. M., 1983, *Nature*, **304**, 709

Grosdidier, Y., Moffat, A. F. J., Joncas, G. & Acker, A., 1998, *ApJ*, **506**, L127

Hamuy, M., 2003, *ApJ*, **582**, 905

Hamuy, M., Pinto, P. A., Maza, J., Suntzeff, N. B., Phillips, M. M., Eastman, R. G., Smith, R. C., Corbally, C. J., Burstein, D., Li, Y., Ivanov, V., Moro-Martin, A., Strolger, L. G., de Souza, R. E., dos Anjos, S., Green, E. M., Pickering, T. E., González, L., Antezana, R., Wischnjewsky, M., Galaz, G., Roth, M., Persson, S. E. & Schommer, R. A., 2001, *ApJ*, **558**, 615

Hamuy, M. & Suntzeff, N. B., 1990, *AJ*, **99**, 1146

Hartmann, D. H., 2010, *Nature Physics*, **6**, 241

Hendry, M. A., Smartt, S. J., Maund, J. R., Pastorello, A., Zampieri, L., Benetti, S., Turatto, M., Cappellaro, E., Meikle, W. P. S., Kotak, R., Irwin, M. J., Jonker, P. G., Vermaas, L., Peletier, R. F., van Woerden, H., Exter, K. M., Pollacco, D. L., Leon, S., Verley, S., Benn, C. R. & Pignata, G., 2005, *MNRAS*, **359**, 906

Herant, M. & Woosley, S. E., 1994, *ApJ*, **425**, 814

Herrmann, K. A., Ciardullo, R., Feldmeier, J. J. & Vinciguerra, M., 2008, *ApJ*, **683**, 630

Hillebrandt, W., Hoeflich, P., Weiss, A. & Truran, J. W., 1987, *Nature*, **327**, 597

Hoppe, P., Leitner, J., Gröner, E., Marhas, K. K., Meyer, B. S. & Amari, S., 2010, *ApJ*, **719**, 1370

Houck, J. R., Roellig, T. L., van Cleve, J., Forrest, W. J., Herter, T., Lawrence, C. R., Matthews, K., Reitsema, H. J., Soifer, B. T., Watson, D. M., Weedman, D., Huisjen, M., Troeltzsch, J., Barry, D. J., Bernard-Salas, J., Blacken, C. E., Brandl, B. R., Charmandaris, V., Devost, D., Gull, G. E., Hall, P., Henderson, C. P., Higdon, S. J. U., Pirger, B. E., Schoenwald, J., Sloan, G. C., Uchida, K. I., Appleton, P. N., Armus, L., Burgdorf, M. J., Fajardo-Acosta, S. B., Grillmair, C. J., Ingalls, J. G., Morris, P. W. & Teplitz, H. I., 2004, *ApJSS*, **154**, 18

Howarth, I. D., Murray, J., Mills, D. & Berry, D. S., 2004, *Starlink User Note 50.24*

Hoyle, F. & Wickramasinghe, N. C., 1970, *Nature*, **226**, 62

Humphreys, R. M., 2010, in C. Leitherer, P. Bennett, P. Morris, & J. van Loon (ed.), *Astronomical Society of the Pacific Conference Series*, volume 425 of *Astronomical Society of the Pacific Conference Series*, pp. 247–+

IRSIST (Instrument Support Team), 2005, *InfraRed Spectrograph S11 Pipeline Handbook*, Spitzer Science Center, California Institute of Technology, Pasadena, USA, version 1.0 edition

Ishihara, D., Kaneda, H., Furuzawa, A., Kunieda, H., Suzuki, T., Koo, B., Lee, H., Lee, J. & Onaka, T., 2010, *A&A*, **521**, L61+

Ivison, R. J., Smail, I., Barger, A. J., Kneib, J.-P., Blain, A. W., Owen, F. N., Kerr, T. H. & Cowie, L. L., 2000, *MNRAS*, **315**, 209

Karachentsev, I. D., Karachentseva, V. E., Huchtmeier, W. K. & Makarov, D. I., 2004, *AJ*, **127**, 2031

Karachentsev, I. D., Sharina, M. E. & Huchtmeier, W. K., 2000, *A&A*, **362**, 544

Kennicutt, R. C., Armus, L., Bendo, G., Calzetti, D., Dale, D. A., Draine, B. T., Engelbracht, C. W., Gordon, K. D., Grauer, A. D., Helou, G., Hollenbach, D. J., Jarrett, T. H., Kewley, L. J., Leitherer, C., Li, A., Malhotra, S., Regan, M. W., Rieke, G. H., Rieke, M. J., Roussel, H., Smith, J.-D. T., Thornley, M. D. & Walter, F., 2003, *PASP*, **115**, 928

Kirshner, R. P., Oke, J. B., Penston, M. V. & Searle, L., 1973, *ApJ*, **185**, 303

Kotak, R., Meikle, P., Pozzo, M., van Dyk, S. D., Farrah, D., Fesen, R., Filippenko, A. V., Foley, R. J., Fransson, C., Gerardy, C. L., Höflich, P. A., Lundqvist, P., Mattila, S., Sollerman, J. & Wheeler, J. C., 2006, *ApJ*, **651**, L117

Kotak, R., Meikle, P., van Dyk, S. D., Höflich, P. A. & Mattila, S., 2005, *ApJ*, **628**, L123

Kotak, R., Meikle, W. P. S., Farrah, D., Gerardy, C. L., Foley, R. J., Van Dyk, S. D., Fransson, C., Lundqvist, P., Sollerman, J., Fesen, R., Filippenko, A. V., Mattila, S., Silverman, J. M., Andersen, A. C., Höflich, P. A., Pozzo, M. & Wheeler, J. C., 2009, *ApJ*, **704**, 306

Kozasa, T., Hasegawa, H. & Nomoto, K., 1989, *ApJ*, **344**, 325

Kozasa, T., Hasegawa, H. & Nomoto, K., 1991, *A&A*, **249**, 474

Krause, O., Birkmann, S. M., Rieke, G. H., Lemke, D., Klaas, U., Hines, D. C. & Gordon, K. D., 2004, *Nature*, **432**, 596

Krause, O., Birkmann, S. M., Usuda, T., Hattori, T., Goto, M., Rieke, G. H. & Misselt, K. A., 2008*a*, *Science*, **320**, 1195

Krause, O., Tanaka, M., Usuda, T., Hattori, T., Goto, M., Birkmann, S. & Nomoto, K., 2008*b*, *Nature*, **456**, 617

Krisciunas, K., Sinton, W., Tholen, K., Tokunaga, A., Golisch, W., Griep, D., Kaminski, C., Impey, C. & Christian, C., 1987, *PASP*, **99**, 887

Kunkel, W., Madore, B., Shelton, I., Duhalde, O., Bateson, F. M., Jones, A., Moreno, B., Walker, S., Garradd, G., Warner, B. & Menzies, J., 1987, *IAU Circ.*, **4316**, 1

Lagage, P. O., Claret, A., Ballet, J., Boulanger, F., Cesarsky, C. J., Cesarsky, D., Fransson, C. & Pollock, A., 1996, *A&A*, **315**, L273

Leonard, D. C., 2010, *ArXiv e-prints*

Leonard, D. C., Kanbur, S. M., Ngeow, C. C. & Tanvir, N. R., 2003, *ApJ*, **594**, 247

Li, A., 2009, in *Small Bodies in Planetary Systems* (Springer Berlin / Heidelberg), volume 758 of *Lecture Notes in Physics*, pp. 1–22

Li, H., McCray, R. & Sunyaev, R. A., 1993, *ApJ*, **419**, 824

Li, W., Filippenko, A. V. & van Dyk, S. D., 2005*a*, *The Astronomer's Telegram*, **492**, 1

Li, W., Filippenko, A. V., Van Dyk, S. D., Hu, J., Qiu, Y., Modjaz, M. & Leonard, D. C., 2002, *PASP*, **114**, 403

Li, W., Li, C., Filippenko, A. V. & Moran, E. C., 1998, *IAU Circ.*, **6829**, 1

Li, W., van Dyk, S. D., Filippenko, A. V. & Cuillandre, J.-C., 2005*b*, *PASP*, **117**, 121

Li, W. D., 1999*a*, *IAU Circ.*, **7149**, 1

Li, W. D., 1999*b*, *IAU Circ.*, **7294**, 1

Litvinova, I. Y. & Nadezhin, D. K., 1985, *Soviet Astronomy Letters*, **11**, 145

Lodders, K. & Amari, S., 2005, *Chemie der Erde - Geochemistry*, **65**(2), 93

Lord, S. D., 1992, *NASA Technical Memorandum*, **103957**

Lucy, L. B., Danziger, I. J., Gouiffes, C. & Bouchet, P., 1989, in G. Tenorio-Tagle, M. Moles & J. Melnick (eds.), *IAU Colloq. 120: Structure and Dynamics of the Interstellar Medium*, volume 350 of *Lecture Notes in Physics, Berlin Springer Verlag*, pp. 164–+

Lucy, L. B., Danziger, I. J., Gouiffes, C. & Bouchet, P., 1991, in S. E. Woosley (ed.), *Supernovae. The Tenth Santa Cruz Workshop in Astronomy and Astrophysics, held July 9-21, 1989, Lick Observatory. Editor, S.E. Woosley; Publisher, Springer-Verlag, New York, 1991. LC # QB856 .S26 1989. ISBN # 0387970711. P. 82, 1991*, pp. 82–+

Maguire, K., di Carlo, E., Smartt, S. J., Pastorello, A., Tsvetkov, D. Y., Benetti, S., Spiro, S., Arkharov, A. A., Beccari, G., Botticella, M. T., Cappellaro, E., Cristallo, S., Dolci, M., Elias-Rosa, N., Fiaschi, M., Gorshanov, D., Harutyunyan, A., Larionov, V. M., Navasardyan, H., Pietrinferni, A., Raimondo, G., di Rico, G., Valenti, S., Valentini, G. & Zampieri, L., 2010, *MNRAS*, **404**, 981

Makovoz, D., Roby, T., Khan, I. & Booth, H., 2006, in *Society of Photo-Optical Instrumentation Engineers (SPIE) Conference Series*, volume 6274 of *Presented at the Society of Photo-Optical Instrumentation Engineers (SPIE) Conference*

Markwick-Kemper, F., Gallagher, S. C., Hines, D. C. & Bouwman, J., 2007, *ApJ*, **668**, L107

Martí-Vidal, I., Marcaide, J. M., Alberdi, A., Guirado, J. C., Lara, L., Pérez-Torres, M. A., Ros, E., Argo, M. K., Beswick, R. J., Muxlow, T. W. B., Pedlar, A., Shapiro, I. I., Stockdale, C. J., Sramek, R. A., Weiler, K. W. & Vinko, J., 2007, *A&A*, **470**, 1071

Masci, F. J., Laher, R., Fang, F., Fowler, J. W., Lee, W., Stolovy, S., Padgett, D. & Moshir, M., 2005, in P. Shopbell, M. Britton & R. Ebert (eds.), *Astronomical Data Analysis Software and Systems XIV*, volume 347 of *Astronomical Society of the Pacific Conference Series*, pp. 468–+

Massey, P. & Davis, L. E., 1992, *A User's Guide to Stellar CCD Photometry with IRAF*, IRAF Programming Group, National Optical Observatories, Tuscon, Arizona 85726, USA

Mathis, J. S., Rumpl, W. & Nordsieck, K. H., 1977, *ApJ*, **217**, 425

Matsuura, M., Barlow, M. J., Zijlstra, A. A., Whitelock, P. A., Cioni, M., Groenewegen, M. A. T., Volk, K., Kemper, F., Kodama, T., Lagadec, E., Meixner, M., Sloan, G. C. & Srinivasan, S., 2009, *MNRAS*, **396**, 918

Mattila, S., Meikle, W. P. S., Lundqvist, P., Pastorello, A., Kotak, R., Eldridge, J., Smartt, S., Adamson, A., Gerardy, C. L., Rizzi, L., Stephens, A. W. & van Dyk, S. D., 2008, *MNRAS*, **389**, 141

McCray, R., 1993, *Ann. Rev. Astr. Astrophys.*, **31**, 175

Meikle, W. P. S., Kotak, R., Farrah, D., Mattila, S., Van Dyk, S. D., Andersen, A. C., Fesen, R., Filippenko, A. V., Foley, R. J., Fransson, C., Gerardy, C. L., Höflich, P. A., Lundqvist, P., Pozzo, M., Sollerman, J. & Wheeler, J. C., 2011, *ApJ*, **732**, 109

Meikle, W. P. S., Mattila, S., Gerardy, C. L., Kotak, R., Pozzo, M., van Dyk, S. D., Farrah, D., Fesen, R. A., Filippenko, A. V., Fransson, C., Lundqvist, P., Sollerman, J. & Wheeler, J. C., 2006, *ApJ*, **649**, 332

Meikle, W. P. S., Mattila, S., Pastorello, A., Gerardy, C. L., Kotak, R., Sollerman, J., Van Dyk, S. D., Farrah, D., Filippenko, A. V., Höflich, P., Lundqvist, P., Pozzo, M. & Wheeler, J. C., 2007, *ApJ*, **665**, 608

Meikle, W. P. S., Spyromilio, J., Allen, D. A., Varani, G. & Cumming, R. J., 1993, *MNRAS*, **261**, 535

Meixner, M., Smee, S., Doering, R. L., Barkhouser, R. H., Miller, T., Orndorff, J., Knezek, P., Churchwell, E., Scharfstein, G., Percival, J. W., Mills, D., Corson, C. & Joyce, R. R., 2010, *PASP*, **122**, 451

Merrill, K. M., 1980, *IAU Circ.*, **3444**, 3

MIPS Instrument Support Team (SSC), MIPS Instrument Team (Uni. of Arziona) & Observer Support Team (SSC), 2007, *Multiband Imaging Photometer for Spitzer (MIPS) Data Handbook*, Spitzer Science Center, California Institute of Technology, Pasadena, USA, version 3.3.1 edition

Misra, K., Pooley, D., Chandra, P., Bhattacharya, D., Ray, A. K., Sagar, R. & Lewin, W. H. G., 2007, *MNRAS*, **381**, 280

Morgan, H. L., Dunne, L., Eales, S. A., Ivison, R. J. & Edmunds, M. G., 2003, *ApJL*, **597**, L33

Morgan, H. L. & Edmunds, M. G., 2003, *MNRAS*, **343**, 427

Morris, P. W., Waters, L. B. F. M., Barlow, M. J., Lim, T., de Koter, A., Voors, R. H. M., Cox, P., de Graauw, T., Henning, T., Hony, S., Lamers, H. J. G. L. M., Mutschke, H. & Trams, N. R., 1999, *Nature*, **402**, 502

Nittler, L. R., Amari, S., Zinner, E., Woosley, S. E. & Lewis, R. S., 1996, *ApJ*, **462**, L31+

Nozawa, T., Kozasa, T., Tominaga, N., Maeda, K., Umeda, H., Nomoto, K. & Krause, O., 2010, *ApJ*, **713**, 356

Nozawa, T., Kozasa, T., Umeda, H., Maeda, K. & Nomoto, K., 2003, *ApJ*, **598**, 785

Nugent, P., Sullivan, M., Ellis, R., Gal-Yam, A., Leonard, D. C., Howell, D. A., Astier, P., Carlberg, R. G., Conley, A., Fabbro, S., Fouchez, D., Neill, J. D., Pain, R., Perrett, K., Pritchet, C. J. & Regnault, N., 2006, *ApJ*, **645**, 841

Panagia, N., 2003, in K. Weiler (ed.), *Supernovae and Gamma-Ray Bursters*, volume 598 of *Lecture Notes in Physics, Berlin Springer Verlag*, pp. 113–144

Patat, F., Barbon, R., Cappellaro, E. & Turatto, M., 1994, *A&A*, **282**, 731

Pizarro, O., Miranda, J., Pasquini, L., Leibundgut, B., Jarvis, B., Sivan, J. P. & Burwitz, V., 1990, *IAU Circ.*, **5003**, 1

Pozzo, M., Meikle, W. P. S., Fassia, A., Geballe, T., Lundqvist, P., Chugai, N. N. & Sollerman, J., 2004, *MNRAS*, **352**, 457

Pozzo, M., Meikle, W. P. S., Rayner, J. T., Joseph, R. D., Filippenko, A. V., Foley, R. J., Li, W., Mattila, S. & Sollerman, J., 2006, *MNRAS*, **368**, 1169

Prieto, J. L., 2008, *The Astronomer's Telegram*, **1550**, 1

Prieto, J. L., Kistler, M. D., Thompson, T. A., Yüksel, H., Kochanek, C. S., Stanek, K. Z., Beacom, J. F., Martini, P., Pasquali, A. & Bechtold, J., 2008, *ApJ*, **681**, L9

Reach, W. T., Megeath, S. T., Cohen, M., Hora, J., Carey, S., Surace, J., Willner, S. P., Barmby, P., Wilson, G., Glaccum, W., Lowrance, P., Marengo, M. & Fazio, G. G., 2005*a*, *PASP*, **117**, 978

Reach, W. T., Surace, J., Glaccum, W., Carey, S., Lacey, M., Brandenburg, H., Lowrance, P. & Im, M., 2005*b*, *Infrared Array Camera Pipeline Description Document*, Spitzer Science Center, California Institute of Technology, Pasadena, USA, version 1.0 edition

Reach, W. T., Surace, J., Glaccum, W., Carey, S., Lacey, M., Wilson, G., Lowrance, P., Nelson, B., Barmby, P., Pahre, M., Wang, Z. & Laine, S., 2006, *Infrared Array Camera Data*

Handbook, Spitzer Science Center, California Institute of Technology, Pasadena, USA, version 3.0 edition

Rho, J., Jarrett, T. H. & Chevalier, R., 2007*a*, *IAU Circ.*, **8799**, 2

Rho, J., Jarrett, T. H., Chugai, N. N. & Chevalier, R. A., 2007*b*, *ApJ*, **666**, 1108

Rho, J., Kozasa, T., Reach, W. T., Smith, J. D., Rudnick, L., DeLaney, T., Ennis, J. A., Gomez, H. & Tappe, A., 2008, *ApJ*, **673**, 271

Richardson, D., Branch, D., Casebeer, D., Millard, J., Thomas, R. C. & Baron, E., 2002, *AJ*, **123**, 745

Rieke, G. H., Blaylock, M., Decin, L., Engelbracht, C., Ogle, P., Avrett, E., Carpenter, J., Cutri, R. M., Armus, L., Gordon, K., Gray, R. O., Hinz, J., Su, K. & Willmer, C. N. A., 2008, *AJ*, **135**, 2245

Rieke, G. H., Young, E. T., Engelbracht, C. W., Kelly, D. M., Low, F. J., Haller, E. E., Beeman, J. W., Gordon, K. D., Stansberry, J. A., Misselt, K. A., Cadien, J., Morrison, J. E., Rivlis, G., Latter, W. B., Noriega-Crespo, A., Padgett, D. L., Stapelfeldt, K. R., Hines, D. C., Egami, E., Muzerolle, J., Alonso-Herrero, A., Blaylock, M., Dole, H., Hinz, J. L., Le Floc'h, E., Papovich, C., Pérez-González, P. G., Smith, P. S., Su, K. Y. L., Bennett, L., Frayer, D. T., Henderson, D., Lu, N., Masci, F., Pesenson, M., Rebull, L., Rho, J., Keene, J., Stolovy, S., Wachter, S., Wheaton, W., Werner, M. W. & Richards, P. L., 2004, *ApJSS*, **154**, 25

Robson, I., Priddey, R. S., Isaak, K. G. & McMahon, R. G., 2004, *MNRAS*, **351**, L29

Roche, P. F., Aitken, D. K. & Smith, C. H., 1991, *MNRAS*, **252**, 39P

Roche, P. F., Aitken, D. K. & Smith, C. H., 1993, *MNRAS*, **261**, 522

Roche, P. F., Aitken, D. K., Smith, C. H. & James, S. D., 1989, *Nature*, **337**, 533

Sahu, D. K., Anupama, G. C., Srividya, S. & Muneer, S., 2006, *MNRAS*, **372**, 1315

Sakon, I., Onaka, T., Wada, T., Ohyama, Y., Kaneda, H., Ishihara, D., Tanabé, T., Minezaki, T., Yoshii, Y., Tominaga, N., Nomoto, K., Nozawa, T., Kozasa, T., Tanaka, M., Suzuki, T., Umeda, H., Ohyabu, S., Usui, F., Matsuhara, H., Nakagawa, T. & Murakami, H., 2009, *ApJ*, **692**, 546

Schlegel, D. J., Finkbeiner, D. P. & Davis, M., 1998, *ApJ*, **500**, 525

Schuster, M. T., Marengo, M., Hora, J. L., Fazio, G. G., Humphreys, R. M., Gehrz, R. D., Hinz, P. M., Kenworthy, M. A. & Hoffmann, W. F., 2009, *ApJ*, **699**, 1423

Shanks, T., Tanvir, N. R., Major, J. V., Doel, A. P., Dunlop, C. N. & Myers, R. M., 1992, *MNRAS*, **256**, 29P

Sibthorpe, B., Ade, P. A. R., Bock, J. J., Chapin, E. L., Devlin, M. J., Dicker, S., Griffin, M., Gundersen, J. O., Halpern, M., Hargrave, P. C., Hughes, D. H., Jeong, W., Kaneda, H., Klein, J., Koo, B., Lee, H., Marsden, G., Martin, P. G., Mauskopf, P., Moon, D., Netterfield, C. B., Olmi, L., Pascale, E., Patanchon, G., Rex, M., Roy, A., Scott, D., Semisch, C., Truch, M. D. P., Tucker, C., Tucker, G. S., Viero, M. P. & Wiebe, D. V., 2010, *ApJ*, **719**, 1553

Smartt, S. J., 2009, *Ann. Rev. Astr. Astrophys.*, **47**, 63

Smith, N., Foley, R. J. & Filippenko, A. V., 2008, *ApJ*, **680**, 568

Smith, N., Hinkle, K. H. & Ryde, N., 2009*a*, *AJ*, **137**, 3558

Smith, N., Silverman, J. M., Chornock, R., Filippenko, A. V., Wang, X., Li, W., Ganeshalingam, M., Foley, R. J., Rex, J. & Steele, T. N., 2009*b*, *ApJ*, **695**, 1334

Spergel, D. N., Bean, R., Dore', O., Nolta, M. R., Bennett, C. L., Hinshaw, G., Jarosik, N., Komatsu, E., Page, L., Peiris, H. V., Verde, L., Barnes, C., Halpern, M., Hill, R. S., Kogut, A., Limon, M., Meyer, S. S., Odegard, N., Tucker, G. S., Weiland, J. L., Wollack, E. & Wright, E. L., 2006, *ArXiv Astrophysics e-prints*

Spitzer Science Team, 2007, *Spitzer Space Telescope Observer's Manual*, Spitzer Science Center, California Institute of Technology, Pasadena, USA, version 8.0 edition

Spyromilio, J., Meikle, W. P. S., Learner, R. C. M. & Allen, D. A., 1988, *Nature*, **334**, 327

Stetson, P. B., 1987, *PASP*, **99**, 191

Stetson, P. B., 1990, *PASP*, **102**, 932

Stetson, P. B., 1992, in D. M. Worrall, C. Biemesderfer & J. Barnes (eds.), *Astronomical Data Analysis Software and Systems I*, volume 25 of *Astronomical Society of the Pacific Conference Series*, pp. 297–+

Stockdale, C. J., Weiler, K. W., van Dyk, S. D., Sramek, R. A., Panagia, N. & Marcaide, J. M., 2004, *IAU Circ.*, **8415**, 1

Sugerman, B., Meixner, M., Fabbri, J. & Barlow, M., 2004, *IAU Circ.*, **8442**, 2

Sugerman, B. E. K., 2005, *ApJ*, **632**, L17

Sugerman, B. E. K., Crotts, A. P. S., Kunkel, W. E., Heathcote, S. R. & Lawrence, S. S., 2005, *ApJSS*, **159**, 60

Sugerman, B. E. K., Ercolano, B., Barlow, M. J., Tielens, A. G. G. M., Clayton, G. C., Zijlstra, A. A., Meixner, M., Speck, A., Gledhill, T. M., Panagia, N., Cohen, M., Gordon, K. D., Meyer, M., Fabbri, J., Bowey, J. E., Welch, D. L., Regan, M. W. & Kennicutt, R. C., 2006, *Science*, **313**, 196

Sugerman, B. E. K., Lawrence, S. S., Crotts, A. P. S., Bouchet, P. & Heathcote, S. R., 2002, *ApJ*, **572**, 209

Sugerman, B. E. K., Wesson, R., Barlow, M. J., Otsuka, M., Meixner, M., Fabbri, J., Clayton, G. C., Gallagher, J., Andrews, J. & Ercolano, B., 2011, *in prep.*

Suntzeff, N. B. & Bouchet, P., 1990, *AJ*, **99**, 650

Suntzeff, N. B., Phillips, M. M., Depoy, D. L., Elias, J. H. & Walker, A. R., 1991, *AJ*, **102**, 1118

Szalai, T., Vinkó, J., Balog, Z., Gáspár, A., Block, M. & Kiss, L. L., 2011, *A&A*, **527**, A61+

Telesco, C., Becklin, E., Koehler, R. & Gatley, I., 1981, *IAU Circ.*, **3613**, 2

Telesco, C. M., Pina, R. K., Hanna, K. T., Julian, J. A., Hon, D. B. & Kisko, T. M., 1998, in A. M. Fowler (ed.), *Proc. SPIE Vol. 3354, p. 534-544, Infrared Astronomical Instrumentation, Albert M. Fowler; Ed.*, volume 3354 of *Presented at the Society of Photo-Optical Instrumentation Engineers (SPIE) Conference*, pp. 534–544

Thatte, D., Dahlen, T. & others, 2009, *NICMOS Data Handbook*, Space Telescope Science Institute, Baltimore, MD, USA, version 8.0 edition

Thompson, T. A., Prieto, J. L., Stanek, K. Z., Kistler, M. D., Beacom, J. F. & Kochanek, C. S., 2009, *ApJ*, **705**, 1364

Tielens, A. G. G. M., Waters, L. B. F. M. & Bernatowicz, T. J., 2005, in A. N. Krot, E. R. D. Scott, & B. Reipurth (ed.), *Chondrites and the Protoplanetary Disk*, volume 341 of *Astronomical Society of the Pacific Conference Series*, pp. 605–+

Todini, P. & Ferrara, A., 2001, *MNRAS*, **325**, 726

Tokunaga, A. T., 1984, *AJ*, **89**, 172

Tomaney, A. B. & Crotts, A. P. S., 1996, *AJ*, **112**, 2872

Travaglio, C., Gallino, R., Amari, S., Zinner, E., Woosley, S. & Lewis, R. S., 1999, *ApJ*, **510**, 325

Trumpler, R. J., 1930, *PASP*, **42**, 214

Turatto, M., 2003, in K. Weiler (ed.), *Supernovae and Gamma-Ray Bursters*, volume 598 of *Lecture Notes in Physics, Berlin Springer Verlag*, pp. 21–36

Tuthill, P. G., Monnier, J. D. & Danchi, W. C., 2002, in A. F. J. Moffat & N. St-Louis (ed.), *Interacting Winds from Massive Stars*, volume 260 of *Astronomical Society of the Pacific Conference Series*, pp. 321–+

Ueta, T. & Meixner, M., 2003, *ApJ*, **586**, 1338

Van Dyk, S. D., Peng, C. Y., Barth, A. J. & Filippenko, A. V., 1999, *AJ*, **118**, 2331

Van Dyk, S. D., Peng, C. Y., King, J. Y., Filippenko, A. V., Treffers, R. R., Li, W. & Richmond, M. W., 2000, *PASP*, **112**, 1532

Walker, A. R. & Suntzeff, N. B., 1991, *PASP*, **103**, 958

Weis, K. & Bomans, D. J., 2005, *A&A*, **429**, L13

Welch, D. L., Clayton, G. C., Campbell, A., Barlow, M. J., Sugerman, B. E. K., Meixner, M. & Bank, S. H. R., 2007, *ApJ*, **669**, 525

Werner, M. W., Roellig, T. L., Low, F. J., Rieke, G. H., Rieke, M., Hoffmann, W. F., Young, E., Houck, J. R., Brandl, B., Fazio, G. G., Hora, J. L., Gehrz, R. D., Helou, G., Soifer, B. T., Stauffer, J., Keene, J., Eisenhardt, P., Gallagher, D., Gautier, T. N., Irace, W., Lawrence, C. R., Simmons, L., Van Cleve, J. E., Jura, M., Wright, E. L. & Cruikshank, D. P., 2004, *ApJSS*, **154**, 1

Wesson, R., Barlow, M. J., Ercolano, B., Andrews, J. E., Clayton, G. C., Fabbri, J., Gallagher, J. S., Meixner, M., Sugerman, B. E. K., Welch, D. L. & Stock, D. J., 2010, *MNRAS*, **403**, 474

Whitelock, P. A., Catchpole, R. M., Menzies, J. W., Feast, M. W., Woosley, S. E., Allen, D., van Wyk, F., Marang, F., Laney, C. D., Winkler, H., Sekiguchi, K., Balona, L. A., Carter, B. S., Spencer Jones, J. H., Laing, J. D., Evans, T. L., Fairall, A. P., Buckley, D. A. H., Glass, I. S., Penston, M. V., da Costa, L. N., Bell, S. A., Hellier, C., Shara, M. & Moffat, A. F. J., 1989, *MNRAS*, **240**, 7P

Whittet, D. C. B. (ed.), 2003, *Dust in the galactic environment*

Wooden, D. H., 1997, in T. J. Bernatowicz & E. Zinner (ed.), *American Institute of Physics Conference Series*, volume 402 of *American Institute of Physics Conference Series*, pp. 317–376

Wooden, D. H., Rank, D. M., Bregman, J. D., Witteborn, F. C., Tielens, A. G. G. M., Cohen, M., Pinto, P. A. & Axelrod, T. S., 1993, *ApJSS*, **88**, 477

Woosley, S. E., Hartmann, D. & Pinto, P. A., 1989, *ApJ*, **346**, 395

Woosley, S. E. & Weaver, T. A., 1986, *Ann. Rev. Astr. Astrophys.*, **24**, 205

Yamaoka, H., Itagaki, K., Klotz, A., Pollas, C. & Boer, M., 2004, *IAU Circ.*, **8413**, 2

Zubko, V. G., Mennella, V., Colangeli, L. & Bussoletti, E., 1996, *MNRAS*, **282**, 1321

Zwitter, T., Munari, U. & Moretti, S., 2004, *IAU Circ.*, **8413**, 1

They will see us waving from such great heights,
"come down now", they'll say
but everything looks perfect from far away,
"come down now", but we'll stay...

– The Postal Service, *Such Great Heights*
(cover by Iron and Wine) 2003